

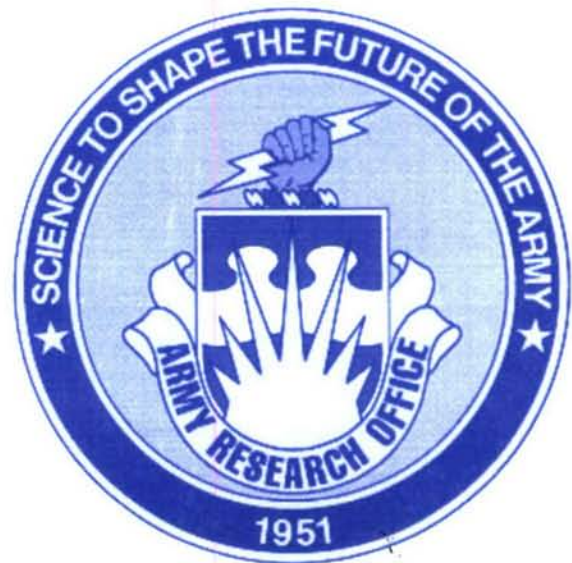
REPORT DOCUMENTATION PAGE

AFRL-SR-AR-TR-07-0334

Public reporting burden for this collection of information is estimated to average 1 hour per response, including the time for reviewing instructions, gathering existing data needed, and completing and reviewing this collection of information. Send comments regarding this burden estimate or any other aspect of this burden to Department of Defense, Washington Headquarters Services, Directorate for Information Operations and Reports (0704-0188) 4302. Respondents should be aware that notwithstanding any other provision of law, no person shall be subject to any penalty for failing to provide information if it does not display a currently valid OMB control number. **PLEASE DO NOT RETURN YOUR FORM TO THE ABOVE ADDRESS.**

1. REPORT DATE (DD-MM-YYYY) 16-08-2006		2. REPORT TYPE Technical		3. DATES COVERED (From - To) 01-06-2005 - 31-05-2006	
4. TITLE AND SUBTITLE (U) Army Research Office and Air Force Office of Scientific Research 2006 Contractors Meeting in Chemical Propulsion				5a. CONTRACT NUMBER	
				5b. GRANT NUMBER	
				5c. PROGRAM ELEMENT NUMBER 61102A, 61102F	
				5d. PROJECT NUMBER	
6. AUTHOR(S) Kevin McNesby and Julian M. Tishkoff				5e. TASK NUMBER	
				5f. WORK UNIT NUMBER	
				8. PERFORMING ORGANIZATION REPORT NUMBER	
7. PERFORMING ORGANIZATION NAME(S) AND ADDRESS(ES) Army Research Office Research Triangle Park NC 27709-2211 Air Force Office of Scientific Research Arlington VA 22203-1768				10. SPONSOR/MONITOR'S ACRONYM(S)	
9. SPONSORING / MONITORING AGENCY NAME(S) AND ADDRESS(ES) AFOSR/NA 875 North Randolph Street Suite 325, Room 3112 Arlington VA 22203-1768				11. SPONSOR/MONITOR'S REPORT NUMBER(S)	
12. DISTRIBUTION / AVAILABILITY STATEMENT Approved for public release; distribution is unlimited					
13. SUPPLEMENTARY NOTES					
14. ABSTRACT Abstracts are given for 6.1 basic research in chemical propulsion sponsored by the Army Research Office and the Air Force Office of Scientific Research.					
15. SUBJECT TERMS Flames, Propulsion, Gas Turbines, Diesel Engines, Scramjets, Pulse Detonation Engines, Hydrocarbon Fuels, Diagnostics, Spray, Droplet, Supercritical Fluids, Turbulence, Combustion					
16. SECURITY CLASSIFICATION OF:			17. LIMITATION OF ABSTRACT UL	18. NUMBER OF PAGES 181	19a. NAME OF RESPONSIBLE PERSON Julian M. Tishkoff
a. REPORT Unclassified	b. ABSTRACT Unclassified	c. THIS PAGE Unclassified			19b. TELEPHONE NUMBER (include area code) (703) 696-8478

**Army Research Office
And
Air Force Office of Scientific Research**



**2006
Contractors' Meeting
In Chemical Propulsion**

20070910359

ARO/AFOSR Contractors' Meeting in Chemical Propulsion

TABLE OF CONTENTS

Agenda	1
AFOSR Sponsored Research in Combustion and Diagnostics Julian Tishkoff, AFOSR.....	5
The ARO Single Investigator Program Kevin McNesby, ARO	9
Advanced Supercritical Fuels T. Edwards, C. Bunker, and T. Jackson, AFRL/PRTG.....	11
Thermodynamic, Transport and Chemical Properties of "Reference" JP-8 T. Bruno, National Institute of Standards and Technology.....	15
The Decomposition of Surrogate Fuel Molecules During Combustion <i>W. Tsang, and J.A. Manion, National Institute of Standards and Technology</i>	19
An Automated Process for Generation of New Fuel Breakdown Mechanisms A. Violi, University of Michigan.....	23
Computational and Experimental Study of Jet Fuel Combustion M.D. Smooke and A. Gomez, Yale University.....	27
Autoignition and Combustion of Diesel and JP-8 K. Seshadri, University of California, San Diego	31
Experimental and Theoretical Studies of Autoignition and Burning Speed of JP-8 and DF-2 H. Metghalchi, Northeastern University	35
Detailed and Simplified Chemical Kinetics of Aviation Fuels and Surrogates <i>R.P. Lindstedt, Imperial College of London</i>	39
Ignition Kinetics in Fuels Oxidation <i>C.K. Law, Princeton University</i>	43
Physical and Chemical Process in Flames <i>C.K. Law, Princeton University</i>	47
Chemical Modeling for Large Eddy Simulation of Turbulent Combustion <i>H. Pitsch, Stanford University</i>	53
Development of a Comprehensive and Predictive Reaction Mechanism of Liquid Hydrocarbon Fuel Combustion <i>H. Wang, University of Southern California</i>	57
A New Paradigm in Modeling and Simulations of Complex Oxidation Chemistry Using a Statistical Approach <i>J. Bellan, California Institute of Technology</i>	61
Experimental and Detailed Numerical Studies of Fundamental Flame Properties of Gaseous and Liquid Fuels <i>F.N. Egolfopoulos, University of Southern California</i>	65

Low Temperature Oxidation Chemistry of JP-8 <i>N.P. Cernansky and D.L. Miller, Drexel University</i>	69
Shock Tube Measurements for Liquid Fuels Combustion <i>R.K. Hanson, Stanford University</i>	73
Supercritical Fuel Pyrolysis <i>M.J. Wornat, Louisiana State University</i>	77
Experimental and Computational Characterization of Combustion Phenomena <i>J.R. Gord, AFRL/PRTC</i>	81
Advanced Diagnostics for Reacting Flows <i>R.K. Hanson, Stanford University</i>	85
Ramjet Research <i>C.D. Carter, M.R. Gruber, and S. Williams, AFRL/PRA</i>	89
Large Eddy Simulations of Supercritical Mixing Layers Based on Subgrid Scale Models Extracted from Direct Numerical Simulations <i>J. Bellan, California Institute of Technology</i>	93
Studies in Flame Propagation and Blowout <i>K.M. Lyons, North Carolina State University</i>	97
LES of Sooting Flames <i>S. Menon, Georgia Institute of Technology</i>	101
Formation of Soot in High-Pressure Diffusion Flames <i>W. Roberts, North Carolina State University</i>	105
Advanced Controls of Diesel Engines <i>N.A. Henein, Wayne State University</i>	109
Breakup of Liquid Streams at High Pressures <i>W.A. Sirignano and D.D. Joseph, University of California, Irvine</i>	113
Plasma-Propellant Interaction Studies <i>S.T. Thynell and T.A. Litzinger, Pennsylvania State University</i>	117
Modeling of Plasma Induced Ignition and Combustion <i>I. Boyd, M. Keidar, and A. Porwitzky, University of Michigan</i>	121
Liquid Fuel Combustion Using Porous Inert Media <i>A.K. Agrawal, University of Alabama and S.R. Gollahalli, University of Oklahoma</i>	125
Abstracts of Work Units Not Presented at the Meeting	
Turbulent Mixing and Combustion for High-Speed, Air-Breathing Propulsion Applications <i>P.E. Dimotakis, California Institute of Technology</i>	129
Plasma Research for Aerospace Propulsion <i>B.N. Ganguly, AFRL/PRPE</i>	133
Filtered Density Function for Subgrid Scale Modeling of Turbulent Diffusion Flames <i>P. Givi, University of Pittsburgh</i>	137

Two-Point Scalar Time-Series Measurements in Turbulent Partially Premixed Flames <i>G.B. King, N.M. Laurendeau, and M.W. Renfro, Purdue University</i>	141
PDF Modeling of Turbulent Combustion <i>S.B. Pope, Cornell University</i>	145
Pulse Detonation Physiochemical and Exhaust Relaxation Processes <i>F. Schauer, AFRL/PRTC</i>	149
Turbine Burners: Turbulent Combustion of Liquid Fuels <i>W.A. Sirignano, F. Liu, and D. Dunn-Rankin, University of California, Irvine</i>	153
Investigation of Scalar Filtered Density Function in Turbulent Partially Premixed Flames <i>C. Tong, Clemson University</i>	157
Concurrent Research on High Gravity (g) Combustion with Enabling Materials <i>J. Zelina, AFRL/PRTC</i>	161
List of Invitees	165

ARO/AFOSR CONTRACTORS MEETING

IN

CHEMICAL PROPULSION

Arlington, VA
12-14 June 2006

MONDAY, 12 JUNE

1:00 - 1:15 AFOSR Sponsored Research in Combustion and Diagnostics
Julian Tishkoff

1:15 - 1:30 Army Research Office Overview – Kevin McNesby

Topic: Hydrocarbon Fuel Characterization

1:30 - 2:00 Advanced Supercritical Fuels
Tim Edwards, AFRL/PR

2:00 - 2:30 Thermodynamic, Transport, and Chemical Properties of
"Reference" JP-8
Thomas Bruno, NIST

2:30 - 3:00 The Decomposition of Surrogate Fuel Molecules During
Combustion
Wing Tsang, NIST

3:00 - 3:30 An Automated Process for Generation of New Fuel
Breakdown Mechanisms
Angela Violi, University of Michigan

3:30 - 4:00 BREAK

4:00 - 4:30 Computational and Experimental Study of Jet Fuel
Combustion
Mitch Smooke, Yale University

4:30 - 5:00 Autoignition and Combustion of Diesel and JP-8
Kal Seshadri, University of California, San Diego

5:00 - 5:30 Experimental and Theoretical Studies of Autoignition and Burning
Speed of JP-8 and DF-2
Mohamed Metghalchi, Northeastern University

5:30 DINNER (on own)

TUESDAY, 13 JUNE

8:15 - 8:30 Announcements

TOPIC: Combustion Chemistry

8:30 - 9:00 Detailed and Simplified Chemical Kinetics of Aviation
Fuels and Surrogates
Peter Lindstedt, Imperial College of London

9:00 - 9:30 Ignition Kinetics in Fuels Oxidation
C. K. Law, Princeton University

9:30 - 10:00 Physical and Chemical Process in Flames
C. K. Law, Princeton University

10:00 - 10:30 BREAK

10:30 - 11:00 Chemical Modeling for Large Eddy Simulation of Turbulent
Combustion
Heinz Pitsch, Stanford University

11:00 - 11:30 Development of a Comprehensive and Predictive Reaction
Mechanism of Liquid Hydrocarbon Fuel Combustion
Hai Wang, University of Southern California

11:30 - 12:00 A New Paradigm in Modeling and Simulations of Complex
Oxidation Chemistry Using a Statistical Approach
Josette Bellan, Jet Propulsion Laboratory

12:00 - 1:00 LUNCH (on own)

TOPIC: Combustion Chemistry

1:15 - 1:45 Experimental and Detailed Numerical Studies of Fundamental
Flame Properties of Gaseous and Liquid Fuels
Fokion Egolfopoulos, University of Southern California

1:45 - 2:15 Low Temperature Oxidation Chemistry of JP-8
Nicholas Cernansky, Drexel University

2:15 - 2:45 Shock Tube Measurements for Liquid Fuels Combustion
Ronald Hanson, Stanford University

2:45 - 3:15 Supercritical Fuel Pyrolysis
M. J. Wornat, Louisiana State University

3:15 - 3:30 BREAK

3:30 - 5:00

TOPIC: Multidisciplinary Aerothermal Materials (ATM) Research Challenges
Discussion Led By Dr. Joan Fuller and Dr. John Schmisser, AFOSR

5:00 - 5:20 AFOSR BUSINESS SESSION
 AFOSR-Funded Researchers

5:20 DINNER (on own)

WEDNESDAY, 14 JUNE

TOPIC: Combustion Characterization

8:00 - 8:30 Experimental and Computational Characterization of
 Combustion Phenomena
 James Gord, AFRL/PR

8:30 - 9:00 Advanced Diagnostics for Reacting Flows
 Ronald Hanson, Stanford University

9:00 - 9:30 Ramjet Research
 Campbell Carter, AFRL/PR

9:30 - 10:00 Large Eddy Simulations of Supercritical Mixing Layers
 Based on Subgrid Scale Models Extracted From Direct
 Numerical Simulations
 Josette Bellan, Jet Propulsion Laboratory

10:00 - 10:30 BREAK

TOPIC: Mutliphase Combustion

10:30 - 11:00 Studies in Flame Propagation and Blowout
 Kevin Lyons, North Carolina State University

11:00 - 11:30 LES of Sooting Flames
 Suresh Menon, Georgia Institute of Technology

11:30 - 12:00 Formation of Soot in High-Pressure Diffusion Flames
 William Roberts, North Carolina State University

12:00 - 1:15 LUNCH (on own)

TOPIC: Engine Control and Plasma Propellant Ignition

1:15 - 1:45 Advanced Controls of Diesel Engines
 Naeim Henein, Wayne State University

1:45 - 2:15	Breakup of Liquid Streams at High Pressures William A. Sirignano, University of California, Irvine
2:15 - 2:45	Plasma-Propellant Interaction Studies Stefan Thynell, Pennsylvania State University
2:45 - 3:00	BREAK
3:00 - 3:30	Modeling of Plasma Induced Ignition and Combustion Iain Boyd, University of Michigan
3:30 - 4:00	Liquid Fuel Combustion Using Porous Inert Media Ajay Agrawal, University of Alabama
4:00 - 4:30	ARO BUSINESS SESSION ARO-Funded Researchers
4:30	ADJOURN

AFOSR SPONSORED RESEARCH IN COMBUSTION AND DIAGNOSTICS

PROGRAM MANAGER: JULIAN M. TISHKOFF

AIR FORCE OFFICE OF SCIENTIFIC RESEARCH

**875 North Randolph Street
Suite 325, Room 3112
Arlington VA 22203-1768**

SUMMARY/OVERVIEW: The Air Force Office of Scientific Research (AFOSR) program in combustion and diagnostics currently is focused on five areas of study: high-speed propulsion, turbulent combustion, diagnostics, supercritical fuel behavior, and plasma-enhanced combustion. An assessment of major research needs in each of these areas is presented.

TECHNICAL DISCUSSION

AFOSR is the single manager for Air Force basic research, including efforts based on external proposals and in-house work at the Air Force Research Laboratory (AFRL). Combustion and Diagnostics is assigned to the AFOSR Directorate of Aerospace and Materials Sciences along with programs in rocket and space propulsion, fluid and solid mechanics, and structural materials.

Interests of the AFOSR Combustion and Diagnostics subarea are given in the SUMMARY section above. Many achievements can be cited for these interests, yet imposing fundamental research challenges remain. The objective of the program is publications in the refereed scientific literature describing significant new understanding of multiphase turbulent reacting flow. Incremental improvements to existing scientific approaches, hardware development, and computer codes fall outside the scope of this objective.

The Combustion and Diagnostics subarea supports the Air Force commitment to aerospace propulsion through the Department of Defense National Aerospace Initiative (NAI). Accordingly, the research in this subarea will address research issues related to chemical propulsion for all Air Force aerospace missions, including combined cycle propulsion for access to space. This program will complement related research activities in space propulsion and energetic materials.

The primary focus of research in turbulent combustion is the creation of computational modeling tools for combustor designers that are both computationally tractable and quantitatively predictive. This research has been directed in two areas: the formulation of augmented reduced chemical kinetic mechanisms for the combustion of hydrocarbon fuels and the development of subgrid-scale models for large eddy simulation of turbulent combustion. In the past year two research areas have received particular emphasis: large eddy simulation modeling of turbulent combustion and surrogates for current and future hydrocarbon fuels.

Future airbreathing and chemical rocket propulsion systems will require propellants to absorb substantial thermal energy, raising their temperatures to supercritical thermodynamic conditions. Understanding and controlling fluid properties at these conditions will be crucial for avoiding thermal degradation and for optimizing subsequent processes within the combustor. Research has focused on the role of supercritical transport in the thermal destabilization of hydrocarbon fuel prior to combustion and on primary and secondary fuel breakup under transcritical and supercritical conditions.

Plasma research is one of six AFOSR Theme topics selected for support beginning in Fiscal Year 2001. The focus primarily is on the utilization of plasmas for ignition and flame stabilization in scramjets; however, the extension of this technology to other modes of chemical propulsion and energy conversion also is of interest. The theme research has been supplemented by research coordinated between universities and small businesses under the Department of Defense Small Business Technology Transfer (STTR) Program. The Air Force also supports related research activity in Russia under the Air Force Research Laboratory Russian Research Initiative. The Theme and Russian research activity was presented as part of a Weakly Ionized Gas Dynamics (WIG) Workshop at the 33rd AIAA Aerospace Sciences Meeting and Exhibit in January 2005. The next workshop will take place in January 2006.

Decisions on support for research proposals are based on scientific opportunities and technology needs. Researchers interested in submitting proposals should contact Dr. Tishkoff for information on time constraints associated with proposal evaluations. Further information on research interests and proposal preparation can be found on the AFOSR web site, <http://www.afosr.af.mil>. The availability of funds places a major constraint on program redirection and growth. Figure 1 shows the recent trend of funding for basic research in combustion and diagnostics from Air Force and DOD sources. Informal inquiries for new research are encouraged throughout the year. Formal proposals should be submitted by 1 April for peer review.

The purpose of this abstract has been to communicate AFOSR perceptions of research trends to the university and industrial research communities. However, communication from those communities back to AFOSR also is desirable and essential for creating new research opportunities. Therefore, all proposals and inquiries for fundamental research are encouraged even if the content does not fall within the areas of emphasis described herein. Comments and criticisms of current AFOSR programs also are welcome.

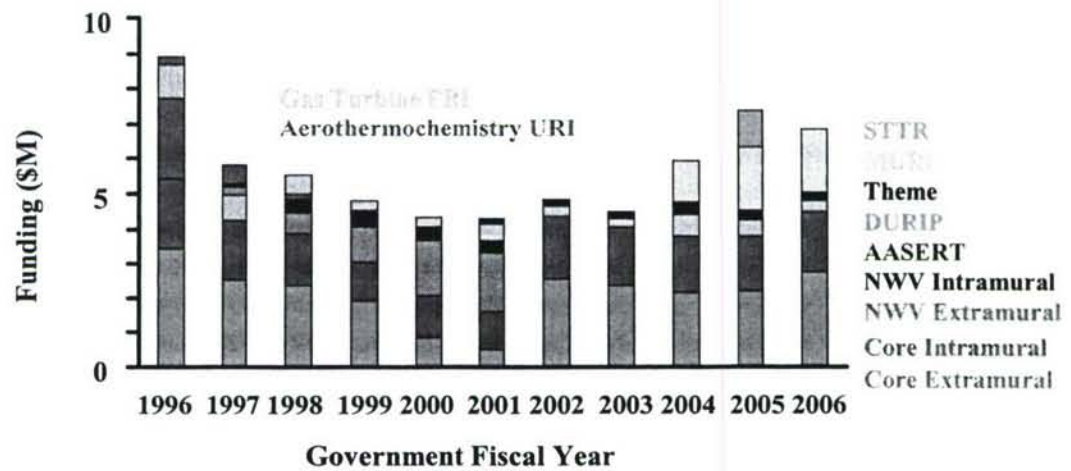


Figure 1. AFOSR Funding for Combustion and Diagnostics Research

THE ARO SINGLE INVESTIGATOR PROGRAM

Kevin L. McNesby, Ph.D.
Interim Program Manager
Propulsion and Energetics
Army Research Laboratory

The ARO core investigator program in the area of Propulsion and Energetics (P&E) is designed to allow highly motivated University-based and National Laboratory-based investigators to pursue research on topics of interest to the Army. In general, the P&E program funds stand alone projects for 3-year duration, providing research funds in the vicinity of \$100K/year. For FY06, there are 15 individual research projects, 12 of which will be represented at the ARO/AFOSR contractors meeting.

As Army needs and interests change, so too do the research topics represented within the single investigator program. Recently, we have seen a partitioning of resources used to fund programs within P&E. Overall, energetic materials (e.g., explosives) research has shifted in the direction of MURI (Multi-University Research Initiative) funding, while research into combustion of hydrocarbon-based fuels is the topic of most single investigator programs. For FY06, approximately 80% of the single investigator programs address some aspect of hydrocarbon fuels combustion.

Although difficult to predict, we are now seeing the direction of research in the single investigator program within the P&E program move towards investigations of synthetic fuels (non-boiling fraction-derived), towards predicting behavior of new fuels in modern, highly efficient combustors, and towards fuels formulation that is fully science-based. The P&E program is well suited to these tasks.

Finally, the P&E program today is the product of the efforts of Dr. David Mann. His influence on the program extends to each researcher, and will continue for many years. The directions of the program, and the abilities of the program to combine cutting edge science with topical Army needs, are due to his stewardship.

ADVANCED SUPERCRITICAL FUELS

LRIR 93PR02COR

Principal Investigators: Tim Edwards, Chris Bunker, Tom Jackson

Air Force Research Laboratory
AFRL/PRTG Bldg 490
1790 Loop Rd N
Wright Patterson AFB, OH 45433-7103

SUMMARY/OVERVIEW:

Increases in aircraft and engine performance are increasing the heat load being transferred into an aircraft's primary coolant--the fuel. This research is aimed at understanding the limitations of operation of fuel heated to 480 C (900 F) and beyond. Important issues are expected to be thermal stability, injection/combustion properties, and fuel characterization.

TECHNICAL DISCUSSION

Work has continued on improving the thermal-oxidative deposition modeling for jet fuels [1, 2]. As described last year, the focus has been on building actual (measurable) fuel species into the model, rather than fitted constants. Currently, the fuel species included in the model (as illustrated in Figure 1) are "AH" (=non-hindered phenols), "SH" (=reactive sulfur, sulfides+disulfides), ROOH (=hydroperoxides), and dissolved metals (primarily Cu). These species are directly measured in various test jet fuels. The previous model was accurate over a wide range of temperatures, but not over a wide range of initial dissolved oxygen saturations. These reduced oxygen concentrations are important in applications where the dissolved oxygen is mechanically or chemically reduced to increase jet fuel thermal stability.

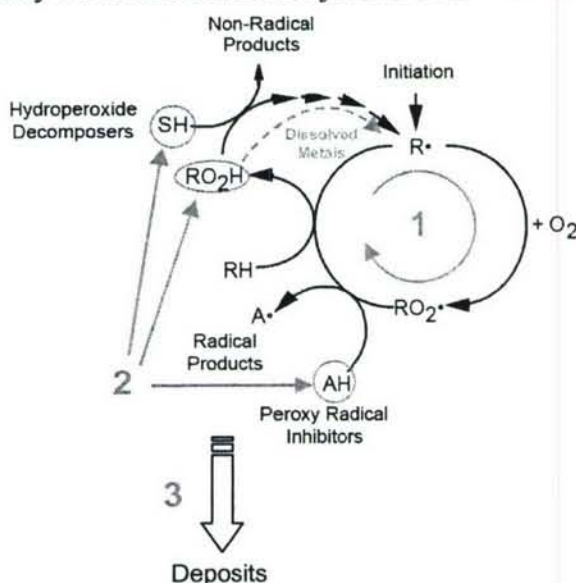


Figure 1. Fuel deposition schematic [1,2].

As shown in Figure 2, the consumption of dissolved oxygen in fuel is well-modeled over a wide variety of fuels (Jet As and JP-8s with a wide variety of AH and SH contents, as shown in Table). Initially, the fuel oxidation cycle (denoted by the label “1” in Figure 1) was developed and tested against a fuel with no AH or SH present. Recent work has improved the modeling of the oxidation cycle by adding an improved simulation of peroxy radical decomposition. Then the effect of AH and SH is added (labeled “2” in Figure 1). Moving on to the deposition problem (“3” in Figure 1), several approximations to wall reactions have been used, with two shown in Table 2.

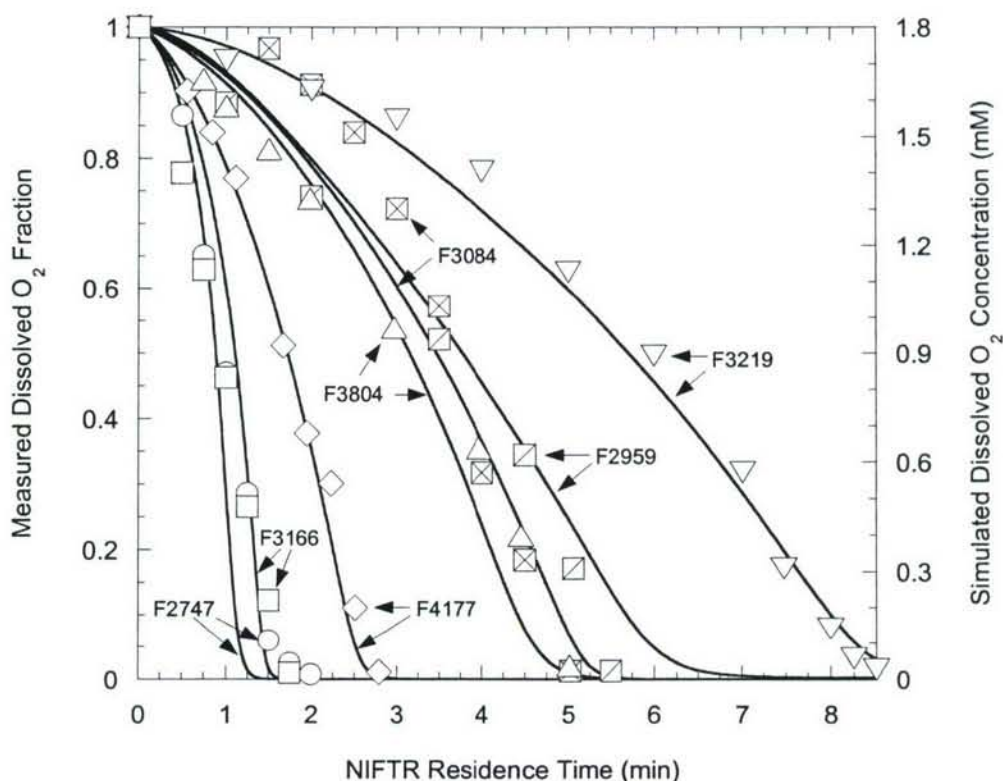


Figure 2. Comparison of modeling and experimental measurements of oxygen consumption for seven jet fuels.

Table 1. Polar, Hydroperoxide, and Reactive Sulfur Content of Figure 2 Fuels

Fuel	Polars		Hydroperoxides	Reactive Sulfurs
	(relative) ^a	(mg/L) ^b	(μ M)	(ppm by weight)
F2747 (Jet A-1)	0.32	167	21	1
F2959 (Jet A)	0.43	222	3	911
F3084 (Jet A)	0.90	465	13	426
F3166 (Jet A)	1.00	515	11	519
F3219 (Jet A)	0.43	223	5	286
F3804 (JP-8)	0.34	177	21	366
F4177 (JP-8)	0.94	486	13	1069

^a Integral of 254 nm UV response obtained using normal-phase HPLC method for polar species quantification [Balster et al., 2002] divided by that obtained for fuel F3166

^b Estimate of absolute polar concentrations based on phenol calibration mixture studies [Balster et al., 2006]

Table 2 – Deposition mechanism alternatives.

Mechanism	#	Type	Reaction	k @ 185°C
b	19	Wall	$\text{Products}_{\text{AH}} + \text{O}_2 \rightarrow \text{Deposits}$	5×10^{-4} (L/mol/s/m)
c	19	Bulk	$\text{Products}_{\text{AH}} \rightarrow \text{Solubles}$	1×10^9 (1/s)
	20	Bulk	$\text{Products}_{\text{AH}} \rightarrow \text{Insolubles}$	3×10^7 (1/s)
	21	Wall	$\text{Insolubles} \rightarrow \text{Deposits}$	5×10^{-5} (1/s/m)

Using these deposition reactions enables the prediction of deposition for various sets of reactor data for the fuels shown in Table 1. This was done for the Near-Isothermal Flowing Test Rig (NIFTR) data, with total deposition compared to predictions in Figure 3. There is obviously room for improvement in the current deposition models. There doesn't appear to be a systematic error related to fuel composition. The 3-reaction deposition sub-mechanism was assessed against data in a non-isothermal flowing rig (the "ECAT" rig) also. In these data sets, fuel flow rate and heating rate were varied such that deposition occurred in different places in a tube of fixed geometry. As shown in Figure 4, the changes in deposit location and the magnitude of deposition are fairly well modeled.

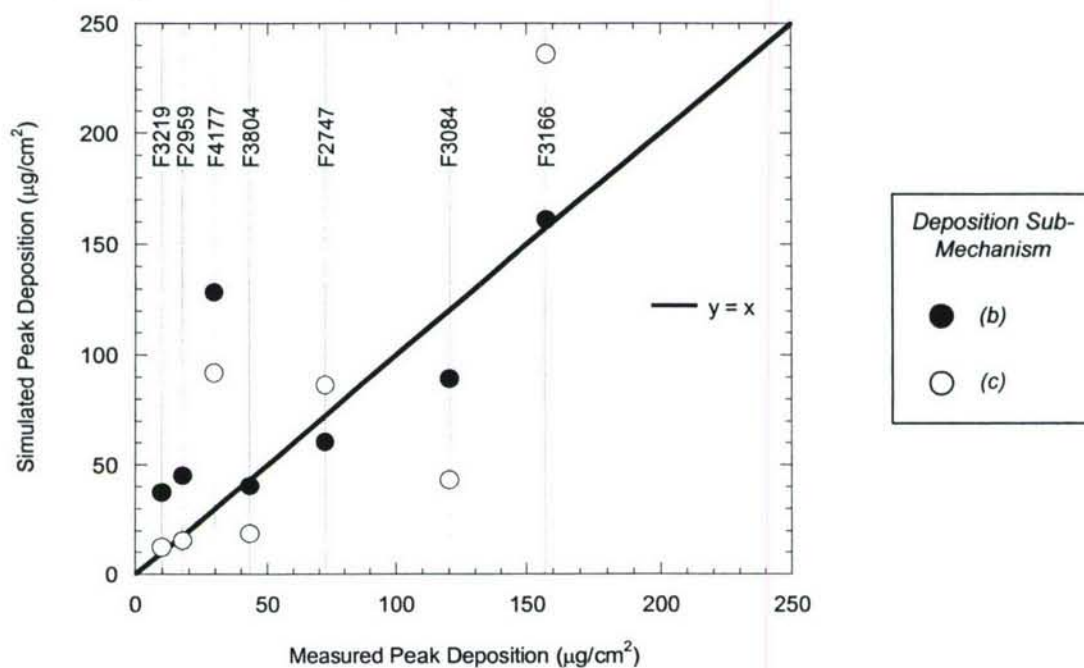


Figure 3. NIFTR deposition from various fuels.

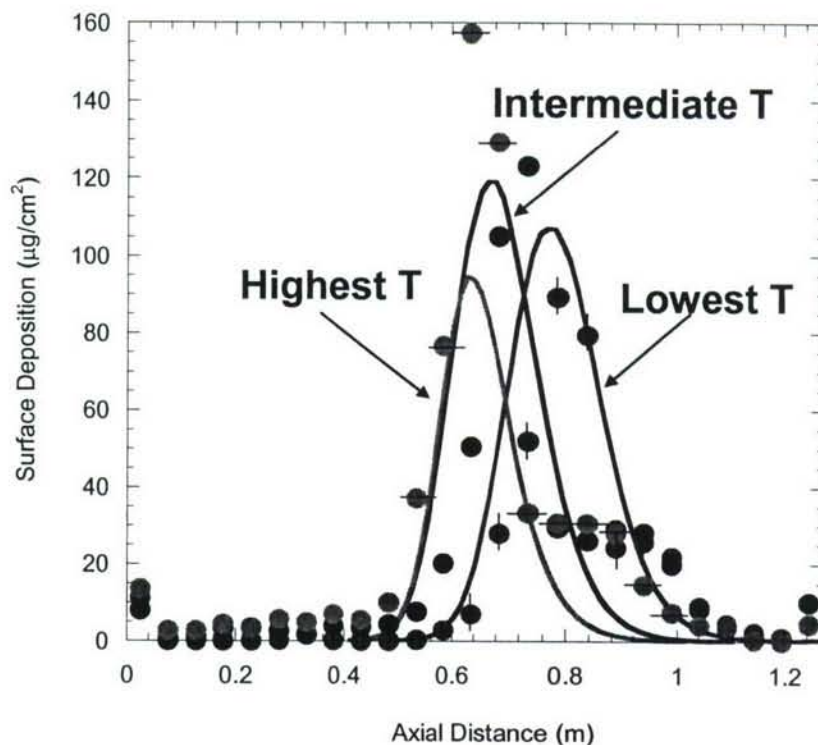


Figure 4. ECAT deposition for various heating rates.

Research is also continuing in pyrolytic deposition, which occurs at higher temperatures during thermal cracking of fuels (often “endothermic” fuels) [3]. Early AFOSR-sponsored research at Princeton and later AFRL showed that deposition during thermal cracking at high pressure was often dominated by “filamentous” carbon formation. This undesirable formation of carbon nanotubes could be controlled by covering superalloy and nickel surfaces with an alumina or silica coating. The deposition currently plaguing endothermic fuels is now arising from molecular growth in fluid phase, originating from rapid PAH growth at high pressure (see Abstract for Judy Wornat of LSU at this meeting). Recent investigations at AFRL have examined various fuel structures (naphthenes, isoparaffins, etc.) for their tendency to retard or enhance this PAH-driven deposit formation. Post-test PAH measurements at LSU are ongoing with samples from these AFRL tests, with early indications that PAH growth from isoparaffins is more facile than expected.

REFERENCES

- 1) Kuprowicz, N., “A Predictive Modeling Approach to Simulate Liquid-Phase Oxidation and Deposition of Jet Fuels,” PhD Thesis, University of Dayton, April 2006.
- 2) S. Zabarnick, Z. West, N. Kuprowicz, L. Balster, J. Ervin, D. Minus, and R. Striebich, “Measurement of Key Species and Development of a Chemical Kinetic Model Toward the Prediction of Jet Fuel Thermal Stability,” Proceedings of the 9th International Conference on Stability, Handling, and Use of Liquid Fuels, Sitges, Spain, 2005.
- 3) Edwards, T., “Cracking and Deposition Behavior of Supercritical hydrocarbon Aviation Fuels,” Combustion Science and Technology, Vol. 178, pp. 307–334, 2006.

THERMODYNAMIC, TRANSPORT AND CHEMICAL PROPERTIES OF "REFERENCE" JP-8

(Contract Number F1ATA06004G004)

Principal Investigator:
Thomas J. Bruno

Physical and Chemical Properties Division
National Institute of Standards and Technology
Boulder, CO 80305

SUMMARY/OVERVIEW:

The NIST research focuses on measurement of major thermophysical and chemical properties of JP-8, to develop it as a reference fluid. The properties include fluid volatility, density, speed of sound, viscosity and thermal conductivity. In addition, we are assessing the global thermal decomposition of the fluid, primarily to guide our property measurements. The measured properties will be used to develop a predictive surrogate fluid model for real JP-8. Three different samples of JP-8 have been obtained, and measurements are in progress on all three.

TECHNICAL DISCUSSION

Chemical Analysis:

A chemical analysis was done on each of the fluid samples by gas chromatography mass spectrometry ((30 m capillary column of 5% phenyl polydimethyl siloxane having a thickness of 1 μm , temperature program from 90 to 250 $^{\circ}\text{C}$, 10 $^{\circ}\text{C}$ per minute). Mass spectra were collected for each peak from 15 to 550 RMM (relative molecular mass) units. Chromatographic peaks made up of individual mass spectra were examined for peak purity, then the mass spectra were used for qualitative identification. Components in excess of 0.5 mole percent were selected for identification and tabulated for each fluid. In addition to this detailed analysis, the hydrocarbon type classification based on ASTM D-2789 was performed. These results figure in the overall mixture characterization, and are also used for comparisons with the chemical analyses of individual distillate fractions (discussed in the section on distillation curves).

Thermal Decomposition:

The thermal decomposition of the JP-8 fluids is being assessed with an ampoule testing instrument and approach that has been developed at NIST[1-4]. It must be understood that this work is meant strictly to support the physical property measurement work, and not to delineate reaction mechanisms. The instrument we developed consists of a 304L stainless steel thermal block that is heated to the desired experimental temperature (here, from 250 – 425 $^{\circ}\text{C}$). The block is supported in an insulated box with carbon rods; the temperature is maintained and controlled (by a PID controller) to within 0.1 $^{\circ}\text{C}$ in response to a platinum resistance sensor embedded in the thermal block. The ampoule cells consist of 6.4 cm lengths of ultrahigh pressure 316L stainless steel tubing (0.64 cm external diameter, 0.18 cm internal diameter) that are sealed on one end with a stainless steel plug welded by a clean tungsten-inert-gas (TIG)

process. Each cell is connected to a high-pressure high-temperature valve at the other end with a short length of 0.16 cm diameter 316 stainless steel tubing with an internal diameter of 0.02 cm, also TIG welded to the cell. Each cell and valve is capable of withstanding a pressure in excess of 105 MPa at the desired temperature. The internal volume of each cell is known and remains constant at a given temperature. Fluid is added to the individual cell by mass (as determined by an approximate equation of state calculation) to give a total pressure of 34 MPa at the final fluid temperature. Thus far, we have completed measurements at 250, 275, 300, and 350 °C. From 250 – 300 °C, little if any decomposition was noted. Decomposition began at 350 °C, and work at 375 °C is in progress.

Distillation Curves:

In previous work, several significant improvements in the measurement of distillation curves for complex fluids were introduced. The modifications to the classical measurement provide for (1) temperature and volume measurements of low uncertainty, (2) temperature control based upon fluid behavior, and most important, (3) a composition-explicit data channel in addition to the usual temperature-volume relationship[5-8]. This latter modification is achieved with a new sampling approach that allows precise qualitative as well as quantitative analyses of each fraction, on the fly. Moreover, as part of the improved approach, the distillation temperature is measured in two locations. The temperature is measured in the usual location, at the bottom of the take-off in the distillation head, but it is also measured directly in the fluid. The measurement in the fluid is a valid thermodynamic state point that can be theoretically explained and modeled. The usual temperature measurement location (in the head) provides a temperature that is not a thermodynamic state point, but which is comparable to historical measurements made for many decades. We also use a modification of the Sidney Young equation (to correct the temperatures to standard atmospheric pressure) in which explicit account is taken of the average length of the carbon chains of the fluid. As applied to JP-8, we have measured the distillation curve of three separate lots of fluid with the new approach. The curves, examples of which are provided in Figure 1, show clearly the variability in the fluids; two are similar in volatility while the third is very different. For each fluid, we have collected sample aliquots of each distillate volume fraction for analysis by GC-MS. These individual fractions have been analyzed, and energy content calculations are planned. In addition, for each fraction, the ASTM D-2789 analysis has been done.

Thermophysical Properties:

The density, viscosity, and speed of sound of three JP-8 samples are being measured in two commercial rapid characterization instruments. A Stabinger viscodensimeter was used to determine the density and the absolute and kinematic viscosity in the temperature range from –40 °C to 100 °C (233.15 K to 373.15 K) at atmospheric pressure. A sound-speed analyzer was used to measure the speed of sound and the density of the JP-10 samples at atmospheric pressure in the temperature range from 5 °C to 70 °C (278.15 K to 343.15 K). The measurements with the Stabinger viscodensimeter were carried out according to ASTM Standard D 7042 – 04 *Standard Test Method for Dynamic Viscosity and Density of Liquids by Stabinger Viscometer (and the Calculation of Kinematic Viscosity)*. Combining a densimeter with a speed of sound measurement makes it possible to obtain the adiabatic compressibility $\kappa_s = -(\partial V/\partial p)_s/V = 1 / (\rho w^2)$ where V denotes volume, p is pressure, and w the speed of sound. The viscometer part of the instrument uses a rotational coaxial cylinder measuring system. The rotational speed of the inner cylinder establishes itself as the result of the equilibrium between the driving torque of the viscous forces and the retarding eddy current torque. This rotational speed is measured by an electronic system (Hall effect sensor) that counts the frequency of the rotating magnetic field of a

magnet and a soft iron ring. The digital density analyzer in the viscodensimeter uses a U-shaped vibrating sample tube and a system for electronic excitation and frequency counting. The density of the sample liquid in the vibrating tube is obtained from the resonant frequency of the vibrating system relative to the resonant frequency with a calibration liquid of known density.

The combination of a viscometer and a densimeter makes it possible to obtain absolute viscosity η as well as kinematic viscosity ν of a sample. This apparatus is depicted in Figure 2. We anticipate measurements of all fluids (at atmospheric pressure) between -40 and 100 °C.

In addition to these atmospheric pressure instruments, an apparatus has been designed and built for the rapid screening of liquid densities over the temperature range of 0 to 200 °C and pressures to 45 MPa. The heart of the apparatus is a commercial vibrating tube densimeter, modified at NIST. The densimeter is housed in a specially designed two-stage thermostat for precise temperature control. The uncertainty in the temperature is 0.03 °C with short-term stability of 0.005 °C. Pressures are measured with an oscillating quartz crystal pressure transducer with an uncertainty of 5 kPa. The densimeter is calibrated with measurements of vacuum, propane and toluene, over the temperature and pressure range of the apparatus to achieve an uncertainty in density of 1 kg/m³. Thus far, one sample lot of JP-8 has been measured from 0-200 °C, and from 1 – 30 MPa. Work on the second and third fluid samples is ongoing.

Model Development:

Upon completion of the experimental measurements of the physical and chemical properties described above, a model for the fluid will be developed. This model will be explicit in Helmholtz energy as a function of density and temperature. All single-phase thermodynamic properties can be calculated as derivatives of the Helmholtz energy. A preliminary equation of state for propane will be used as the starting point for the equation of state. The properties of individual mixture components, identified and evaluated in the experimental steps above, will be incorporated into the mixture model.

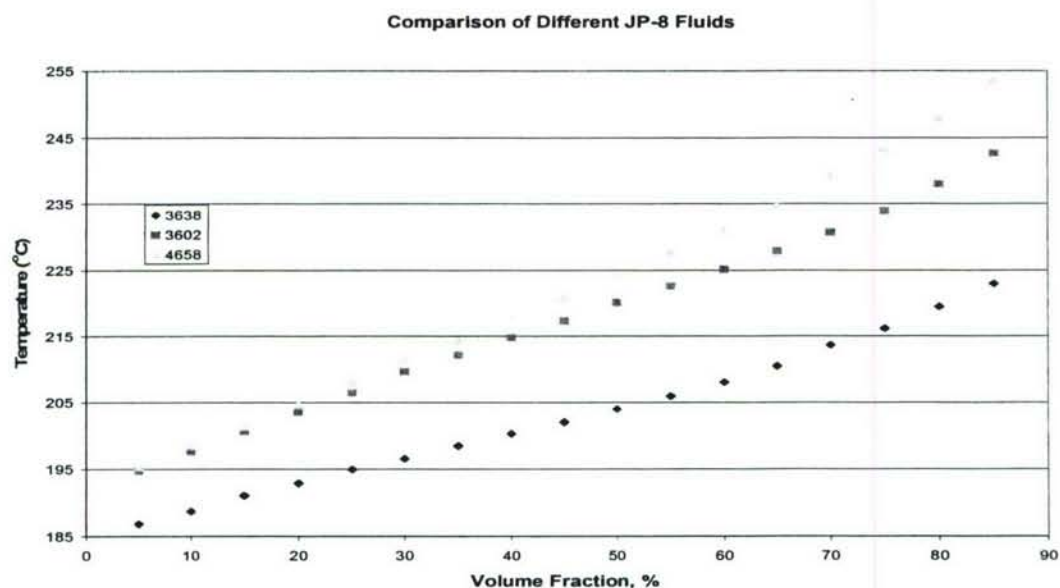


Figure 1: The distillation curves of three different lots of JP-8, showing the variability that can be encountered.

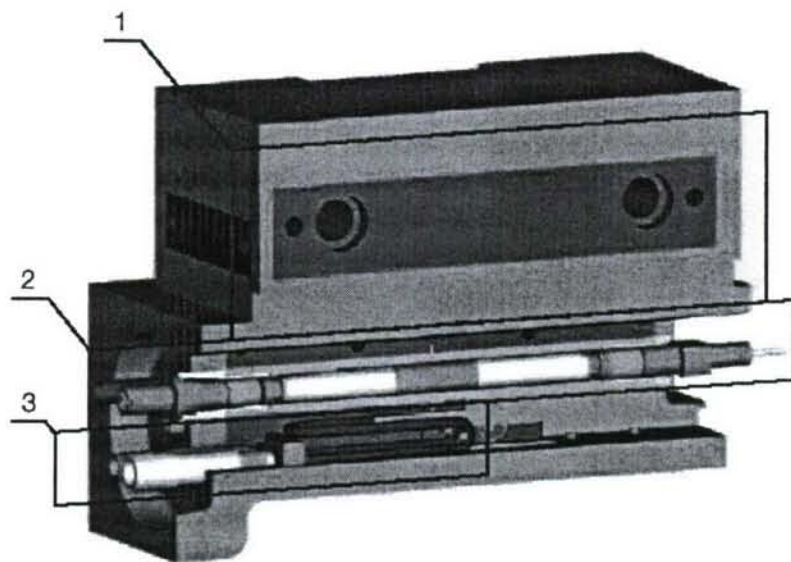


Figure 2: Main components of the Stabinger viscodensimeter SVM 3000.

1 – Thermostating Peltier block, 2 – Concentric cylinder viscometer, 3 – Vibrating tube densimeter.

References:

1. Andersen, P.C., Bruno, T.J., *Thermal decomposition kinetics of RP-1 rocket propellant*. Ind. Eng. Chem. Res., 2005. **44**(6): p. 1670-1676.
2. Andersen, W.A., Bruno, T.J., *Rapid screening of fluids for chemical stability in organic rankine cycle applications*. Ind. Eng. Chem. Res., 2005. **44**: p. 5560-5566.
3. Magee, J.W., Bruno, T.J., Friend, D. G., Huber, M.L., Laesecke, A., Lemmon, E.W., McLinden, M.O., Perkins, R.A., Baranski, J., Widegren, J.A., *Thermophysical Properties Measurements and Models for Rocket Propellant RP-1: Phase I, NIST- IR 6644, National Institute of Standards and Technology (U.S.)*,. 2006.
4. Bruno, T.J., Huber, M.L., Laesecke, A., Lemmon, E.W., Perkins, R.A., *Thermochemical and thermophysical properties of JP-10, NIST-IR 6640, National Institute of Standards and Technology (U.S.)*,. 2006.
5. Bruno, T.J., *Method and apparatus for precision in-line sampling of distillate*. Sep. Sci. Technol., 2006. **41**(2): p. 309-314.
6. Bruno, T.J., *Improvements in the measurement of distillation curves - part 1: a composition-explicit approach*. Ind. Eng. Chem. Res., in press, 2005.
7. Bruno, T.J., Smith, B.L., *Improvements in the measurement of distillation curves - Part 2: application to aerospace/aviation fuels RP-1 and S-8*. Ind. Eng. Chem. Res., in press, 2006.
8. Smith, B.L., Bruno, T.J., *Advanced distillation curve measurement with a model predictive temperature controller*. Int. J. Thermophys., 2006. **submitted**.

THE DECOMPOSITION OF SURROGATE FUEL MOLECULES DURING COMBUSTION

F1AT06004G003

Wing Tsang and Jeffrey A. Manion

National Institute of Standards and Technology
Gaithersburg, MD 20899

SUMMARY AND OVERVIEW: This project is aimed at developing a chemical kinetic database consisting of the rate constants of fundamental single step reactions that describe the pyrolytic decomposition of surrogate fuels molecules. These reactions represent an integral part of any complete combustion kinetics database. They can be competitive with oxidation processes and hence extend the range of current combustion models to richer mixtures. They lead to the unsaturated fragments that are the inputs to PAH/SOOT models and are therefore necessary for the use of such models for the description of particle formation with realistic fuels.

TECHNICAL DISCUSSION: This project began on February 1, 2006. Work that is being reported here are therefore of a preliminary nature. Our first task was to obtain a series of compounds that can be used as precursors for the formation of the various radicals of interest. A number of compounds have now been obtained and studies have been initiated.

Surrogate fuel mixtures contain compounds that have structural features that are the same as found in real fuels. The type of compounds include linear alkanes, branched alkanes, branched

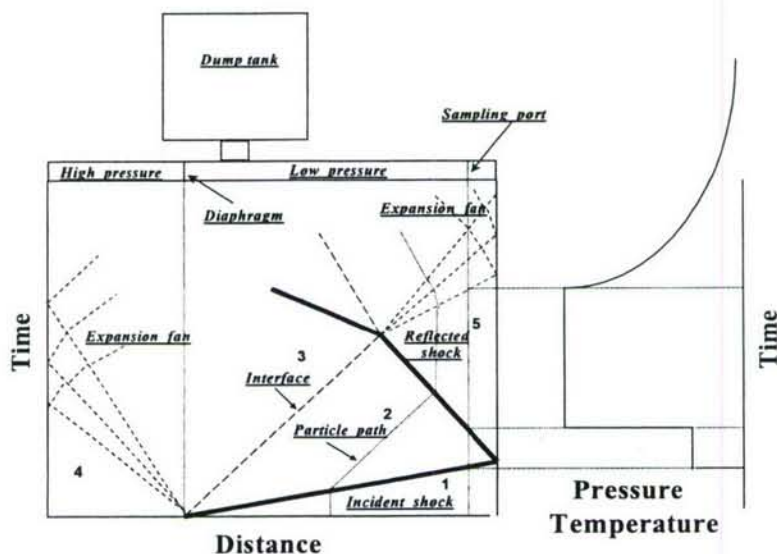


Figure 1: Schematic of single pulse shock tube and associated wave diagrams.

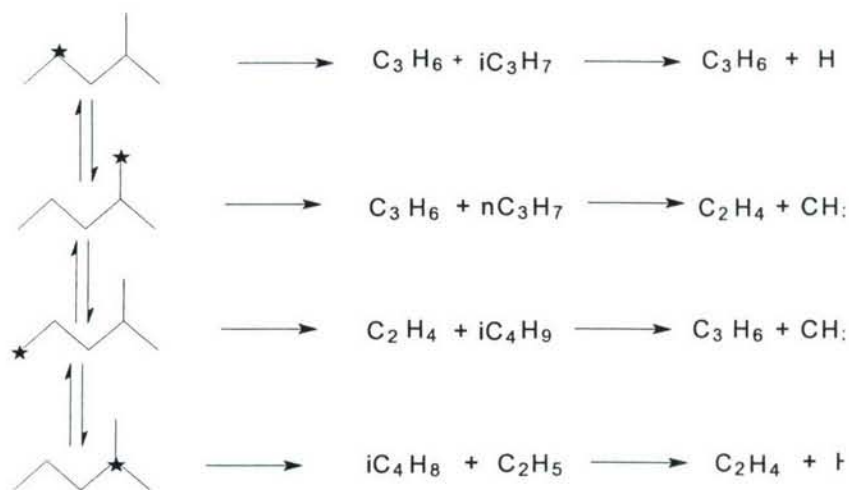


Figure 2: Mechanism for the decomposition of 4-methylpentyl radical. The olefins are those detected from the gas chromatographic analysis.

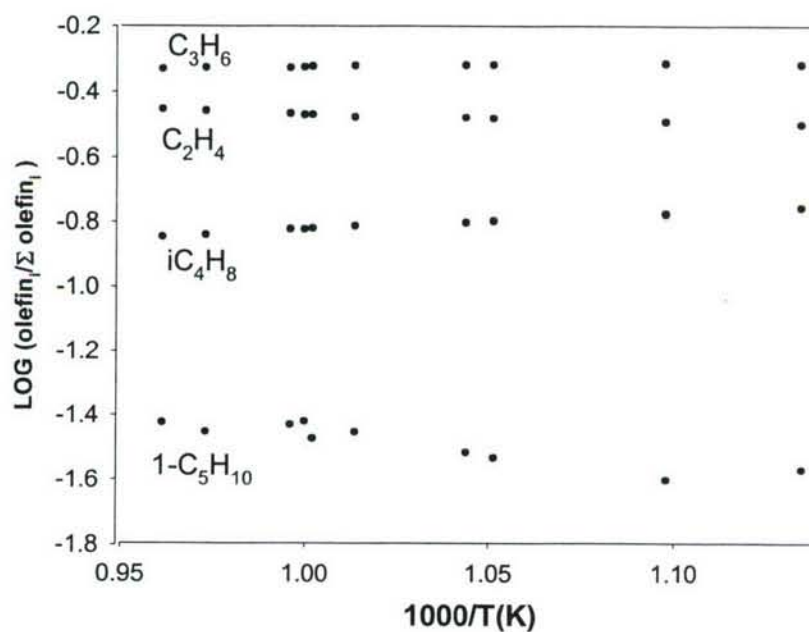


Figure 3: Olefin distribution as a function of temperature from the decomposition of 4-methylpentyl-1 radicals from single pulse shock tube experiments at approximately 3 bar.

cyclanes, and branch aromatics. In a combustion system these compounds are converted into radicals. The radicals can be oxidized or be pyrolyzed. Much of the existing work on combustion models have focused on oxidative degradation. However pyrolytic decomposition is the

competitive process and is usually neglected. This is the justification for the present work. It is expected that when combined with oxidative models it will be possible to extend the models to richer situations. The products from pyrolytic decompositions are the precursors to SOOT/PAH models and hence relates sooting tendencies to the fuel.

Our initial interest is to extend our past work on linear alkanes to cover branched alkanes. Hence we begin our studies on the decomposition of 4-methyl-pentyl iodide in single pulse shock tube experiments. Figure 1 is a schematic of our experimental configuration. The decomposition of the iodide leads to the formation of 4-methylpentyl-1 radical. The results will be compared with earlier results on the decomposition of 1-pentyl radical. Our primary interest will be the effect of methyl substitution on 1-4 isomerization processes. We have detected all the expected products from the decomposition process. They are ethylene, propene, isobutene and 1-pentene. The specific reaction processes are in Figure 2. The branching ratios in terms of olefin yields can be seen in Figure 3. We are in the process of analyzing the results in terms of the specific rate

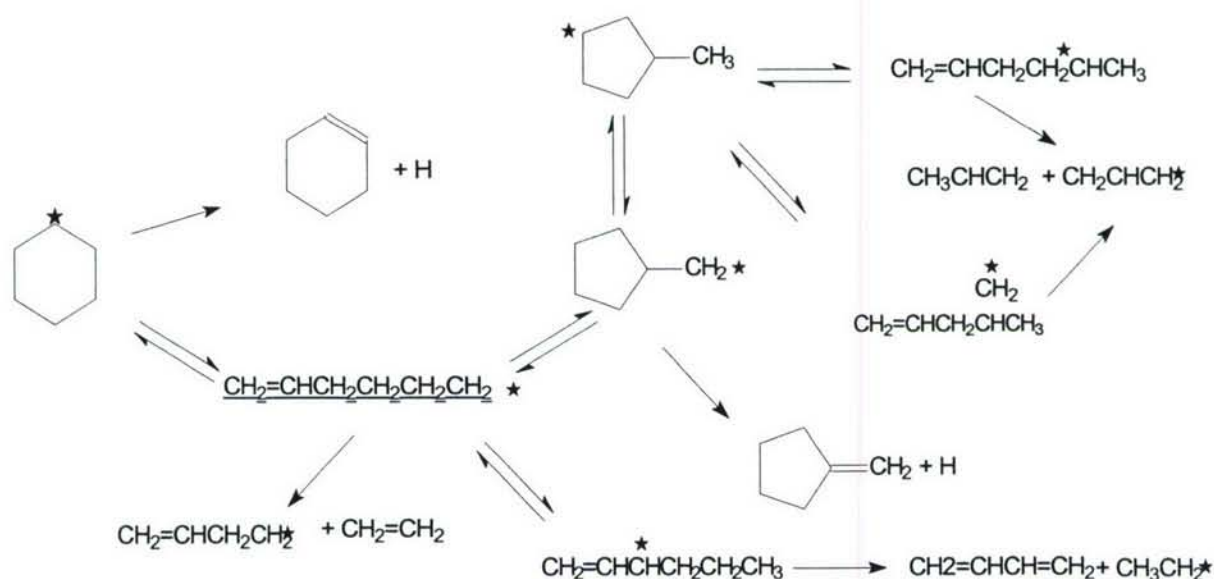


Figure 4: Mechanism for the decomposition and interconversion of 1-hexenyl-6 and cyclohexyl radicals.

constants. As in the case of the normal alkyl radicals we will begin by deriving rate constants for beta bond scission from experiments on related molecules. This will involve direct studies as well as results derived from the rate constants of the reverse radical addition process. The added features from this study are the effects of methyl substitution for 1-4 isomerization and the consequences of changing an exothermic 1-5 hydrogen transfer from a primary to a secondary position to a thermally neutral process involving primary hydrogen atoms. Systematic studies of this type should lead to the construction of a library of rate constant for hydrogen transfer isomerization in alkyl radicals. A major problem in deriving such data is the difficulties in obtaining the requisite precursors. The 4-methyl pentyl iodide was a custom synthesized sample and cost \$3000.00 for 10 grams. Fortunately one of the great advantages of single pulse

shock tube studies is the need for very small samples. We will therefore wait for the analysis of the results before carrying out further studies aimed at discerning the methyl substitution effect for 1-5 hydrogen transfer isomerization in 5-methyl-hexyl radical as derived from the iodide.

We have also carried out preliminary experiments for the decomposition of 1-hexenyl-6 and cyclohexyl radicals. The 1-olefinyl radicals are formed from the 1-olefins that are in turn derived from the decomposition of alkyl radicals. Their decomposition leads to the formation of dienes. These are known to be very important soot precursors. The overall mechanism is very complex and can be seen in Figure 4. There are three isomerization pathways superimposed on beta bond scissions. Previous lower temperature experiments on cyclohexyl radicals have established the relative stability of the cyclic structures (cyclohexyl and cyclopentylmethyl) in comparison to the linear 1-hexenyl-6 radical. In our experiments we see extensive butadiene formation. This is indicative of the more important role of the linear structure at the higher temperatures. In combination with the earlier work, it should now be possible to describe in a quantitative manner the rate constants of the reactions in Figure 4. These results are also of interest in that they shed light on the decomposition of cyclohexyl radicals. This is the result of radical attack on cyclohexane. Cyclohexane type compounds are important components of tar sands. The latter are expected to form increasingly important component of fuel mixtures. Information on their combustion and sooting behavior is expected to be important in the simulation of these new fuels.

AN AUTOMATED PROCESS FOR GENERATION OF NEW FUEL BREAKDOWN MECHANISMS

Principal Investigator:

Angela Violi

Assistant Professor
Department of Mechanical Engineering and Department of Chemical Engineering
University of Michigan
2150 G.G. Brown
2350 Hayward Rd.
Ann Arbor, MI 48109

SUMMARY/OVERVIEW:

This work revolves around an innovative, comprehensive, and integrated approach for predicting new fuel reaction mechanisms. It combines advanced computational techniques in a synergistic study of the critical processes in fuel decomposition at a level of detail that can help distinguish, correct, and quantify mechanisms for these processes. The innovative aspect of the modeling effort is to integrate computational tools that can be used to build reaction pathways for new fuel mechanisms, starting from the structure of the proposed fuel components and ending with a list of reactions pathways, rate constants, thermodynamic, and transport data that can be feed into existing combustion mechanisms. This will be accomplished by using a combination of two well-defined techniques: Molecular Dynamics and ab initio electronic structure calculations.

While the efforts present in the literature are targeted to build kinetic mechanisms in terms of kinetic and thermochemical data often based on similarity or to gather data from different sources, they do not address the other main problem related to the reliability of reaction mechanisms, that is the exclusion of significant pathways from the list of the reactions that are included in the mechanisms. The approach presented in this proposal will allow the identification of new reaction pathways to produce a more complete description of the system of interest.

The final objective of this project is to convert the building of kinetic mechanisms into science, automate the methodology, and make the results available in a prompt and convenient form for the user. The project refers to automation in the sense that a rigorous process is proposed to go from fuel structure to kinetic mechanism without requiring the intervention of the investigator. One of the advantages is that it avoids the introduction of bias based on the preconceived notions of the community.

2. TECHNICAL DISCUSSION

When dealing with complex real fuels, surrogates are formulated and used in place of the real fuel both for experimental and computational applications. A surrogate is a mixture of a limited number of hydrocarbons with a well defined and reproducible composition that can be used in place of the real fuel. The use of a surrogate blend, comprised of a relatively small number of

high purity hydrocarbons blended to simulate the combustion performance of practical fuel, has the advantage of allowing fuel composition to be accurately controlled and monitored. In addition to providing a model fuel for the study of the effect of fuel properties and chemical composition on combustor performance, the compositional control afforded by a surrogate fuel is attractive for the development and verification of computational codes for combustor design or fire simulation.

The type of surrogate mixture used is dependent ideally upon the fuel properties that are being simulated: surrogates may be tailored to reproduce the physical, chemical, or more comprehensive behavior of a fuel in a given application. A physical surrogate can be designed to reproduce physical properties such as density, thermal conductivity, heat capacity, viscosity, surface tension, and volatility. A chemical surrogate, on the other hand, has similar hydrocarbon types and distribution, and can reproduce chemical properties such as oxidation stability, ignition temperature, rates of reaction, sooting behavior. As an example, for JP-8 pool fires the relevant properties include volatility (boiling range, flash point, vapor pressure), chemical kinetics (particularly of reactions leading to soot formation, needed for accurate simulation of radiative heat transfer in fires) and other combustion properties such as ignition, peak heat release rate and local flame extinction.

Usually surrogates match only some particular aspects of the behavior of the real fuel. And new formulations are frequently proposed to improve their capabilities and to expand the number of properties they reproduce. As a consequence, there is a continuing need for additional kinetic mechanisms to cover the chemistry of new species and/or new conditions. The problem is that when new species are introduced in the surrogate, there is no good method for updating the kinetic mechanism to incorporate the new species.

The approach presented below makes it possible to identify new reaction pathways for real fuels to produce a complete description of the system of interest in terms of intermediates, products, kinetics, thermochemical and transport properties.

Below we report on the new approach that can be taken to *generate new fuel mechanisms*. This process utilizes an Accelerate Molecular Dynamics methodology to identify reaction pathways at relevant temperatures in conjunction with *ab initio* calculations to determine the rates of new reactions. The approach allows the identification of new gas phase products and reaction pathways for new fuel mechanisms, starting from the structure of the proposed fuel components and ending with a list of reaction pathways, rate constants, and thermodynamic data.

2.1 COMPUTATIONAL METHODOLOGY

Two combined steps are required for these calculations. The first one is represented by an accelerated MD simulation that is used to evaluate alternative/additional reaction pathways for molecular systems with many conformational degrees of freedom, and quantum chemistry runs to validate the results obtained by the MD code.

Step 1: The input to Step 1 is the structure of the fuel compound. The Parallel Replica Molecular Dynamics (PRMD)¹ code is used to extend the MD simulation time in an accurate way. In the PRMD method, starting with an N atom system in a particular state, the system is replicated on many processors. After a dephasing stage, where momenta are randomized, each processor carries out an independent Molecular Dynamics trajectory. Whenever a structural transition is detected on any processor, all processors are alerted to stop. The simulation clock is advanced by the accumulated trajectory time summed all over replicas, and the PR simulation is restarted, continuing onward until the next transition occurs and the process is repeated. In this way, the effective time of the MD simulation is “boosted” (usually significantly).²

In summary:

Input to Step 1: the user defines the fuel structure

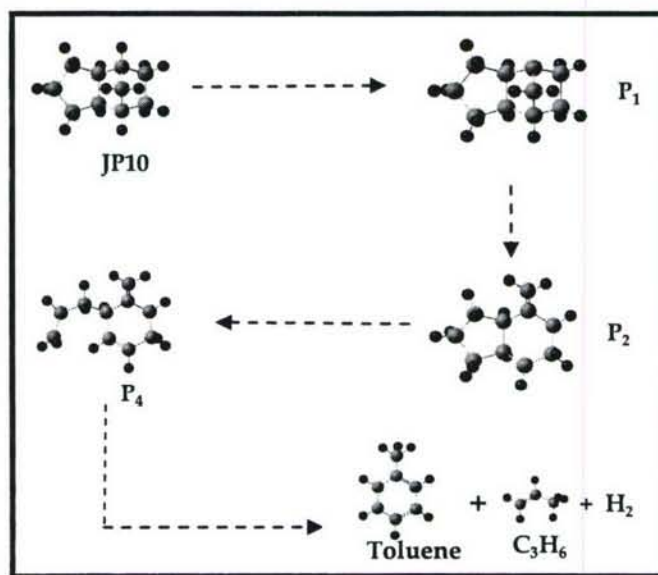
Outputs from Step 1: reaction pathways and products $P_{i,j}$ – the first index refers to the identity of the product within a particular pathway and the second to the identity of the reaction pathway. For example $P_{2,1}$ is the second product identified in pathway 1.

Step 2: The new reaction pathways identified with the PRMD code – in *Step 1* – will be validated and further studied using *ab initio* methods to determine kinetic and thermodynamic properties of the new routes. An essential requirement to build reliable kinetic mechanism is the availability of accurate kinetic parameters. Even small uncertainties in rate parameters may induce substantial deviations in model predictions of soot yields due to the accumulation of errors in the large number of growth steps necessary for the description of large compounds.

2.2 RESULTS

In order to emphasize the importance of this new methodology preliminary results have been obtained for JP10 fuel, whose mechanism is not well understood. The kinetic mechanism available in the literature for JP10³ includes a few reactions leading to C_3H_3 , C_2H_4 , C_5H_8 , C_2H_2 , C_4H_6 , C_3H_5 , but recent experimental data reported on JP10 pyrolysis show the presence of benzene, toluene, cyclopentadiene as initial decomposition products in a temperature range between 900 – 1300K.⁴

Using the approach reported above, Step 1 and Step 2 were applied to the JP10 molecule in a pyrolytic environment at a temperature of 1500 K. As input to the process, the structure of the JP10 molecule was defined. The next figure shows an example of the results obtained after Step 1. In the example showed in the figure, the run stops when the species produced are previously known and exist in large scale mechanisms. In this case toluene, C_3H_6 and H_2 . After Step 1 the



Example of output from Step 1: intermediates and products identified with PRD.

first reaction pathway and the intermediates are identified. This information is used as input for

the *ab initio* calculations and after Step 2 the reaction pathway is completed and the transition states calculated.

The results obtained through the use of the computational tool described above can be integrated into a hierarchically constructed kinetic model already available for the oxidation of alkanes and simple aromatic molecules (benzene, toluene, ethylbenzene, xylene etc.).⁵

REFERENCES

- [1]. Voter A.F. "Parallel replica method for dynamics of infrequent events" *Phys. Rev.B: Condens. Matter* 57(22) 13985–88 (1998).
- [2]. Voter A.F., Montalenti F., Germann T.C. *Annu. Rev. Mater. Res.* 32: 321–46 (2002).
- [3] <http://maemail.ucsd.edu/combustion/cermech/JP10-Reactions>
- [4] Nakra S., Green R.J., Anderson S.L., *Combust. Flame* (2005) in print.
- [5] A. Violi, S. Yan, E.G. Eddings, A.F. Sarofim, S. Granata, T. Faravelli, E. Ranzi, *Combust. Sci. Tech.* 174(11-12), 399 (2002).

COMPUTATIONAL AND EXPERIMENTAL STUDY OF JET FUEL COMBUSTION

Grant #FA9550-06-1-0018

Principal Investigators: M. D. Smooke and A. Gomez

Department of Mechanical Engineering
Yale University
New Haven, CT 06520-8284

SUMMARY/OVERVIEW

A coordinated experimental and computational program is needed to develop chemical models of jet fuel that can be used within a larger research and development program. In this proposal we will initiate a joint experimental and computational program designed to test the feasibility of surrogate formulations of JP-8 capable of matching overall properties of the complex fuel and more detailed aspects of its combustion, such as flame structures. The work proposed herein will be leveraged on complementary research at the University of Utah and the University of Milan (Italy). The work will help establish a research infrastructure to provide a better understanding of the combustion of jet fuel, to the benefit of both commercial and military users.

TECHNICAL DISCUSSION

With a starting date of 2/15/06, we initiated a joint experimental and computational program designed to test the feasibility of surrogate formulations of JP-8 capable of matching overall properties of the complex fuel and more detailed aspects of its combustion, such as flame structures. Once the surrogate is identified, its kinetic behavior will be modeled and, after additional validation, the model will be reduced to a sufficiently small subset of critical kinetic reactions to be incorporated in realistic computational codes. Specifically, a comprehensive campaign of measurements and computations in prototypical flame environments, such as premixed flames and diffusion flames will be undertaken which will include measuring and computing global properties such as laminar flame speeds, S_L , extinction strain rates, a_{ext} , and ignition strain rates, a_{ign} . We will also compare flame structure including the temperature and gaseous hydrocarbons up to C_{12} . All of the above would be studied as critical variables, such as inlet temperature, composition, overall mixture equivalence ratio, vitiation equivalence ratio and pressure are varied.

Experimental Approach

A counterflow burner will be the workhorse of the experimental activity. A schematic of the counterflow experimental setup is shown in Figure 1. It uses a carefully contoured geometry to ensure flow uniformity at the burner mouths. Experiments can be

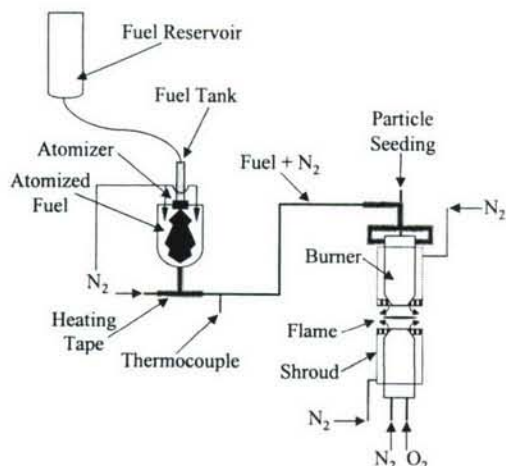


Figure 1. Schematic of the nonpremixed counterflow JP-8 configuration.

prevent soot formation at the interface of the flame with the room air, a shroud flow of N_2 is provided. The fuel side is maintained at a temperature above the dew point of the nitrogen-diluted fuel mixture admitted into the burner. The flow rates of the reactant streams are measured using mass flow controllers.

The vaporization of the liquid fuel is a critical issue. For the multicomponent mixture, to avoid fractional distillation, an ultrasonic nebulizer, capable of generating rapidly vaporizing droplets a few microns in diameter, is used to introduce liquid fuel droplets into a heated nitrogen stream, yielding complete vaporization. This vaporized fuel/inert mixture is then conveyed to the burner through a heated tube maintained at elevated temperature and monitored via thermocouples. Temperature measurements are obtained using coated Pt/10%Pt-Rh thermocouples. The measurements will be corrected for radiative losses using both spherical and cylindrical geometries. The thermocouple probe is custom-designed to minimize perturbations on the low strain velocity field.

Premixed flame studies will be conducted in a modification of the counterflow configuration. In principle, premixing the feed streams and splitting them between the two burners with valves on each line to match pressure drops, would make the experimental system suitable for the “twin flame” approach to the measurement of flame speeds [2] and flammability limits. This approach is very appealing because of its inherent adiabaticity, but is potentially affected by uncertainties in the extrapolation of the measured flame speeds to zero strain, although with large nozzle separations these uncertainties are perhaps acceptable. A more recent technique that can be easily implemented in our set-up relies upon using the transition from planar to conical Bunsen flames in a jet/wall configuration [3]. Detailed work from the same group has shown that at low strain rates the flame is affected minimally by the wall [4]. We have recently begun experimenting with the set-up in Figure 2 and it appears to work well except under very lean conditions. As a result, we will apply both approaches, each with its own advantages, both being aerodynamically “clean.”

conducted with a fuel mixture introduced from the upper burner, in order to benefit from the heating of the exhaust gas and reduce the risk of condensation, and an oxidizer mixture introduced from the lower burner. The fuel and oxidizer inlet concentrations can be chosen to inhibit the formation of soot, a particularly significant advantage of this configuration when using fuels prone to soot such as those under consideration. Typically, overall fuel-lean flames will be examined. Furthermore, to enhance the flame stability and

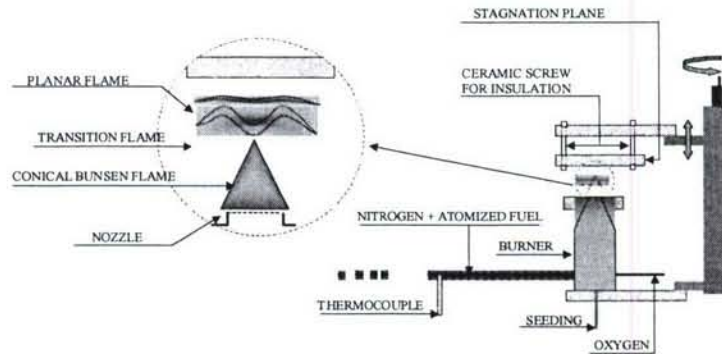


Figure 2. Schematic of the premixed counterflow JP-8 configuration.

Computational Methodology

The form of the governing equations for both the freely propagating and counterflow flame models are well documented. In the freely propagating case, conservation equations for the species and energy are solved together with an equation for the mass flow that is formulated in terms of an eigenvalue problem for the adiabatic flame speed. The counterflow problem is modeled by considering a similarity solution of the two-dimensional conservation equations of mass, momentum, species and energy, valid along the stagnation point streamline. In both problems, the resulting set of equations can be written in terms of a nonlinear boundary value problem on a fixed spatial domain.

Of inherent importance to both the premixed and nonpremixed studies will be the ability to vary one or more quantities as the remaining system parameters are held fixed. For example, in the premixed problems we are interested in allowing the equivalence ratio to change as the pressure and inlet temperature are held fixed or we may want to vary the inlet temperature as the pressure and equivalence ratio are fixed. For the diffusion flames, the strain rate, inlet mass flow rates and temperatures are parameters of interest. While we could compute a single flame with specified values of these parameters and then use this computed solution as a starting estimate for a new problem with different parameter values, this is extremely inefficient. Instead, we will apply a continuation method such that the grid and the solution smoothly change as the parameter is varied.

Once a solution to the flame equations has been obtained, it is often useful to investigate those parameters to which the solution is most “sensitive” (see, e.g., [5]). In the past, however, the major obstacle in obtaining sensitivity information systematically was the additional amount of computation required for solving the sensitivity equations. An advantage of solving the premixed and counterflow flames by a Newton based method is that first-order sensitivity information can be obtained at a fraction of the cost of the total calculation [6]. Critical parameters to be investigated include reaction rate and transport coefficients as it is important to understand whether the agreement, or lack thereof, of global properties and flame structure is originating from the kinetics of the surrogate or the transport properties employed.

In parallel with the proposed experimental program, we will initiate a process to reduce the surrogate mechanism. We envision the procedure occurring in several stages due, in part, to the large number of chemical species (> 220) and the large number of elementary chemical steps (> 5000) in the surrogate formulation. The first stage of the reduction process would generate a “skeletal” mechanism—one which is significantly reduced in the number of chemical species and reactions from the parent mechanism but one that is still untenable for use in a turbulent reacting flow model. The mechanism can be reduced further by employing a steady-state analysis ultimately leading to a system so that partial equilibrium and truncated steady-state approximations can be used to produce a mechanism that we envision will be small enough to be computationally effective in turbulent reacting flow models. An alternative approach includes the intrinsic low dimensional manifold method (ILDM) [7]. No reduction process involving flames has been attempted on a mechanism as large as the one proposed herein and, hence, the tradeoffs between the two reduction methodologies need to be assessed in practical computations before one method is recommended over the other. We point out that the specific level of the reduction process will depend upon what parameters the reduced mechanism will be required to reproduce. For example, if one wants to match soot volume fractions and radiation levels, significant species reduction may not be as viable compared to matching peak temperatures and flame speeds.

We will discuss results obtained in the counterflow diffusion flame briefly [8] and system modifications since the grant’s inception

References

1. Cooke, J.A., Smooke, M.D., Bellucci, M., Gomez, A., Violi, A., Faravelli, T., and Ranzi, E., *Proceedings of the Third Joint Meeting of the U.S. Sections of The Combustion Institute*, Chicago, Illinois (2003).
2. Chao, B. H., Egolfopoulos, F. N. and Law, C.K., “Structure and Propagation of Premixed Flame in Nozzle-Generated Counterflow,” *Combust. and Flame*, **109**, (1997).
3. Vagelopoulos, C.M. and Egolfopoulos, F. N., “Direct Experimental Determination of Laminar Flame Speeds, *Proceedings of the Combustion Institute*, **27**, (1998).
4. Egolfopoulos, F. N., Zhang, H. and Zhang, Z., “Wall Effects on the Propagation and Extinction of Steady, Strained Laminar Premixed Flames,” *Combust. and Flame*, **109**, (1997).
5. Frank, P. M., *Introduction to System Sensitivity Theory*, Academic Press, New York, (1978).
6. Smooke, M. D., Rabitz, H., Reuven, Y. and Dryer, F. L., “Application of Sensitivity Analysis to Premixed Hydrogen-Air Flames,” *Combust. Sci. and Tech.*, **56**, (1988).
7. Maas, U. and Pope, S. B., “Simplifying Chemical Kinetics: Intrinsic Low-Dimensional Manifolds in Composition Space,” *Combust. and Flame*, **88**, (1992).
8. Cooke, J.A., Bellucci, M., Smooke, M.D., Gomez, A., Violi, A., Faravelli, T. and Ranzi, E. “Computational and Experimental Study of JP-8 Counterflow Diffusion Flame,” *Proceedings of the Thirtieth Symposium (International) on Combustion*, Chicago, 2004, p. 439.

AUTOIGNITION AND COMBUSTION OF DIESEL AND JP-8

(Grant/Contract Number 45241-EG)

Principal Investigator: Dr. Kalyanasundaram Seshadri

Department of Mechanical and Aerospace Engineering
University of California at San Diego
La Jolla, California 92093

SUMMARY/OVERVIEW:

Experimental and numerical studies are carried out to construct reliable surrogates that can reproduce aspects of combustion of JP-8 and Jet-A. The combustion characteristics considered are extinction and autoignition in laminar non premixed flows. Three surrogates are constructed. The measured values of the critical conditions of extinction and autoignition for the surrogates are compared with those for the jet fuels. Numerical calculations are carried out using a semi-detailed chemical-kinetic mechanism. The calculated values of the critical conditions of extinction and autoignition for the surrogates are found to agree well with experimental data. The research is performed in collaboration with Professor Eliseo Ranzi at Politecnico di Milano, Italy.

TECHNICAL DISCUSSION:

The major components of jet fuels are straight chain paraffins, branched chain paraffins, cycloparaffins, aromatics, and alkenes [1, 2]. Surrogate fuels are defined as mixtures of few hydrocarbon compounds whose relative concentrations can be adjusted so that the physical and chemical properties pertinent to combustion approximate those for jet fuels. Starting from the pioneering work of Schulz [3], who proposed a 12-component surrogate mixture for JP-8, several investigators have proposed surrogates for jet fuels. Examples are the Drexel surrogate of Ref. [4] and the Utah surrogate of Ref. [5]. Here three surrogates labeled (A), (B), and (C) are constructed and tested. The composition of these surrogates are

Surrogate (A) : 60 % *n*-decane, 20 % methylcyclohexane, and 20 % toluene.

Surrogate (B) : 60 % *n*-decane, 20 % methylcyclohexane, and 20 % *o*-xylene.

Surrogate (C) : 60 % *n*-dodecane, 20 % methylcyclohexane, and 20 % *o*-xylene.

Experiments are carried out employing the counterflow configuration. The burner used in the experimental study is made up of two ducts. A fuel stream made up of prevaporized fuel and nitrogen is injected from the fuel-duct, and an oxidizer stream of air is injected from the oxidizer-duct. Critical conditions of extinction are presumed to be given by the strain rate, $a_{2,e}$, and the mass fraction of fuel, $Y_{F,1}$, at the fuel boundary. Critical conditions of autoignition are presumed to be given by the strain rate, $a_{2,I}$, the temperature of the oxidizer

stream, $T_{2,i}$, and the mass fraction of fuel, $Y_{F,1}$, at the fuel boundary. The strain rate is calculated using the injection velocities of the counterflowing streams at the boundaries [6].

Experiments are carried out at a pressure of 1.013 bar. In the extinction experiments the temperature of the fuel stream is $T_1 = 503 (\pm 10)$ K, and the temperature of the oxidizer stream, $T_2 = 298$ K. The accuracy of the strain rate is $\pm 10\%$ of recorded value and that of the fuel mass fraction $\pm 3\%$ of recorded value. The experimental repeatability on reported strain rate is $\pm 5\%$ of recorded value. In the autoignition experiments the temperature of prevaporized fuel and nitrogen at the fuel boundary was maintained at 503 K. The temperature of air was increased until autoignition takes place. The accuracy of the measurement of the temperature of air at autoignition is expected to be ± 30 K, the strain rate $\pm 10\%$, and fuel mass fraction $\pm 3\%$ of recorded value. The experimental repeatability in the measurement of the temperature of air at autoignition is expected to be ± 6 K.

Numerical calculations were performed by Professor Eliseo Ranzi at Politecnico di Milano, Italy, using the chemical-kinetic in Ref. [7]. The high molecular weight compounds, used as reference fuels here, undergo a sequential reduction to lower molecular weight hydrocarbons during combustion. The semi-detailed approach uses a lumped description of the primary propagation reactions for the large species to smaller species, and then treats the successive reactions of smaller species with a detailed chemical-kinetic scheme. The overall chemical-kinetic scheme for the simulation of pyrolysis and combustion of high molecular weight hydrocarbon fuels, including those for the reference fuels considered here, is made up of 7878 reactions among 283 species. The computational model used here is a modified version of the opposed-flow diffusion flame code (OPPDIF [8]). The boundary conditions employed in the calculations are identical to those in the experiments. Flame structures and critical conditions of extinction and autoignition are obtained.

First, numerically calculated values of the critical conditions of extinction and autoignition of the reference single component fuels are compared with measurements. Next, similar comparisons are made for the surrogates (A), (B), and (C). Selected results are shown in Figs. 1, 2, and 3. The symbols in these figures represent experimental data, and the lines are results of numerical calculations. Figure 1 shows the temperature of the oxidizer stream at autoignition as a function of the strain rate for *n*-decane, *n*-dodecane, methylcyclohexane, and toluene. This figure shows data obtained at a fixed value of the mass fraction of fuel in the fuel stream $Y_{F,1} = 0.3$. The numerical results agree well with experimental data. Figure 2 shows the mass fraction of fuel as a function of the strain rate at extinction. The experimental data for surrogates are compared with those for JP-8 and Jet-A. Figure 2 shows that the extinction characteristics of JP-8 and Jet-A are similar. Moreover the extinction characteristics of the mixture (C) are close to those for JP-8 and Jet-A. Figure 3 shows the temperature of the oxidizer stream at autoignition as a function of the strain rate for the surrogates. Figure 3 shows that the fuel mixtures are slightly more reactive than Jet-A. The autoignition characteristics of mixture (C) are closest to those for Jet-A.

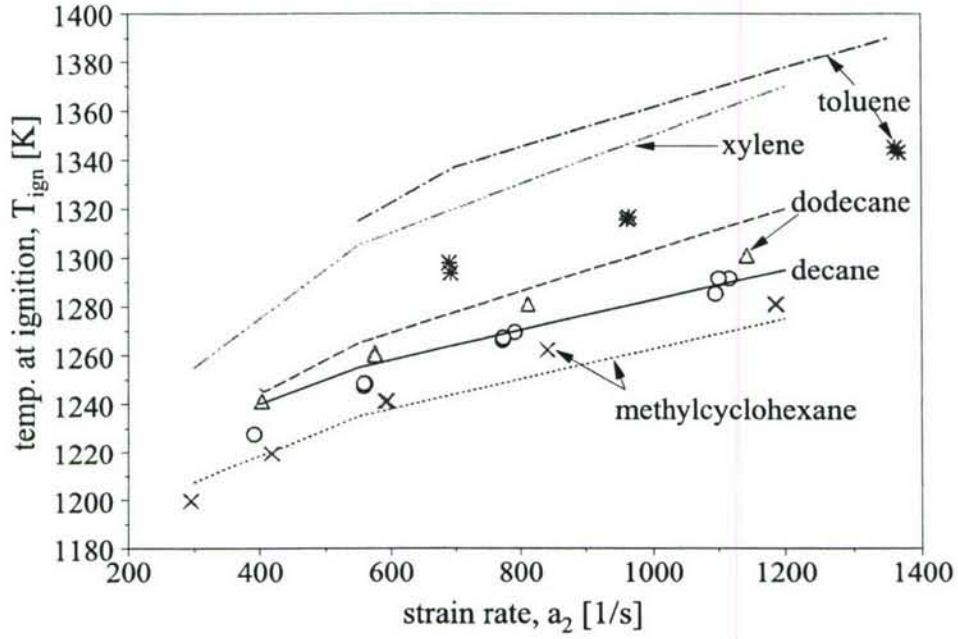


Figure 1: The temperature of the oxidizer stream at autoignition as a function of the strain rate. The figure shows experimental data obtained at fixed values of the mass fraction of fuel in the fuel stream $Y_{F,1} = 0.3$.

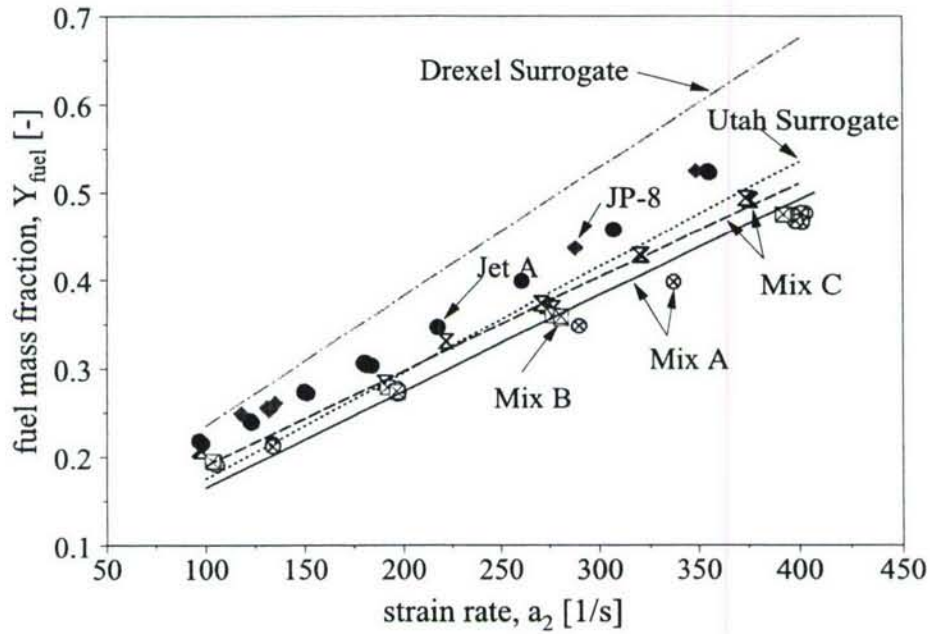


Figure 2: The mass fraction of fuel as a function of the strain rate at extinction.

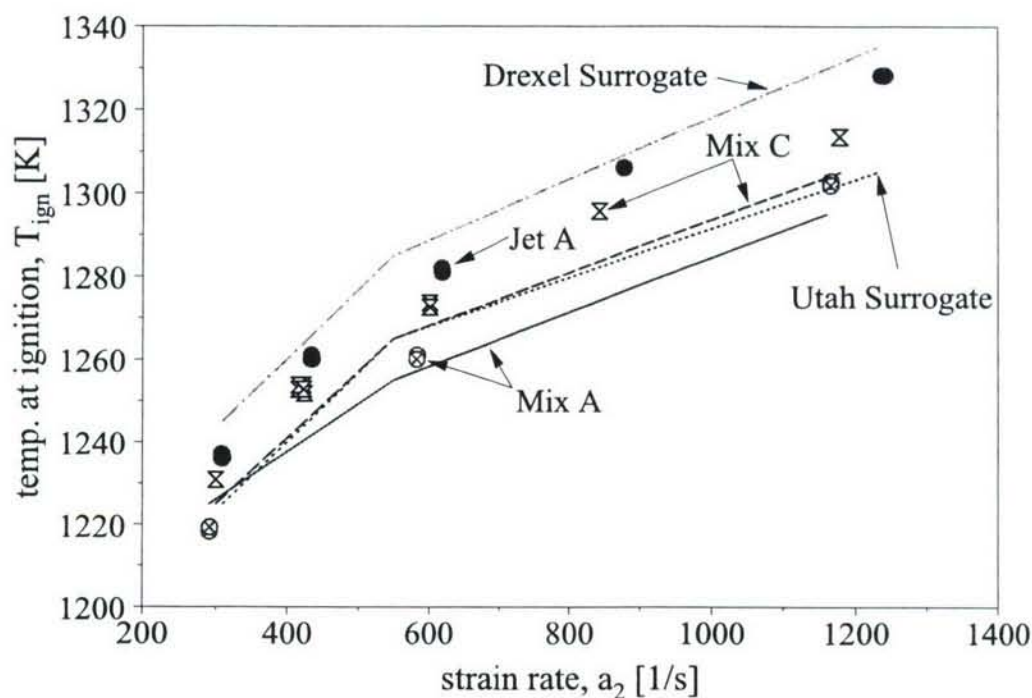


Figure 3: The temperature of the oxidizer stream at autoignition as a function of the strain rate.

References

- [1] T. Edwards, L. Q. Maurice, *Journal of Propulsion and Power* 17 (2001) 461–466.
- [2] T. Edwards, *2001 Fall Technical Meeting, Eastern States Section of the Combustion Institute*.
- [3] W. Schulz, *ACS Petroleum Chemistry Division Preprints* 37 (2) (1991) 383–392.
- [4] A. Agosta, N. P. Cernansky, D. L. Miller, T. Faravelli, E. Ranzi, *Experimental Thermal and Fluid Science* 28 (2004) 701–708.
- [5] A. Violi, S. Yan, E. G. Eddings, A. F. Sarofim, S. Granata, T. Faravelli, E. Ranzi, *Combustion Science and Technology* 174 (2002) 399–417.
- [6] K. Seshadri, F. A. Williams, *International Journal of Heat and Mass Transfer* 21 (2) (1978) 251–253.
- [7] <http://www.chem.polimi.it/CRECKModeling>.
- [8] A. Lutz, R. Kee, J. Grcar, F. Rupley, Tech. Rep. SAND96-8243, Sandia National Laboratories (1997).

EXPERIMENTAL AND THEORETICAL STUDIES OF AUTOIGNITION AND BURNING SPEED OF JP-8 AND DF-2

Grant No.: W911NF0510051

Principal Investigator: **Hameed Metghalchi**

*Mechanical, Industrial and Manufacturing Engineering,
Northeastern University,
Boston, Massachusetts 02115*

Summary

The capabilities of the combustion laboratory at Northeastern University have increased tremendously over the past year. The construction of the new experimental apparatus has allowed for much greater productivity. The addition of thick windows for the cylindrical vessel has allowed the lab to undertake testing at higher pressures and temperatures. Follow up the previous reports; we have used our modified burning model to measure laminar burning speed of JP-8, 21% O₂ and 79% He at wide range of temperature, pressure and equivalence ratio.

Technical Discussion

1. Review of the Burning Model Using Pressure Method

More detail of the burning model has been presented in the previous reports. Here for the sake of review we bring up the general equations. The total volume of the gas in the combustion chamber is

$$V_i = V_c - V_e = V_b + V_u \quad 1.1$$

The energy conservation equation is

$$E_i - Q_e - Q_w - Q_r = E_b + E_u \quad 1.2$$

where E is the initial energy of the unburned gas, Q_w is the conduction heat loss to the wall, Q_e is the conduction heat loss to the electrodes, Q_r is the heat loss due to radiation from the burned gas.

The radiation heat loss from the burned gas was calculated using

$$Q_r = \int \dot{Q}_r(t') dt' = 4\alpha_p V_b \sigma T_b^4 \quad 1.3$$

where α_p is the Planck mean absorption coefficient and σ is the Stefan- Boltzman constant.

Burning speed may be defined

$$S_b = \dot{m}_b / \rho_u A_b = m\dot{x} / \rho_u A_b \quad 1.4$$

where A_b is the area of a sphere having a volume equal to that of the burned gas. This expression is valid for smooth, cracked, or wrinkled flames of any shape.

2. Laminar Burning Speed Measurements

In the previous reports we have presented our experimental results for the burning speeds of JP-8 and air over a wide range of temperature, pressure and equivalence ratio. We have

facilitated our cylindrical vessel with heating elements, thicker windows and more elaborate data acquisition system. Figure 1 shows the flame shadowgraph images of stoichiometric JP-8 air at initial pressure of 1 atm and temperature of 450 k. It can be seen that flame turns cellular and is not laminar at the end stages of the combustion as pressure and temperature are high.

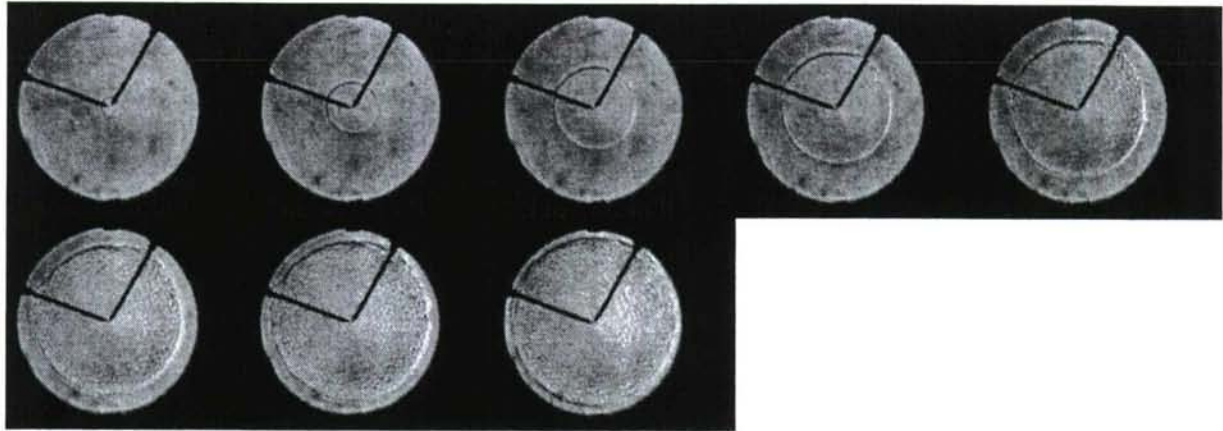


Figure 1: Shadowgraph images of premixed JP-8 and air ignited at equivalence ratio of 1, initial pressure of 1 atm and temperature of 450 K. Step size is 4 ms.

It has long been known that the replacement of the Nitrogen as the diluent with Helium will allow for the flame to become laminar. The Lewis number for Helium is less than that of Nitrogen, which decreases the tendency towards the formation of thermal diffusive cellular structures in the flame. It was decided to replace the Nitrogen with an equal percentage of helium. As it shown in Figures 2-4, this addition did make the flame laminar over a range of initial pressures and equivalence ratios.

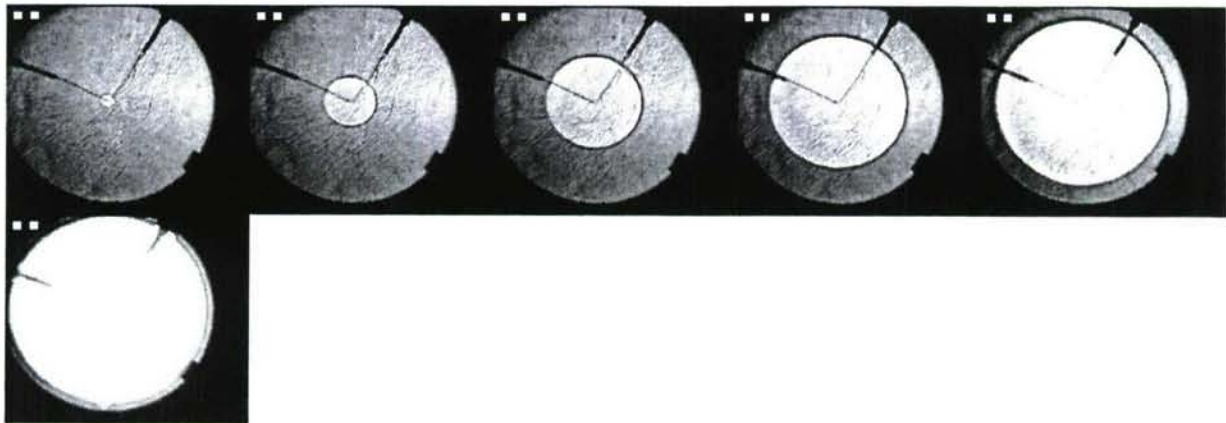


Figure 2: Shadowgraph images of premixed JP-8, 21% O₂ and 79% He ignited at equivalence ratio of 1, initial pressure of 1 atm and temperature of 473 K. Step size is 4 ms.

After this observation, laminar burning speed of JP-8 has been measured using the pressure method and our burning model over $1 < P < 13 \text{ atm}$, $450 < T < 750 \text{ K}$ and $0.8 < \phi < 1$. The results are shown in Figures 6-7.

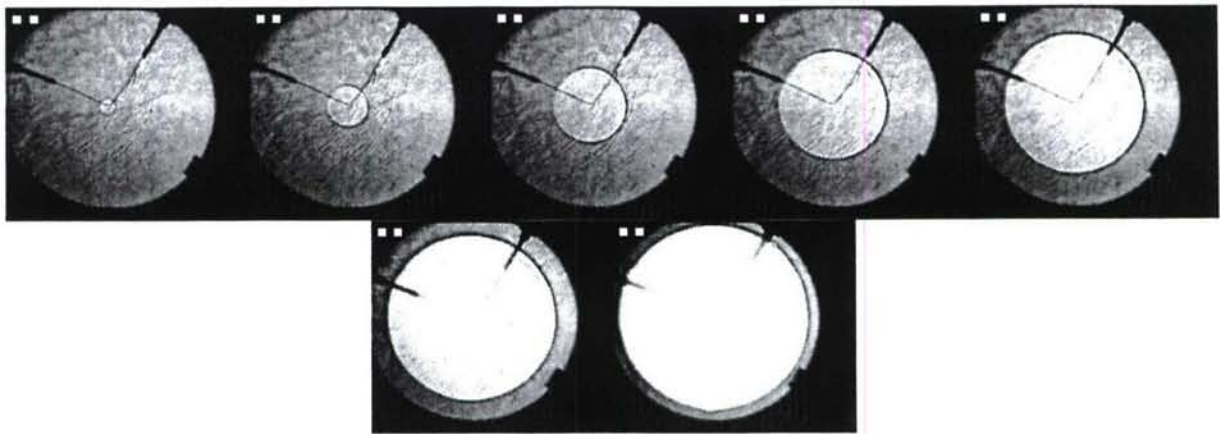


Figure 3: Shadowgraph images of premixed JP-8, 21% O₂ and 79% He ignited at equivalence ratio of 0.8, initial pressure of 1 atm and temperature of 473 K. Step size is 4 ms.

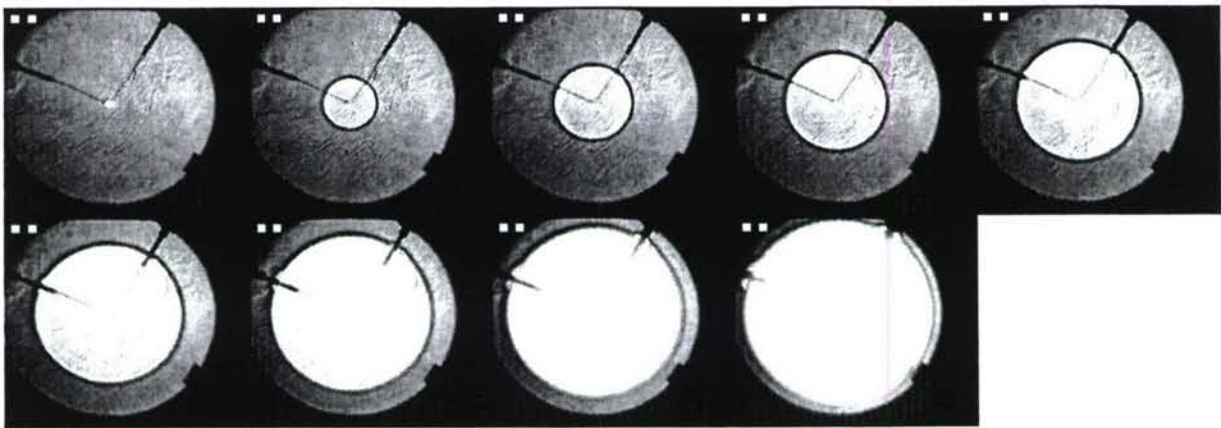


Figure 4: Shadowgraph images of premixed JP-8, 21% O₂ and 79% He ignited at equivalence ratio of 1, initial pressure of 2 atm and temperature of 473 K. Step size is 4 ms.

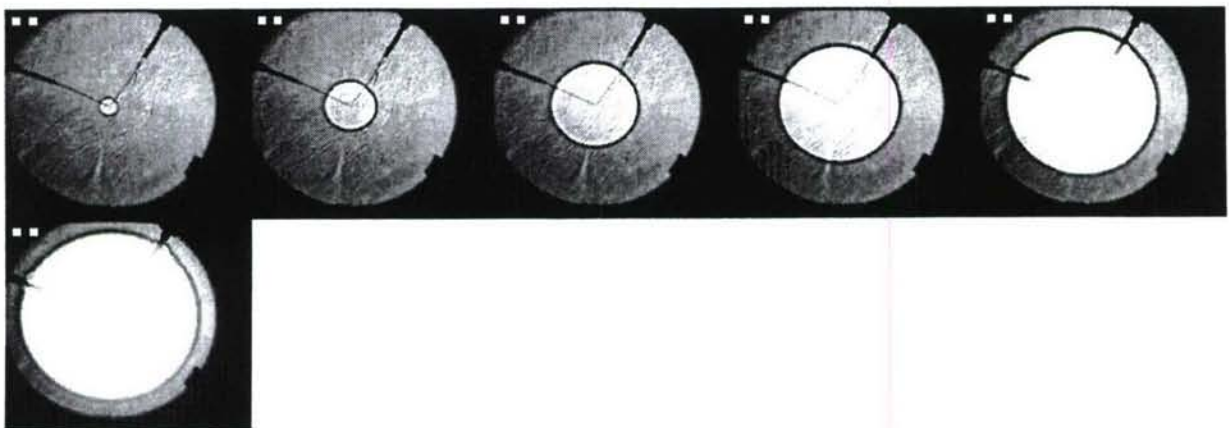


Figure 5: Shadowgraph images of premixed JP-8, 21% O₂ and 79% He ignited at equivalence ratio of 0.8, initial

pressure of 2 atm and temperature of 473 K. Step size is 4 ms.

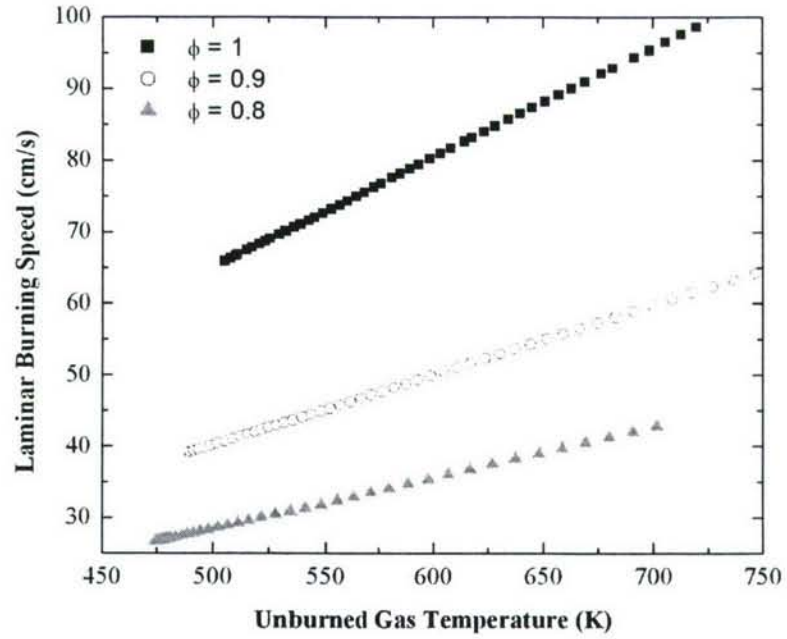


Figure 6: Laminar Burning Speed of JP-8, O₂ and He. $P_i = 1$ atm, $T_i = 473$ K

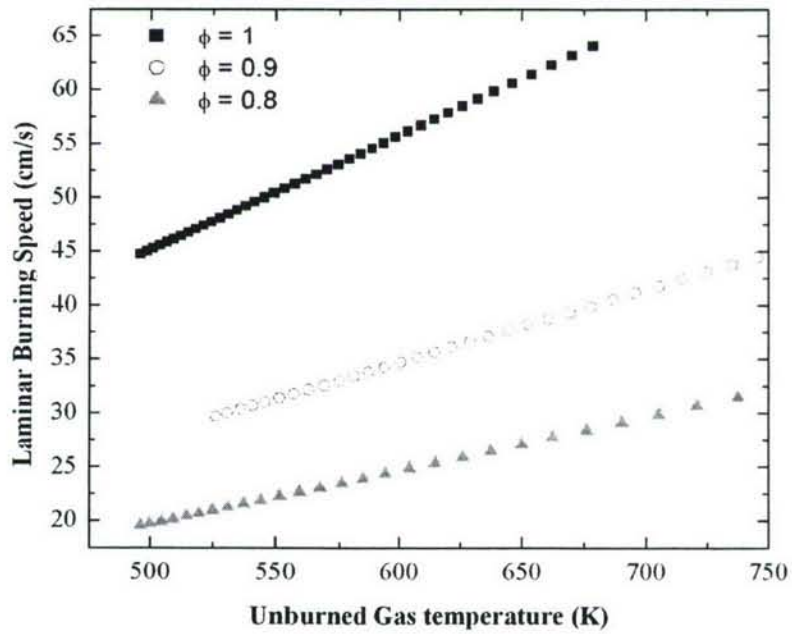


Figure 7: Laminar Burning Speed of JP-8, O₂ and He. $P_i = 2$ atm, $T_i = 473$ K

DETAILED AND SIMPLIFIED CHEMICAL KINETICS OF AVIATION FUELS AND SURROGATES

Grant Number FA8655-06-1-3052

R.P. Lindstedt

Department of Mechanical Engineering, Imperial College London,
Exhibition Road, London SW7 2 AZ, UK.

SUMMARY/OVERVIEW

The removal of the high Damköhler number assumption from modeling approaches is essential for the computational simulation of combustor flows where strong direct kinetic effects are present. Examples of relevant physical phenomena include flame extinction and re-light as well as pollutant emissions. Calculation methods (e.g. LES/FMDF) aimed at including such effects are computationally demanding and simplified reaction mechanisms that represent the desired chemical features with sufficient accuracy are required. Difficulties are augmented for aviation fuels due to the wide range of fuel components and sufficiently accurate detailed surrogate mechanisms are required for the subsequent derivation of further simplifications under actual operating conditions prior to the implementation into calculation methods for turbulent flows. The present paper addresses the issue of substituted aromatics and outlines a reaction class based route to the derivation of detailed chemical kinetic mechanisms. The example given considers the toluene/1-methyl naphthalene system.

TECHNICAL DISCUSSION

Flow timescales encountered in high performance propulsion devices increasingly lead to difficulties associated with kinetically controlled or influenced phenomena such as flame stability, extinction and re-light [1]. The accuracy of surrogate fuel models ultimately needs to be assessed with respect to the reproduction of selected key parameters in practical applications. The issue is therefore arguably best addressed in the context of turbulent flame simulations where the relative impact of flow and chemistry can be assessed. However, operating conditions of practical devices are typically far removed from the conditions under which validation of computational sub-models is possible. In the present context, detailed chemical kinetic models are then required to (i) facilitate the extrapolation to relevant conditions and (ii) serve as a basis for further simplifications under such conditions. The current paper illustrates the use of a reaction class based approach for the generation of detailed chemical mechanisms for substituted aromatics such as 1-methyl naphthalene. The subject is challenging and the use of chemical similarities with the oxidation of cyclopentadiene, benzene and toluene is explored in the context of quantitative species predictions.

The starting point for the toluene sub-mechanism stems from Lindstedt and Maurice [2] with subsequent developments by Potter [3] and as part of ongoing work. The mechanism consists of 88 reactions and 13 species and considers oxidation and pyrolysis of the CH_3 group as well

as radical attack on the ring. The underlying small hydrocarbon chemistry exerts a significant influence and was derived using a hierarchical approach [2,3]. An analysis of uncertainties and a reconciliation of sub-mechanisms with those produced by other workers forms part of the current effort. The corresponding mechanism for 1-methyl naphthalene oxidation was based directly on the equivalent toluene reactions and features decomposition and radical attack on the aromatic rings and the methyl group. The mechanism has also been applied to model the oxidation of species such as naphthalene with encouraging results [3].

A wide range of conditions has been used to validate the toluene sub-mechanism. However, the scarcity of experimental data for higher substituted aromatics presents a significant limitation in the context of validation of proposed reaction mechanisms. In the present case, the obtained accuracy is illustrated by comparisons with experimental data for toluene and 1-methyl naphthalene obtained in a Jet Stirred Reactor (JSR) [4,5]. The single case presented here was chosen to facilitate direct comparisons of toluene and 1-methyl naphthalene oxidation under similar conditions. The toluene data was obtained at a stoichiometry (ϕ) of 1.5, $1000 < T \text{ (K)} < 1380 \text{ K}$, a mean residence time (τ) of 120 ms and at atmospheric pressure. The dominant fuel consumption paths at higher temperatures under these conditions is via $C_7H_8 + H/OH = C_7H_7 + H_2/H_2O$ (1). The adopted rates follow the CEC recommendations by Baulch et al. [6]. The consumption of toluene and oxygen is reproduced with reasonable accuracy along with the formation of primary aromatic products such as benzene, styrene and ethyl-benzene as shown in Fig. 1. The generation of H radicals is partly via H/O ring substitution $C_7H_8 + O = OC_7H_7 + H$ (2). The rate has been adopted from Hoffmann et al. [7] who considered a temperature range of 1100 – 1350 K at a pressure of 300 Pa. Reaction (2) is interesting as it also initiates a primary C_6H_6 formation channel with OC_7H_7 eventually leading to benzene via fulvene. The calculated concentrations of C_7H_6O are somewhat over-predicted and the primary channel at 1160 K is via thermal decomposition $C_7H_7O = C_7H_6O + H$ (3). The formation of C_7H_7O is via O_2 and HO_2 attack on the benzyl radical and, in particular, the latter reaction is subject to significant uncertainties.

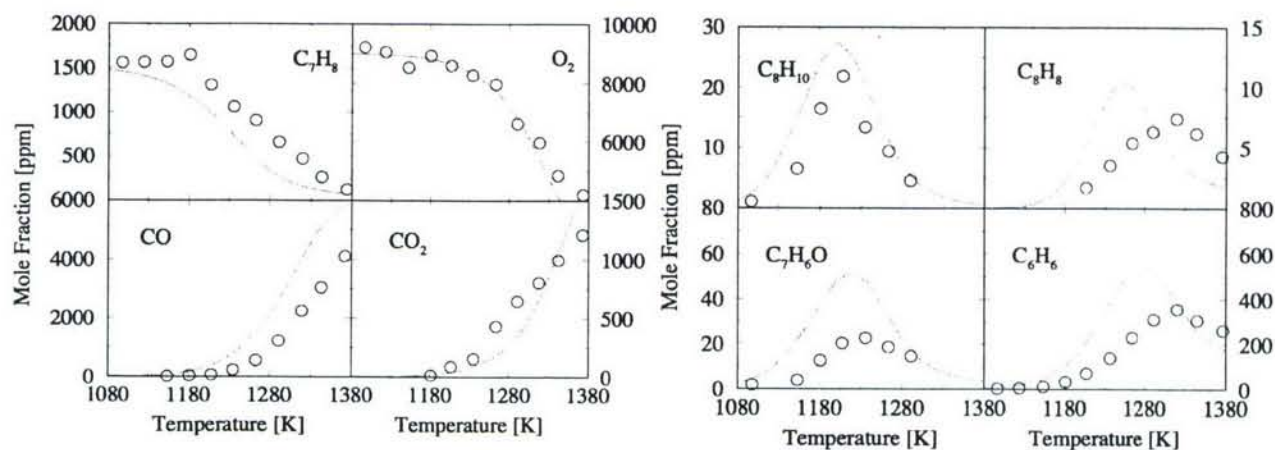


Fig. 1. Consumption of C_7H_8 and O_2 along with CO and CO_2 formation (left) and major primary intermediates (right) formed during the oxidation of toluene in a JSR [4].

The rate for reaction (3) was estimated from the heat of reaction (64 kJ/mol) plus an additional 4 kJ/mol and a frequency factor of $3.0 \cdot 10^{12} \text{ m}^3 \text{ kmol}^{-1} \text{ s}^{-1}$ was assigned. Alternative chemical mechanisms feature a rate expression with a high frequency factor ($1.3 \cdot 10^{14} \text{ m}^3 \text{ kmol}^{-1} \text{ s}^{-1}$) and a low barrier (4.6 kJ/mol), which is incompatible with the current data sets. The issue is raised as an illustration of current uncertainties. The developed toluene mechanism

does reproduce, with reasonable accuracy, the H radical concentrations formed during toluene pyrolysis, as measured by Braun-Unkoff et al. [8], and the more recent time resolved OH radical data obtained by Vasudevan et al. [9]. The corresponding 1-methyl naphthalene chemistry was derived directly from the toluene mechanism with appropriate adjustments (e.g. to frequency factors). The ability of the resulting mechanism to reproduce 1-methyl naphthalene JSR data was explored and the case presented here features $\phi = 1.5$, $1090 < T$ (K) < 1440 , a mean residence time of 100 ms and a pressure of 1 atm. Selected results are shown in Fig. 2 and principal reaction paths in Fig. 3. The overall agreement is encouraging with fuel and oxygen consumption along with levels of naphthalene and indene well reproduced. The small levels of (s,t)-C₉H₈ shown in Fig. 2 correspond to phenyl with C₃ side chains (ϕ -CHCCH₂ and ϕ -CH₂CCH) [10].

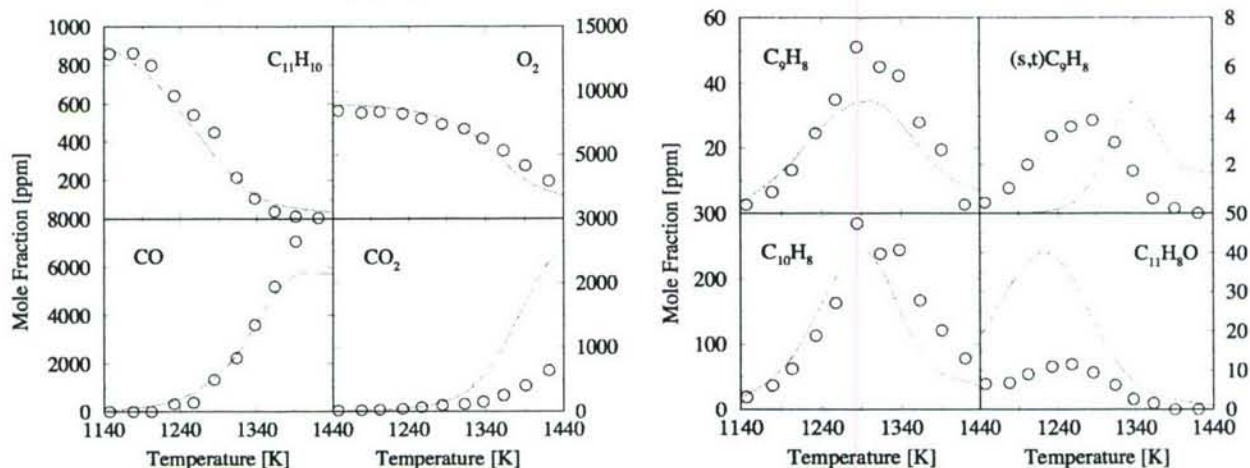


Fig. 2. Consumption of C₁₁H₁₀ and O₂ along with CO and CO₂ formation (left) and major primary intermediates (right) formed during the oxidation of 1-methyl naphthalene in a JSR at atmospheric pressure with a mean residence time of 100 ms [5].

The formation of C₁₁H₉ is predominantly via H (30%) and OH (15%) radical attack. The rate for the analogous C₇H₈ + OH step was used for the model reaction. The dominant channel for the corresponding abstraction to C₁₁H₉P is via OH radical attack and the rate for the analogous reaction was obtained from Baulch et al. [6]. The analogous [7] O atom attack on the ring also generates H radicals and consumes about 15% of the fuel at 1260 K. The subsequent formation of indene was based on an analogy with the C₆H₆/C₅H₆ system [11]. Similarly to the results obtained for toluene, the principal aldehyde (C₁₁H₈O) is overpredicted. The path responsible follows by analogy as C₁₁H₉O = C₁₁H₈O + H along with the uncertainties associated with O₂

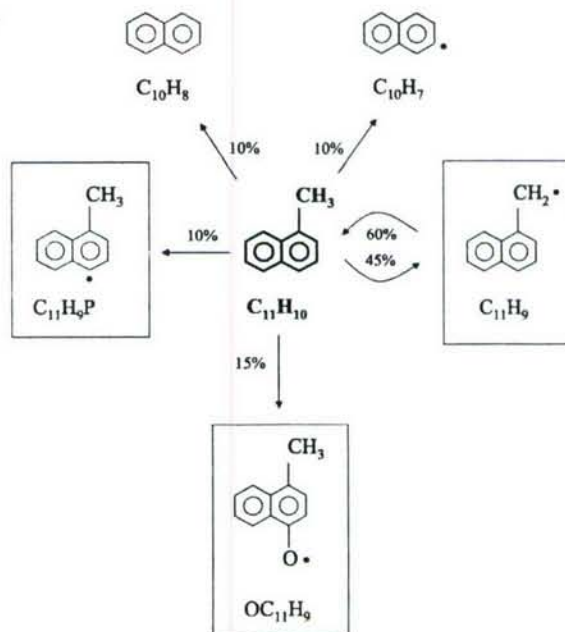


Fig. 3. Consumption paths of 1-methyl naphthalene in a JSR ($T = 1260$ K, $P = 1$ atm and $\phi = 1.5$).

and HO₂ attack on C₁₁H₉ as mentioned above in the context of the benzyl radical. The formation of naphthalene and the naphthyl radical follows via paths directly analogous with benzene formation from toluene. The extraction of CO from the C₆ ring, eventually leading to indene, follows from the work by Lindstedt and Rizos [11].

CONCLUSIONS

The current paper has sought to illustrate the use of a reaction class based approach for the oxidation of substituted aromatics. An analogy with toluene was used to develop a comprehensive detailed chemical kinetic mechanism for 1-methylnaphthalene with encouraging results. A particular benefit with the approach is that validation data from simpler systems can be used to mitigate the scarcity of such data for practical fuel components. The approach has also been used to create the basis of a simple two-component surrogate mechanism for Jet-A based on n-decane [12] and n-propyl benzene [13]. However, common problems were also found and, for example, predictions of C₇H₆O and C₁₁H₈O were found to be consistently high. Recent work on the toluene/benzyl system (e.g. [9]) opens up the possibility of removing such anomalies as part of the current grant. In future work, the mechanism generation part will be automated through the adaptation of an existing JAVA based tool developed for heterogeneous chemistry. It must also be emphasized that the creation of large detailed mechanisms is predominantly useful in the context of providing a reference frame for extrapolation to practical operating conditions and for further simplifications aimed at the inclusion of chemical kinetic effects into turbulent flows [14].

ACKNOWLEDGEMENT

The contributions made by M Potter are gratefully acknowledged along with the access to unpublished data obtained by P Dagaut and co-workers.

REFERENCES

- [1] Tishkoff, J.M., Drummond, J.P., Edwards, T. and Nejad, A.S., Paper AIAA 97-1017 (1997).
- [2] Lindstedt, R.P. and Maurice, L.Q., *Combust. Sci. and Technol.*, 120:119-167 (1996).
- [3] Potter, M. L. Detailed Chemical Kinetic Modelling of Propulsion Fuels, PhD Thesis, Imperial College London, 2003.
- [4] Dagaut, P., Pengloan, G. and Ristori, A. *Phys. Chem. Chem. Phys.* 4: 1846 (2002)
- [5] Dagaut, P. Private Communication, March 2003.
- [6] Baulch, D.L. Cobos, C.J., Cox, R.A., Esser, C., Frank, P., Just, Th., Kerr, J.A., Pilling, M.J., Troe, J., Walker, R.W. and J. Warnatz, J., *J. Phys. Chem.* 21:411 (1992).
- [7] Hoffmann, A., Klatt, M. and Wagner, G. Gg., *Z. Phys. Chem.* 168:1 (1990)
- [8] Braun-Unkhoff, M., Frank, P. and Just, Th., *Proc. Combust. Inst.* 22:1053 (1988).
- [9] Vasudevan, V., Davidson, D. and Hanson, R.K. *Proc. Combust. Inst* 30:1155 (2005).
- [10] Lindstedt, R.P., Maurice, L.Q. and Meyer, M. The Royal Society of Chemistry, Faraday Discussion 119:409-432 (2001).
- [11] Lindstedt, R.P. and Rizos, K.-A., *Proc. Comb. Inst.* 29:2291-2298 (2002).
- [12] Lindstedt, R.P. and Maurice, L.Q. *AIAA J. Propul. Power* 16:187-195 (2000).
- [13] Final Report, Computational Fluid Dynamics for Combustion (CFD4C), CEC Project No: GRD1-1999-10325 (2003).
- [14] Kuan, T.S. and Lindstedt, R.P. *Proc. Combust. Inst.* 30:767 (2005).

IGNITION KINETICS IN FUELS OXIDATION

(ARO Grant No. W911NF-04-1-0151)

Principal Investigator: Chung K. Law

Princeton University
Princeton, NJ 08544

SUMMARY/OVERVIEW

This program studies fundamental chemical kinetics as well as its individual and coupled effects with aerodynamics on laminar nonpremixed ignition and flame propagation for hydrocarbons, through experimental, computational, and theoretical approaches. During the reporting period, three projects were undertaken, namely: (1) Experimental determination of high-pressure laminar flame speeds and kinetic modeling of carbon-monoxide / hydrogen combustion; (2) experimental and computational determination of the ignition temperatures and reaction mechanism of 1,3-butadiene at atmospheric and elevated pressures; and (3) experimental and computational studies on the ignition of the butene isomers.

TECHNICAL DISCUSSION

1. Experimental determination of high-pressure laminar flame speeds and kinetic modeling of carbon-monoxide / hydrogen combustion

The objective for the present study is to experimentally determine high-pressure laminar flame speeds and update $CO-H_2$ mechanism for enhanced accuracy and comprehensiveness. The experimental data, obtained in our high-pressure combustion chamber up to 40 atm, are shown in Figs. 1 and 2.

A detailed reaction mechanism was developed based on the latest evaluation of the kinetic data for combustion modeling and recently published literature. The reaction of OH with CO is responsible for the major fraction of energy release in the oxidation of hydrocarbons to CO_2 and H_2O , and the reaction rate is the most sensitive for the prediction of $CO-H_2$ flame speeds. The reaction $H+O_2+M \rightarrow HO_2+M$ provides another route for the conversion of CO to CO_2 through $CO+HO_2 \rightarrow CO_2+OH$ at high pressures or in the initial stages of CO oxidation. However, the rate constant for $CO+HO_2$ at temperatures above 800 K is limited to indirect determinations. To further investigate this reaction rate, we performed high-level *ab initio* calculations and follow the reaction mechanism with the first stage in the reaction being the formation of a free radical intermediate $HO_2+CO \rightarrow HOOC\bullet O$ which then decomposes to yield the products, and with the rate of formation of the intermediate equal to the formation of the products. By using the MP2(full)/6-31G(d,p) optimized geometries and canonical transition state theory, we calculated this rate constant to be $k = 1.15 \times 10^5 T^{2.2785} \exp(-17.55 \text{ kcal/RT}) \text{ cm}^3 \text{ mol}^{-1} \text{ s}^{-1}$ at 300 – 2500 K.

The modeling results indicated that our current kinetic model accurately predicts the measured flame speeds and the non-premixed counterflow ignition temperatures determined in our previous study (Fig. 3) as well as homogeneous system data from literature, such as concentration profiles from flow reactor and ignition delay time from shock tube experiments.

This work is reported in Publication No. 1.

2. Experimental and Computational Determination of Counterflow Ignition Temperatures at Atmospheric and Elevated Pressures, and Reaction Mechanism of 1,3-butadiene

1,3-Butadiene is a common product of hydrocarbon combustion and an industrial chemical used to produce polymers such as poly-butadiene and styrene-butadiene rubbers. There have been quite a number of kinetic studies of 1,3-butadiene, although they are mainly for homogeneous systems. Few kinetic studies have been performed for inhomogeneous systems, particularly tailored for low- to intermediate-

temperature chemistry. In the present study, nonpremixed ignition of 1,3-butadiene was investigated experimentally employing the counterflow configuration.

Specifically, the ignition temperature of nitrogen-diluted 1,3-butadiene by heated air in counterflow was experimentally determined for system pressures from 1.0 to 5.1 atmospheres at pressure-weighted strain rates from 100 to 240 s⁻¹. These experimental data were compared to calculations based on the mechanism developed by Laskin *et al.* and the results are shown in Figs. 4 and 5. In general, the Laskin-mechanism over-predicts the ignition temperature by 25-40K, and the differences become slightly larger at higher pressures and lower temperatures. Sensitivity analyses showed that the ignition of 1,3-butadiene is sensitive not only to the H₂/CO chemistry as well as the reaction pathways involving ethylene oxidation, and O addition to and H abstraction of 1,3-butadiene, but is also to the binary diffusion between 1,3-butadiene and nitrogen since it determines the amount of diffusion-constrained fuel available for ignition.

The attempt to obtain a reduced mechanism has evolved into a substantial and rewarding effort in that a new algorithm combining DRG and sensitivity analysis was developed that is capable of identifying skeletal mechanisms of minimal size for given accuracy requirements. A 46-species skeletal mechanism was thus developed which was further simplified to a 30-step reduced mechanism based on QSS assumptions. These two mechanisms were then validated against the detailed mechanism for both auto-ignition and PSR under a variety of parameter ranges, and were further validated for heterogeneous systems: counterflow ignition and laminar flame speeds. Excellent agreements between these two mechanisms and the detailed one were found over extensive parametric ranges. The error is less than 4K for counterflow ignition temperatures and 2cm/s for laminar flame speeds, and the reduction error under atmospheric pressure is smaller than the difference in detailed mechanism and experiment data. Both mechanisms conserve all the important reaction pathways and major species constituting the detailed mechanism, and as such, they provide a more efficient platform for the study of the controlling mechanisms and expedited combustion simulations of 1,3-butadiene.

This work is reported in Publication No. 2.

3. Experimental and Kinetics Study of Ignition Temperatures of Butene Isomers at Atmospheric and Elevated Pressures

Previous studies on the effects of molecular structure on ignition have been mainly on alkanes. Similar studies of alkenes, however, have been relatively few, even though they are the major intermediates of alkane oxidation and are important fuels themselves. In view of the need for further information on the effects of molecular structure of alkenes on ignition, we have conducted a systematic study on the ignition of the four isomers of butene, namely 1-butene, cis-2-butene, trans-2-butene, and isobutene. Butene isomers were selected for study because butene is the smallest alkene which has more than one isomer.

Specifically, the ignition temperatures of the four butene isomers were determined in the counterflow. The measured ignition temperatures were found to increase in the order of 1-butene, 2-butenes and isobutene. The ignitability of cis-2-butene and trans-2-butene cannot be compared because the difference between their ignition temperatures is less than 7 K, which is within the $\pm 2\sim 5$ K repeatability range of the experimental data. Nevertheless, cis-2-butene was determined to be slightly easier to ignite than trans-2-butene (Figs. 6 and 7).

A thorough comprehension of the observed trend of butene ignition is however hampered by the lack of adequately validated mechanism for the C₄ hydrocarbons. Alternatively, we performed the kinetic analysis on three important pathways for ignition, namely the initiation by O₂ abstraction, and HO₂ and OH addition, as numerous literatures have illustrated their importance on ignition. While any single pathway or even all three together is not comprehensive enough to predict ignition, it is nevertheless recognized that a study of the present nature does yield useful insights into ignition. For example, the calculated reaction rate constants (*k*) for four abstraction reactions are shown in Fig. 8 as functions of temperature. It is seen that they vary with temperature and increase in the order of isobutene, trans-2-butene, 1-butene and cis-2-butene in the lower-temperature ignition regime. The trend for these calculated rate constants can be understood by the allylic C-H bond energy and the number of equivalent H atoms in the butenes. We first note that since the differences between the allylic C-H bond energies for the four butenes are small, less than 5 kcal/mol, there is no dramatic difference between their rates for the H-abstractions. Secondly, the lower value of the bond dissociation energy generally corresponds to the higher abstraction rates except that cis-2-butene has higher values of *k* than 1-butene. This exception is

due to the different number of equivalent H atoms which affects the Arrhenius factor: 2-butenes and isobutene all have six equivalent allylic H atoms, but 1-butene has only two and therefore has a smaller A factor. Therefore, except for the fact that *cis*-2-butene is slightly more reactive than 1-butene, the trend for the reaction rate constants of the H-abstraction reactions qualitatively agrees with our experimental results on ignitability. The present study has provided reliable thermochemical and kinetic data, which are essential components in the future development of C_4 hydrocarbon mechanisms.

This work is reported in Publication No. 3.

JOURNAL PUBLICATIONS

- [1] "High-pressure laminar flame speeds and kinetic modeling of carbon-monoxide / hydrogen combustion" by H. Y. Sun, S. I. Yang, and C. K. Law, *Proc. Combust. Inst.* 31, in press.
- [2] "Experimental counterflow ignition temperatures and reaction mechanisms of 1,3-butadiene" by X. L. Zheng, T. F. Lu, and C. K. Law, *Proc. Combust. Inst.* 31, in press.
- [3] "Ignition of the butene Isomers: an experimental and kinetics study" by X. L. Zheng, H. Y. Sun, and C. K. Law, submitted.
- [4] "Thermochemical and kinetic analyses on oxidation of isobutenyl radical and 2-hydroperoxy-methyl-2-propenyl radical" by X. L. Zheng, H. Y. Sun, and C. K. Law, *J. Phys. Chem. A*, **2005**; *109*, 9044-9053.

4. Figures

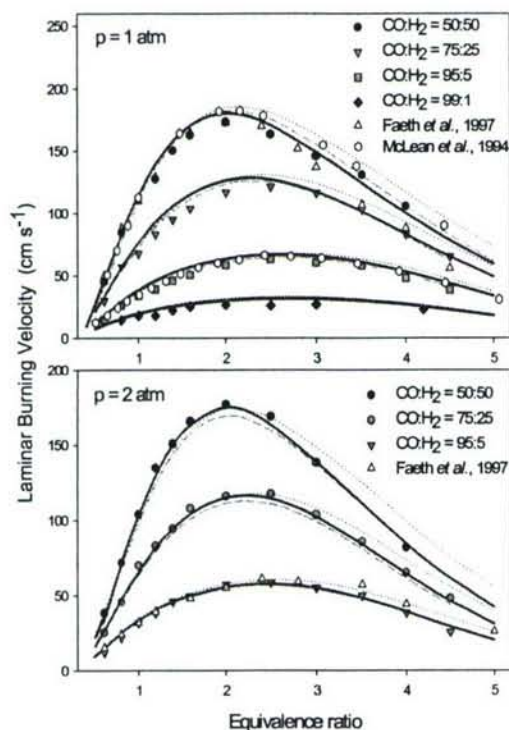


Fig. 1. Measured and calculated laminar flame speeds vs. equivalence ratio for different CO/H₂/air mixtures at 1 and 2 atmospheres.

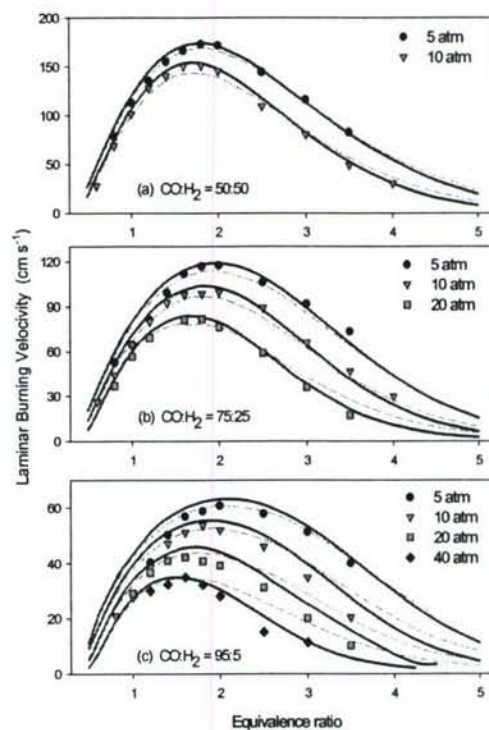


Fig. 2. Measured and calculated laminar flame speeds vs. equivalence ratio for different CO/H₂/He/O₂ mixtures at 5, 10, 20, and 40 atmospheres

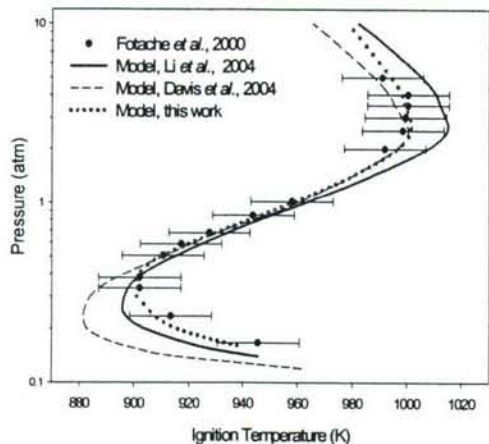


Fig.3. Comparison of calculated ignition temperatures vs. pressure with the experimental data at the strain rate of 100 s^{-1} for 5% H_2 in CO .

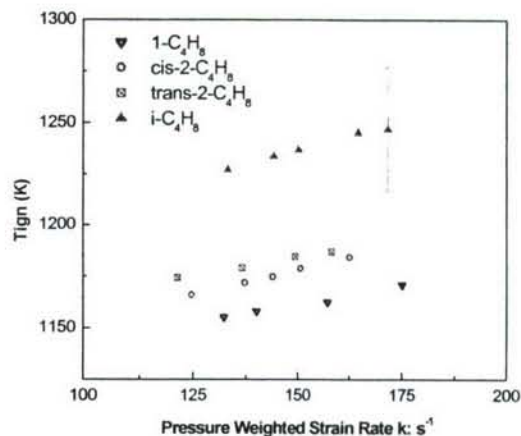


Fig.6. Effect of strain rate on the ignition temperatures for butene isomers. Conditions: 5.9% Fuel in N_2 and 2.4atm.

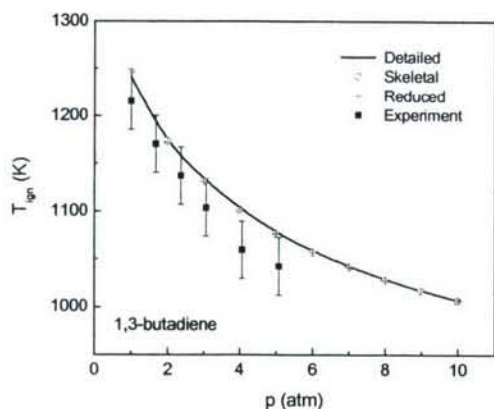


Fig.4. Ignition temperatures of 5.9% 1,3-butadiene in N_2 as a function of pressure. Condition: pressure weighted strain rate of 150 s^{-1} .

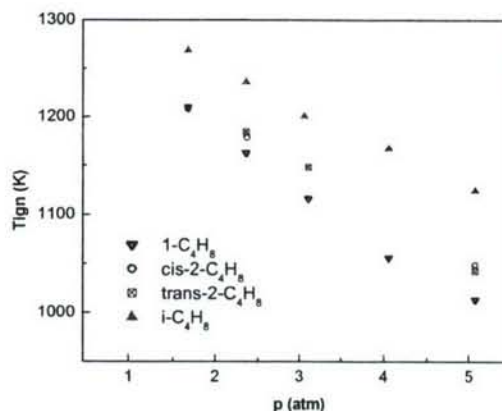


Fig.7. Effect of pressure on the ignition temperatures for butene isomers. Conditions: 5.9% Fuel in N_2 and $k=150 \text{ s}^{-1}$.

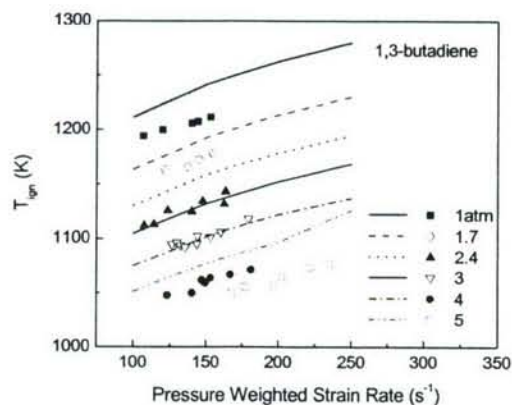


Fig.5. Ignition temperatures of 5.9 % 1,3-butadiene in N_2 as a function of pressure-weighted strain rate under different pressures.

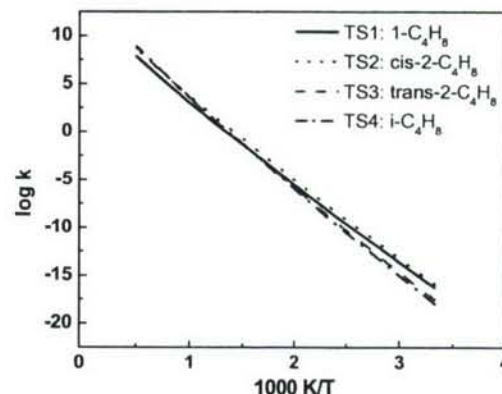


Fig.8. Reaction rate constants as functions of temperature for the H abstraction reaction by oxygen: $\text{C}_4\text{H}_8 + \text{O}_2 = \text{C}_4\text{H}_7 + \text{HO}_2$.

PHYSICAL AND CHEMICAL PROCESS IN FLAMES

(AFOSR Grant No. FA9550-04-1-0003)

Principle Investigator: Chung K. Law

Department of Mechanical and Aerospace Engineering
Princeton University, Princeton, NJ 08544

SUMMARY/OVERVIEW

The objectives of the present program are to develop detailed and simplified chemical kinetics models for hydrocarbon combustion, and to understand and quantify the dynamics of flames. During the reporting period progress were made in the following projects: (1) Skeletal reduction using sensitivity analysis aided by directed relation graph; (2) derivation of analytical solution of quasi-steady state species using directed graph; (3) derivation of a reduced mechanism for lean premixed methane/air flames; (4) extinction and stability analyses of diffusion flames with radiation heat loss; and (5) study of the response of premixed flames to velocity fluctuations with flame stretch effects.

TECHNICAL DISCUSSION

1. Skeletal Reduction with Directed Relation Graph Aided Sensitivity Analysis (DRGASA)

The method of DRG (directed relation graph) was developed in our previous work to reduce large detailed mechanisms to smaller skeletal mechanisms with linear-time algorithm and user-specified accuracy. In this year, the DRG was further extended. First, the conditions for DRG to be applicable was formally studied and it was found that the method is valid for detailed mechanisms for which detailed balancing is honored, which is true for most practical mechanisms of hydrogen and hydrocarbon fuels. Second, DRG was combined with sensitivity analysis to obtain skeletal mechanisms of minimum size for given accuracy requirement.

Specifically, we note that while in many situations DRG reduction can already provide sufficiently compact skeletal mechanisms that can be either directly applied in simulations, the skeletal mechanisms from DRG are frequently not minimal. This is because DRG retains a species if it has a non-negligible effect on any species in the skeletal mechanism, and that not every species in the skeletal mechanism is of equal importance to the major species and global parameters. Therefore it is possible to further eliminate the species which have only minor effects on the major species or global parameters, even though it might have more significant effect on other species which are not of major interests. The identification of the entire set of such eliminable species is nevertheless not straightforward, considering that the induced error by elimination is not small and the coupling of the species is highly nonlinear. A simple and reliable method to eliminate such species has thus been developed by computing the worst-case induced error by the elimination of each species, one at a time. This approach is similar to sensitivity analysis, except it directly evaluates the effects of species elimination instead of using perturbations of the species concentrations. This reduction process is more CPU-time demanding than DRG due to the evaluation of global sensitivities. However, the procedure appears to be

straightforward, reliable, and executable for mechanisms of moderate sizes obtained by DRG reduction.

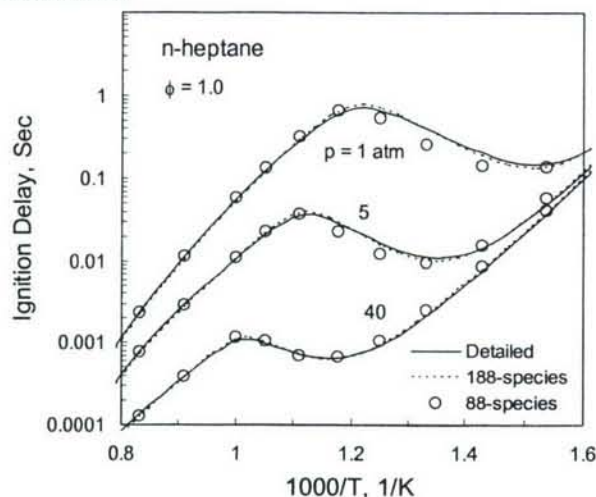


Figure 1

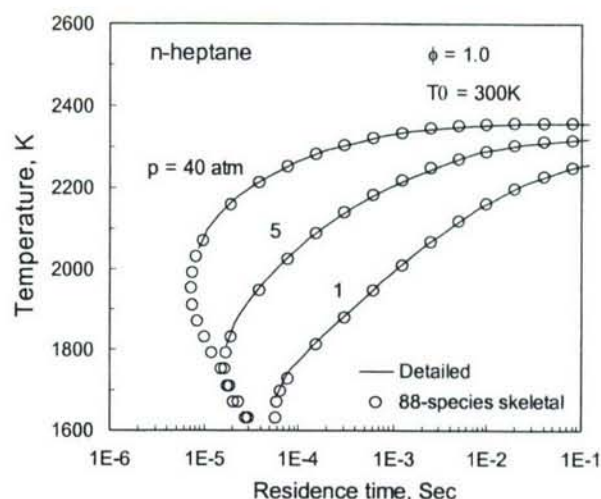


Figure 2

The method of DRGASA developed employs an iterative procedure. In each loop of the iteration, the information obtained from a DRG analysis is exploited to facilitate the subsequent process of sensitivity analysis. Species found to be unimportant by DRG can be directly eliminated, and species found to be highly important by DRG are directly retained. Only the species which are uncertain for DRG need to be tested by sensitivity analysis. As such, the number of species for sensitivity test is significantly reduced. This procedure can be repeated until there is no species further eliminable, and the resulting skeletal mechanism is therefore the minimal.

The method of DRGASA was applied to further reduce the skeletal mechanism of heptane with 188 species and 939 reactions. An 88-species mechanism with 384 reactions was obtained. The skeletal mechanism was validated against the 188-species and detailed mechanism for both ignition processes in auto-ignition and extinction in perfectly stirred reactor (PSR). Figures 1 and 2 show that, while there is significant reduction in mechanism size, only slightly increased error is observed in ignition delays near NTC regime.

2. Analytical Solution of Quasi-Steady State equations with Directed Graph (QSSDG)

A systematic approach was developed to obtain analytical solutions for reduced mechanisms based on QSS assumptions. The method approximates the set of nonlinear algebraic equations for QSS species concentrations with a set of linear equations with good accuracy. This is based on the observation that QSS species are typically low in concentrations, and therefore the reaction rates involving two trace species are likely to be small compared with those of the rate-controlling reactions. The linear

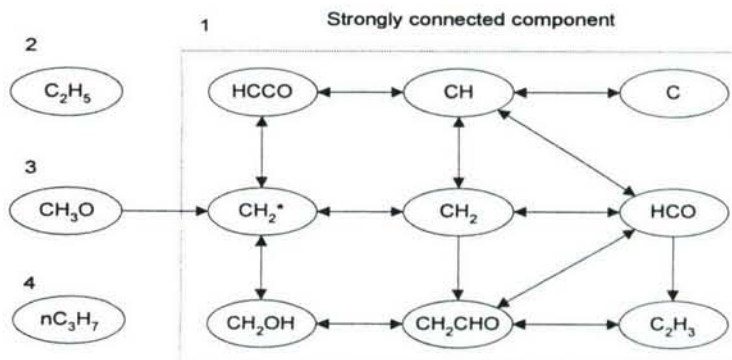


Figure 3

system was then solved with a directed graph abstracted from the dependence of QSS species. A sample QSSDG for the 16-step ethylene mechanism is shown in Fig. 3.

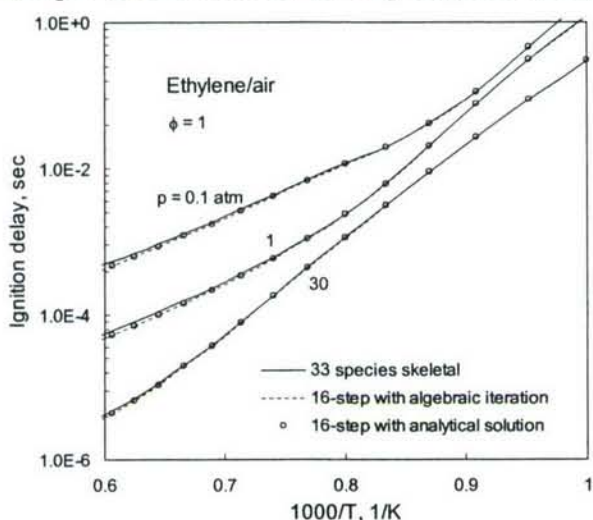


Figure 4

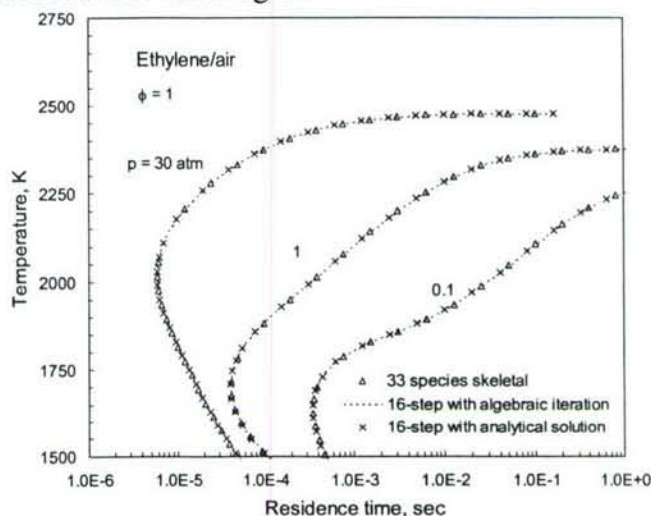


Figure 5

In QSSDG, each node represents a QSS species, and there is a directed edge from QSS species A to B if it directly involves the concentration of B in the QSS expression of A. Strongly connected species form cycles in the graph and result in intrinsically implicit couplings, while couplings between the strongly connected components in QSSDG are acyclic and can be topologically sorted by graph theory. The inner-group couplings were solved efficiently with an algorithm based on eigenvalue analysis of the adjacent matrix of the graph, and the algorithm identifies an optimal or near-optimal sequence for solving the QSS species concentrations within each strongly connected group. The method of QSSDG has been applied to generate a 16-step reduced mechanism for ethylene/air with analytic solution of QSS species concentrations. Good accuracy as well as high efficiency was observed as shown in Figs. 4 and 5 for auto-ignition and PSR respectively, and demonstrates the validity of the linear approximation of the QSS equations.

3. A reduced mechanism for lean premixed methane/air flames

A reduced mechanism for lean methane/air premixed flames was developed from GRI1.2 using the integrated methods of DRG, DRGASA, and QSSDG. The final reduced mechanism contains 9-steps and 4 QSS species, with the QSS relations solved analytically. The 9-step mechanism was applied to a state-of-the-art 3D DNS simulation for a turbulence Bunsen flame through our collaboration with Sandia National Lab. The solver is explicit 6th-order Runge-Kutta. Stiffness of the mechanism was removed such that the time step of integration was comparable to that of transport. The simulated flame surface is shown in Figure 6.



Figure 6

4. Extinction and stability analyses of diffusion flames with radiation heat loss

We performed rigorous theoretical analyses on the dual extinction limit behavior and intrinsic flame oscillations near both the extinction states for diffusion flames with radiation heat loss. We first developed a model with the effects of radiation loss in the form of jump relations and reactant leakages across the reaction zone using multi-scale activation energy asymptotics. This model considers properly the excess enthalpy overlooked by previous analyses and incorporates non-unity Lewis numbers of the reactants. It is then applied to study the extinction and stability characteristics of diffusion flames. Figure 7 shows the dependence of fuel leakage, S_F , on the Damköhler number Da^* for different Γ , where Γ is the relative strength of radiation loss to the chemical heat release and the superscript “*” denotes the Damköhler number evaluated at a reference state. It is seen that the solutions are bounded by the two turning points, with the one at smaller Da^* , marked by “■”, represents the kinetic extinction limit, $Da_{E,K}^*$, and the one at larger Da^* , marked by “▲”, represents the radiative limit, $Da_{E,R}^*$. The neutral stability points, $Da_{C,K}^*$ and $Da_{C,R}^*$, marked by “□” and “Δ”, respectively, indicate that intrinsic flame oscillations develop near both the extinction limits. The flame is unstable within the Damköhler number ranges $Da_{E,K}^* < Da^* < Da_{C,K}^*$ and $Da_{C,R}^* < Da^* < Da_{E,R}^*$. Consequently, steady burning is only possible for $Da_{C,K}^* < Da^* < Da_{C,R}^*$ when flame instability is considered.

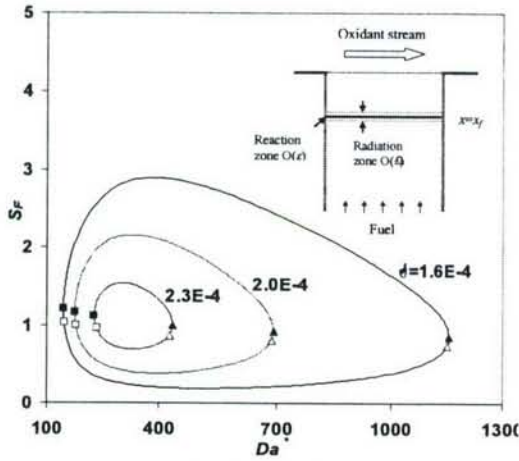


Figure 7

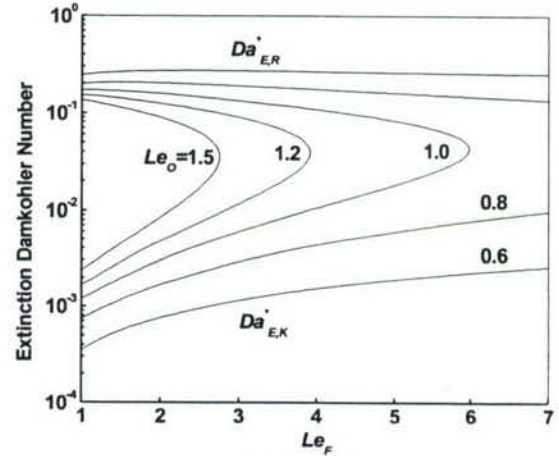


Figure 8

Figure 8 shows variations of the dual extinction Damköhler numbers with the fuel Lewis number, Le_F , for different oxidant Lewis number, Le_O , with fixed Γ . It is seen that the flammable range of Da^* decreases with Le_O and Le_F as it is sufficiently large. When they are both large enough, steady burning is impossible for this value of Γ . With the increase of Le_O , the maximum value of Le_F the system can sustain decreases. Figure 8 indicates that steady burning for the radiative diffusion flames is only possible within a limited range of Lewis numbers. This is because thermal diffusion and radiation are both heat loss mechanisms for flame extinction. Either of them that is large enough is able to induce flame extinction.

Figure 9 shows the normalized unstable range of Damköhler number, $\Omega_R = (Da_{E,R}^* - Da_{C,R}^*) / Da_{E,R}^*$, versus Le_F for different Γ with $Le_O = 1$. It is seen that flame oscillation can indeed develop for Le_F equal to and even well below unity and the unstable range of Le_F is extended with increasing radiation loss. An important result from this analysis is that radiation

loss enhances the heat conduction away from the reaction zone to the fuel and oxidant sides to compensate for the loss, and at the same time suppresses the conduction through the reduction of flame temperature. In general these two opposite effects are not equal and as such radiation loss plays the similar role as varying the thermal diffusivity of the reactants. Therefore, it can be concluded that the imbalance between the thermal and mass diffusions induced by radiation loss under unity Lewis numbers triggers the flame oscillations near the radiation extinction limit. Consequently, the oscillatory instability near the radiation limit can still be considered to be thermal-diffusive in nature.

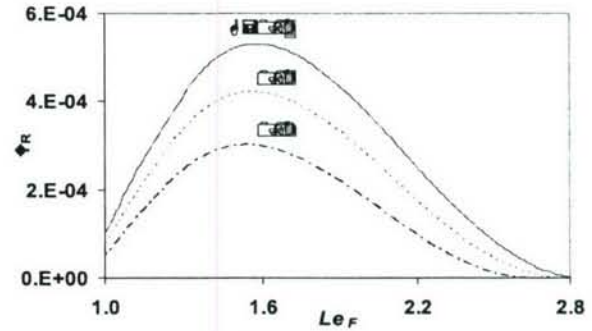


Figure 9

5. Response of premixed flames to velocity fluctuations with flame stretch effects.

To better understand the resonant coupling between unsteady heat release and the natural acoustic modes of combustors, the response of the rate of heat release to velocity fluctuations is studied. Different from previous investigations, the present study considers the variable flame speed due to flame stretch because such a variation is believed to be responsible for some of experimentally observed phenomena. For example, when the Bunsen flame was forced with high frequency, low amplitude disturbances, flame wrinkling was evident only at the flame base and quickly decayed with the axial location farther downstream. Here we only show the results for the effects of flame stretch on the transfer function, defined as the ratio of the normalized fluctuation of heat release rate to that of velocity. In a premixed combustion system, heat release responds to the acoustic modulation through its perturbation to the flame surface area and local burning rate, i.e. flame speed.

Figure 10 shows the spatial distributions of the oscillation amplitude of the flame surface area for different nondimensional flame thickness δ quantifying the extent of flame stretch. The real line corresponds to the case of constant flame speed ($\delta=0$). It is seen that with increasing δ , the flame near the tip region oscillates with increasingly uniform amplitude, implying that flame wrinkling near this region is significantly moderated and the wrinkling is more evident for the flame surface near the burner rim. This explains the experimental observation of more evident flame wrinkling near the flame base. Furthermore, it is seen from the $\delta=0$ case that fluctuation of the flame surface area is a consequence of the superimposition of its string-like oscillation (between nodal points) and bulk oscillatory movement (between the center line and its nearest nodal point). When flame stretch is considered, the nodal points are eliminated so that the flame surface exhibits more bulk movement and less string-like oscillation, which contribute positively and negatively to the fluctuation of flame surface area, respectively.

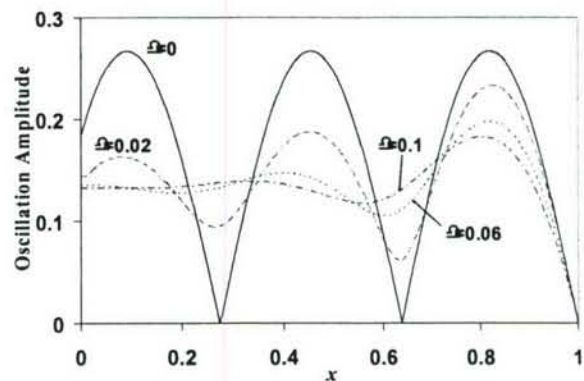


Figure 10

JOURNAL PUBLICATIONS

1. Leylegian, J.C., Sun, H.Y., and Law, C.K., "Laminar flame speeds and kinetic modeling of hydrogen/chlorine combustion," *Combustion and Flame*, Vol. 143, pp. 199-210 (2005).
2. Yuan, J., Ju, Y., and Law, C.K., "Coupled hydrodynamic and diffusional-thermal instabilities in flame propagation at sub-unity Lewis numbers," *Physics of Fluids*, Vol. 17, Art. No. 074106 (2005).
3. Lu, T.F., and Law, C.K., "Linear-time reduction of large kinetic mechanisms with directed relation graph: n-heptane and iso-octane," *Combustion and Flame*, Vol. 144, pp. 24-36, (2005).
4. Yuan, J., Ju, Y., and Law, C. K., "Pulsating and hydrodynamic instabilities at large Lewis numbers," *Combustion and Flame*, Vol. 144, pp. 386-397 (2005).
5. Law, C.K., "Propagation, structure, and limit phenomena of laminar flames at elevated pressures," *Combustion Science and Technology*, Vol. 178, pp. 335-360 (2006).
6. Wang, H.Y., Bechtold, J.K., and Law, C.K., "Nonlinear oscillations in diffusion flames," *Combustion and Flame*, Vol. 145, pp. 376-389 (2006).
7. Law, C.K., Makino, A., and Lu, T.F., "On the off-stoichiometric peaking of adiabatic flame temperature with equivalence ratio", *Combustion and Flame*, in press.
8. Lu T. F. and Law C. K., "On the applicability of directed relation graph to the reduction of reaction mechanisms," *Combustion and Flame*, in press.
9. Zheng X. L., Lu T. F., and Law C. K., "Experimental counterflow ignition temperatures and reaction mechanisms of 1,3-butadiene," *Proceedings of the Combustion Institute*, in press.
10. Sankaran R., Hawkes E. R., Chen J. H., Lu T. F. and Law C. K., "Structure of a spatially-developing turbulent lean methane-air Bunsen flame," *Proceedings of the Combustion Institute*, in press.
11. Wang, H.Y., and Law, C.K., "Oscillation in radiation-affected diffusion flames," *Proceedings of the Combustion Institute*, in press.
12. Egolfopoulos, F.N., Holley, A.T., and Law, C.K., "An assessment of the lean flammability limits of CH₄/air and C₃H₈/air mixtures at engine-like conditions," *Proceedings of the Combustion Institute*, in press.

CHEMICAL MODELING FOR LARGE EDDY SIMULATION OF TURBULENT COMBUSTION

Grant number: FA9550-06-1-0060
Principal Investigator: Heinz Pitsch

Flow Physics and Computation Group
Department of Mechanical Engineering
Stanford University
Stanford, CA 94305-3030

1 STATUS OF EFFORT

This research program consists of two major efforts: (I) the development of improved turbulence/chemistry interaction models for large eddy simulations (LES), and (II) the development of reduced kinetic mechanisms for JP-8 surrogate fuels based on a component library approach.

With regard to part I, a new numerical method for solving the level set equation to understand the effect of numerical errors was developed. This method has interesting implications for turbulent burning velocity models and can be used potentially for error estimation in LES. With regard to part II, an efficient multi-stage approach for the reduction of large kinetic mechanisms was developed and validated.

2 TECHNICAL DISCUSSION

2.1 Combustion Models for LES

In a typical LES of a premixed flame, reaction zones exist on a sub-filter length-scale. Since these zones are not resolved, they can be treated effectively as interfaces. Such an approach is taken in the *G*-equation model, in which a level set is used to describe these interfaces. The *G*-equation model was the subject of prior work performed under AFOSR funding, and was used to simulate real premixed combustion cases successfully [1]. Throughout this work, however, the effects of numerical errors on level set transport were understood poorly. Accurate numerics are important in any type of computational simulation, but they are especially so when level sets are used. The level set equation is valid only on a two-dimensional surface of a three-dimensional space. As a result, a special filtering procedure must be used when deriving a level set formulation of a filtered interface for LES. Moreover, the level set field variable away from the front must be reinitialized to a smooth function periodically, which can alter the location of the front artificially.

Some standard test-cases exist, which can be used to check the accuracy of different numerical level set schemes. These test-cases include advecting Zalesak's disk, evolving a sphere in a deformation field, and releasing a drop of water under the influence of gravity. These tests assess how well a scheme performs some specific task, such as transporting sharp corners or conserving area. The results of these tests, however, cannot be used readily to assess the accuracy in real flow fields where turbulence and front propagation may occur.

To overcome this problem, an adaptive mesh refinement technique was adopted and applied to a turbulent flame.

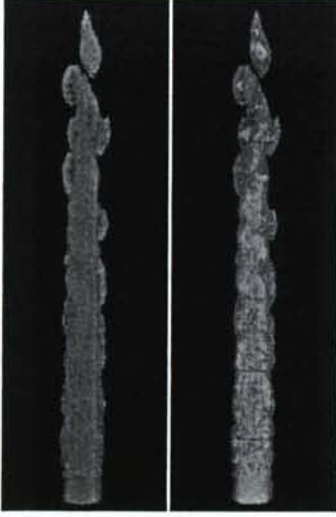


Figure 1: The opaque RLSG mesh is on the left. On the right, the mesh is made transparent, showing the flame front around which it was created.

In this technique, which is called the Refined Level Set Grid (RLSG) approach, a computational mesh is created locally around the level set of interest. This mesh is created in addition to, and with more resolution than the mesh on which the flow is solved. The refined mesh adapts to the level set as it moves, and the level set is transported entirely on the refined mesh. Figure 1 demonstrates how this mesh is created around the flame front during the simulation of the F3 flame, the characteristics of which were described in a previous report.

Because of the refinement, the RLSG approach effectively increases the order of accuracy of the schemes used for transport and reinitialization. Thus, the influence of numerical errors on flame location may be assessed by running with increasingly refined level set meshes. If the numerical errors that occur by solving the level set on the flow solver mesh are significant, then the more accurate, refined solutions should be different, and should also converge to the correct solution as resolution is increased.

To assess the effect of the numerical methods, the turbulent premixed F3 bunsen flame was computed using several different levels of refinement for the solution of the G -equation. For the spatial discretization, a 3rd order WENO scheme was used. The comparison of the results in Figure 2 shows that there are only minor differences between the results of the different simulations. Slight differences occur however, especially in the regions closer to the nozzle. At $x/D = 2.5$, the more refined mesh shows a wider distribution of the water profile, which is in better agreement with the experiments. This trend is to be expected, since the finer resolution should describe the turbulent motions of the front with better accuracy. Although the differences between the simulations are small, the trends also seem to indicate that the solution converges with increased refinement.

For the present example, the differences among the coarse and the fine simulations are much smaller than remaining differences of any of the simulations with experiments, which would indicate that even the coarsest resolution is appropriate. This observation, however, is not a general result. The solution depends on the numerical schemes used for the advection and reinitialization of the level set function. Further, the solution depends on the resolution of the flow solver mesh. In a turbulent combustion case, numerical errors are

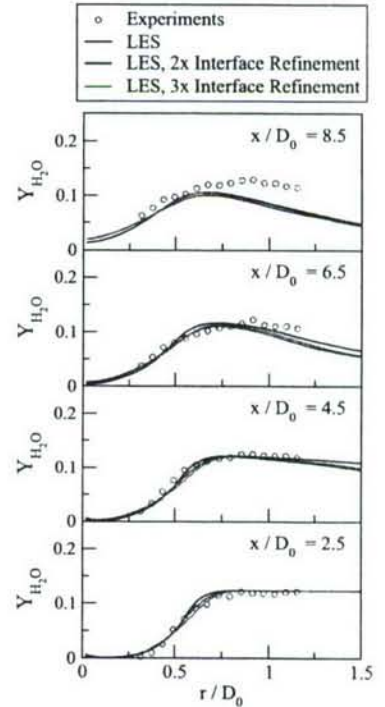


Figure 2: Water mass fraction results as a function of interface mesh refinement

not important if the consumption of flame surface because of the numerical errors is small compared with the production of flame surface on the filter scale, which is caused by the turbulent energy transfer. Using the RLSG method, the level set equation can be solved simultaneously on two different levels of grid refinement. From this, an error can be estimated, which can be compared with the change of flame surface caused by physical phenomena. In the future, the RLSG method will be used to provide error estimates and the effect of numerical errors for test-cases that are more sensitive to the small-scale turbulent motions will be assessed. A good test-case will be a lifted turbulent jet flame.

2.2 Automatic Multi-stage Reduction of Large Chemical Kinetic Mechanisms

A new automatic multi-Stage approach for the reduction of large kinetic mechanisms was developed, that combines advantages of several techniques. The user needs to specify the detailed mechanism, some targets (e.g. ignition delay times, species profiles), an error tolerance and a domain of applicability in terms of temperatures, pressures or equivalence ratios. The first step explicitly removes negligible species and reactions through the Directed Relation Graph method with Error Propagation (DRGEP). The DRGEP method is based on path-dependent coefficients that estimate the error introduced in a target when other species are changed or removed. Although this technique is very efficient in removing minor chemical paths, resulting skeletal mechanisms are still too large for practical purposes.

An important feature of hydrocarbon oxidation is that a large number of isomers of certain species are needed to represent oxidation correctly. A new lumping technique was designed to combine a number of isomers S_i , $i = 1..n$ into one single representative species S defined such that:

$$[S] = \sum_{i=1}^n [S_i].$$

where $[S_i]$ refers to the concentration of species S_i . This lumping reduces the size of the mechanism by $n - 1$ species. Each reaction involving S_i is modified to include only species S and the rate coefficients of the consumption reactions are reduced to account for the increase of the reactant's concentration (S instead of S_i).



becomes

$$S + A \longrightarrow B \quad \omega = \tilde{k} [S] [A] = \alpha_i k [S] [A] \quad \text{with} \quad \alpha_i = \frac{[S_i]}{\sum_{j=1}^n [S_j]}.$$

This transformation is exact if α_i is a known function of time and space. Unfortunately, this function is most often unknown and a closed form has to be assumed. Here, rather than specifying α_i as a function of physical space and time, α_i will be expressed as a function of the state space

$$\alpha_i = \alpha_i \left(T, [S_j]_{j=1..N-n+1} \right),$$

where $[S_j]_{j=1..N-n+1}$ are the concentrations of all species remaining in the system. α_i can then be determined as the conditional average over all conditions used for the reduction validation. This method surely would provide quite accurate results. However, if the dependence on the entire state space is retained, the resulting mechanism cannot easily be used in standard

chemistry packages, such as the Chemkin libraries. For this reason, only the temperature dependence of α_i is considered, which, if expressed in Arrhenius form, can be absorbed into the Arrhenius parameters of the involved reactions. The basis function for representing the temperature

$$\alpha_i(T) = \beta T^\gamma e^{-\frac{\delta}{RT}}.$$

The various coefficients β , γ , and δ are fitted from the detailed solutions. The quality of the fit determines the quality of the lumping. Figure 3 shows an example of a fit obtained for the lumping of the $C_7H_{15}O_4$ isomers.

The last step of the reduction procedure is the introduction of quasi steady-state assumptions. The Level of Importance (LOI) criteria developed by Løvas et al. [2] was found to be an efficient way of automatically selecting species for which steady-state assumptions can be applied. Here, DRGEP coefficients for the targets, $R_{T,i}$, were used as sensitivity coefficients. The LOI index is given by

$$LOI_i = -R_{T,i} c_i \left[\frac{\partial \omega_i}{\partial c_i} \right]^{-1}$$

where c_i is the concentration and ω_i is the production rate of species S_i .

This combined reduction procedure was applied to the LLNL mechanism for *n*-heptane auto-ignition and oxidation. The mechanism was reduced from 558 species to only 58 species and 36 steady-state species, while the error introduced on the targets had a maximum value of 25% around the NTC region and an average value of less than 14%. Ignition delay times for stoichiometric mixtures of *n*-heptane and air are shown in Figure 4 for different pressures. It is obvious that the error introduced by the mechanism reduction is much smaller than the error of the original mechanism compared with experimental data.

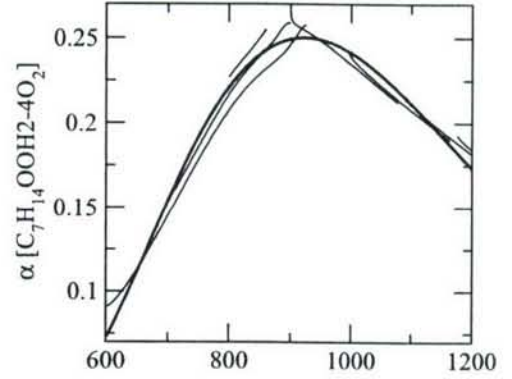


Figure 3: α_i for one $C_7H_{15}O_4$ isomer plotted as function of the temperature. Comparison between exact (thin lines) and fitting (bold line) functions.

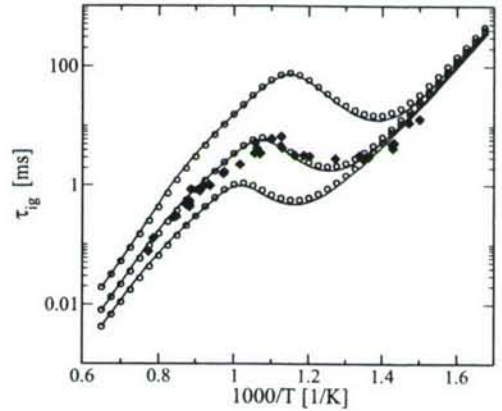


Figure 4: Ignition delay times for a stoichiometric mixture of *n*-heptane and air at $p = 3.2$, 13 and 42 bar. Comparison between experiments (filled symbols), detailed (solid line) and 58 species reduced (symbols) mechanisms.

References

- [1] H. Pitsch and L. Duchamp de Lageneste. Large-eddy simulation of premixed turbulent combustion using a level-set approach. *Proc. Combust. Inst.*, 29:2001–2008, 2002.
- [2] T. Lovas, P. Amneus, F. Mauss, and E. Mastorakos. Comparison of automatic reduction procedures for ignition chemistry. *Proc. Combust. Inst.*, 29:1387–1393, 2002.

DEVELOPMENT OF A COMPREHENSIVE AND PREDICTIVE REACTION MECHANISM OF LIQUID HYDROCARBON FUEL COMBUSTION

(Grant/Contract Number FA9550-05-1-0010)

Principal Investigator:

Hai Wang

Department of Aerospace and Mechanical Engineering
University of Southern California, Los Angeles, CA 90089

SUMMARY/OVERVIEW:

Studies were conducted in several relevant areas, including (1) a gas-kinetic analysis for the transport properties of long chain molecules in dilute gases, (2) quantum-chemistry, master equation modeling of the unimolecular decomposition of *ortho*-benzyne, (3) extension of the previously developed H₂/CO model to combustion pressure as high as 600 atm, and (4) a methodology for kinetic uncertainty propagation currently under development. These projects represent the two key ingredients that are necessary for the success of the overall research program: (a) an accurate physico-chemical property database for combustion kinetics, and (b) a unified and optimized kinetic model for liquid aliphatic and aromatic fuel combustion with quantifiable uncertainties.

TECHNICAL DISCUSSION:

1. Transport Theory of Long Chain Molecules in Dilute Gases

One of the major theoretical hurdles to obtain a quantitative understanding of the combustion chemistry of jet fuels and their surrogates is the lack of a suitable theory to describe the diffusion coefficient of long chain aliphatic molecules. Although the Chapman-Enskog theory is traditionally employed to calculate the binary diffusion coefficient, its underlying assumption of spherical potentials for the collision pair renders the applicability of the theory questionable. In this work, a rigorous, gas-kinetic theory analysis was carried out, and analytical equations are developed for the diffusion coefficient of long-chain molecules in the limits of specular and diffuse scattering.

A long-chain molecule may be approximated as a straight and rigid cylinder. Consider a cylinder with length equal to L and diameter D . Gas-kinetic theory analysis shows that the instantaneous drag force due to relative motion of a cylinder in a dilute gas may be given by

$$F_{s/d} = \frac{1}{2} \sqrt{(1 + 5 \sin^2 \alpha/4)} 2\pi m_r k T N L D V \Omega_{s/d}^{(1,1)*} \quad (1)$$

where the subscript " s/d " denotes specular or diffuse scattering, α is the angle of the cylinder relative to the flow, m_r is the reduced mass, k is the Boltzmann constant, T is the temperature, N is the gas number density, V is the relative velocity. In eq. (1) $\Omega_{s/d}^{(1,1)*}$ is the reduced collision integral given by

$$\Omega_{s/d}^{(1,1)*} = \frac{\int_0^\infty \gamma^5 \exp(-\gamma^2) \mathcal{Q}_{s/d}(\gamma) d\gamma}{LD} \quad (2)$$

where $\mathcal{Q}_{s/d}(\gamma)$ is the collision cross section, defined in the two limiting scattering scenario as

$$\mathcal{Q}_s(\gamma) = L \int_{-\infty}^{\infty} (1 - \cos \chi) db, \quad (3a)$$

and

$$\mathcal{Q}_d(\gamma) = L \left[\int_{-b_0}^{b_0} \left(1 + \frac{1}{\gamma} \sqrt{\frac{\pi k T}{2 m_r}} \sin \frac{\chi}{2} \right) db + \int_{b_0}^{\infty} (1 - \cos \chi) db + \int_{-\infty}^{-b_0} (1 - \cos \chi) db \right], \quad (3b)$$

respectively. In eqs (3), the angle χ is given by

$$\chi(\gamma, b) = \pi - 2b \int_{r_m}^{\infty} \frac{dr}{r^2 \sqrt{1 - \frac{b^2}{r^2} - \frac{\Phi(r, L)}{m_r \gamma^2 / 2}}} \quad (4)$$

where r is the center-to-axial distance between the gas molecule and cylinder, r_m is the distance of the closest encounter, and $\Phi(r, L)$ is the potential function between the gas molecules and cylinder. In the limit of rigid-body collision, it may be shown that

$$\Omega_s^{(1,1)*} = 4/3 \quad (5a)$$

and

$$\Omega_d^{(1,1)*} = 1 + 3\pi^2/64. \quad (5b)$$

Realistically molecular scattering always lies between the two limiting scattering models. Similar to the treatment of nanoparticle transport, a parameter may be introduced here to give a mixed scattering model, such that an average, reduced collision integral may be defined as

$$\Omega_{avg}^{(1,1)*} = \varphi \Omega_s^{(1,1)*} + (1 - \varphi) \Omega_d^{(1,1)*}, \quad (6)$$

where φ is termed as the momentum accommodation function, which ranges from 0 to 1. From the knowledge of gas-nanoparticle scattering, it may be speculated that for long-chain aliphatic molecules φ is close to unity.

The instantaneous binary diffusion coefficient of a cylinder in a dilute gas may be obtained from the Stokes-Einstein relation, through the drag coefficient, as

$$D_{12} = 2 \sqrt{\frac{kT}{(1 + 5 \sin^2 \alpha / 4) 2\pi m_r}} \frac{1}{NLD \Omega_{avg}^{(1,1)*}}. \quad (7)$$

An angle-averaged diffusion coefficient is obtained by replacing α by the mean angle $\bar{\alpha}$ of the orientation of the cylinder with respect to its diffusion direction.

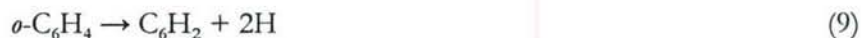
The remaining work will be (a) to examine the potential function $\Phi(r, L)$ and to determine a suitable, parameterized form for this function, and (b) to carry out suitable experiments to determine the diffusion coefficients of representative, long-chain aliphatic molecules. Both components of the study are required to validate the theory developed.

2. Kinetics of unimolecular decomposition of *ortho*-benzynes

The kinetics of *ortho*-benzynes is an integral part of aromatics oxidation at high temperatures. Previously, it was concluded that the dominant channel of *ortho*-benzynes decomposition is through the concerted unimolecular dissociation leading to diacetylene and acetylene,



Recent shock-tube studies at DLR suggest that an additional reaction channel may become active at temperatures > 1600 K. This channel is characterized by the production of the H atom,



The shock tube study used 1,2-diiodobenzene is the precursor for *ortho*-benzynes.

In this study, we examined the potential energy surface of *ortho*-benzynes decomposition by molecular orbital calculations. The computation was carried out at the CCSD(T)/6-31G(d)//B3LYP/6-31G(d) level of theory. The minimum energy barrier for H production was computed to be 106 kcal/mol from *ortho*-benzynes. This energy barrier renders direct H production implausible below 2000 K. Subsequently, the reaction rate coefficient was analyzed by master equation modeling. Kinetic modeling shows that below 2000 K the apparent production of the H atom is due to the decomposition of the precursor compound, rather than the decomposition of *ortho*-benzynes.

3. H_2/CO combustion up to 600 atm

This is a collaborative research project with Professor Brezinsky at UIC. In this study, the high pressure oxidation of dilute CO mixtures doped with 150-200 ppm of H_2 has been studied behind reflected shock waves in the UIC high pressure single pulse shock tube. The experiments were performed over the temperature range from 1000-1500 K and pressures spanning 21-500 bars for stoichiometric ($\Phi=1$) and fuel lean ($\Phi=0.5$) oxidation. Stable species sampled from the shock tube were analyzed by standard GC, GC/MS techniques. The experimental data obtained were simulated using a previously published detailed model for H_2/CO combustion. Simulations showed that within experimental error the kinetic model was able to capture the experimental trends for the lower pressure data sets (average nominal pressures of 24 and 43 bars). However the model under predicts the CO and O_2 decay and subsequent CO_2 formation for the higher pressure data sets (average nominal pressures of 256 and 450 bars). The current elevated pressure data sets span a previously unmapped regime and have served to probe HO_2 radical reactions which appear to be among the most sensitive reactions in the model under these conditions. With updated rate parameters for

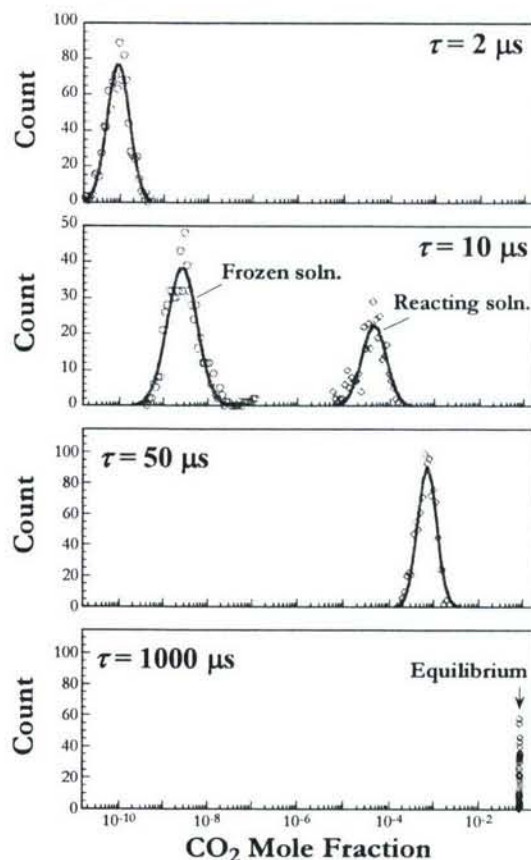
$\text{HO}_2 + \text{OH} = \text{O}_2 + \text{H}_2\text{O}$ the model is able to reconcile the elevated pressure data sets thereby extending the capability of the reaction model to an extreme range of conditions.

This work is reported in ref. [1].

4. Methodology of kinetic uncertainty propagation

We begin to develop a mathematical procedure to propagate kinetic uncertainty into combustor flow simulations. Figure 1 shows the statistical distributions of CO_2 mass fraction of ethylene oxidation in air in a perfectly stirred reactor ($\phi = 1.0$, $T = 1400$ K and $p = 1$ atm) as a function of the residence time τ . These distributions were obtained by Monte Carlo simulations. Although they nicely predict the wide distributions under the conditions where the residence time is limited, and the bifurcation of the distribution near the turning points, Monte Carlo simulations are inherently expensive. Currently, we are looking at a suitable mathematical procedure by which these distribution functions can be computed directly.

Figure 1. Statistical distributions of PSR solutions for the CO_2 mass fraction (C_2H_4 -air mixture, $\phi = 1.0$, $T = 1400$ K and $p = 1$ atm).



AFOSR SPONSORED PUBLICATIONS AND PRESENTATIONS:

1. Sivaramakrishnan, R., Comandini, A., Tranter, R. S., Brezinsky, K., Davis, S. G. and Wang, H. "Combustion of CO/H_2 mixture at elevated pressures," *Proceedings of the Combustion Institute*, in press, 2006.
2. Joshi, A. V. and Wang, H. "Master equation modeling of wide temperature and pressure dependence of $\text{CO} + \text{OH} \rightarrow \text{products}$," *International Journal of Chemical Kinetics*, **38**, pp. 57-73 (2006).
3. Joshi, A. V., You, X., Barckholtz, T., and Wang, H., "Thermal decomposition of ethylene oxide: potential energy surface, master equation analysis and detailed kinetic modeling," *Journal of Physical Chemistry A* **109**, pp. 8016-8027 (2005).
4. Middha, P. and Wang, H. "First-principle calculation for the high-temperature diffusion coefficients of small pairs: the H-Ar case," *Combustion Theory and Modeling* **9**, pp. 353-363 (2005).
5. Sheen, D., Kinslow, R., Holley, A. T., You, X., Wang, H., and Egolfopoulos, F. N. "A detailed study of CO/H_2 oxidation kinetics in synthesis-gas/air premixed flames," 2005 Fall Meeting of the Western States Section of the Combustion Institute, Stanford, CA, October 16-18, 2005, paper 05-F13.
6. Chen, X., You, X., Braun-Unkhoff, B., Naumann, C., Frank, P., Just, T., and Wang, H. "Shock tube pyrolysis of 1,2-diiodobenzene—kinetics of H atom production in high-temperature thermal decomposition of *ortho*-benzyne," poster paper presented at the 6th International Conference of Chemical Kinetics, National Institute of Standards and Technology, Gaithersburg, Maryland, July 25-29, 2005.

A NEW PARADIGM IN MODELING AND SIMULATIONS OF COMPLEX OXIDATION CHEMISTRY USING A STATISTICAL APPROACH

(Grant Number: ARO-W911NF-05-1-0526)

Principal Investigator: Dr. Josette Bellan

Jet Propulsion Laboratory
California Institute of Technology
4800 Oak Grove Drive
MS 125-109
Pasadena, Ca 91109-8099

SUMMARY/OVERVIEW:

The computationally accurate and efficient prediction of turbulent reactive flows remains an important research topic for several reasons, one of which is that the modeling of chemistry is still cumbersome, relatively inaccurate, and cannot portray the complex reactions associated with real fuels. To reduce computational costs and enable the description of concurrent reactions from complex fuels containing a multitude a species, a new concept is here proposed that relies on statistical instead of deterministic concepts for modeling chemical kinetics of oxidation reactions. In this new concept, each species has a time scale associated with it, and the goal is to solve only for the significant scales of the problem and model those scales that are not significant. A set of reaction-species mole fractions is considered a vector and the objective is to map this vector into a much smaller multidimensional vector space of base chemical fragments. The goal is to inquire whether such a base can be found for oxidation reactions, and whether one can derive corresponding reaction-coordinate rates for the base that portray the energetics of the system. In essence, there is a functional mapping representing the transformation from the mole fraction PDF of the species to the mole fraction PDF of the base and the interest is not in calculating this functional but its moments (e.g. statistical means, variances, etc.) needed to adequately describe the fragment vector.

TECHNICAL DISCUSSION

The first step in this new research was to concentrate on finding a potential set of base fragments. The transformation between the vector of the species and the base fragments vector would be represented by a matrix $[w^c]$ having elements representing the decomposition of each species on the base. Then, the rate of change of the base species is related to the rate of change of the reaction coordinates through the transformation $[w^c][\chi]$ where the matrix $[\chi]$ has for elements the stoichiometric coefficients of the initial set of detailed reactions. An example of a detailed kinetic model is the LLNL set of reactions for n-heptane oxidation which involves a total of 160 species and 1540 reactions. The requirement for this reduced set of reactions for the base fragments is that it preserves the heat release, indicating in particular that the heat capacity and heats of combustion must be appropriately modeled. The concept is that although there is a functional mapping representing the transformation from the mole fraction PDF of the species to the mole fraction PDF of the base, if one wants to reduce the complexity of the system, it is not necessary to explicitly know this functional; the goal is to obtain an implicit model based on correlations

resulting from numerical simulations using detailed models, because this implicit model would be much simpler than the explicit one. The following describes a proposed base that is relatively simple, yet potentially accurate.

The guiding idea for the base search is similar to that of group additivity [1]; however, group additivity accounts not only for interactions of a group with its nearest neighbor, but also for interactions with groups not immediately adjacent and for steric effects. The present intention is to only account for the interaction with immediately adjacent groups as the complexity of the correlations in [1] must be decreased if computational efficiency must be improved. Thus, although the idea is very similar to the 'groups' of the group contribution methods of estimating species properties [2], the present focus is on a combination of comprehensiveness, accuracy and relative simplicity in that only first order (compositional) effects are allowed. Examination of alkanes and olefins with a vinyl radical shows that the linearity of thermal properties in carbon (C) number implies that the proper building blocks are 'component radicals' listed in Table 1. Listed in Table 1 are also values of thermodynamic properties and correlations for calculating C_p , listed here as NC_p to indicate that these are components. The fitting of the simple formula (much simpler than in [1]) is tested by computing C_p/R (R is the universal gas constant) and is plotted in Figs. 1a (alkanes) and 1b (alkenes); the agreement with the correlation is remarkable given its simplicity.

However, for species with double bonds not at the end of the chain or for oxidized species, the simplicity of the component radicals as building blocks no longer rigorously, but only approximately, holds. To calculate combustion energies once either breakup of a hydrocarbon into free radicals or oxidation reactions occur, the assumption is made that one can associate a constant partial energy with all component radicals, independent of the species to which they belong. The data [3-5] show that although this assumption is not entirely correct (when subtracting contributions from CH_2 , CH_3 , etc.), the variation across species is not that substantial; an average over species is taken. The error in the overall heat of formation for the entire molecule is rather small; two-digit accuracy is normally reached. In Fig. 1c, C_p/R is plotted for some ethers using the information of Table 1; although there are minor deviations from the data, mostly at low T , the fits are adequate. The lightest species are not subject to meaningful decomposition. Free radicals occur when a species splits in two (e.g., hydrogen abstraction) by a reaction, forming species with unsatisfied valence bonds; component radicals could also exist as free radicals. Properties of light species and free (component) radicals are given in Table 2. The corrections for the heavier free radicals may be estimated using the increments in hydrogen bond strengths as given in [6]. Figure 1d illustrates C_p fits for a few free radicals, and good reproduction of the data is shown. Similar fits (not shown) for the light species of Table 2 were equally successful.

Thus, it appears that the base will be formed of 13 component radicals, 11 free radicals and 5 light species. A total of 29 fragments will compose the base, having excluded the final products of combustion (i.e. CO_2 and H_2O), O_2 and N_2 , for which the mole fraction can be computed from atomic conservation.

1. Benson, S. W., *Thermochemical Kinetics.*, John Wiley & Sons., Inc., 1968
2. Reid, R. C., Prausnitz, J. M. and Poling, B. E., *The Properties of Gases and Liquids*, McGraw-Hill Book Co., 4th edition, 1987, Chapt. 6
3. National Institute of Standards and Technology, Chemistry WebBook website; <http://webbook.nist.gov/chemistry>
4. CRC Handbook of Chemistry and Physics, 85th Ed., D. R. Lide, Ed.-in-chief, CRC Press, Boca Raton, Fl., 2004 (internet edition)

5. Gas Research Institute website, <http://www.me.berkeley.edu/gri-mech/>

6. Lay, T. H., Bozzelli, J. W., Dean, A. M. and Ritter, E. R., *J. Chem. Phys.*, 99, 14514-14527, 1995

Radical	δh^o	δh^c	δh^f	a^h	b^h
CH ₃ (methyl)	-42.0	714	188	3.137	3.433
CH ₂ (methylene)	-20.8	614.3	411	2.784	2.812
CH (methylidyne)	$\cong -7$	$\cong 507$	$\cong 603$	2.068	3.038
C ₂ H ₃ (vinyl)	62.5	1212	237	4.432	4.468
C ₂ H ₂ (CH=CH) ^o	73 \pm 2	1102 \pm 2	not relevant	3.82	3.72
C ₂ (C \equiv C, dicarbon)	230	1017	608	2.919	1.796
HC ₂ (HC \equiv C, ethynyl)	227	1135	339 **	3.937	2.2515
CO (keto)	-133 \pm 2	260.5	23	2.892	1.531
HCO (formyl)	-124 \pm 3	390.3	167	3.37	2.92
HO (hydroxyl)	-166 \pm 6 ***	-45	204	2.084	1.0945
HOO (hydro-peroxy) ^{*\oplus}	-205+116/n	-84+116/n	215-116/n	4.194	1.908
OO (peroxy) [*]	-16-13n	-16-13n	not relevant	3.65	2.135
O (ethers) ^{*#}	-74-13n	-74-13n	323+13n	-1.46	2.44

^o trans: -2, cis: +2; for a molecule with one or more vinyl also present (i.e., polyene), $\delta C_p/R$ is increased by 12%; ** Alternate value (op. cit. NIST) is 250 from older data; *** value $\cong -180$ if combined with CH radical; * 'n' is the number of carbon atoms in attached radicals; ^{\oplus} effective n = 1.16 with ring or branched attached radical; # max value $\Delta n = 2$ for an attached chain, effective n = 3 for a ring with n ≥ 4 . If at least one vinyl also present, then add $\Delta n = +1$. For a ring with n = 2 or 3, a correction $\delta h^o \approx 90$ applies. ($\delta C_p/R$ fit is for ring ethers; for a chain, $\delta C_p/R \cong 2.5$); Note: if the keto (or formyl) radical is attached to oxygen (or hydroxyl), then a correction $\delta h^o \approx -90$ applies.

Table 1. Thermodynamic properties of component radicals. (δh^o , δh^c , δh^f heats of formation, combustion, and component-to-free transition, respectively, in kJ/mol; constants a^h and b^h for partial molar heat capacity in the form $\delta C_p/R = a^h + b^h \ln(T/T_o)$; $T_o = 25^\circ\text{C} = 298.15\text{ K}$)

Molecule/radical	h^o	h^c	a^h	b^h
H ₂	0.0	241.5	3.282	0.400
O ₂	0.0	0.0	3.476	0.5663
N ₂	0.0	0.0	3.388	0.469
C	717	1111	2.50	0.0
H ₂ O	-241.5	0.0	3.688	1.217
CO ₂	-393.5	0.0	4.690	1.390
N	473	473	2.50	0.0
H	218.0	339	2.50	0.0
HO	38	159	3.385	0.3637
HOO	10.5	131	4.150	1.307
O	249.2	249.2	2.536	0.0
CO	-110.5	283	3.426	0.4749
HCO	43.1	558	4.154	1.2875
CH ₄	-74.6	802	3.797	4.305
CH ₃	146	902	4.440	2.249
CH ₂	390	1025	3.973	1.3015

CH	596	1110	3.220	0.7136
C ₂ H ₃	300	1449	5.1	3.5
HC ₂	566	1474	4.434	1.404
C ₂	838*	1625	4.58	0.0
NO	90.3	90.3	3.533	0.4508
NO ₂	33.2	33.2	4.691	1.151
H ₂ O ₂	-136	106	5.269	1.880
C ₂ H ₂	228	1257	5.368	2.294
C ₂ H ₄	52.5	1323	5.383	4.676

*Alternate value of 832 from CRC tables

Table 2. Thermodynamic properties of molecules and free radicals. (h^o , h^c heats of formation and combustion, respectively, in kJ/mol; constants a^h and b^h for molar heat capacity in the form $C_p/R = a^h + b^h \ln(T/T_0)$.)

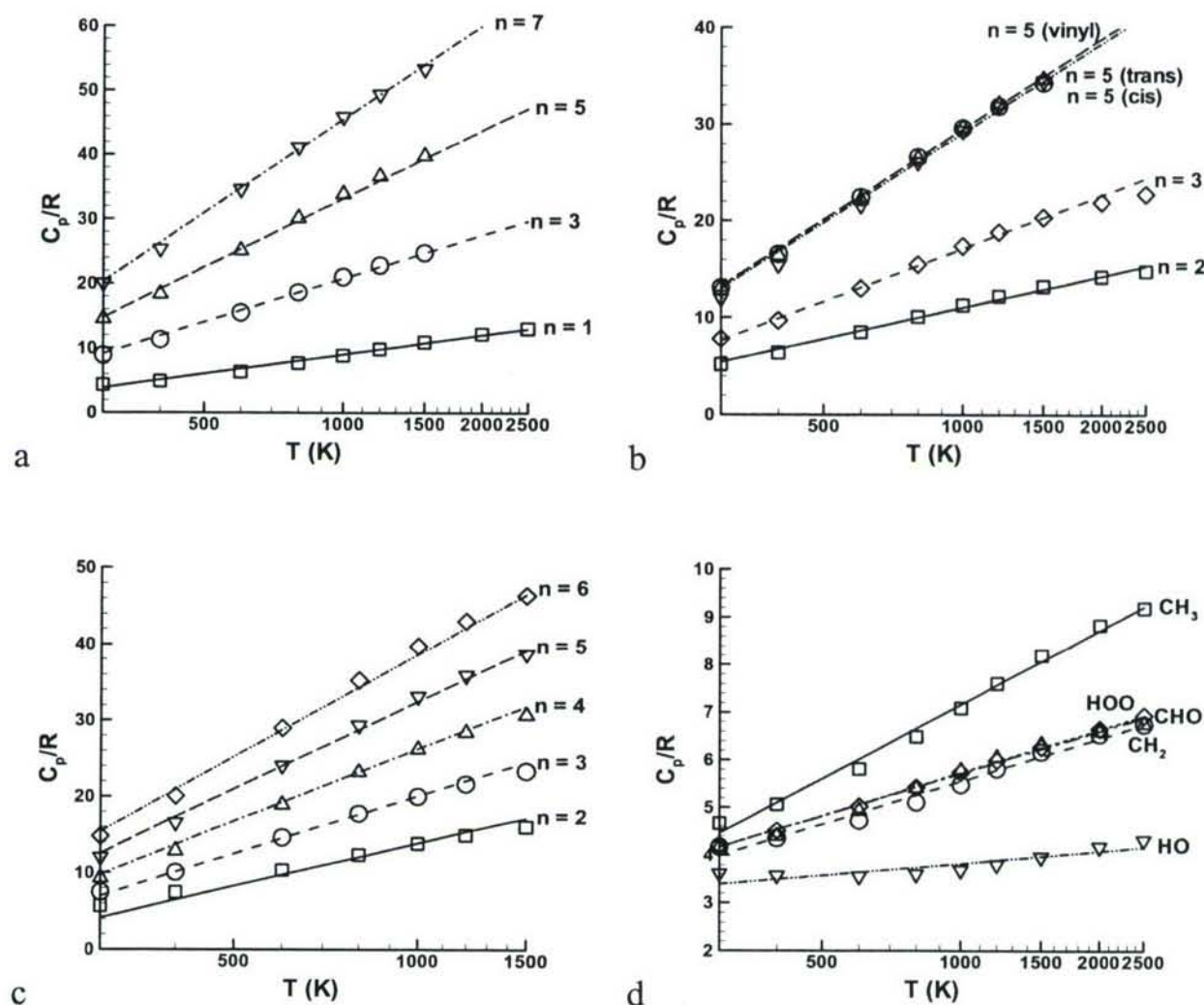


Figure 1. Plot of C_p/R vs $\log(T)$ where T is in degrees K. Data values are as symbols; lines portray the fit constants. a. alkanes, constants from Table 1; b. alkenes, constants from Table 1; c. ring ethers $(CH_2)_nO$, constants from Table 1; d. some free radicals, constants from Table 2.

EXPERIMENTAL AND DETAILED NUMERICAL STUDIES OF FUNDAMENTAL FLAME PROPERTIES OF GASEOUS AND LIQUID FUELS

(AFOSR Grant No. FA9550-04-1-0006)

Principal Investigator: Fokion N. Egolfopoulos

Department of Aerospace & Mechanical Engineering
University of Southern California
Los Angeles, California 90089-1453

SUMMARY/OVERVIEW

The main goal of this research is to provide archival experimental data and provide insight into the physical and chemical mechanisms that control various flame phenomena for a wide range of conditions. Fuel type, equivalence ratio, flame temperature, and combustion mode are the parameters considered. The experimental data are important for a number of reasons. First, they constitute a basis for *partially* validating the combustion chemistry of a large number of fuels ranging from hydrogen to gaseous and liquid hydrocarbons and alcohols. Second, they can be used in order to assess the effect of uncertainties of diffusion coefficients on the prediction of global flame properties. Finally, such data are essential for assessing the reliability of proposed surrogates of realistic fuels, which are of relevance to air-breathing propulsion. The results and findings of this program are of immediate interest to the design and performance of advanced air-breathing propulsion devices. During the reporting period, progress was made in the following: (1) Studies of flame and ignition kinetics of dry synthesis gas mixtures; (2) Assessment of diffusion and kinetics effects on flame ignition; (3) Determination of lean flammability limits of methane/air and propane/air mixtures under engine-like conditions; (4) Determination of ignition and extinction limits of premixed and non-premixed flames for a wide range of jet and gasoline fuels and their surrogates.

TECHNICAL DISCUSSION

The studies include both experiments and detailed numerical simulations. The experiments are conducted in the opposed jet configuration that allows for the systematic determination of the fluid mechanics effects on flames and can be also modeled directly along its stagnation streamline. The experiments are performed in a variable pressure chamber. The reported measurements, were performed at $p = 1 \text{ atm}$ through the use of a Digital Particle Image Velocimetry (DPIV) technique [1] and thermocouples with appropriate corrections to account for radiative losses. The numerical simulations include the use of CHEMKIN-based codes. Several chemical kinetics schemes have been tested.

1. Studies of flame and ignition kinetics of dry synthesis gas mixtures with air

This is a collaborative effort with Professors Hai Wang of USC and Eric L. Petersen of University of Central Florida, and more details can be found in Ref. 2. The reaction kinetics of

H₂ and CO mixtures were examined experimentally and computationally under mixture and reaction conditions of immediate interest to synthesis gas combustion. Shock-tube ignition delay times were obtained for five CO-H₂-air mixtures (equivalence ratio $\phi = 0.5$) over the pressure range of 1 to 20 atm and temperatures from 950 to 1330 K. The influence of synthesis gas composition variations on flame ignition and propagation was also examined. Two types of experiments were carried out for H₂/CO/CO₂ mixtures with air. Laminar flame speeds were determined in the twin-flame counterflow configuration using Digital Particle Image Velocimetry [1]. Ignition temperatures were determined by counterflowing a vitiated air jet against a premixed fuel/air jet [3]. Computationally, detailed modeling of the experiments were performed, using a recently developed H₂/CO reaction model [4]. Numerical simulations showed generally good agreement with the experimental data.

2. Assessment of diffusion and kinetics effects on flame ignition

The relative importance of molecular transport and chemical kinetics on flame ignition was investigated through detailed numerical simulations, and more details can be found in Ref. 5. The study was conducted in stagnation-type flows for atmospheric, laminar premixed and non-premixed *iso*-C₈H₁₈, *n*-C₇H₁₆, and H₂ flames.

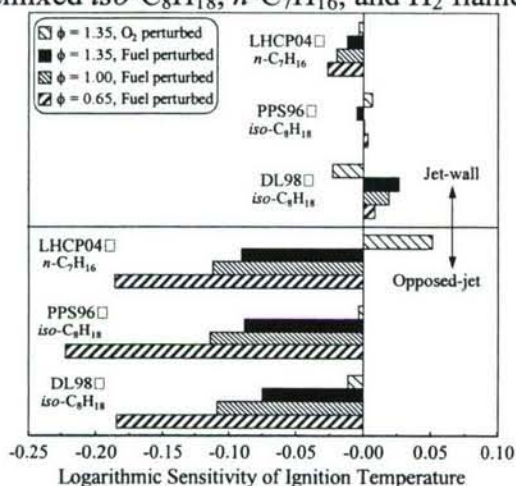


Fig. 1. Logarithmic sensitivity coefficients of ignition temperature of *iso*-C₈H₁₈/air and *n*-C₇H₁₆/air flames on diffusion.

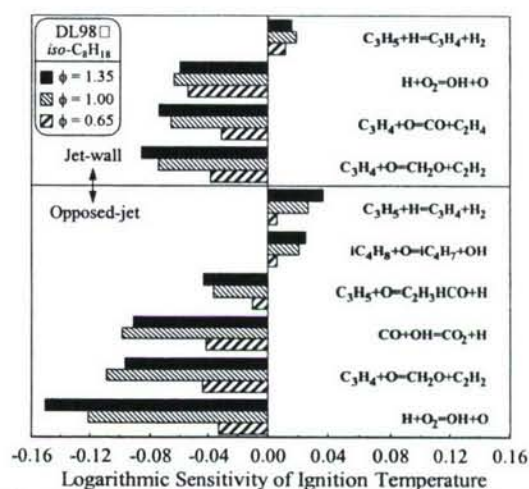


Fig. 2. Logarithmic sensitivity coefficients of ignition temperature of *iso*-C₈H₁₈/air on kinetics

Ignition of premixed flames was studied by: (1) increasing the temperature of a N₂ jet counterflowing against a fuel/air jet, (2) increasing the temperature of a solid wall against which a fuel/air jet was injected. Ignition of non-premixed flames was studied by increasing the temperature of an air jet counterflowing against a fuel-containing jet. The simulations were performed along the stagnation streamline, and included detailed descriptions of chemical kinetics, molecular transport, and radiative heat transfer. Sensitivity analyses of the ignition temperatures to the diffusion coefficients of the reactants as well as to the kinetics were performed. Results revealed that premixed flame ignition is rather sensitive to the fuel diffusivity in the opposed-jet configuration, and notably less in the jet-wall. This is due to the diffusive transport that is required to convey the reactants towards the ignition kernel in the opposed-jet. It was found that the two approaches result in similar ignition temperatures only for fuel-rich cases and that the ignition temperatures tend to be lower as the equivalence ratio increases in the opposed-jet configuration. However, the ignition temperatures were found to

depend mildly on the equivalence ratio in the jet-wall configuration. The sensitivity of ignition to diffusion in non-premixed systems was found to also be notable, especially for cases in which the fuel is highly diluted by an inert. For both premixed and non-premixed flames, the sensitivity of ignition to diffusion coefficients was found to be of the same order or larger than that to kinetics, and representative results are shown in Figs. 1 and 2. This is important when flame ignition data are used to validate kinetics, as rate constants could be potentially falsified. This has been also shown to be the case for the extinction of H_2 [6] and liquid fuel flames [7] by demonstrating that the sensitivity of the extinction limits on diffusion can be of the same or even greater order compared to that of kinetics.

3. Determination of lean flammability limits of methane/air and propane/air mixtures under engine-like conditions

This is a collaborative effort with Professor Chung K. Law of Princeton University, and more details can be found in Ref. 8. In this study, the lean flammability limits of CH_4 /air and C_3H_8 /air mixtures were numerically determined for a wide range of pressures and unburned mixture temperatures in order to assess the near-limit flame behavior under conditions of relevance to internal combustion engines. The study included the simulation of freely propagating flames with the inclusion of detailed descriptions of chemical kinetics and molecular transport, radiative loss, and a one-point continuation method to solve around singular points as the flammability limit is approached. Results revealed that both pressure and unburned mixture temperature have significant effects on the lean flammability limit as well as the attendant limit flame temperature. Specifically, the lean limit was found to first increase and then decrease with pressure, while the limit temperature decreases with pressure in general, and can be reduced to values as low as 900 K under engine-like conditions. Through sensitivity and species consumption path analyses it was further shown that the chain mechanisms that control the near-limit flame response critically depend on the thermodynamic state of the mixture. Thus, mechanisms that are identified as important at near-atmospheric conditions may not be relevant at higher pressures and unburned mixture temperatures. In particular, the response of near-limit flames was found to resemble the homogeneous explosion limits of hydrogen/oxygen mixtures in that while at low pressures the main branching and termination reactions are respectively $H + O_2 \rightarrow OH + O$ and $H + O_2 + M \rightarrow HO_2 + M$, at the elevated pressures relevant to internal combustion engines the system branching is controlled by the HO_2 - H_2O_2 kinetics. Potential avenues for extending the lean operation limits of internal combustion engines were suggested based on the understanding gained from this analysis.

4. Determination of ignition and extinction limits of premixed and non-premixed flames for jet and gasoline fuels and their surrogates.

The jet fuels study is a collaborative effort with Dr. Tim Edwards of AFRL, and more details can be found in Ref. 9. Extinction strain rates and ignition temperatures of a wide range of jet fuels were experimentally determined in the counterflow configuration under non-premixed conditions. Similar measurements were also made for single-component hydrocarbon fuels and surrogate fuels, and were compared with those obtained for the jet fuels. The experiments were conducted at atmospheric pressure and elevated temperatures. Comparing single-component hydrocarbon fuels, it was found that those with lower carbon number exhibit greater resistance to extinction and greater ignition propensity. The results for the jet fuels revealed that there is a large variation in both extinction and ignition limits. Jet fuels with similar extinction behavior were found to display a rather different ignition response. Two recently proposed JP-8 surrogates

were also tested, and both the ignition and extinction states of a reference JP-8 fuel were not predicted satisfactorily. Both surrogates were found to exhibit a more robust combustion behavior compared to JP-8, as manifested by their increased ignition propensity and their increased resistance to extinction.

Ignition and extinction limits of samples of gasoline, mixtures of gasoline, proposed gasoline surrogates, and selected single-component liquid hydrocarbons with air, were experimentally determined in the counterflow configuration, and more details can be found in Ref. 10. The experiments were conducted at atmospheric pressure and elevated temperatures. Results revealed that different samples of gasoline exhibit notably different ignition and extinction characteristics while averaged mixtures of gasoline behave rather similarly. Comparing the single-component hydrocarbons, the lower molecular weight paraffins were found to have greater ignition propensity and reduced extinction resistance compared to the larger molecular weight ones. Comparing *n*-C₈H₁₈ and *iso*-C₈H₁₈, it was found that while *n*-C₈H₁₈ flames ignite more readily, as expected, they also exhibit greater resistance to extinction compared to *iso*-C₈H₁₈ flames.

REFERENCES

1. Y. Dong, C.M. Vagelopoulos, G.R. Spedding & F.N. Egolfopoulos, *Proc. Combust. Inst.* **29**, (2002) 1419-1426.
2. Y. Dong, X. You, D.A. Sheen, H. Wang, R. Kinslow, M. Call, A.T. Holley, M.G. Andac, F.N. Egolfopoulos, D.M. Kalitan & E.L. Petersen "Flame and Ignition Kinetics of Dry Synthesis Gas-Like Mixtures," in preparation.
3. J.A. Langille, Y. Dong, M.G. Andac, F.N. Egolfopoulos & T.T. Tsotsis, T.T., *Comb. Sci. Tech.*, **178** (4) (2006) 635-653.
4. S.G. Davis, A.V. Joshi, H. Wang & F.N. Egolfopoulos, *Proc. Combust. Inst.* **30**: 1283-1292 (2005).
5. M.G. Andac & F.N. Egolfopoulos "Diffusion and Kinetics Effects on the Ignition of Premixed and Non-Premixed Flames," accepted for presentation at the 31st International Symposium on Combustion, University at Heidelberg, Heidelberg, Germany, August 6-11, 2006.
6. Y. Dong, A.T. Holley, M.G. Andac, F.N. Egolfopoulos, S.G. Davis, P. Middha & H. Wang, *Combust. Flame*, **142** (2005) 374-387.
7. A.T. Holley, Y. Dong, M.G. Andac & F.N. Egolfopoulos, *Combust. Flame*, **144** (2006) 448-460.
8. F.N. Egolfopoulos, A.T. Holley & C.K. Law "An Assessment of the Lean Flammability Limits of CH₄/Air and C₃H₈/Air Mixtures at Engine-Like Conditions," accepted for presentation at the 31st International Symposium on Combustion, University at Heidelberg, Heidelberg, Germany, August 6-11, 2006.
9. A.T. Holley, Y. Dong, M.G. Andac, F.N. Egolfopoulos & T. Edwards "Ignition and Extinction of Non-Premixed Flames of Single-Component Liquid Hydrocarbons, Jet Fuels, and their Surrogates," accepted for presentation at the 31st International Symposium on Combustion, University at Heidelberg, Heidelberg, Germany, August 6-11, 2006.
10. A.T. Holley, Y. Dong, M.G. Andac & F.N. Egolfopoulos "Ignition and Extinction Studies of Mixtures of Air with Single-Component Liquid Hydrocarbons, Gasoline, and Gasoline Surrogates," paper No. 05F-074 Fall Technical Meeting, *Western States Section/Combustion Institute*, Stanford University, California, California, October 17-18, 2005.

LOW TEMPERATURE OXIDATION CHEMISTRY OF JP-8

Contract No. DAAD19-03-1-0070; 44458-EG

Nicholas P. Cernansky and David L. Miller
Department of Mechanical Engineering and Mechanics
Drexel University, Philadelphia, PA 19104

In an effort to develop surrogate fuels for engine modeling and development, this project is examining the low and intermediate temperature oxidation chemistry of JP-8, potential JP-8 surrogates, and their components at elevated pressure. Experiments are being run in a pressurized flow reactor (PFR) and/or a single cylinder research engine. A fundamental understanding of the preignition chemistry of high molecular weight hydrocarbons, similar to, if not including, components of real fuels, is necessary to advance the development of fuel surrogates. This project is providing information necessary to determine the chemical reaction mechanisms of such hydrocarbons. In prior work, we developed a four-component JP-8 surrogate and a four-component gasoline surrogate, and we characterized their reactivity in the low and intermediate temperature regimes (600 – 800 K) using our PFR facility to oxidize the fuels and our gas chromatography/mass spectrometer facility to measure the intermediate species. This year, we examined the behavior of jet fuels and the JP-8 surrogate in our single cylinder engine facility, and we used our PFR to explore the autoignition of Fischer-Tropsch JP-8 and a potential Fischer-Tropsch JP-8 surrogate.

For the engine experiments, the test facility consists of a 611 cm³, single cylinder, Waukesha Motor Corporation Model 48D, Cooperative Fuels Research engine directly coupled to a GE CD258AT DC motor dynamometer. The engine has an 8.255 cm cylinder bore and an 11 cm piston stroke. The compression ratio was fixed at 16:1, the inlet manifold pressure was set at 1.0 bar, and the engine was operated at a speed of 800 rpm. Experiments were run at an inlet temperature of 476 K, which is above the boiling point of the fuels tested, thereby eliminating concerns about fuel condensation. Each test fuel was injected into the air stream of the heated inlet manifold well upstream of the intake valve to assure complete vaporization and mixing. The autoignition behavior of these fuels was monitored by measuring the in-cylinder pressure with a water cooled, piezoelectric pressure transducer coupled to a charge amplifier.

Three JP-8 samples and three Jet A samples, acquired from Wright-Patterson Air Force Base and described in Table 1, were stressed to the point of autoignition in the engine at equivalence ratios of 0.28, 0.35, 0.42, and 0.49. The low and intermediate temperature reactivity of the samples had been measured in the PFR facility, and these engine experiments were run to provide additional information relevant for modeling. Figs. 1 and 2 show the pressure traces of the JP-8 and Jet A samples, respectively, as functions of the crank angle degree (CAD).

Table 1: Engine test matrix of jet fuel samples

Fuel	% Alkanes	% Aromatics	% Alkenes	Cetane Index
*JP-8 #3684	80.6	18.1	1.3	44.8
JP-8 #3804	79.8	9.7	0.5	47.0
JP-8 #3773	83.4	15.9	0.7	46.0
*Jet A #3593	79.1	19.0	1.9	44.4
Jet A #3602	75.1	24.0	0.9	40.7
Jet A #3638	86.6	12.0	1.4	45.9

*Specific samples that matched the “average” composition and properties of JP-8 and Jet A

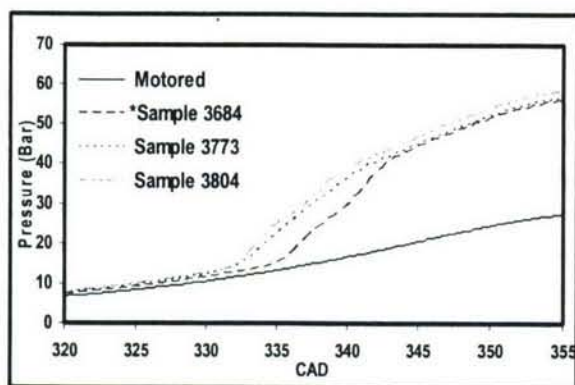


Figure 1: Autoignition of JP-8 samples at $\phi = 0.49$, CR = 16, and $T_{in} = 476$ K

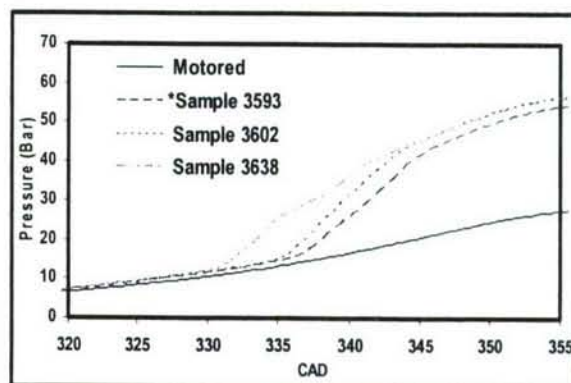


Figure 2: Autoignition of Jet A samples at $\phi = 0.49$, CR = 16, and $T_{in} = 476$ K

The differences in autoignition behavior are due to differences in the preignition chemistry, as defined by fuel properties, such as aromatic content, cycloalkane content, and cetane index (CI). The results showed that increasing aromatic content delayed ignition timing. For the JP-8 samples, increasing cetane index shortened ignition timing. However, the Jet A samples, 3593 and 3602, with significantly different CI values (44.4 and 40.7) had essentially the same ignition time, although they had similar aromatic content. This confirms our prior conclusion that the ASTM formula (D 976) used for calculating these CI indices may not be valid for all jet fuels. Furthermore, comparison of results from the four equivalence ratios showed that increasing equivalence ratio to closer to 1 advanced the ignition timing, as expected.

n-Dodecane, iso-cetane, methylcyclohexane, and 1-methylnaphthalene (the JP-8 surrogate components) were run in the engine as representative components for linear alkanes, branched alkanes, cycloalkanes, and aromatics, respectively. Methylcyclohexane and 1-methylnaphthalene showed no reactivity as neat fuels so they were run with n-dodecane as a reaction initiator. For comparison a mixture of n-dodecane and iso-cetane was also run. Figs. 3 and 4 show the measured pressure traces. Mixes 1, 2, and 3 had CI values of 41.0, 42.2, and 40.8, respectively. Fig. 4 shows that the difference in ignition time for Mixes 1 and 2, with a CI difference of 1.2, is very small. However, Mix 3, with almost the same CI as Mix 1, showed a significantly different ignition time. This demonstrates that the autoignition behavior of mixtures cannot simply be predicted by CI values.

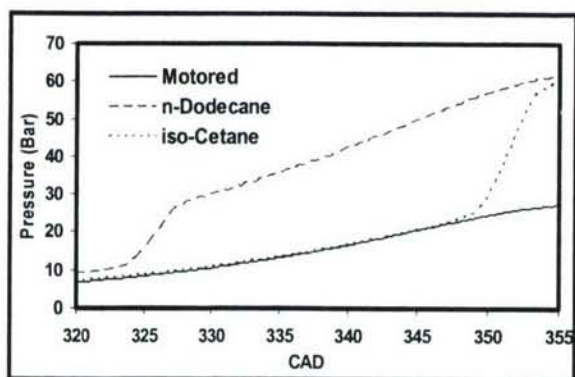


Figure 3: Autoignition of neat n-dodecane and neat iso-cetane at $\phi = 0.49$, CR = 16, and $T_{in} = 476$ K

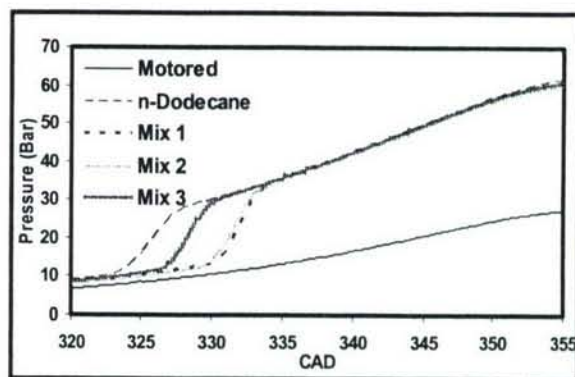


Figure 4: Autoignition of binary mixtures at $\phi = 0.49$, CR = 16, and $T_{in} = 476$ K

Mix 1: 40 % n-dodecane, 60 % iso-cetane

Mix 2: 37 % n-dodecane, 63 % methylcyclohexane

Mix 3: 51 % n-dodecane, 49 % 1-methylnaphthalene

In our PFR experiments, a mixture of 43% n-dodecane, 27% iso-cetane, 15% methylcyclohexane, and 15% 1-methylnaphthalene was shown to match the low and intermediate temperature reactivity of the average JP-8 sample, #3684. For further exploration of this mixture as a JP-8 surrogate, it was run in the engine test facility at equivalence ratios of 0.20, 0.32, and 0.35. Figs. 5 and 6 show the pressure traces for the $\phi = 0.20$ and 0.32 experiments, respectively; the $\phi = 0.35$ data have slightly shorter ignition times than the $\phi = 0.32$ data. The results with this mixture matched the average behavior of JP-8 and Jet A to within ~ 1.5 CAD, suggesting that a surrogate fuel developed in a pressurized flow reactor mimics the corresponding autoignition behavior in an engine.

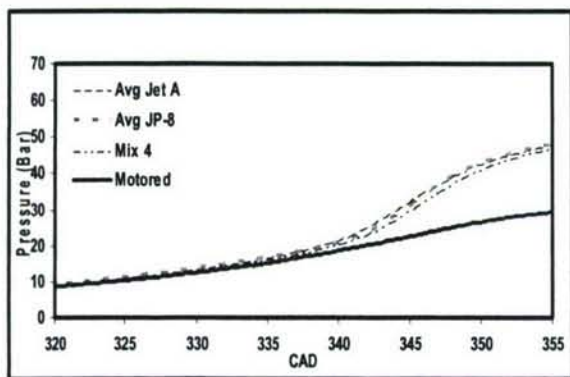


Figure 5: Comparison of the average JP-8 and Jet A samples and the surrogate mixture (Mix 4) at $\phi = 0.20$, CR = 16, and $T_{in} = 476$ K

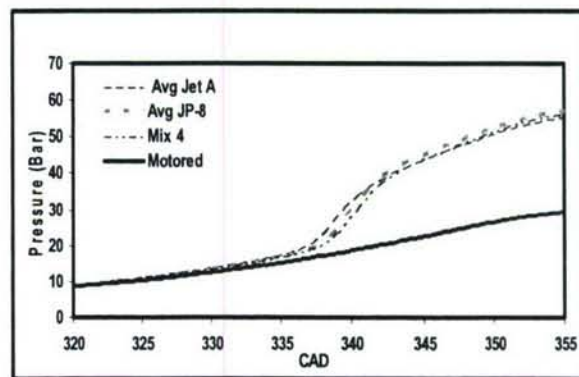


Figure 6: Comparison of the average JP-8 and Jet A samples and the surrogate mixture (Mix 4) at $\phi = 0.32$, CR = 16, and $T_{in} = 476$ K

In our PFR facility, the oxidation of Fischer-Tropsch JP-8 (100% alkanes) and its potential surrogate was explored. The PFR was designed to study the effects of temperature and pressure on the oxidation of hydrocarbon species at temperatures of 600 – 1000 K and pressures of 2 – 20 atm with relative isolation from fluid mechanics and temperature gradients. Synthetic air is formed by mixing nitrogen and oxygen. The liquid fuel is injected into a separate stream of nitrogen for vaporization. This vaporized fuel and the synthetic air are injected into the reactor in an opposed jet nozzle. The mixture then flows into a quartz reaction tube. A gas sampling probe is moved inside the reactor tube to collect oxidized samples from the reaction zone at selected reaction times or positions. For these experiments, the PFR was preheated to 800 K and once the reaction stabilized, the PFR was cooled at a rate of 2-5 K/min. During this cool down, CO and CO₂ were continuously monitored. All of the experiments were run at 8 atm pressure, 0.30 equivalence ratio, 120 ms residence time, and 80.0% N₂ dilution in the fuel.

Figs. 7 and 8 show the CO and CO₂, respectively, produced by the petroleum-derived JP-8 (#3684) and Fischer-Tropsch JP-8 (#4734) samples. In the low and intermediate temperature regimes of hydrocarbon oxidation, the negative temperature coefficient (NTC) region is considered to start when the reactivity of the fuel, as represented by CO production, decreases with increasing temperature. Competition between different reaction paths causes this phenomenon. In these experiments, the NTC region for petroleum-derived JP-8 started at 692 K, where it produced 600 ppm CO. The NTC region for Fischer-Tropsch JP-8 started at approximately the same temperature, 690 K, yet it produced much more CO, 890 ppm.

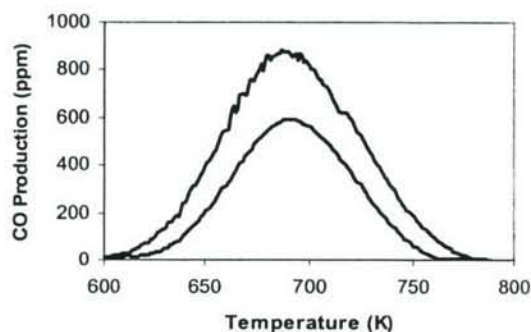


Fig. 7: CO production of Fischer-Tropsch (upper) and petroleum-derived (lower) JP-8's in the PFR

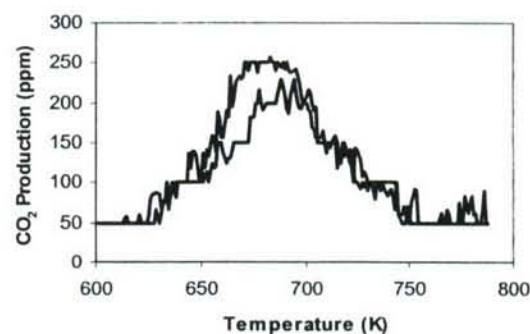


Fig. 8: CO₂ production of Fischer-Tropsch (upper) and petroleum-derived (lower) JP-8's in the PFR

While petroleum-derived JP-8 consists of approximately 60% alkanes, 20% cycloalkanes, and 20% aromatics, Fischer-Tropsch JP-8 consists of 100% alkanes. The petroleum-derived JP-8 formed significantly less CO because the 40% cycloalkanes and aromatics produce a much lower CI and also because the aromatics act as radical scavengers. This implies that different surrogates may be necessary for petroleum-derived and Fischer-Tropsch JP-8's. Thus, while Mix 4, as defined above, may be appropriate for petroleum-derived JP-8, the development of a surrogate for Fischer-Tropsch JP-8 is necessary.

As a first step, the autoignition reactivity of linear and branched alkanes, n-decane and iso-octane, respectively, were investigated as surrogate components. Figs. 9 and 10 show the CO and CO₂ production of neat n-decane and a mixture of 59.4% n-decane/40.6% iso-octane, respectively. n-Decane produced a maximum CO concentration of 1790 ppm at 707 K, while the mixture produced a maximum CO concentration of 990 ppm at 694 K. The mixture produced 100 ppm more CO than the Fischer-Tropsch JP-8, and thus a slight adjustment of the mixture composition should properly match the low temperature reactivity.

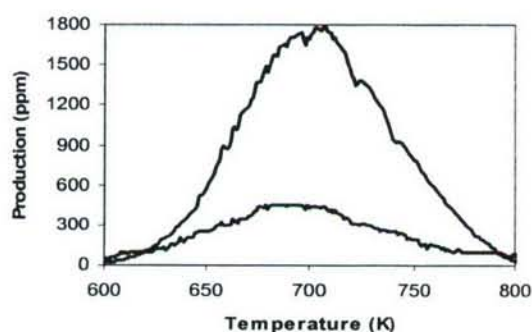


Fig. 9: CO (upper) and CO₂ (lower) production of n-decane in the PFR

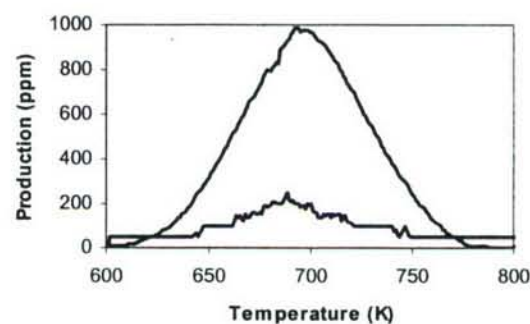


Fig. 10: CO (upper) and CO₂ (lower) production of 59.4% n-decane/40.6% iso-octane mixture in the PFR

In summary, recent studies have focused on examining jet fuels and a JP-8 surrogate in an engine and on exploring a Fischer-Tropsch JP-8 surrogate in a flow reactor. Future work will focus on identifying and quantifying intermediate species in both sets of experiments, as was previously done with the JP-8 surrogate in the flow reactor.

SHOCK TUBE MEASUREMENTS FOR LIQUID FUELS COMBUSTION

ARO Contract Number DAAD19-01-1-0597

Principal Investigator: Ronald K. Hanson

Mechanical Engineering Department
Stanford University, Stanford CA 94305-3032

SUMMARY/OVERVIEW:

We report results of basic research aimed at improving knowledge of the combustion behavior of diesel and jet-related fuels. The work is intended to develop a reference database of gas-phase chemical kinetics and two-phase spray measurements applicable to engine modeling. Research is being conducted in three Stanford shock tube facilities and focuses on two topics: (1) shock-induced ignition time and species time-history measurements and comparisons with current detailed kinetic models of jet fuels and cyclo-alkanes at both high and low pressures; (2) fundamental studies of fuel spray evaporation rates and ignition times of low-vapor pressure fuels such as JP-8, diesel fuel and normal alkane surrogates in a new aerosol shock tube using state-of-the-art optical diagnostic and imaging techniques.

TECHNICAL DISCUSSION:

Validation of reaction mechanisms and development of new and improved reduced mechanisms describing the pyrolysis, oxidation and ignition of practical fuels require a reliable database of experimental combustion targets. Only a limited amount of shock tube ignition time data presently exist for the heavier practical fuels and fuel components, and these data exhibit substantial scatter and are of varying reliability. Stable species data from flames or bench-top reactors exist and have been used to partially validate reaction mechanisms, but little or no data is available on small transient radical species, such as OH, HCO, CH₃, and benzyl, that play important roles in ignition processes. To help remedy these deficiencies, we are currently building a new database of ignition time and species concentration time-history measurements derived from shock tube studies. This database will cover: fuel components such as n-alkanes, branched alkanes, cyclo-alkanes, alkenes and aromatics; surrogate mixtures; and practical fuels including gasoline, kerosene and diesel. Current work is described below.

Methylcyclohexane: Though we have measured ignition times in aromatic species, e.g. toluene, little data exists for cyclo-alkanes. Recently, we have measured ignition delay times of methylcyclohexane (MCH) over a range of conditions: 1.3 to 2.9 atm, 1225 to 1560 K, X_{MCH} from 0.25% to 1%, and equivalence ratios from 0.5 to 2. An initial correlation for the ignition time of MCH was generated, see Fig. 1. These preliminary results have been compared with the existing data and current model of Orme, Curran and Simmie (2006) and though there is agreement in magnitude, there is a significant difference in activation energy. High-pressure ignition experiments to continue testing of these mechanisms are planned. As MCH readily condenses in the mixing manifold and shock tube, a species-specific method to measure low *in situ* fuel concentration is needed for accurate ignition time measurement. Accordingly, we have

developed a mid-IR (3.39 μm) laser absorption detection scheme to accurately measure fuel concentration in the shock tube; the advantages of this direct fuel-loading sensor are applicable to other practical and surrogate fuels.

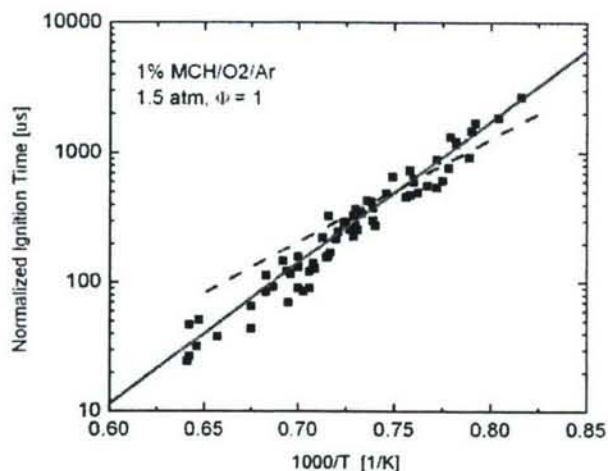


Fig. 1. Ignition delay times: 1% methylcyclohexane/ O_2/Ar , $\Phi = 1$, 1.5 atm. Dashed line: Orme et al. 2006 mechanism. Solid line: best fit to current data, $\tau_{\text{ign}} = 7.5 \times 10^{-14} P^{-0.96} X_{\text{MCH}}^{-0.82} \Phi^{1.47} \exp(25560/T)$ [s].

Jet Fuel and Kerosene: We are continuing our experimental and modeling study of the ignition time of jet fuel. We have completed modification of our high-pressure shock tube facility (HPST) which will allow improved experimental control in the preparation of test gas mixtures of liquid fuels. We have compared the predictions of several current kinetic mechanisms for jet fuel and used these mechanisms to predict and plan our upcoming set of high-pressure (15 to 60 atm) ignition time experiments. [1]

n-Heptane and Iso-Octane: Methyl radical concentration time-histories were measured during the oxidation and pyrolysis of iso-octane and n-heptane behind reflected shock waves. [2] Initial reflected shock conditions covered temperatures of 1100 to 1560 K, pressures of 1.6-2.0 atm and initial fuel concentrations of 100-500 ppm. Methyl radicals were detected using cw UV laser absorption near 216 nm; three wavelengths were used to compensate for time- and wavelength-dependent interference absorption. Methyl time-histories were compared to the predictions of several current oxidation models. While some agreement was found between modeling and measurement in the early rise, peak and plateau values of methyl, and in the ignition time, none of the current mechanisms accurately recover all of these features. Sensitivity analysis of the ignition times for both iso-octane and n-heptane showed a strong dependence on the reaction $\text{C}_3\text{H}_5 + \text{H} = \text{C}_3\text{H}_4 + \text{H}_2$, and a recommended rate was found for this reaction. Sensitivity analysis of the initial rate of CH_3 production during pyrolysis indicated that for both iso-octane and n-heptane, reaction rates for the initial decomposition channels are well isolated, and overall values for these rates were obtained. The present concentration time-history data provides strong constraints on the reaction mechanism of both iso-octane and n-heptane oxidation, and in conjunction with OH concentration time-histories and ignition delay times, recently measured in our laboratory, should provide a self-consistent set of kinetic targets for the validation and refinement of iso-octane and n-heptane reaction mechanisms.

Fundamental Kinetics Database Utilizing Shock Tube Measurements: We have published Volume 1 of this database on-line at <http://hanson.stanford.edu/>. [3] This volume includes ignition delay time measurements and details of species concentration time-history profiles from shock tube experiments at Stanford University. Fuel species included in this database include: hydrogen, methane, and ethylene; normal alkanes including ethane, propane, n-butane, n-heptane and n-decane; branched alkanes including iso-butane, iso-pentane, and iso-octane; JP-10;

butadiene; toluene; gasoline and ternary gasoline surrogates. Fuels for which high-pressure ignition delay time data exist includes hydrogen, methane, n-heptane, iso-octane, toluene, gasoline, and gasoline surrogates. Also included in the database are OH concentration time-history measurements for most of these fuels, and CH, CH₃, and CO₂ measurements for the small fuels. Work is continuing on database development including: interaction with model developers, measurements of higher hydrocarbons including soot formation, and an extension of this database to a wider pressure range and lower temperatures relevant to flameless oxidation.

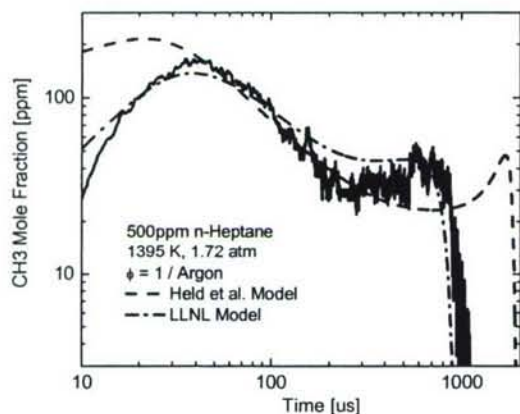


Fig. 2. Example methyl absorption data: n-heptane oxidation.

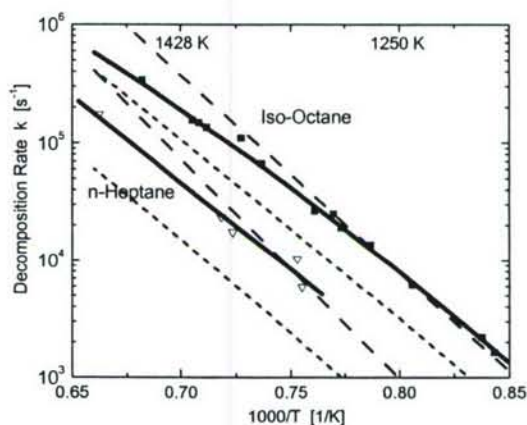


Fig. 3. First-order decomposition rates k for iso-octane and n-heptane, 1.75 atm. Upper three lines, iso-octane; lower three lines, n-heptane. Solid lines, fit to data; dashed lines, Davis and Law rates; short dashes, Curran et al. LLNL rates.

Aerosol Shock Tube: Ignition Time Measurements of Low-Vapor-Pressure Fuels: We have developed a method to measure shock tube ignition delay times in low-vapor-pressure fuels without heating the shock tube. This method which uses the aerosol shock tube has several advantages, not the least of which is that we do not heat and chemically react the fuel in a heated shock tube before the ignition time experiment. It also permits the direct measurement of ignition times at high concentrations for fuels such as JP-8 and diesel and surrogates such as decane, dodecane and hexadecane. To quantify the amount of fuel in our mixtures for these experiments we have developed two fuel diagnostic methods: one using multi-wavelength Mie extinction for liquid fuel loading and one using gas phase absorption, both with IR lasers. Figure 4 presents initial n-dodecane/air ignition times for an equivalence ratio of 0.66 and 8 atm measured using the aerosol shock tube. This amount of fuel loading would require heating to over 50 C in a conventional shock tube. We have found no previous experimental work at these fuel loadings. Experiments are in progress to extend these measurements to decane, hexadecane, JP-8 and diesel fuel for a wider range of reaction temperatures and pressures, and to include investigations of soot formation.

Measurements of Droplet Evaporation behind Shock Waves: We have developed a suite of tools for studying aerosols behind shock waves. These include the aerosol shock tube itself, a laser-based Mie-extinction particle sizing diagnostic, a tunable near-infrared laser diagnostic for vapor concentration, and a one-dimensional computational model. With these tools, we measured the behavior of water aerosols in the range of 1-10 μm behind shock waves with temperatures between 450-600 K and pressures between 0.65-1.1 atm. See Fig. 6. From these data we

determined evaporation rates and found a correlation that provides the non-continuum evaporation rate in terms of a d^2 evaporation rate and a correction function. [4]

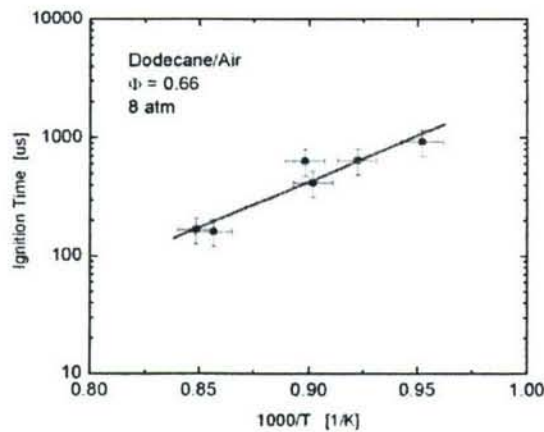


Fig. 4. Ignition delay times: n-dodecane/air, 8 atm, $\Phi = 0.66$. Data derived using the aerosol shock tube.

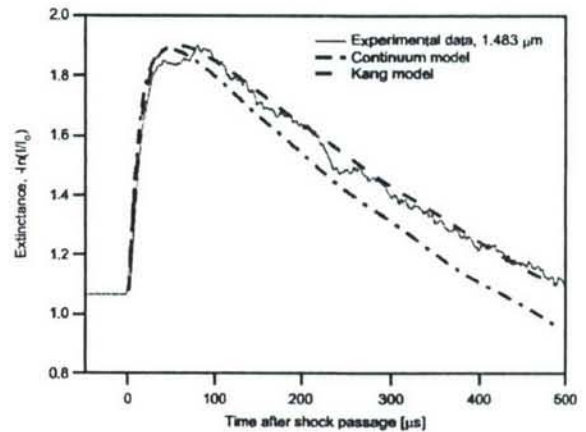


Fig. 5. Water droplet evaporation: experimental and model. Pre-shock conditions: 223 torr, 295 K; with a log-normal droplet distribution parameters: $d = 2.8 \mu\text{m}$, $k = 1.48$; and droplet loading of 9.9 ppmv. The incident shock speed is 513 m/s, and the immediate post-shock conditions are 0.85 atm and 458 K.

ARO-SPONSORED PUBLICATIONS (2005-2006):

1. S. Vasu, D. F. Davidson, R. K. Hanson, "Shock Tube Ignition Delay Times and Modeling of Jet Fuel Mixtures," submitted for publication, 42nd AIAA/ASME/SAE/ASEE Joint Propulsion Conference and Exhibit, 2006.
2. D. F. Davidson, M. A. Oehlschlaeger, R. K. Hanson, "Methyl Concentration Time Histories during iso-Octane and n-Heptane Oxidation," accepted for publication, Proceedings of the Combustion Institute 2006.
3. D. F. Davidson and R. K. Hanson, "*Fundamental Kinetics Database Utilizing Shock Tube Measurements*," Mechanical Engineering Department Report, Stanford University, November 2005.
4. T. C. Hanson, D. F. Davidson, R. K. Hanson, "Shock Induced Behavior in Micron-Sized Water Aerosols," submitted for publication, Physics of Fluids 2006.

SUPERCRITICAL FUEL PYROLYSIS

AFOSR Grant No. FA9550-04-1-0005

Principal Investigator: Mary Julia (Judy) Wornat

Louisiana State University
Department of Chemical Engineering
Baton Rouge, Louisiana 70803

SUMMARY/OVERVIEW:

The fuels used in the next generation of hypersonic aircraft will have to operate under very high pressures (beyond the critical pressures of most hydrocarbons) and will have to sustain very high heat loads in order to meet aircraft cooling requirements [1-3]. Critical to the development of the fuel systems in these aircraft is an understanding of the fuel pyrolysis reaction mechanisms under the conditions that the fuels will be operating. Of particular interest are the reactions leading to polycyclic aromatic hydrocarbons (PAH), which can serve as precursors to fuel-line deposits [3,4], a problem of critical importance to avoid, for safe aircraft operation. In order to better elucidate the mechanisms and kinetics of the reactions of fuel pyrolysis and PAH formation under supercritical conditions, pyrolysis experiments are being conducted, under the present research program, with model fuels at temperatures of 300-600 °C, pressures of 20-100 atm, and residence times of 30-1000 sec. The model fuels include the jet fuel components toluene, 1-methylnaphthalene, and mixtures of toluene and *n*-heptane—as well as the "endothermic" fuel methylcyclohexane. The supercritical pyrolysis experiments are conducted in an isothermal silica-lined stainless-steel coil reactor specially designed [4,5] for such experiments, and PAH reaction products are analyzed by high-pressure liquid chromatography with diode-array ultraviolet-visible absorbance and mass spectrometric detection (HPLC/UV/MS), an isomer-specific technique ideally suited for the analysis of PAH [6]. It is anticipated that the results from this research will provide information of critical importance to the design and development of fuel systems for high-speed aircraft.

TECHNICAL DISCUSSION

Acquisition of the new HPLC/UV/MS instrument this past year, through DURIP funds, has facilitated the identification of many new PAH products from our supercritical pyrolysis experiments with toluene, methylcyclohexane, and 1-methylnaphthalene. In the cases of toluene and methylcyclohexane, several new eight-ring PAH products have been recently identified [6], and the reaction schemes responsible for their formation are the subject of a paper in preparation. In the case of 1-methylnaphthalene, 17 additional PAH products have been recently identified, and a paper describing the reactions responsible for the formation of PAH from the supercritical pyrolysis of 1-methylnaphthalene has just been accepted [7]. This report thus focuses on the results of 1-methylnaphthalene (critical temperature, 499 °C; critical pressure, 36 atm), a two-ring aromatic component of jet fuels [8].

Figure 1 presents the HPLC chromatogram of the aromatic products of 1-methylnaphthalene pyrolysis at 585 °C, 110 atm, and 140 sec. In addition to that of 1-methylnaphthalene itself (unreacted fuel), Figure 1 displays the structures of the 37 individual two- to seven-ring PAH

products that have been identified by HPLC/UV/MS, as well as the molecular masses of the eight- and nine-ring PAH products whose exact identities are not yet known. Fifteen of the PAH of ≥ 5 rings in Figure 1 have never before been identified as products of 1-methylnaphthalene pyrolysis or combustion. The structures of the earliest-eluting products of Figure 1—naphthalene, 2-methylnaphthalene, the dimethylnaphthalenes, and the bi-naphthyls—reveal that within the supercritical 1-methylnaphthalene pyrolysis environment, it is possible to break the methyl C-H bond (bond dissociation energy, BDE, 85.1 kcal/mole [9]), the methyl-aryl C-C bond (BDE, 103.8 kcal/mole [9]), and the aryl C-H bond (BDE, 112.2 kcal/mole [9]). Since we find no single-ring aromatics among our products and since the gaseous hydrocarbon products we observe (90 % methane, 5% ethane, and the balance C_3 to C_4 alkanes, with only a trace of ethylene—and no acetylene) can all come from methyl and hydrogen—we see that the only kind of bond that appears not to be broken in this reaction environment is the aromatic C-C bond (BDE, 122.3 kcal/mole [10]). We could thus expect the larger aromatic products in this reaction environment to be formed by different combinations of methyl, hydrogen, naphthalene, and 1-methylnaphthalene radicals and molecules—forming bonds in ways that preserve the 2-ring aromatic units of the reacting naphthalene and methylnaphthalene entities.

That this hypothesis is indeed the case is borne out by the structures of the five- to seven-ring PAH products of supercritical 1-methylnaphthalene pyrolysis, shown in Figure 1 and listed in the left-most column of Table 1. All of the product PAH structures in the left column of Table 1 reveal the intactness of the two two-ring naphthalene or 1-methylnaphthalene units required in their construction. This finding, along with consideration of BDEs and relative abundances of reactant species, has been used to construct [7] radical reaction pathways responsible for the five- to seven-ring product PAH—reaction pathways that involve species plentiful in the supercritical 1-methylnaphthalene pyrolysis environment: 1-naphthylmethyl radical, methyl radical, 1-methylnaphthalene, naphthalene, and (to a lesser extent) 2-methylnaphthalene. Examples of such pathways are given in the middle column of Table 1.

Because the HPLC/UV/MS analysis technique affords such isomer specificity, we can say with certainty that the 5- to 7-ring PAH listed in the left column of Table 1 definitely are products of 1-methylnaphthalene pyrolysis, and all other isomers of those particular PAH classes (some of which are listed in the two right-most columns of Table 1) are not. This ability to distinguish which particular PAH isomers are products and which are not has revealed that the 5- to 7-ring PAH products that form are those whose structures preserve the intactness of the parent two 2-ring naphthalene units, whose reaction pathways involve the species most abundant in the reaction environment, and whose formation involves bond breakage at the sites of lowest BDE.

The remaining PAH products of Figure 1 are the six 8-ring $C_{32}H_{18}$, whose peaks are labelled “402” in Figure 1, and the 9-ring $C_{34}H_{18}$, whose peak is labelled “426.” As there are hundreds of possible structures in these latter two families, the fact that certain peaks of these molecular formulas exhibit some prominence suggests that a high degree of product selectivity is in effect for these 8- and 9-ring products, just as it has been demonstrated in the 5- to 7-ring PAH products of supercritical 1-methylnaphthalene pyrolysis. The $C_{32}H_{18}$ PAH can be constructed from 1-naphthylmethyl radical reacting with naphthalene and 1-methylnaphthalene; the $C_{34}H_{18}$ PAH can be constructed from 1-naphthylmethyl radical, methyl, and two 1-methylnaphthalenes. Even though the exact identities of these 8- and 9-ring products have not yet been determined, their presence, along with their suggested selectivity, serve as evidence that the types of reaction mechanisms outlined in Table 1—for the combination of two naphthalene and methylnaphthalene entities in the formation of 5- to 7-ring PAH—are likely to apply to the combination of three and more such entities in the formation of larger-ring-number PAH and eventually carbonaceous solids.

REFERENCES

1. Heneghan, S.P., Zabarnick, S., Ballal, D.R., Harrison W.E. III. "JP-8+100: The Development of High-Thermal Stability Jet Fuel," *Journal of Energy Resources Technology* 118: 170-179 (1996).
2. Dounghip, T., Ervin, J.S., Williams, T.F., and Bento, J. "Studies of Injection of Jet Fuel at Supercritical Conditions," *Industrial and Engineering Chemistry Research* 41: 5856-5866 (2002).
3. Edwards, T., Zabarnick, S. "Supercritical Fuel Deposition Mechanisms," *Industrial and Engineering Chemistry Research* 32: 3117-3122 (1993).
4. Stewart, J.F. "Supercritical Pyrolysis of Endothermic Fuels," Ph.D. Thesis, Department of Mechanical and Aerospace Engineering, Princeton University, 1999.
5. Davis, G.D. "An Experimental Study of Supercritical Methylcyclohexane Pyrolysis," M.S.E. Thesis, Department of Mechanical and Aerospace Engineering, Princeton University, 1994.
6. McClaine, J. W., Zhang, X., and Wornat, M.J., "First Identification of Benzo[ghi]naphtho-[8,1,2-*bcd*]perylene as a Product of Fuel Pyrolysis," submitted to *Journal of Chromatography A* (2006).
7. Somers, M. L., McClaine, J. W., and Wornat, M. J., "The Formation of Polycyclic Aromatic Hydrocarbons from the Supercritical Pyrolysis of 1-Methylnaphthalene," accepted to *Proceedings of the Combustion Institute* 31 (2006).
8. Bernabei, M., Reda, R. Galiero, R., and Bocchinfuso, G., "Determination of Total and Polycyclic Aromatic Hydrocarbons in Aviation Jet Fuel," *Journal of Chromatography A* 985: 197-203 (2003).
9. Y.-R. Luo, *Handbook of Bond Dissociation Energies in Organic Chemistry*, CRC Press, Boca Raton, FL, 2003, pp. 38, 39, 110.
10. R.T. Sanderson, *Chemical Bonds in Organic Compounds*, Sea and Sand, Scottsdale, AZ, 1976, Chapter.

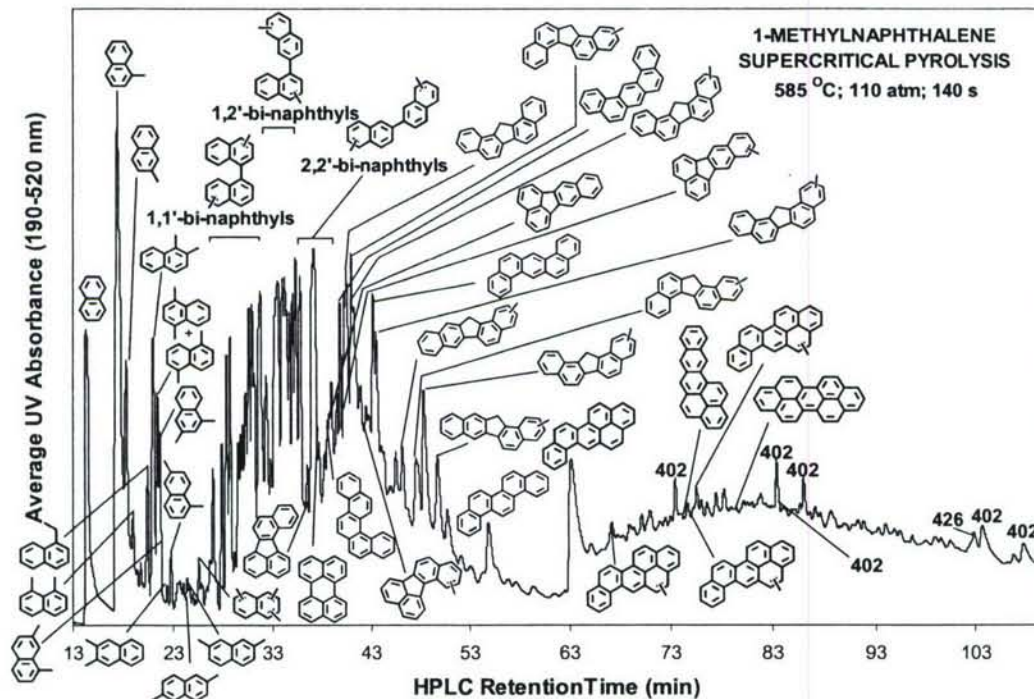
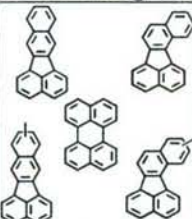
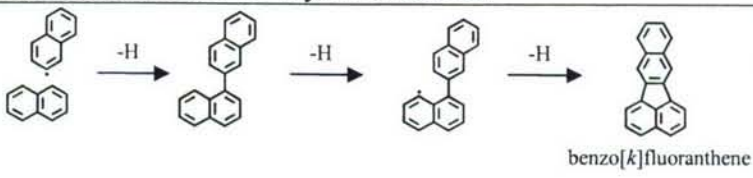
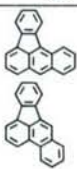
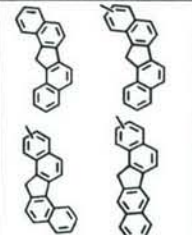
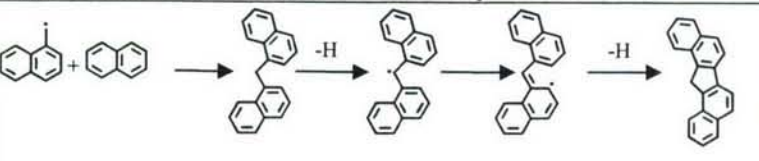
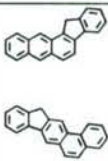
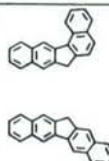
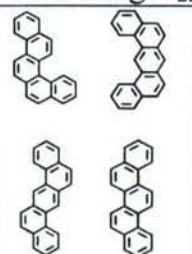
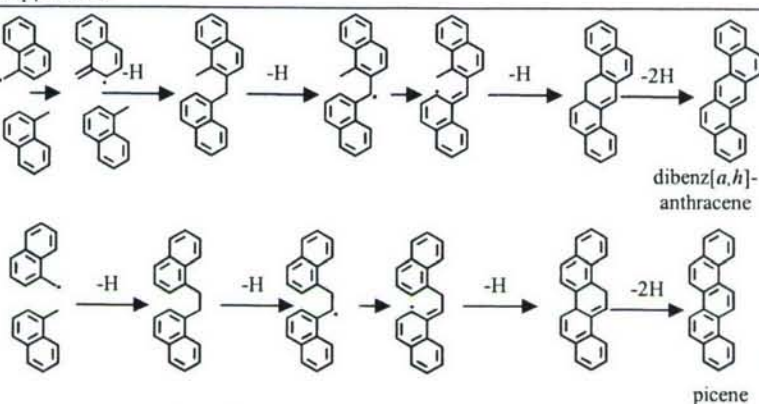
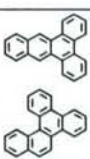
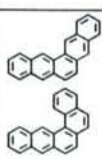
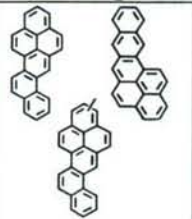
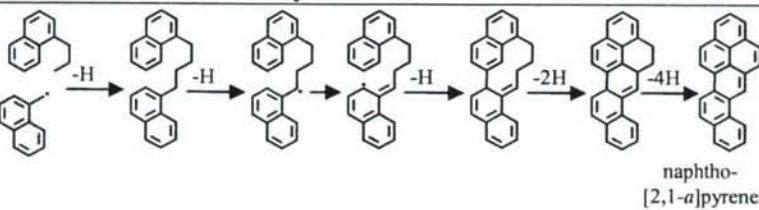
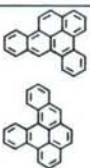
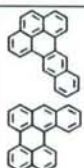

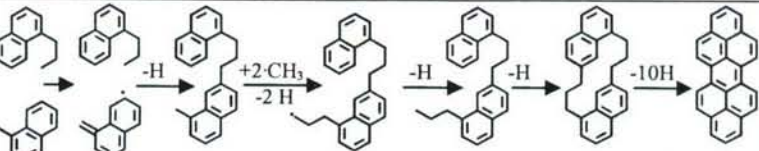



Figure 1. HPLC chromatogram of products of 1-methylnaphthalene pyrolysis. The rise in baseline at 63 minutes corresponds to a change in mobile-phase composition to UV-absorbing dichloromethane. Chromatographic peaks are labelled with the structures of PAH that have been unequivocally identified by their mass and UV spectra. Numbers "402" and "426" signify molecular masses of PAH whose exact structures have not yet been determined.

Table 1. Five- to Seven-Ring PAH Products of Supercritical 1-Methylnaphthalene Pyrolysis

Observed Products	Reaction Pathways Responsible for Formation of Observed Products	Examples of Isomers not Observed*	
Five-Ring C ₂₀ H ₁₂ PAH and their Methyl Derivatives		A	B
	 benzo[k]fluoranthene		
Five-Ring C ₂₁ H ₁₄ Dibenzofluorenes and their Methyl Derivatives			
	 dibenzo[a,i]-fluorene		
Five-Ring C ₂₂ H ₁₄ PAH			
	 dibenz[a,h]-anthracene picene		
Six-Ring C ₂₄ H ₁₄ PAH and their Methyl Derivatives			
	 naphtho[2,1-a]pyrene		
Seven-Ring C ₂₆ H ₁₄ PAH			
	 dibenzo[cd,lm]perylene		

*Examples of PAH isomers not observed in 1-methylnaphthalene products: Those in Column A do not preserve the intactness of two 2-ring naphthalene units; those in Column B require involvement of one or more 2-methylnaphthalene entities in their construction.

EXPERIMENTAL AND COMPUTATIONAL CHARACTERIZATION OF COMBUSTION PHENOMENA

AFOSR Task No. 02PR01COR

Principal Investigator: James R. Gord

Air Force Research Laboratory
AFRL/PRTC Bldg 5
1950 Fifth St
Wright-Patterson AFB OH 45433-7251

SUMMARY/OVERVIEW

Propulsion systems represent a substantial fraction of the cost, weight, and complexity of Air Force aircraft, spacecraft, and other weapon-system platforms. The vast majority of these propulsion systems are powered through combustion of fuel; therefore, the detailed study of combustion has emerged as a highly relevant and important field of endeavor. Much of the work performed by today's combustion scientists and engineers is devoted to the tasks of improving propulsion-system performance while simultaneously reducing pollutant emissions. Increasing the affordability, maintainability, and reliability of these critical propulsion systems is a major driver of activity as well. This research effort is designed to forward the scientific investigation of combustion phenomena through an integrated program of fundamental combustion studies, both experimental and computational, supported by parallel efforts to develop, demonstrate, and apply advanced techniques in laser-based/optical diagnostics and modeling and simulation.

TECHNICAL DISCUSSION

Extension of Diode-Laser-Based Sum- and Difference-Frequency Generation to Two-Line Thermometry and Wavelength-Modulation Spectroscopy. Compact, high-speed-tunable, diode-laser-based ultraviolet (UV) and mid-infrared (MIR) laser sources have been developed to take advantage of strong electronic transitions and fundamental vibrational bands for *in-situ* combustion sensing. These sources are based on sum- and difference-frequency generation, respectively, and have been operated with data-acquisition bandwidths of 10 to 20 kHz. Measurements of species concentration and temperature have been achieved by resolving the lineshape of single transitions, although the accuracy of this approach can be limited by uncertainties in the collisional environment. In unsteady flames, for example, the concentration of various colliding species may not be known. In addition, collisional cross-sections may not be available for all conditions encountered in realistic combustors. To improve measurement accuracy over a wide range of conditions, we have implemented a two-line thermometric approach using both direct absorption and wavelength-modulation spectroscopy (WMS). WMS requires additional calibration procedures but offers improved sensitivity for low concentrations. Demonstration measurements are performed for various equivalence ratios in a H₂-air diffusion flame stabilized over a Hencken burner. Figure 1 shows a wavelength scan over two OH transitions, along with the corresponding WMS signal. Improved temperature accuracy is achieved by taking the ratio of the integrated absorption across two transitions, which reduces uncertainties associated with collisional broadening.

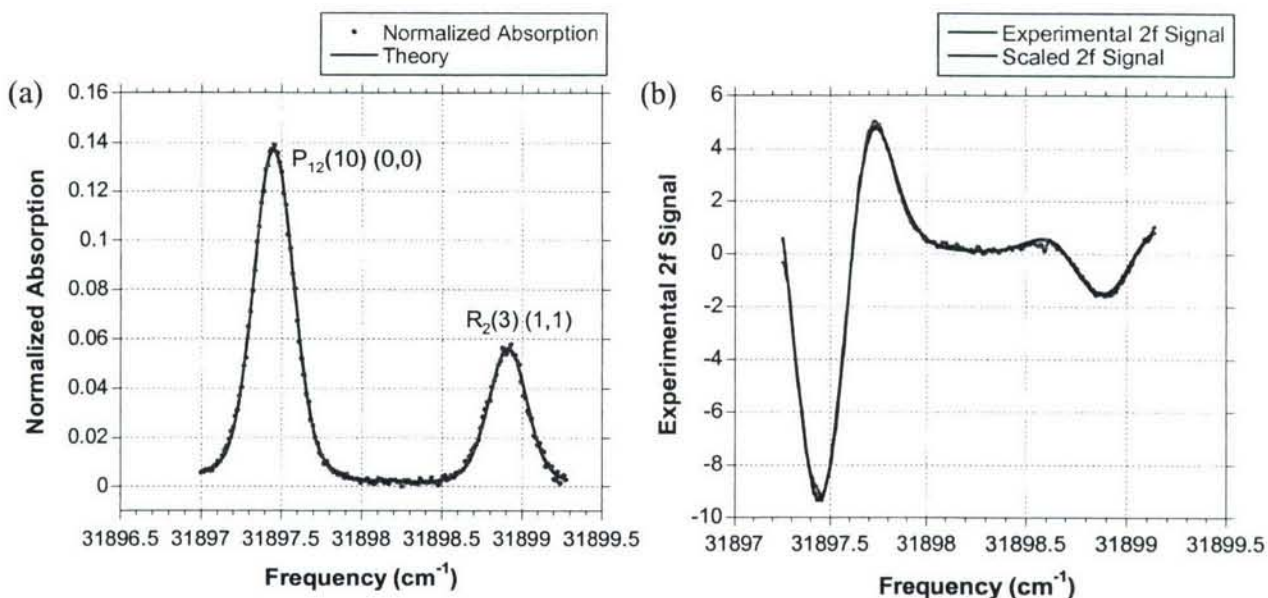


Fig. 1. Two-line OH spectra using (a) direct absorption and (b) wavelength-modulation spectroscopy.

Ultrafast Coherent Anti-Stokes Raman Scattering for Thermometry. Most previous CARS thermometric measurements in gas-phase or reacting flows have been performed using ns laser pulses. A major limitation of ns-laser-based CARS thermometry is the contribution of the nonresonant signal, which limits the accuracy and degrades the sensitivity of the technique. Moreover, most of these measurements are generally performed at low repetition rate (generally 10-20 Hz) due to the unavailability of high-rep-rate, high-power ns lasers. This temporal resolution complicates efforts to resolve turbulence phenomena in reacting flows.

In fs CARS, also known as FAST (Femtosecond Adaptive Spectroscopic Technique) CARS, a coherence is established in the medium by using two nearly transform-limited fs lasers whose frequency difference corresponds to the resonant frequencies of the excited molecule, covering the whole vibration-rotation manifold in the ground electronic state. On the order of one hundred fs after the initial excitation, the coherently excited transitions begin to dephase with respect to each other due to slight frequency differences between neighboring transitions, and the overall signal starts to decay. In our work, we focus on the initial decay of the coherence for extracting the temperature of the medium. The initial decay rate of the coherence is very sensitive to temperature and is not affected by collision rates or Stark shifts, two factors which significantly complicate frequency-domain nanosecond CARS measurements.

In general, there are four promising advantages of short-pulse CARS spectroscopy: (1) it improves accuracy by reducing or eliminating the non-resonant contribution to the CARS signal when the probe beam is delayed with respect to the pump beam, (2) it minimizes the effects of collisions on the CARS signal, thereby reducing modeling uncertainty and increasing signal-to-noise ratio, (3) it improves sensitivity and might enable the detection of minor species due to reduction or elimination of interference from the non-resonant background, and (4) it has the capability of generating signals at rates up to 1 kHz. These advantages have the potential to enhance the performance of CARS thermometry in high-pressure, high-temperature combustors of practical interest by overcoming known limitations of ns-based systems.

A schematic diagram of the fs CARS system at WPAFB and CARS signals obtained as a function of probe delay in atmospheric-pressure nitrogen with a nearly transform-limited, 50-fs probe beam are shown in Fig. 2 for three different temperatures. The CARS signals decrease sharply for probe delays from 0-4 ps through initial dephasing due to the frequency spread of the

rovibrational transitions in the fundamental Raman band. At 300 K, the fundamental band has a FWHM of approximately 4 cm^{-1} , corresponding to a characteristic decay time of approximately 3-4 psec. Following this initial decay, the CARS signal exhibits a long-lived beating pattern due to constructive and destructive interference of the Raman coherences. This long-lived beating pattern decays slowly through collisional dephasing. The 500 K signal decays much faster because the frequency spread of those Raman transitions with significant induced intensity is much greater at the higher temperature.

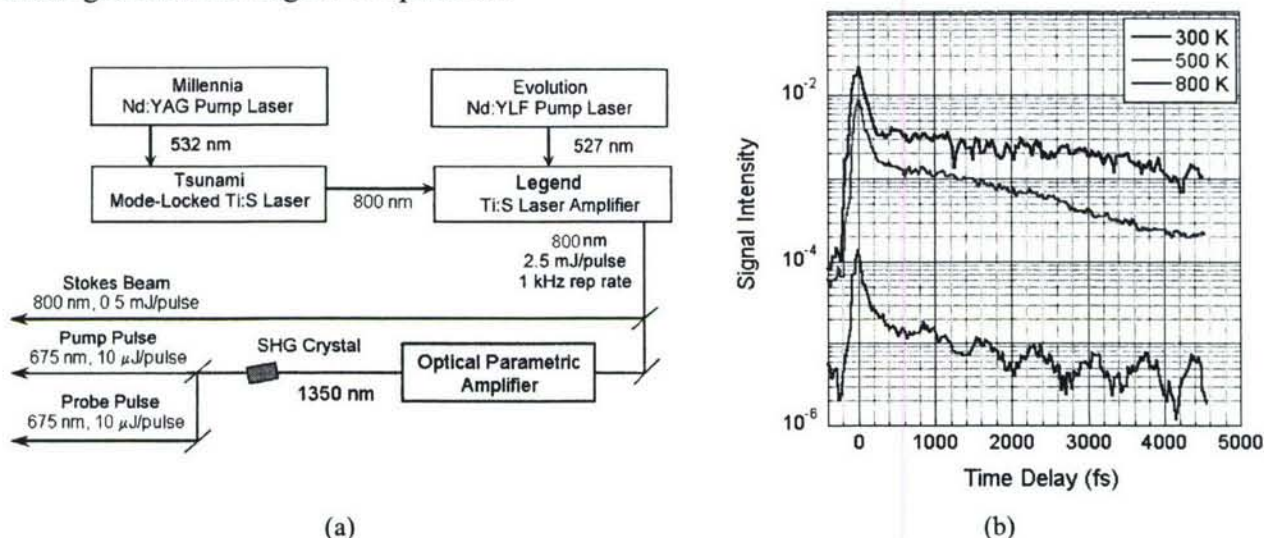


Figure 2. (a) Schematic diagram of the fsec CARS system and (b) fsec CARS signal for three different temperatures for the temporal region near the pump/Stokes excitation.

Electronic-Resonance-Enhanced CARS for Detection of Nitric Oxide. Accurate measurement of NO concentration in high-pressure combustors is very difficult but critical for minimization of pollutant emissions. Current state-of-the-art measurements of NO concentration in high-pressure liquid-fueled combustors are based on laser-induced fluorescence (LIF), which has four major limitations: (1) significant quenching of the NO LIF signal by O_2 , CO_2 , H_2O , and other molecules, (2) decreasing NO LIF signal with increasing pressure for a given temperature and NO mole fraction, (3) interferences from soot luminescence typical of complex jet fuels, and (4) absorption of the laser beam and LIF signal at high pressures by CO_2 , O_2 , and other hydrocarbon molecules. Preliminary measurements suggest ERE-CARS as a potential solution to these limitations.

A schematic diagram of the ERE-CARS system is shown in Fig. 3. Experimental NO ERE-CARS signals generated with this system are compared with calculated NO LIF signals in Fig. 4. The spectral sum of the square root of the ERE-CARS signals and the NO LIF signals are plotted in Fig. 4 for different concentrations of O_2 and CO_2 in a jet flow. It is evident that the NO ERE-CARS signal is essentially independent of the electronic quenching rate whereas the NO LIF signal decreases by more than three orders of magnitudes as the quenching rate increases by a factor of 400-800. The pressure scaling of the NO ERE-CARS and NO LIF signals are shown in Fig. 5, while an ERE-CARS spectrum acquired in a sooty acetylene-air flame is shown in Fig. 6. These measurements show significant promise for the application of ERE-CARS in gas-turbine combustors of interest.

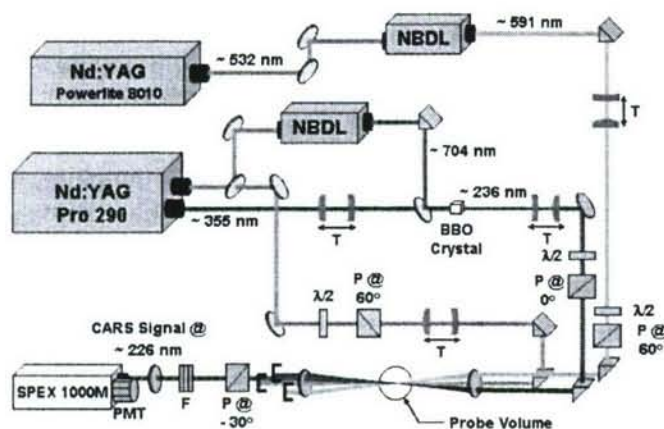


Fig. 3. Schematic diagram of NO ERE-CARS system.

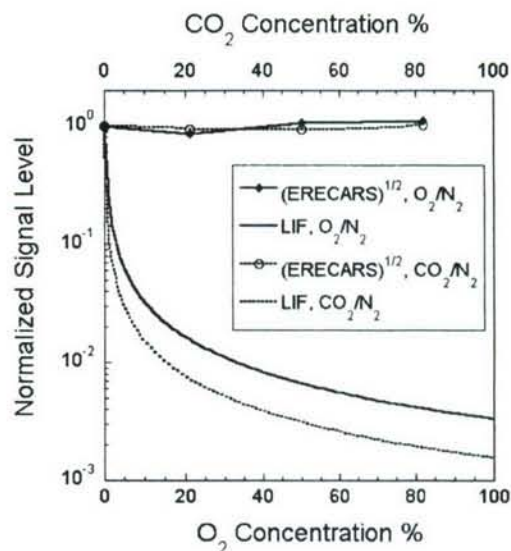


Fig. 4. Dependence of experimental ERE-CARS signals and calculated LIF signals on composition of the NO/N₂/O₂ or NO/N₂/CO₂ jet flow.

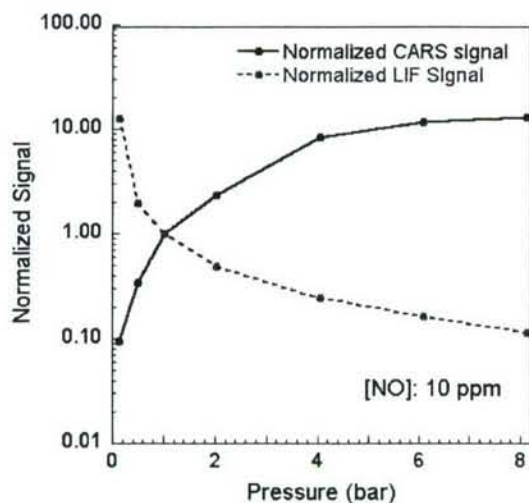


Fig. 5. Pressure-scaling behavior of experimental NO ERE-CARS and calculated NO LIF signals in a high-pressure cell.

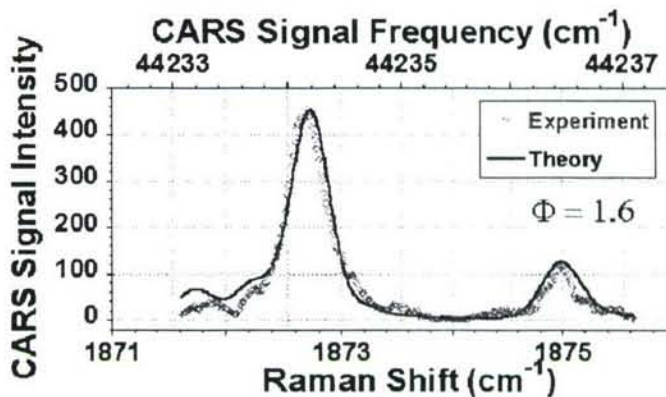


Fig. 6. NO ERE-CARS spectra recorded at a height of 55mm above the burner surface in a C₂H₂/air sooting flame of $\phi = 1.6$ stabilized over the Hencken burner.

SELECTED RECENT PUBLICATIONS

- "Application of a Difference-Frequency-Mixing Based Diode-Laser Sensor for Carbon Monoxide Detection in the 4.4-4.8 μm Spectral Region," R.B. Jimenez, J.A. Caton, T.N. Anderson, R.P. Lucht, T. Walther, S. Roy, M.S. Brown, and J.R. Gord, in press, Applied Physics B, 2006.
- "Velocity Imaging for the Liquid-Gas Interface in the Near Field of an Atomizing Spray: Proof Of Concept," D.L. Sedarsky, M.E. Paciaroni, M.A. Linne, J.R. Gord, and T.R. Meyer, Opt. Lett. **31**, 906-908, 2006.
- "Ballistic Imaging of the Liquid Core for a Steady Jet in Crossflow," M.A. Linne, M. Paciaroni, J.R. Gord, and T.R. Meyer, Appl. Opt. **44**, 6627-6634, 2005.
- "Diode-Laser-Based Ultraviolet-Absorption Sensor for High-Speed Detection of the Hydroxyl Radical," T.N. Anderson, R.P. Lucht, T.R. Meyer, S. Roy, and J.R. Gord, Opt. Lett. **30**, 1321-1323, 2005.
- "Time-Resolved Dynamics of Resonant and Nonresonant Broadband Picosecond Coherent Anti-Stokes Raman Scattering Signals," S. Roy, T.R. Meyer, and J.R. Gord, Appl. Phys. Lett. **87**, 264103, 2005.
- "Measurements of OH Mole Fraction and Temperature up to 20 kHz Using a Diode-Laser-Based UV Absorption Sensor," T.N. Anderson, T.R. Meyer, S. Roy, R.P. Lucht, and J.R. Gord, Appl. Opt. **44**, 6729, 2005.
- "10 kHz Detection of CO₂ at 4.5 μm Using Tunable Diode-Laser-Based Difference-Frequency Generation," T.R. Meyer, S. Roy, T.N. Anderson, R.P. Lucht, and J.R. Gord, Opt. Lett. **30**, 3087, 2005.
- "Broadband Coherent Anti-Stokes Raman Scattering Spectroscopy of Nitrogen Using a Picosecond Modeless Dye Laser," S. Roy, T.R. Meyer, and J.R. Gord, Opt. Lett. **30**, 3222, 2005.

ADVANCED DIAGNOSTICS FOR REACTING FLOWS

AFOSR Grant F49620-04-1-0009

Principal Investigator: Ronald K. Hanson

Mechanical Engineering Department
Stanford University, Stanford, California 94305-3032

SUMMARY/OVERVIEW:

Recent advances in this program's research and development of non-intrusive diagnostics for air-breathing combustion applications are reported. Progress is highlighted on: the validation of infrared-planar laser induced fluorescence (IR-PLIF) models for quantitative CO₂ detection; quantitative NO PLIF in high-pressure flames; increased tunable diode laser (TDL) absorption sensor temperature fidelity in scramjet flowfields using wavelength-modulation techniques; differential-absorption with novel new light sources in the mid-IR for fuel sensing; use of wavelength-multiplexed TDL sensing for gas temperature in non-uniform flow fields; and advances in toluene photophysics to enable tracer-based PLIF imaging of temperature fields.

TECHNICAL DISCUSSION:

1. Infrared-PLIF Imaging Diagnostics using Vibrational Transitions

IR-PLIF allows for imaging a group of molecular species important for hydrocarbon combustion that are not accessible using single-photon UV/visible PLIF; this includes CO, CO₂, and hydrocarbon fuels. IR-PLIF is the excitation of IR-active vibrational modes with imaging of the subsequent vibrational fluorescence. Quantitative interpretation requires knowledge of the vibrational energy transfer processes, and hence in recent years we have been developing models for infrared fluorescence. During the past year, measurements at atmospheric pressure and room temperature have been used to validate portions of the vibrational energy transfer model for CO₂. This model has been used to estimate IR-PLIF performance and design experiments for previously untested conditions, including high-speed flows at sub-atmospheric pressures and low-speed flows at elevated pressures (1-10 atm).

2. PLIF of NO at High Pressures and Temperatures – Multi-Wavelength Detection Strategies

LIF of NO at high pressures is complicated by pressure broadening of the excitation transitions and interference from O₂ and CO₂, as we have described previously. We now report a multi-wavelength detection strategy optimized for sensing NO with simultaneous detection in other wavelength windows to quantify signals from O₂ and CO₂. The concept of the three detection bands is illustrated in Fig. 1 by overlap of detection bandpasses with the fluorescence spectra of NO, O₂ and CO₂. Design rules have been developed to select the optimum bandpasses for NO detection and correction for O₂ and CO₂ interference. Fig. 2 illustrates

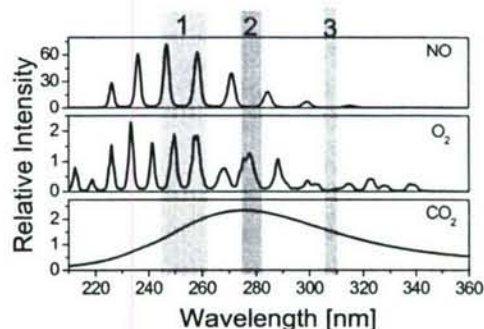


Fig. 1. Illustration of LIF from NO, O₂, and CO₂ at 2000K and 40 atm with detection windows (1) for NO and (2) and (3) to quantify the interference from O₂ and CO₂

corrected images for NO in slightly-lean ($\phi=0.9$) and slightly-rich ($\phi=1.1$) flames over the range of pressure investigated (1–60bar). This concept offers the potential for simultaneous imaging of all three species, and work is underway to understand how to optimize the excitation wavelengths and detection bandpasses for measurements in rich and lean high-pressure flames.

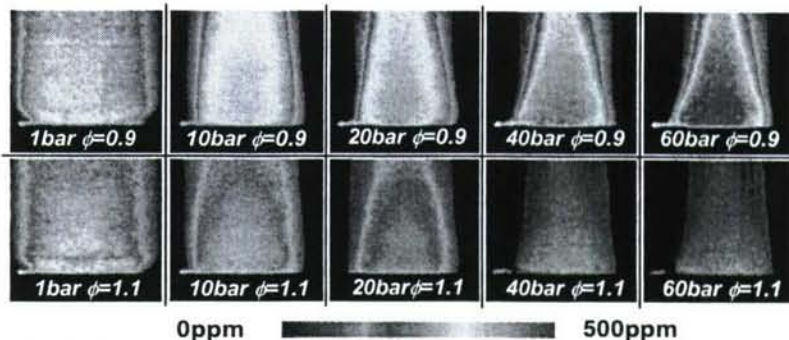


Fig. 2. NO concentrations from multi-wavelength NO-PLIF imaging (1–60 bar, $\phi = 0.9$ and 1.1 with 300 ppm NO seeding). In fuel-rich flames the NO concentrations are reduced by NO reburn.

3. Advanced Absorption Spectroscopy

3.1 Wavelength-Multiplexed WMS-2f TDL Sensing in a Scramjet Combustor Previously, our TDL sensor development concentrated on scanned-wavelength direct-absorption spectroscopy for aeroengine ground-test applications because of this method's simplicity, accuracy, and capability for time-resolved measurements. However, complications of mechanical and gasdynamic beam-steering, weak absorption at high temperatures and fiber-mode noise conspire to reduce signal-to-noise ratios (SNRs). In practice, we have found that the scanned-wavelength direct-absorption technique requires careful optical engineering to reduce these noise sources to acceptable levels in large-scale facilities. As a result, we have explored an alternative approach, namely wavelength modulation spectroscopy (WMS) with second harmonic detection (2f), and

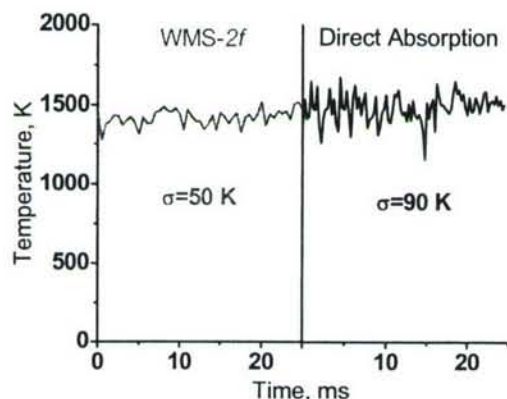


Fig. 3. Comparison of measured temperature using direct absorption and WMS-2f with the 1392/1469 nm line pair in a scramjet combustor. The direct absorption data was filtered from 4 kHz to 2 kHz to match the WMS-2f sampling rate.

have shown this method to offer advantages for sensitive detection of absorption in noisy environments. In the past, this technique has seen limited use with practical sensors, because of calibration requirements. During the past year, however, we have discovered how to take advantage of the intensity modulation of injection-current-tuned diode lasers to provide simultaneous calibration and normalization signals. This advance has enabled absolute WMS-2f measurements of temperature and gas concentration with relative simplicity. Figure 3 illustrates TDL absorption measurements of time-resolved gas temperature in a model scramjet combustor at Wright Patterson AFB; note a twofold improvement in the scatter of the data using WMS-2f versus direct absorption with the same optical engineering and sensor installation.

3.2 Mid-IR Differential Absorption for Fuel Sensing Monitoring and control of fuel concentration is critical to maximizing performance and efficiency and minimizing pollutants emitted by propulsion systems. Mid-infrared absorption diagnostics using a single, fixed-wavelength laser can provide sensitive, time-resolved measurements of fuel concentration in these environments. However, often laser sources of suitable wavelength are not available, and in addition single-fixed-wavelength absorption is sensitive to optical interferences common in practical engine environments, including droplet scattering, window fouling, and interference absorption. Recently, we have acquired a novel mid-IR laser based on difference-frequency-

generation from two near-IR diode lasers to provide tunable single-wavelength output. We have subsequently modified this laser to provide two rapidly alternating ($\sim 100\text{kHz}$) wavelengths of mid-IR output, thereby enabling either two channels of single-wavelength absorption or a direct measurement of differential absorption at the two wavelengths, with $10\mu\text{s}$ time resolution. Differential absorption uses the beam of two alternating wavelengths (colors) and extracts the species concentration from the difference in absorption at the two wavelengths. This difference technique allows rejection of interference and noise common to the two beams. The basic absorption data for differential absorption of n-dodecane, a representative large hydrocarbon fuel surrogate is illustrated in Fig. 4. Recent work has illustrated that this technique can be used to sensitively detect gas concentrations in the presence of interference from aerosol scattering. We believe this new multi-color diode-laser-based diagnostic has the potential for a wide variety of practical applications.

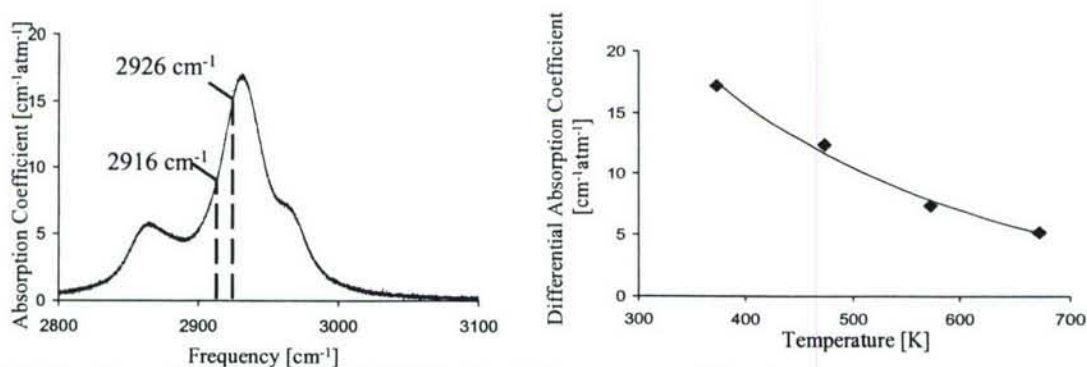


Fig. 4. Left: absorption coefficient via FTIR of n-dodecane vapor dilute in 1 atm. of nitrogen @675K. Right: differential absorption coefficient versus temperature for n-dodecane vapor @ 2916 and 2926 cm^{-1} .

3.3 TDL LOS Absorption Diagnostics for Non-Uniform Flows TDL absorption spectroscopy has proven to be a successful line-of-sight (LOS) gas-sensing strategy for a variety of important applications. However, quantitative measurements have been hampered by the usual assumption of a uniform temperature and species concentration along the line-of-sight. During the past year, we have begun the systematic development of a multi-line thermometry strategy that seeks to extend TDL absorption spectroscopy to temperature sensing in non-uniform flows. The sensor concept is to measure the LOS absorptions for multiple transitions with different temperature dependences, from which the non-uniform temperature distribution along the LOS can be inferred using either of two strategies. The first strategy, called profile fitting, fits a temperature distribution profile postulated using physical constraints; the second strategy, called temperature binning, determines the temperature probability distribution function (PDF) along the LOS using prescribed temperature bins. Investigation of this concept has included simulations and initial experimental proof-of-concept tests using water vapor absorption in combustion gases, and the results include the development of systematic selection criteria for the absorption transitions.

4. Fuel Tracer Photophysics for Quantitative Diagnostics

Previous studies of the photophysical properties of toluene have shown that its fluorescence quantum yield is highly sensitive to temperature. Current work has demonstrated that this sensitivity can be exploited for precise PLIF temperature imaging of gas flows seeded with toluene. Fig. 5 illustrates a single-shot temperature image of a nitrogen flow, seeded with

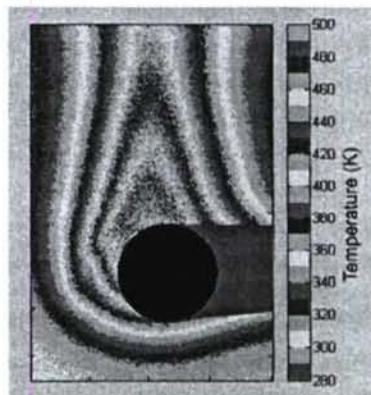


Fig. 5. Single-shot PLIF temperature image using toluene tracer of a nitrogen flow around a heated cylinder.

toluene, passing over a cylinder heated to 500 K. Temperature differences of 5 K can be identified in this image. Fundamental work on the photophysical properties of toluene has revealed that the fluorescence yield is significantly higher than with previously studied ketone tracers. Current work focuses on characterization of toluene's photophysical properties over a wider range of temperature, pressure and gas composition (e.g. O₂) to create a fundamental database of toluene's photophysical properties, from which a physics-based model will be developed (similar to our current model for acetone). This model will facilitate more quantitative use of toluene PLIF and the development of new measurement strategies, e.g. simultaneous imaging of concentration and temperature. The strong dependence of the fluorescence yield on O₂ concentration may additionally provide a means of quantitatively imaging fuel/air ratios.

AFOSR-SPONSORED PUBLICATIONS (2005-2006):

1. G.B. Rieker, J.T.C. Liu, J.B. Jeffries, R.K. Hanson, T. Mathur, M.R. Gruber, and C. Carter, "Wavelength-multiplexed tunable diode laser sensor for temperature and water concentration in a scramjet combustor," *41st Joint Propulsion Conf.*, AIAA-2005-3710.
2. A.E. Klingbeil, J.B. Jeffries, R.K. Hanson, C. Brophy, and J. Sinibaldi, "Mid-IR laser absorption measurements of ethylene in a pulsed detonation engine," *41st Joint Propulsion Conf.*, AIAA-2005-4375.
3. M.A. Oehlschlaeger, D.F. Davidson, J.B. Jeffries, and R.K. Hanson, "Carbon dioxide thermal decomposition: observation of incubation," *Zeitschrift fur Physikalische Chemie*, December, **219** (2005) 555-567.
4. M.A. Oehlschlaeger, D.F. Davidson, J.B. Jeffries, "Temperature measurements behind shock waves using ultraviolet laser absorption of carbon dioxide," *Applied Optics*, **44** (2005) 6599-6605.
5. W. Juchmann, J. Luque, and J.B. Jeffries, "Two-photon laser-induced fluorescence of atomic hydrogen in a diamond depositing dc-arcjet," *Applied Optics* **44** (2005) 6644-6652.
6. J.T.C. Liu, G.B. Rieker, J.B. Jeffries, R.K. Hanson, M.R. Gruber, C.D. Carter, and T. Mathur, "Near-infrared diode laser absorption diagnostics for temperature and water vapor in a scramjet combustor," *Applied Optics* **44** (2005) 6701-6711.
7. T. Lee, W.G. Bessler, H. Kronmayer, C. Schulz, J.B. Jeffries, "Quantitative temperature measurements in high-pressure flames with multi-line NO-LIF thermometry," *Applied Optics*, **44** (2005) 6718-6728.
8. X. Zhou, J.B. Jeffries, R.K. Hanson, "Development of a fast temperature sensor for combustion gases using a single tunable diode laser," *Applied Physics B*, **81** (2005) 711-722.
9. X. Liu, X. Zhou, J. B. Jeffries and R. K. Hanson, "Experimental study of H₂O spectroscopic parameters in the near-IR (6940-7440 cm⁻¹) for gas sensing applications at elevated temperature," *J. Quant. Spectrosc. Rad. Trans.* (2006) in press.
10. Ronald K. Hanson (invited) and Jay B. Jeffries, "Advances in diode laser sensors for combustion and propulsion," *Western States Section Meeting of the Combustion Institute*, paper 05-F1, Stanford, CA, October, 2005.
11. Xiang Liu, Jay B. Jeffries, Ronald K. Hanson, "Measurement of non-uniform temperature distribution measurement using line-of-sight absorption spectroscopy," *44th Aerospace Sciences Meeting*, American Institute of Aeronautics and Astronautics, AIAA 2006-834.
12. Ronald K. Hanson (invited) and Jay B. Jeffries, "Advances in diode laser absorption sensors for combustion and propulsion," in *Laser Applications to Chemical, Security, and Environmental Analysis*, Optical Society of America, Washington, D.C., 2006.
13. Ronald K. Hanson (Invited), "Diode laser sensors for ground testing," *24th Applied Aerodynamics Conference*, American Institute of Aeronautics and Astronautics, AIAA 2006-3441.
14. A.E. Klingbeil, J.B. Jeffries, and R.K. Hanson, "Temperature- and pressure-dependent absorption cross-sections of gaseous hydrocarbons at 3.39 μ m," *Measurement Science and Technology* (2006) in press.
15. A.E. Klingbeil, J.B. Jeffries, and R.K. Hanson, "Tunable mid-IR laser absorption for time-resolved hydrocarbon fuel measurements," *Proc. Combustion Institute* **31** (2006) in press.
16. T. Lee, J.B. Jeffries, and R.K. Hanson, "Experimental evaluation of strategies for quantitative laser-induced-fluorescence imaging of nitric oxide in high-pressure flames (1–60bar)," *Proc. Combustion Institute* **31** (2006) in press.
17. H. Li, X. Zhou, J.B. Jeffries, and R.K. Hanson, "Active control of lean blowout in a swirl-stabilized combustor using a tunable diode laser," *Proc. Combustion Institute* **31** (2006) in press.
18. D.A. Rothamer and R.K. Hanson, "Visualization of high-speed flows using infrared planar laser induced fluorescence of CO and CO₂," *42nd Joint Propulsion Conf.*, American Institute of Aeronautics and Astronautics, AIAA-2006-4300.

TITLE: RAMJET RESEARCH

AFOSR TASK 2308BW

Principal Investigators: Campbell D. Carter
Mark R. Gruber
Skip Williams

Aerospace Propulsion Division, Propulsion Directorate (AFRL/PRA)
Air Force Research Laboratory
Wright-Patterson AFB OH 45433

SUMMARY/OVERVIEW

This research task includes work in three primary focus areas: (1) multiphase flows relevant to fuel injection into high-speed, oxidizing streams, (2) shock/boundary-layer interactions within the scramjet flowpath, and (3) multidisciplinary laser measurements for benchmarking modeling and simulation and for elucidating the physics of high-speed flows. Within each of these areas, there is a strong relevance to the scramjet propulsion system, and that relationship helps frame the context of our research. The motivation for this program is the need to develop the science basis to enable the design of high-speed, air-breathing propulsion systems. Lack of a science basis—and, in general, technology basis—is a limiting factor in design of scramjet vehicles. The approach will be to couple numerical computations and experimentation, to yield a thorough and fundamental understanding of each problem.

TECHNICAL DISCUSSION

Areas of focus in the past year have included the following:

- 1) Development/Application of laser diagnostic techniques for use in scramjet testing;
- 2) Study of fuel injection, gaseous and supercritical, and the development/testing of plasma-based flameholding/ignition schemes.

Three collaborations are ongoing with AFOSR extramurally funded personnel: Profs. R. Hanson (Stanford, tunable diode laser absorption for scramjets) M. Gundersen (Southern California, corona discharge ignition), and Y. Ju (Princeton, non-equilibrium discharges). Other university collaborators (and their respective contributions) include Profs. E. Gutmark (Cincinnati, advanced gaseous injector concepts), R. Pitz (Vanderbilt, NRC Summer Faculty, molecular tagging velocimetry), J. Driscoll (Michigan, URETI, cavity flameholding), J. Edwards (N.C.S.U., modeling of two-phase and supercritical injection), C. Tong (Clemson, generation of LES validation data). AFRL collaborations worth noting are those with Drs. J.T. Edwards (PRTG, supercritical fluids/injection) and F. Schauer (PRTC, PDE ignition). Drs. S. Lin, Taitech, and K.-Y. Hsu, Innovative Scientific Solutions, lead our in-house contractor efforts

For the second year, a focus for diagnostics development has been on hydroxyl tagging velocimetry (HTV), in collaboration with Prof. R. Pitz, Vanderbilt. Here, an ArF excimer laser beam (193 nm) is formed into a grid of beams (Fig. 1). The 193-nm radiation photo-dissociates water vapor to create H+OH; thus, if OH is probed at a later time—using PLIF—two velocity components can be obtained from the grid displacement (and potentially the out-of-plane component through a stereo measurement). For this second-year effort, a new set of optics was de-

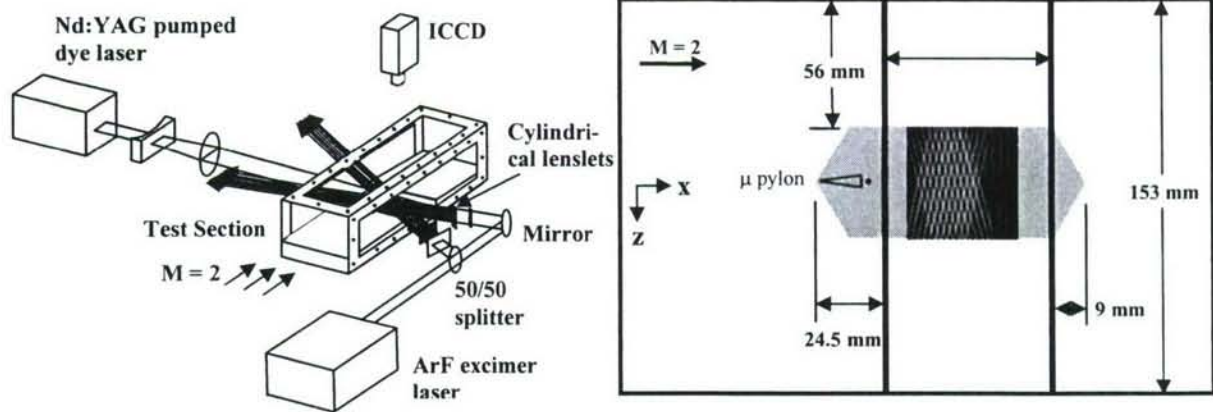


Fig. 1. HTV layout to probe M-2 flow over a cavity. Right, cavity layout with time-averaged grid. Gray region represents measurement domain. The micro-pylon injector was not installed for these measurements.

signed for generating an 11×11 grid (the previous was 7×7). Nearly the entire set of crossing points was then imaged, as shown in Fig. 2. Here, the left-hand figure shows velocities derived from the irregular grid of crossing points while the right-hand figure shows the regular grid with interpolated velocities. A comprehensive velocity map in and around the cavity with a M-2 freestream was thus obtained.

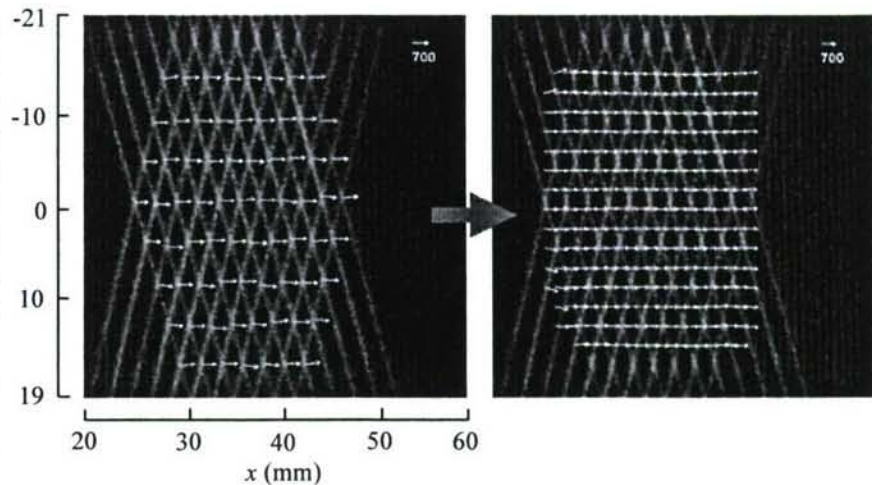


Fig. 2. Single-shot HTV velocity image with an irregular (left) and regular grid (right) in M-2 nonreacting cavity flow (at $y=15.6$ mm, where $z=0$ is the center-line of the cavity and $x=0$ is at the front face of the cavity).

Velocities range from $V=680$ m/s in the freestream to -100 m/s within the cavity. Furthermore, because the read step is based on OH A-X(1,0)/(1,1) excitation/detection—of the overlapped $Q_1(1)+R_2(3)$ line—rejection of laser scattering using Schott WG filters is good and near-wall regions can thus be probed. RMS values result from a combination of turbulence, determination of the crossing point (± 0.1 pixel for OH signal-to-noise, $SNR=10$), and timing jitter between the two lasers (± 8.5 ns); indeed, instrumental RMS values were small—contributing as little as ± 10 m/s uncertainty to freestream V_s —in spite of the small 193-nm energy per individual beam, ~ 1 mJ. Some issues, however, remain: grid signal strength within a re-

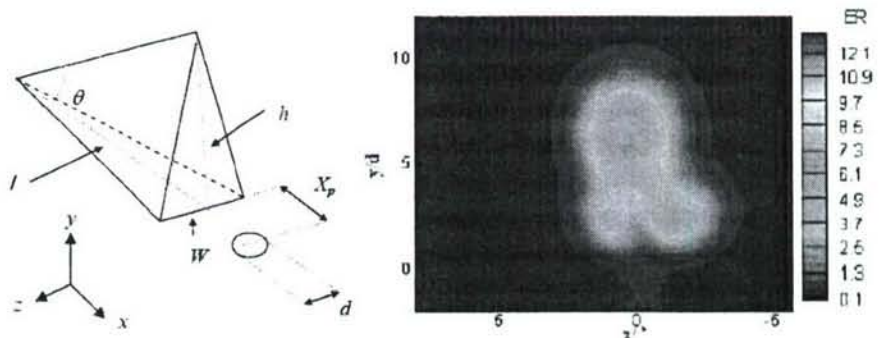


Fig. 3. μ -pylon schematic (left) and spanwise ER image from Raman scattering (right) for “wide” pylon ($h=6.3$, $W=2.5$, $l=11$, and $d=1.6$ mm). For the image the downstream x/d probe location was 12, while the momentum flux ratio was 4.

acting cavity flow, where there is abundant H_2O , is very weak, while OH grid signal strength within an ordinary hand-held torch is well above nascent OH levels from the flame. This appears to indicate that beam absorption (from hot H_2O or other species) is a limiting factor. Ideally, the laser is designed to operate narrowband, so that absorption by the ambient O_2 is mitigated through wavelength tuning but narrowband operation was not achieved.

Continuing from FY05 fuel injection research has been an important theme. Russian literature has shown advantages of fuel injection behind a μ -pylon (Fig. 3); however, detailed information on penetration and mixing is not available. Thus, spontaneous vibrational Raman scattering was employed to characterize the penetration/mixing. Here, a Spectra-Physics Millennia laser operating at 8 W ($\lambda=532$ nm) was transmitted across the span of the M-2 duct (see Fig. 1), while scattering from the gases was collected and dispersed within a Kaiser HoloSpec f/1.8 imaging spectrometer, equipped with a high efficiency holographic transmission grating; the Raman signals were then recorded with an Andor back-illuminated CCD array. Individual line images were collected (averaging for 20 seconds), and 2-D images, see Fig. 3, were acquired from a collection of the individual line images of N_2 and C_2H_4 . (the O_2 Raman line was beyond the spectral detection region). By measuring both fuel and air constituents, the mixing can be quantified, as shown in Fig. 3, with the 2-D map of the equivalence ratio; efficient collection of the scattering ensures a favorable *SNR*, even for sub-atmospheric tunnel conditions. Three μ -pylon injectors, differing in width or height—along with a single-hole injector—were characterized with Raman scattering (as they had been with NO PLIF previously). Fig. 4 shows a comparison of penetration height for two jet-to-freestream momentum flux ratios, $\bar{q}=1$ and 4. Clearly pylons are effective in improving the penetration, though this does come at the cost of decreased jet width.

In another effort, one continuing from last year, NO PLIF measurements of penetration with the so-called cascade injector have been compared to simulations using the VULCAN code and the low-diffusion flux vector split scheme. Here, the MUSCL parameter was set to 1/3 to minimize truncation error, and the Van Leer flux limiter was employed to enforce the *Total Variation Diminishing* condition. Each solution was advanced in time with a diagonalized approximate

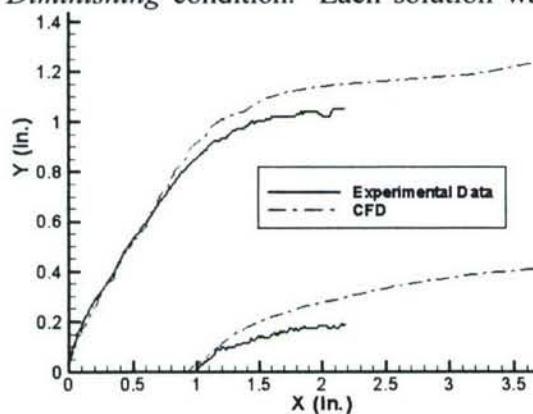


Fig. 5. Plume boundary from cascade injector: upper boundary=10% of local max; lower boundary=25% of local max.

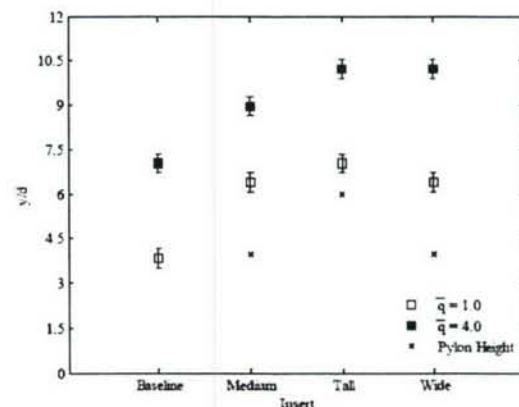


Fig. 4. Penetration normalized by injector hole diameter d for different pylon designs at jet to freestream momentum flux ratios of 1 and 4. The “baseline” is the simple round injector.

factorization scheme and with a Courant number ≈ 4 . Steady-state solutions were obtained for all cases considered and convergence was assessed by inspection of the L2-norm of the residual and the integrated mass flow rate. The majority of the calculations were performed with the Wilcox $\kappa-\omega$ turbulence model. The result for an injection pressure of 10 atm into a M-3 crossflow is shown in Fig. 5. It is seen that the penetration is about half the ~ 51 -mm duct height. The comparison between measurements and computations is good: the computed penetration is greater while the lateral spreading is less than measured. One interesting aspect is that while NO PLIF can be difficult to use for quantita-

tive mixing characterization due to the local variation in temperature and pressure, the boundary of the plume is not strongly affected. Furthermore, one can convert the computed injectant mole fraction into a synthetic LIF signal and thus compare measurements and computations.

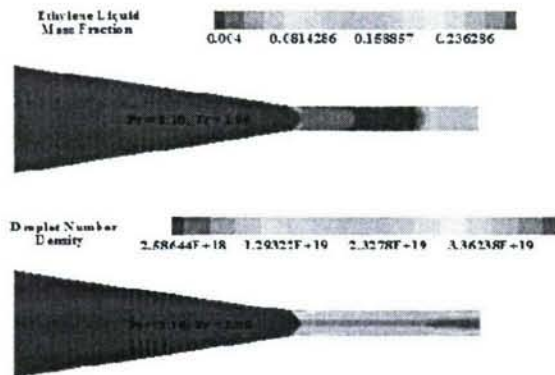


Fig. 6. Modeling of injection with $T_{inj} \approx T_{crit}$.

when $T_{inj} > T_{crit}$. A two-phase jet with a large quantity of nucleated droplets, however, can be generated when $T_{inj} \approx T_{crit}$ (see Fig. 6), and thus a longer length/time will be needed for the injectant to reach the desired fuel-air mixing state; further, the local density change of the injectant dramatically changes the injector operating characteristics. Onset conditions for condensation and the content and properties of the liquid phase within the injector are being studied, in collaboration with Drs. J.T Edwards (AFRL) and J. Edwards (N.C.S.U.). Modeling results (J. Edwards) within the injector are shown above (Fig. 6) for ethylene. As noted with $T_{inj} \approx T_{crit}$, droplets are formed; unfortunately, typical optical methods do not allow us to probe this jet; future efforts will explore alternatives to conventional diagnostics.

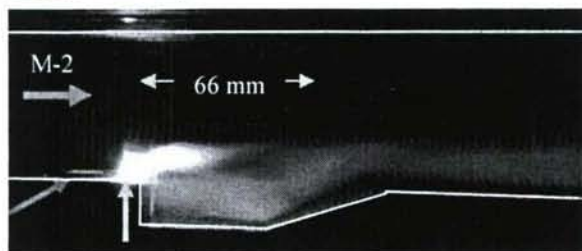


Fig. 7. Flame emission from injector-torch-cavity interaction in M-2 flow. Air, fuel, and plasma-jet flows are shown with blue, red, and yellow arrows.

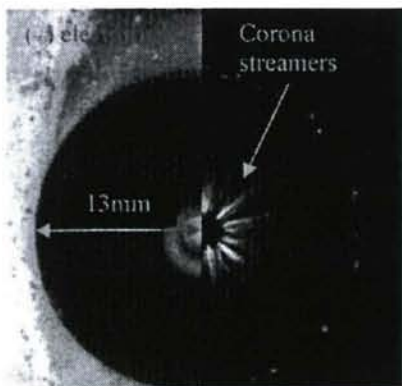


Fig. 8. Composite image: left, the electrode configuration without discharge; right, corona for single 100-ns exposure and 40-kV, 100-ns pulse.

Injection of a supercritical fluid into a superheated, low-pressure, high-speed crossflow—a problem relevant to much of the flight envelope—is vital to the scramjet operability, yet poorly understood. Extensive studies conducted in our laboratory have shown that the plume structure of supercritical fuel jets can be dramatically different from those of liquid or gaseous jets, due to the thermodynamic properties of the supercritical fluid and the occurrence of condensation. Typically, supercritical jets behave like ideal-gas jets

Another focus area is plasma-assisted ignition. Both the plasma jet and corona discharge are currently being studied: Fig. 7 shows a flame emission image from recent efforts investigating the coupling of the main fuel injector, the plasma torch (inline with the injector), and the flameholder cavity. For this work the cavity was independently fueled with ethylene and ignited with the torch; subsequently, the main fuel injector flow rate was increased and a substantial flame plume resulted. Indeed, without

the cavity the flame plume generated with the inline injector and torch is small, due to the likewise small flammable region (see Fig. 3, for example) within the fuel plume. However, the cavity promotes mixing of plume/air and further enhances plume flammability when the cavity's hot effluent mixes with the plume. Current efforts are underway to test our corona discharge system in a small-scale M-2 flow. The principal advantages of the corona-based system are that it can generate i) a discharge away from the wall (unlike the torch in a supersonic flow) and ii) radical and atomic species in a volume. As an example multiple streamers are shown for an axisymmetric electrode configuration for a single 100-ns discharge; this was one of several ignition configurations tested in a pulse detonation engine, PDE, in an effort to minimize the ignition delay.

LARGE EDDY SIMULATIONS OF SUPERCRITICAL MIXING LAYERS BASED ON SUBGRID SCALE MODELS EXTRACTED FROM DIRECT NUMERICAL SIMULATIONS

(Contract Number (with NASA): AFOSR-NMO715852)

Principal Investigator: Dr. Josette Bellan

Jet Propulsion Laboratory
California Institute of Technology
4800 Oak Grove Drive
MS 125-109
Pasadena, Ca 91109-8099

SUMMARY/OVERVIEW:

The objective of this study is the fundamental understanding of fuel disintegration and mixing in a supercritical environment (relative to the fuel) in order to determine parameter regimes advantageous to mixing. The approach is based on the future goal of developing a model for a supercritical, turbulent jet mixing with surrounding fluid. The method is one that combines the modeling of supercritical fluids with a systematic development based on the Large Eddy Simulation (LES) approach. This systematic development includes a consistent protocol based upon Direct Numerical Simulations (DNS) for developing a Subgrid Scale (SGS) Model appropriate to supercritical fluids, rather than choosing in an ad hoc manner an existing SGS model developed under assumptions inconsistent with supercritical fluid behavior. This SGS model should be used in future studies of supercritical turbulent jets utilizing the LES methodology.

TECHNICAL DISCUSSION

During this initial year, our activities focused on first deriving the correct Large Eddy Simulation (LES) conservation equations, through filtering, from the Direct Numerical Simulation (DNS) equations. These LES equations contain several types of terms; (1) terms which are akin to those of the DNS equations except that they are now functions of the filtered dependent variables, and thus are called “resolved” because the equations are solved at the scale of the filtered variables variation, (2) subgrid scale fluxes of momentum, enthalpy and species, and (3) terms that are gradients of the difference between a LES (i.e. filtered) quantity and the DNS mathematical form of the same quantity calculated as a function of the filtered variables, with other terms such as the difference between triple correlation terms also appearing in the energy equation. Type (1) terms are the basic terms in the LES equations. Type (2) terms are the classical subgrid scale (SGS) fluxes that are usually modeled in the LES equations to reproduce the behavior of the scales that have been filtered; below we discuss the modeling of these terms. Type (3) terms are usually neglected without justification other than to state that they are believed negligible – these are called “the LES assumptions”; we have found that for supercritical situations neglecting these terms is certainly not correct, as discussed below.

To evaluate the LES assumptions as well as to assess the mathematical form of the SGS fluxes, we used a DNS database of a temporal mixing layer portrayed in Fig. 1. The initial conditions for

the several DNS of the database are listed in Table 1, where p_r is the reduced pressure, which in all cases is approximately 2. In each DNS, a transitional state has been reached, and it is this transitional case that has been analyzed for SGS model development. The details of the DNS and the flow behavior have been described in detail in [1–3].

(i)LES assumptions. To analyze the terms in the LES equations, budgets of the filtered equations were calculated over the entire domain volume at the transitional states. It turns out that in the momentum equation, the leading terms are: the resolved convective term, the pressure gradient and the gradient of the difference between the LES pressure and the pressure computed using the real-gas equation of state (EOS) and the filtered variables. The next terms in order of magnitude are the resolved stresses, the subgrid stresses, and the gradient of the difference between the filtered stresses and the stresses calculated as a function of the filtered variables; these terms are at least an order of magnitude smaller than the leading terms. In the species equations, in decreasing order the leading terms are: convection, SGS flux and resolved flux which is of same order of magnitude as the gradient of the difference between the filtered flux of species and the flux calculated using the filtered variables. Similarly, in the energy equation, the convection term is the largest, followed by a group of terms at least an order of magnitude smaller: the pressure work, the SGS flux term and the gradient of the difference between the filtered heat flux and the heat flux computed as a function of the filtered variables. The next batch of terms in decreasing order of magnitude are the resolved viscous term, the gradient of the difference between the LES pressure and the pressure computed using the real-gas EOS and the filtered variables, and the triple correlation. The smallest terms are those resulting from the LES assumptions on the triple correlations and the stresses. It is thus clear that terms so far neglected in **ALL** existing LES under supercritical conditions are important in that they are of same magnitude as resolved terms. Because the budget represents a volumetric average, it is also clear that locally, at the high density-gradient-magnitude regions identified in all supercritical turbulent flows, both in DNS [1–3] and in experiments (e.g. [4,5]), the contribution of the so far neglected terms in LES may be entirely dominating all other terms.

These conclusions indicated that modeling of novel terms must be undertaken. As a model, expressions for these terms are first sought for the pressure. The idea was thus to employ a Taylor expansion of the pressure around the filtered set of variables as a representation of the large gradient differences between filtered and EOS pressure computed using the filtered quantity. However, the EOS is function of (ν, X, T) , ν the molar volume, X the molar fraction and T the temperature, whereas the conservation equations are solved for the conservative variables. Moreover, the thermodynamic related variances that are modeled in the SGS fluxes are associated with the mass fraction Y and the enthalpy H rather than the intrinsic thermodynamic variables (ν, X, T) . The quandary as to the choice of the appropriate variables for the Taylor expansion, with several possibilities tried, occupied a considerable portion of time, as did the derivation of the Jacobian for the change of variables from one set of dependent variables to another. Handling of the very large DNS datasets with the uncertain set of variables for the Taylor expansion also proved very difficult. It was finally decided to adopt a one-dimensional problem as a test case for assessing the Taylor expansion effectiveness for several sets of variables. In this problem, the X and T profiles are prescribed through a hyperbolic tangent as a function of an index in such a manner that p calculated through the EOS is constant. Results of the assessment are shown in Fig. 2. In Fig. 2a one can see that the Taylor series expansion in the variables (ν, X, T) is a much better approximation of the filtered p than is p computed from the EOS as a function of the filtered variables, and this holds whether the Taylor expansion is calculated analytically or numerically; therefore the principle of the Taylor

expansion for such calculation is validated. Figure 2b shows that the set (ρ, Y, H) is not as appropriate as the set $(\rho, \rho Y, \rho E)$ for approximating the filtered pressure through the Taylor expansion. This observation indicates the set of variables to choose for the transformation from the intrinsic set, a task that is currently underway as a precursor for *a priori* assessment of the models on the databases.

An evaluation on the DNS database of a model previously used for the filtered triple correlation difference under atmospheric conditions [6] proved that the previous model remains valid under supercritical conditions.

(ii) **SGS fluxes.** Three models were tested for the SGS fluxes: (1) the Smagorinsky (SM) model with the trace computed using the Yoshizawa (YO) model, (2) the Scale Similarity (SS) model, and (3) the Gradient (GR) model of [7]. These tests were *a priori*, meaning that the mathematical form was tested (the correlation) and a proportionality coefficient was computed (through a least square fit) using the DNS database. An example of this assessment is shown in Fig. 3 for the SGS species flux for the OHe600 layer, which is that having the highest Reynolds number at transition. The assessment is shown for the larger of the two grid filters considered, and for the SS model at two test filters, model SS1 (test filter has same size as the grid filter) and SS2 (test filter is twice the size of the grid filter). The results are typical of the findings for all SGS fluxes. The SM model shows poor correlation with the exact SGS fluxes, while the GR and SS models have high correlations. Furthermore, the calibrated coefficients for the GR and SS models yielded good quantitative agreement with the SGS fluxes. However, comparison among the layers in the DNS database revealed that statistically, the calibrated coefficients were not generally valid, indicating that most likely a dynamic strategy would be necessary for computing these coefficients in *a posteriori* calculations.

1. Okong'o, N. and Bellan, J., *J. Fluid Mech.*, 464, 1-34, 2002
2. Okong'o, N., Harstad, K. and Bellan, J., *AIAA J.*, 40(5), 914-926, 2002
3. Okong'o, N. and Bellan J., *Phys. Fluids*, 16(5), 1467-1492, 2004
4. Chehroudi, B., Talley, D., and Coy, E., AIAA 99-0206
5. Oschwald, M. and Schik, A., *Experiments in Fluids*, 27, 497-506, 1999
6. Okong'o, N. and J. Bellan, J., *J. Fluid Mech.*, 499, 1-47, 2004
7. Clark, R., Ferziger, J., and Reynolds, W., *J. Fluid Mech.*, 91(1), 1-16, 1979

Name	HN400	HN500	HN600	HN800	OH750	OH550	OH500	OHe600
Species 2	C ₇ H ₁₆	C ₇ H ₁₆	C ₇ H ₁₆	C ₇ H ₁₆	O ₂	O ₂	O ₂	O ₂
Species 1	N ₂	N ₂	N ₂	N ₂	H ₂	H ₂	H ₂	He
T ₂ (K)	600	600	600	600	400	400	235	235
T ₁ (K)	1000	1000	1000	1000	600	600	287	287
ρ_1/ρ_2	12.88	12.88	12.88	12.88	24.4	24.4	24.51	12.17
p ₀ (atm)	60	60	60	60	100	100	100	100
Re ₀	400	500	600	800	750	550	500	600

Table 1. Initial conditions of the Direct Numerical Simulations (DNS) database. In all simulations $M_{c,0} = 0.4$, $\delta_{w,0} = 6.859 \times 10^{-3}$ m (see Fig. 1). For the C₇H₁₆/N₂ layers, $p_r = 2.22$ and $((\rho_2 U_2)/(\rho_1 U_1)) = 5.276$; for the O₂/H₂ layers, $p_r = 2.01$ and $((\rho_2 U_2)/(\rho_1 U_1)) = 5.001$ for OH550 and OH750, and $((\rho_2 U_2)/(\rho_1 U_1)) = 4.951$ for OH500 and for the O₂/He layer $p_r = 2.01$ and $((\rho_2 U_2)/(\rho_1 U_1)) = 3.500$.

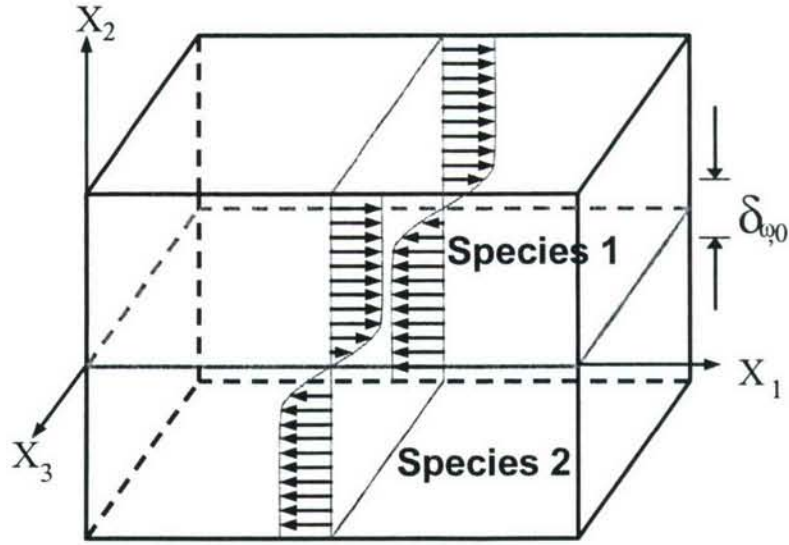


Figure 1. Mixing layer configuration for the DNS listed in Table 1.

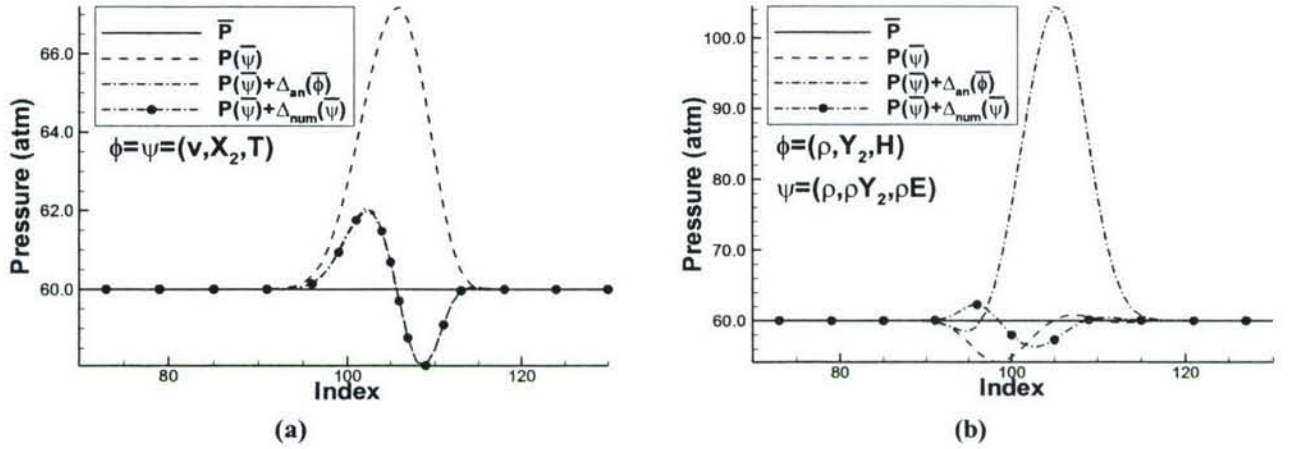


Figure 2. Filtered pressure and pressure computed as a function of the filtered field and pressure computed as a Taylor expansion of different sets of variables. (a) Intrinsic thermodynamic variables, (b) Two other sets of thermodynamic variables.

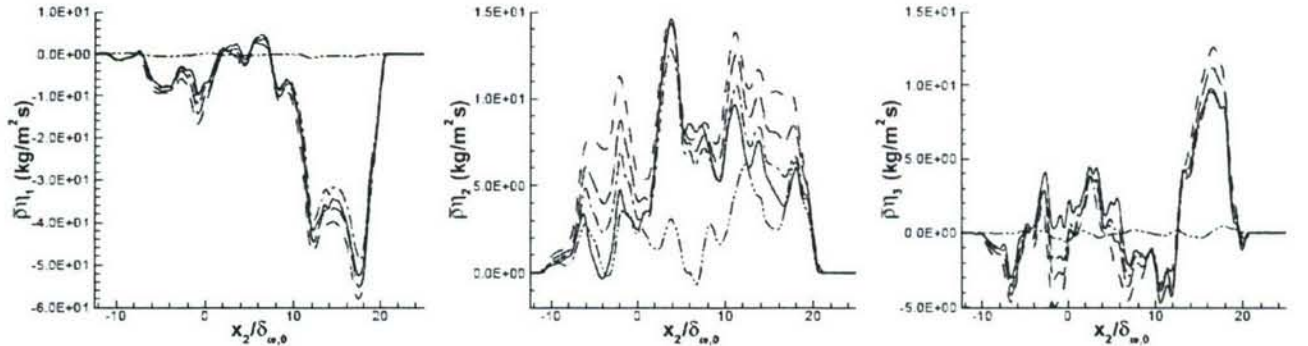


Figure 3. *A priori* assessment for the species SGS flux computed on the DNS database OHe600 (Table 1). The legend is: --- Exact; -- $\tau \tau$ -- GR, $C_{GR}=0.1180$; - - $\tau \tau$ - - SM, $C_{SM}=0.0622$; ---- SS1, $C_{SS1}=1.4671$; - - - SS2, $C_{SS2}=0.5369$.

STUDIES IN FLAME PROPIGATION AND BLOWOUT

Supported by ARO Grant/Contract Number: W911NF-05-1-0045

Principal Investigator: Kevin M. Lyons

North Carolina State University
Department of Mechanical and Aerospace Engineering
Raleigh, NC 27695-7910
lyons@eos.ncsu.edu

SUMMARY/OVERVIEW:

This report outlines our most recent research work on the topic of upstream flame propagation and blowout in hydrocarbon jet flames. Outlined specifically are the recent elements of the research for the study of fundamental structural characteristics of jet flames and related flame/spray/flow interactions. Specifically, the scope encompasses further optical imaging investigations of flame structure and behavior, and an exploratory study of the effects of co-flow air on extinction and blowout. Analysis of the results of experiments to understand the behavior of gaseous and spray flame counterparts is the main deliverable. The methodology of the research is largely experimental, emphasizing the application of optical diagnostic techniques to instantaneously visualize reaction zones. The main efforts to report since the last update are the following: 1) Studies have been launched that examine the development of combustion in an initially non-reacting methane jet after ignition at a downstream location and 2) The driving mechanisms that cause jet-flame blowout, particularly in the presence of air co-flow, have been investigated. This work attempts to determine the role of fuel velocity and air co-flow in the blowout phenomenon.

TECHNICAL DISCUSSION:

1) Observations on Upstream Flame Propagation in Ignited Hydrocarbon Jets

While laminar lifted jet flames have been extensively investigated both analytically and experimentally, transitional and turbulent regions have received less attention. The goal of this study is to investigate downstream ignition in initially non-reacting turbulent hydrocarbon jets (Lyons and Watson 2001) issuing with air co-flow. The farthest distance from the burner at which the flame will propagate upstream to its stable position upon application of an ignition source, hereafter referred to as the “upper propagation limit”, is determined and presented for eleven different cases. The nine prime cases consisted of three jet Reynolds numbers at three co-flow velocities. In addition to the nine prime cases two outlier cases were also examined. It is seen that there is an inverse relationship between the upper propagation limit position and the Reynolds number. There is also an inverse relationship between the upper propagation limit and the co-flow velocity. The effect of co-flow is partially explained by the approach presented by Han and Mungal (2000). The overall goal is to report what these results imply about the stabilization and propagation of turbulent lifted jet flames.

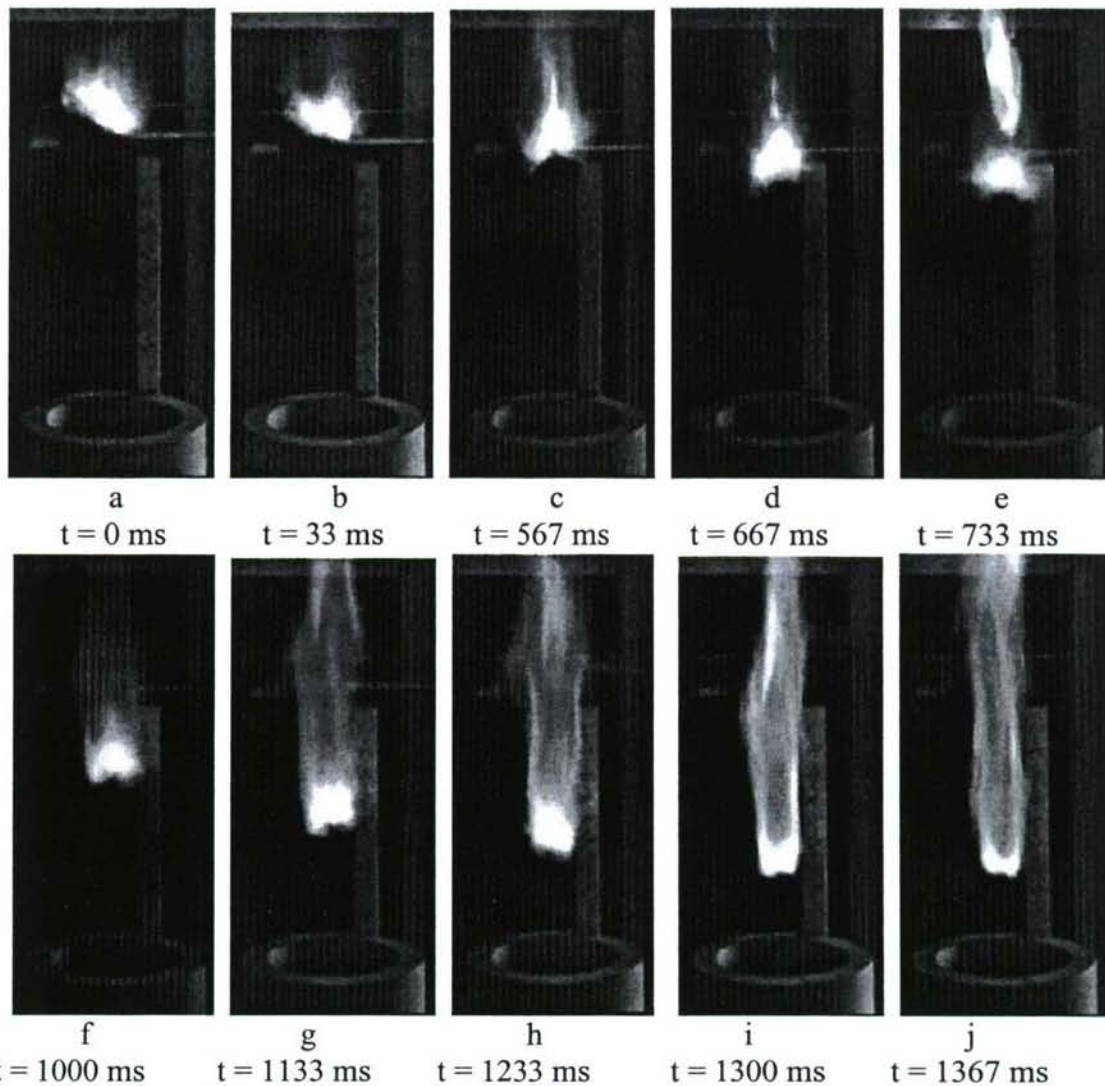


Figure 1: Propagation of methane flame from upper propagation limit (23.7 cm) to stable height (7.62 cm).

Figure 1 is the depiction of a methane flame propagating from its upper propagation limit to its stable height. The fuel velocity for this case was 35.6 m/s and there was no co-flow present. The Reynolds number for this case was 8242. These particular conditions caused the flame to be lifted from the burner. The height at which the flame stabilized at was 7.6 cm downstream from the nozzle. The upper propagation limit for this case was 23.7 cm (this is the axial position above which (further downstream) a locally ignited region with the same ignition source cannot counter-propagate against the incoming flow and the local ignition kernel goes out/blows off – ignition attempted closer to the nozzle than 23.7 cm permits the reaction zone to propagate upstream).

At 0 ms, a, the flame is unable to sustain itself. The ignition source is required to keep the flame burning locally. In c the flame begins to propagate on its own. The total time for the flame to fully propagate from the upper propagation limit to its stable height of 7.62 cm is 800 ms. Many cases have been examined for various jet velocities, co-flow velocities and work to understand the data is ongoing (McCraw et al. 2006).

2) Effects of Co-flow on Turbulent Lifted Flames near Blowout Condition

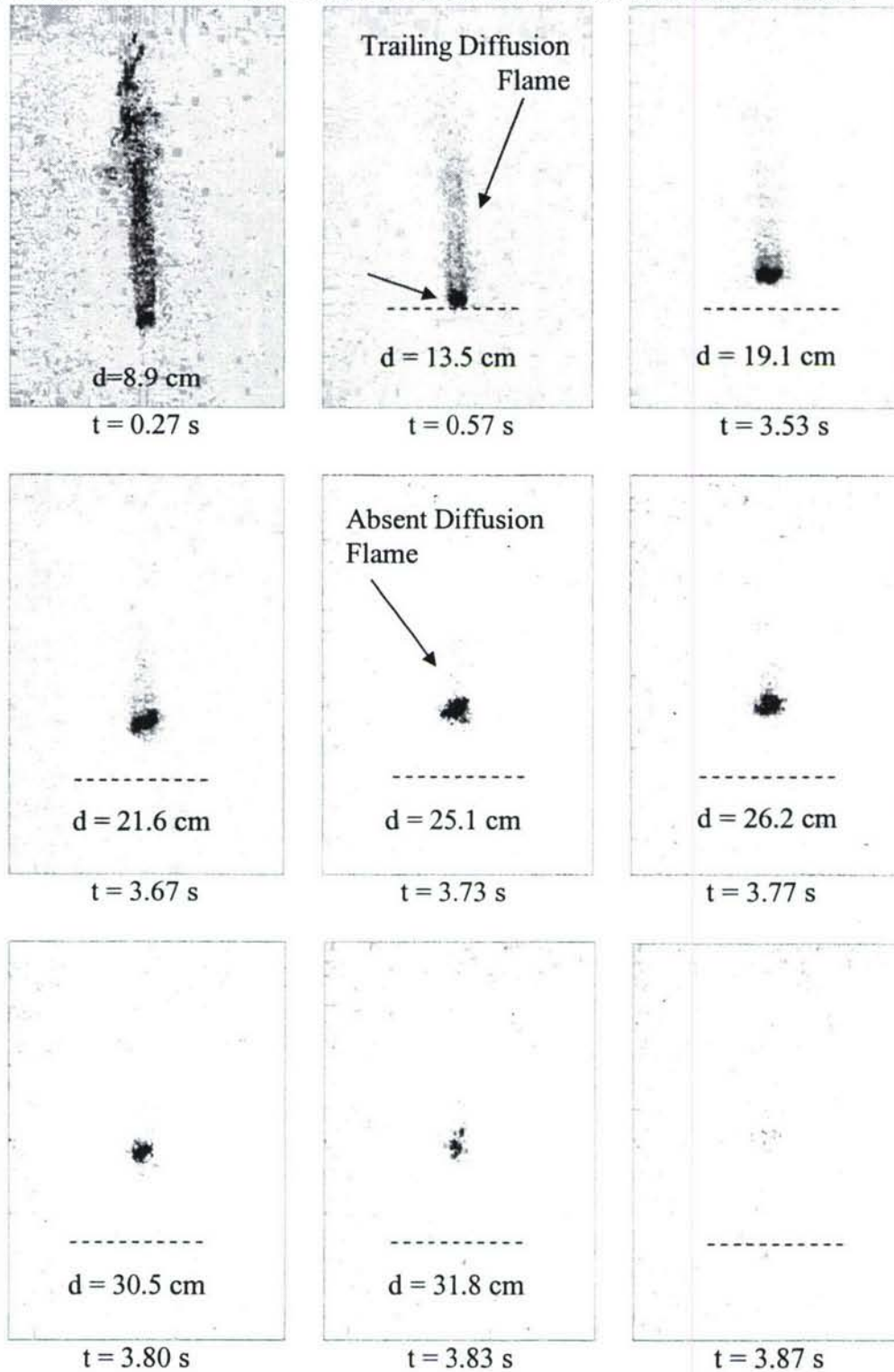


Figure 2. Images after re-ignition at the fuel nozzle at $t = 0$ with d indicating the distance downstream of the flame front from the nozzle. The nozzle is within the image borders but is not visible in these enhanced images. The dotted line indicates the position of the meta-stable flame front.

The driving mechanisms that cause jet-flame blowout, particularly in the presence of air co-flow, are not completely understood. This work attempts to determine the role of fuel velocity and air co-flow in the blowout phenomenon. The results of video imaging of the reaction zone upon removal of the ignition source at blowout conditions are characterized. Data from a series of experiments are collected at various co-flow and jet velocities. Images are used to ascertain the changes in the leading edge of the reaction zone prior to flame extinction. These changes can help develop a physically-based model to describe jet-flame blowout.

Figure 2 contains a sequence of images of the flame re-ignited at the nozzle with 0.55 m/s co-flow and 34.3 m/s fuel. After 0.57 seconds, the flame has reached a meta-stable position of 135 mm. It stays at this lifted height for approximately 3 seconds, at which time the trailing diffusion flame begins to disappear indicating the beginning of the blowout sequence. The diffusion flame is absent 3.73 seconds after re-ignition and blowout occurs 0.14 seconds later with complete loss of the leading edge reaction zone. The duration at the meta-stable lifted position appears random. However, the behavior of the flame beyond this position is independent of co-flow or fuel velocity. Analysis of the blowout conditions are currently underway utilizing the approach of Tieszen et al. (Moore et al. 2006).

References

- Broadwell, J. E., Dahm, W. J. A., and Mungal, M. G., 1984, Blowout of Turbulent Diffusion Flames. *Twentieth Symposium (International) on Combustion*, The Combustion Institute, Pittsburgh, pp. 303-310 (1984).
- Dahm, W.J.A. and Dibble, R.W., Coflowing Turbulent Jet Diffusion Flame Blowout. *Twenty-Second Symposium (International) on Combustion* : 801-808 (1988).
- Han, D. and Mungal, M. G., Observations on the Transition from Flame Liftoff to Flame Blowout. *Proc. Combust. Inst. 28th Symposium (International) on Combustion*, The Combustion Institute, Pittsburgh, pp. 537-543 (2000).
- Lyons, K. M., and Watson, K. A., Visualizing Diffusion Flame Formation in the Wake of Partially Premixed Combustion. *J. Energy Resour. Technol. Trans. ASME* 123: 221-227 (2001).
- McCraw, J. L., Moore, N. J. and Lyons, K.M., Observations on Upstream Flame Propagation in Ignited Hydrocarbon Jets, Western States Meeting Of Comb. Institute, Boise 2006 (and expanded version in review, *Flow Turbulence and Combustion*).
- Moore, N. J., McCraw, J. L. and Lyons, K. M., Effects of Co-flow on Turbulent Lifted Flames near Blowout Conditions, Western States Meeting Of Comb.Institute, Boise 2006.
- Savas, O and Gollahalli, S. R., Stability of Lifted Laminar Round Gas-Jet Flame. *J. Fluid Mechanics*, 165, pp. 297-318 (1986).
- Su, L.K., Sun, O. S. and Mungal, M. G., Experimental Investigation of Stabilization Mechanisms in Turbulent, Lifted Jet Flames, *Combust. Flame*, 144, pp. 494-512 (2006).
- Terry, S. D. and Lyons, K. M, Low Reynolds Number Turbulent Lifted Flames in High Co-Flow, *Combustion Science and Technology* 178 (1) 1-22 (2006).
- Tieszen, S. R., Stamps, D. W., and O'Hern, T. J., A Heuristic Model of Turbulent Mixing Applied to Blowout of Turbulent Jet Diffusion Flames, *Combustion and Flame*, 106 pp. 442-466 (1996) .

LES OF SOOTING FLAMES

Grant/Contact Number: DAAD19-03-1-0049

Principal Investigator: Suresh Menon

School of Aerospace Engineering
Georgia Institute of Technology, Atlanta, GA 30332

SUMMARY/OVERVIEW

Prediction of soot formation in turbulent flames is a major challenge due to the chemical complexity and the barely understood coupling between soot formation and the other flow transient processes. The current objective is to develop a unified, general methodology for large-eddy simulation (LES) of soot formation and transport in turbulent flames.

TECHNICAL DISCUSSION

A subgrid model for soot dynamics is developed for LES, which uses the method of moment approach with Lagrangian Interpolative closure (MOMIC) so that no a priori knowledge of the particle distribution is required. The non-coalescent limit, as well as the soot transport by diffusion and thermophoretic forces is included. The soot model is implemented within a subgrid mixing and combustion model based on the linear-eddy mixing (LEM) model so that gas phase reaction-diffusion and soot related MOMIC coupling is implemented without ad hoc filtering. Relatively detailed multi-species ethylene-air kinetics mechanism [1] is employed for gas phase combustion, and is combined with a four-step soot formation model. The LES model is used to study the effect of turbulence and the C/O ratio effect on soot production in a turbulent premixed flames in the thin reaction zone regime. In addition, a study is conducted to evaluate the effect of using a constant versus variable transport properties for the gas phase species. Finally, two non-premixed cases, sooting and non-sooting are compared with experiment to validate the model.

The general methodology of the subgrid model is shown in Fig. [1]. The soot nucleus is assumed to be composed of two carbon atoms. Acetylene is decomposed to give a soot nucleus and hydrogen dioxide around 1000 K as shown in Fig. [2]. Soot nuclei collide together to coalesce and give larger soot particles. During which, oxidative attack of oxygen and hydroxyl continue to decay the soot surface and reduce the soot particle mass by oxidizing carbon atoms to carbon monoxide and hydrogen radicals. After a transient period the soot particle diameter exceed a certain threshold, after which coalescent collision is not physical anymore and the soot particles start to agglomerate. These processes are coupled with soot diffusion, gas phase chemistry and thermophoretic transport due to temperature gradients. The thermophoretic forces and soot diffusion has been implemented based on a recent generalized study that satisfy the specular as well as the diffuse collision limits in the free molecular regime [2].

(a) LES of Turbulent Premixed Ethylene Flames

Earlier studies [3] addressed the effect of C/O ratio and turbulence on soot formation in a turbulent premixed flame. Two studies have also been conducted to compare the effect of using detailed variable binary diffusion coefficients [1]. Since, the critical C/O ratio for soot formation in ethylene/air premixed flames is around 0.6, the C/O ratio for both cases is 0.677. The test conditions for these cases are summarized in Table [1]. The grid resolution is a 64x64x64 cube

of a domain of $1.5 \times 1.5 \times 1.5$ mm, with 12 LEM cells. The LEM resolution is chosen to capture the flame thickness and to resolve close to the Kolomogorov length scale ($1-2 \eta$).

The turbulent flame is highly strained and the curvature effect changes the species profiles according to the ratio of the thermal to the molecular diffusivity. The flame stretch is induced by the flow non-uniformity (strain effect) and the curvature due to the wrinkling of the flame surface area, which increases its reaction front. When the flame has negative curvature (concave towards the reactants) the mass is focused towards the products side, and the heat is focused inwards to the reactants side. If the Lewis number (Le) is greater than unity, the thermal diffusivity will increase the temperature in the preheat zone and the flame burns strongly with a higher flame temperature. These observations are confirmed in Fig. [3], where the C_2H_4 reaction rate and temperature profile across a concave and a convex flame elements are plotted. The flame shows higher temperature and reaction rate across the concave element. Figure [4] shows the PDF of mean curvature for both test cases. The figure shows that the constant diffusion flame is skewed towards the positive curvature (convex towards reactants), while the variable diffusion case is more symmetric with higher probabilities in the negative curvature side. The wide range of curvature indicates the turbulence effect on the flame structure and the surface area. In addition, the variable diffusivity case shows wider tails and no sharp peaks in the middle. The wider tails indicates the presence of more flames close to the spherical and saddle shapes. The mean in both cases is around zero. The variable diffusion case predicts higher peak value of the soot volume fraction. However, the constant diffusivity case shows a slightly wider profile for the temperature and the soot volume fraction. The wider profile is a direct consequence of the higher Le (higher thermal diffusivity). The higher soot production is a direct result of the higher surface growth rate. Figure [5] shows that the higher relative thermal to molecular diffusivity in the constant diffusion coefficients increases the collision frequency and the coagulation rate and that in turn reduces the number density and the soot surface growth rate.

(b) LES of Turbulent Premixed Flames

The eventual goal of the current development is to study soot formation in realistic turbulent non-premixed flames of practical interest. As a precursor to this goal, two studies are conducted for a non-premixed hydrocarbon flame. A non-sooting methane swirling, bluff body stabilized flame is used for initial validation. Figures [6] show the centerline mean axial velocity component for three simulated experimental flames [3]. The centerline shows existence of a centerline recirculation bubble for the SM1 flame. The rate of decay of the central jet is captured reasonably using the LEMLES approach. The flame and flow structure visualization is shown in Figs [7, 8] for the SM1 and SMA2 flames, respectively. More discussion are given elsewhere [5]. A base recirculation zone RZ is established for the SM1 flame in addition to a centerline recirculation bubble VBB. In-between the base RZ and the swirl-induced VBB, there exists a collar-like vertical shear region with high rotational (azimuthal) velocity as the separated shear layer first turns towards the centerline and then diverges around the VBB. The contour plots of constant mean ϕ are superimposed to show the flame structure. The black boundary is the stoichiometric line. In comparison, the SMA2 flame shows only a single elongated RZ downstream of the bluff body and no VBB is observed due to the higher fuel jet axial velocity.

The case is a sooting ethylene jet flame [6]. This study is still underway. Figure [9] shows the iso-surface for the axial velocity component. The jet spread rate grows roughly linear with the axial distance, which is consistent with the classical results for the axisymmetric turbulent jet. Figure [10] shows the flame structure on a median cross section and the soot mass fraction contours. The flame is slightly lifted, which is similar to the experimental results, soot is formed at the centerline far downstream. More details will be reported soon.

SUMMARY and FUTURE PLANS

The soot validation jet case will be continued to compare with the experimental jet results. The effect of coagulation and soot diffusion, thermophoresis and agglomeration is all under current investigation as well. Finally, the soot model will be connected to a Lagrangian approach to track the soot particles formation and destruction history.

Flame	C/O	Re	Da	Ka	S_L (m/sec)	δ_F	u'	l (mm)	u'/S_L	l/δ_F	η (mm)
F1	0.67	271	1.15	23.76	0.24	0.11	2.86	1.47	11.9	13.71	0.02

Table [1]

REFERENCES

- [1] T.F. Lu and C.K. Law, *Proc. Combust. Inst.*, 30 (1) (2005) 1333-1341
- [2] Zhigang Li and Hai Wang, *Physical Review E*, 70, 021205 (2005)
- [3] <http://www.aeromech.usyd.edu.au/thermofluids/switl.html>, University of Sydney, 2005
- [4] H. El-Asrag, S. Menon, AIAA-2006-153, 2006.
- [5] H. El-Asrag, S. Menon, *Proc. Combust. Inst.*, accepted, 2006
- [6] B. Yang, U. Koylu, *Combust. Flame*, 144 (2005) 55-65

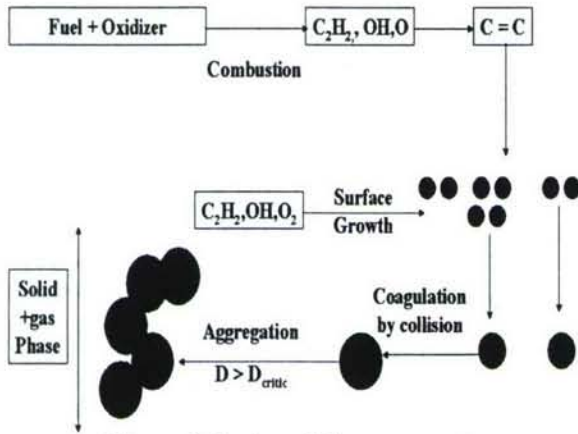


Figure 1 Soot model components

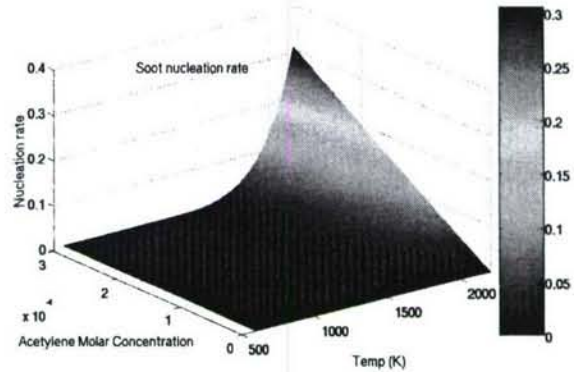


Figure 1 Nucleation rate (vertical axis) variation with temperature and acetylene molar fraction

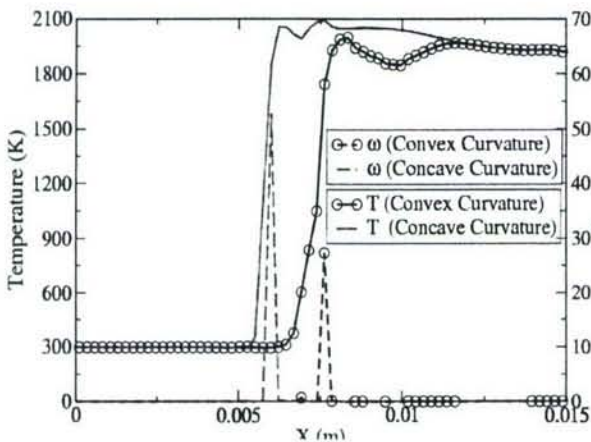


Figure 2 Temperature and ethylene reaction rate at a concave and convex flame segments with variable diffusion coefficients

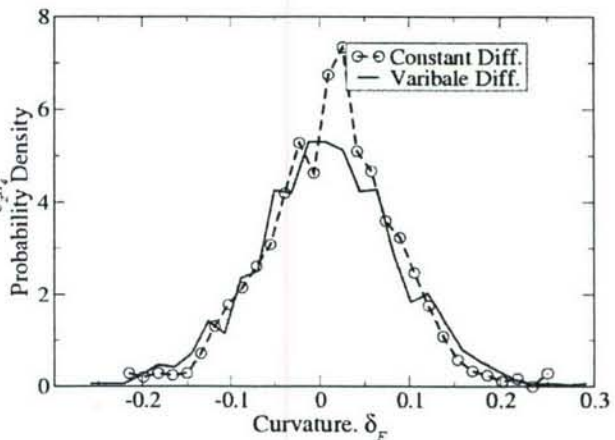


Figure 3 Mean Curvature probability density function (PDF)

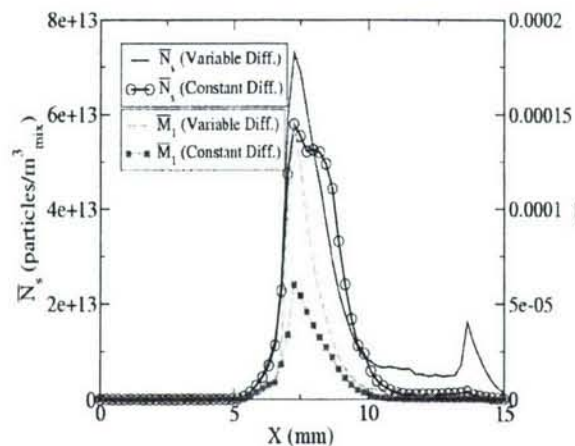


Figure 5 Mean soot number density (left) and average mass per unit volume (right)

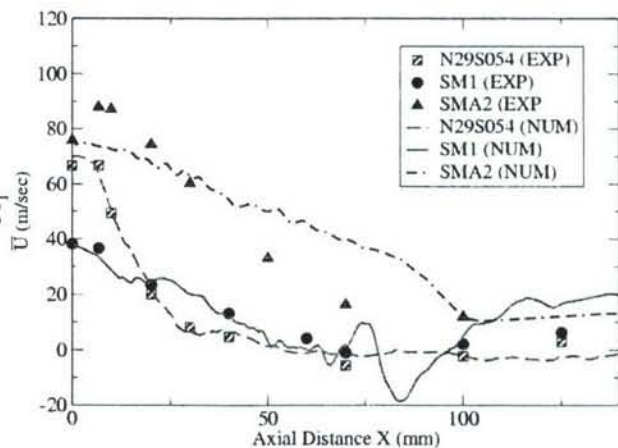


Figure 4 Centerline variation of time averaged axial velocity

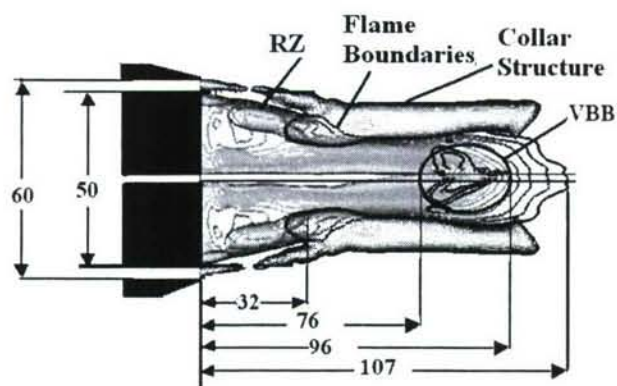


Figure 6 SM1 flame flow field and flame structure

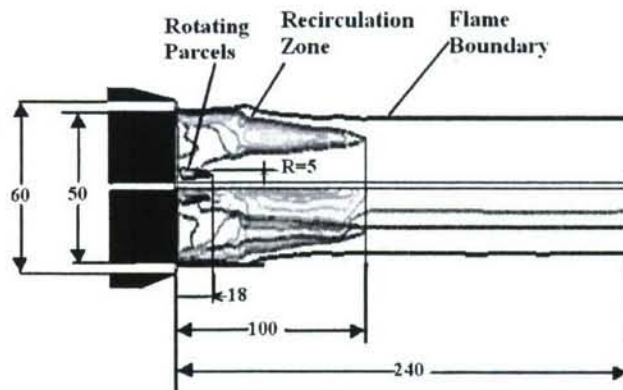


Figure 8 SMA2 flame flow field and flame structure

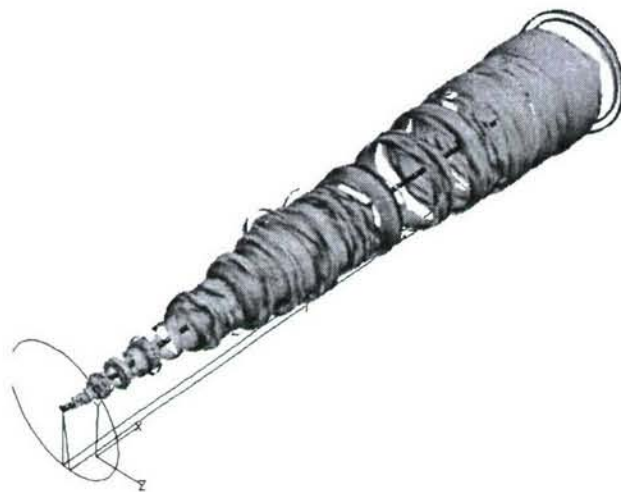
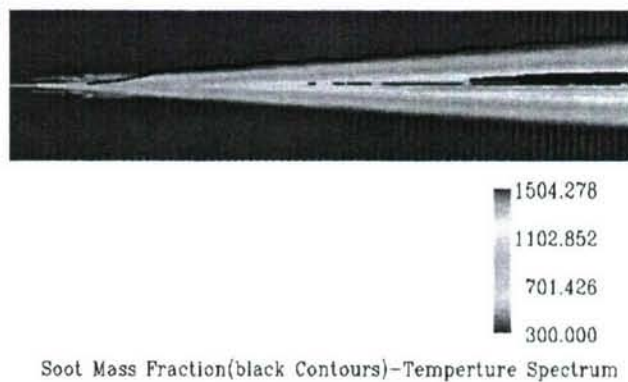


Figure 8 Axial velocity iso-surface



Soot Mass Fraction(black Contours)-Temperature Spectrum

Figure 7 Temperature (spectrum) and soot contours

FORMATION OF SOOT IN HIGH-PRESSURE DIFFUSION FLAMES

(Grant/Contract Number W911NF-05-1-0060)

Principal Investigator(s): William Roberts

Dept. of Mechanical and Aerospace Eng.
North Carolina State University

SUMMARY/OVERVIEW:

Diesel engines continue to be the primary powerplant for the Army, both for propulsion and power generation. These engines operate at high pressures to maximize thermodynamic efficiency. Pressure has a direct effect on the peak temperature, the thermal and species gradients, and the species diffusion coefficients, all of which in turn affect the formation of soot in these flames. However, high-pressure flames have received very limited attention, primarily due to the experimental difficulty in operating these flames. Measurements of flame-generated species (using both sampling and non-intrusive optical diagnostics) will be made to help illuminate the chemistry-fluid mechanics interaction and the role of transport at high pressures. The overall goal is to reduce soot emission from these diesel powered vehicles in an effort to minimize their thermal signature.

TECHNICAL DISCUSSION

Specific Second Year Objectives

The objectives for the second twelve months of this effort were to (1) determine the effect of various diluents (nitrogen, argon, helium, and carbon dioxide) on smoke point in ethylene and methane flames up to 8 atm pressure, (2) to determine the reason for the discrepancy between smoke point heights measured in this flame compared with measurements by others in nominally similar flames, (3) begin to make soot surface temperature measurements using pyrometry, (4) design and build sampling system for extractive measurements of stable species.

Experimental Apparatus

The apparatus used for this experiment, shown in Fig. 1, is a classic over-ventilated Burke-Schumann flame inside a water-cooled pressure vessel that is rated at pressures up to 30

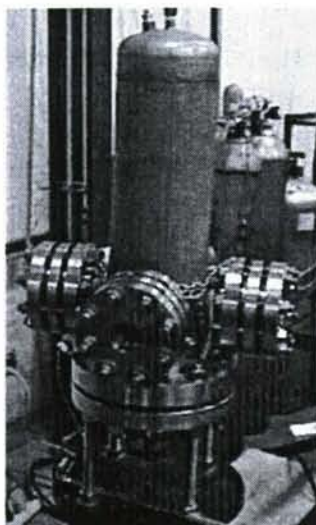


Figure 1. High pressure burner.

atmospheres. Surrounding the 4.5 mm fuel tube is a 65 mm co-flow, and this is all housed in a 380 mm tall quartz chimney. A ceramic honeycomb insert straightens the air co-flow surrounding the fuel tube. The fuel tube is filled with super fine grit steel wool to make the fuel flow rate less sensitive to pressure fluctuations upstream. {The addition of this steel wool flow straightener in the fuel tube turns out to be critical in the behavior of the smoke point with dilution and pressure.} To ignite the flame within the pressure vessel, an electrode is installed and used to produce a spark against the lip of the fuel tube. The vessel has three non-intrusive glass windows to allow for optical viewing and diagnostics. Due to the high sooting tendencies of the fuels used, and the effect pressure has on these tendencies, the vessel has air ports at the windows to purge the area and prevent soot accumulation on the window surface.

To understand the effect of the flow straightener in the fuel tube, a larger burner was used at atmospheric pressure, with a fuel tube diameter of 11.9 mm and an air co-flow diameter of 101.6 mm. For all cases at velocity matched fuel and air flow rates, the flame is highly overventilated. At stoichiometric conditions for ethylene burning in air there is a 1:14.3 fuel-to-air mole ratio. For the current research, conducted at atmospheric conditions, with a fuel-to-air velocity ratio of 0.37 (which is the smallest fuel-to-air velocity ratio tested) the smoke point was reached with a volumetric fuel flow rate of 147 sccm. The air flow rate for a velocity ratio of 0.37 was 28 slpm, which is more than an order of magnitude larger than necessary to over-ventilate the flame. Thus, all flames studied here, regardless of fuel-to-air velocity ratio, were highly over-ventilated. In order to achieve a plug flow exit velocity profile, glass beads, each with a diameter of 3 mm, were placed in the fuel tube to a height of 300 mm. To achieve a parabolic exit velocity profile, the beads were removed from the fuel tube. A combination of screens and ceramic honeycomb was used to ensure a uniform air co-flow exit profile. A quartz chimney, with an inside diameter of 120 millimeters, protected each flame from the perturbations of the ambient air surrounding the burner. Images of each flame were taken at the flame's smoke point with a digital camera.

Results and Discussion

Figure 2a-b shows the effect of dilution level on the smoke point by plotting the reactant (fuel and various diluents) volumetric flow rate as a function of the inverse temperature for ethylene and methane flames in air at 1 and 8 atmospheres, respectively, in log-linear space. The temperature is calculated using a standard chemical equilibrium calculator. As seen in this figure, at 8 atmospheres, the smoke point for methane is higher than that for ethylene and both increase with dilution level. From this figure, it is clear that the actual diluent is not as important as the dilution level. This is contrary to what has been reported previously by McLintock [1] and Schug et al. [2], where they observed a distinct difference between the diluents, with the soot suppression ability scaling with the heat capacity (i.e., CO₂ being most effective and He being least effective). It is believed that this is an effect of the velocity ratio and the shear layer. Lin and Faeth [3] have shown that the velocity ratio has a strong influence on the smoke point. At atmospheric pressure in undiluted ethylene flames, the current research measured the smoke point at various velocity ratios and observed a dramatic difference. For instance, at a velocity

ratio of unity, the fuel flow rate at the smoke point is 140 sccm, but at a fuel to air velocity ratio of 1.2 the fuel flow rate increases to 175 sccm. At a fuel to air velocity ratio of 0.5, the fuel flow rate decreases to 105 sccm. In the work of McLintock and Schug, the air flow rate was held fixed at a certain value throughout the experiments, so in addition to the velocity ratio being non-unity, but it changed for each value of dilution. The slope of the fuel flow rate to diluent flow rate relationship is shown in Table I with the initial velocity ratio listed (it is not known in the work by Schug as they only state that the flame is highly over-ventilated.) In this table, the slope for the velocity-matched case is given as a best-fit second order polynomial, while the other entries are for a fixed air flow rate. It is clear from this table that the velocity ratio plays a major role in determining the diluents ability to suppress soot formation.

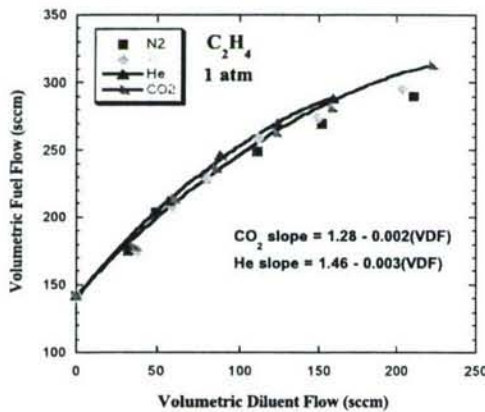


Fig 2a. Ethylene at smoke point at 1 atm vs dilution

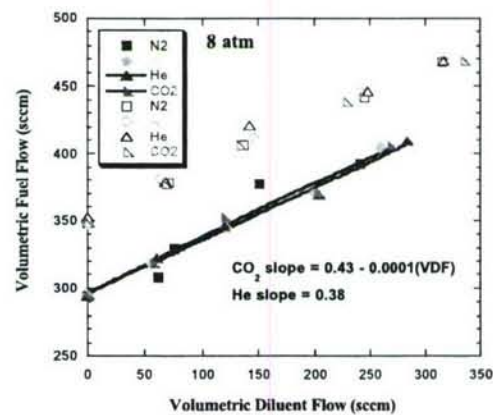


Fig 2b. Ethylene at smoke point at 8 atm vs dilution

Table I

Initial f-a velocity ratio	CO ₂ slope	He slope	Reference
1.38	0.75	~0	McLintock
Unknown	1.10	0.2	Schug et al
1	1.28 - 0.002	1.46 - 0.003	This work
0.5	0.45	0.273	This work
1.2	0.33	0.36	This work

The visible flame height is measured from digital photographs and then normalized by the fuel tube diameter of 4.5 mm. The flame height is a strong function of the fuel to air velocity ratio, and for all of these measurements, the ratio is unity. Dilution has a much more pronounced effect on the lengthening of the flame at low pressures and virtually no effect at 8 atmospheres. It is also observed in these figures that the actual diluent is of much less importance than the dilution level, as no clear trends with heat capacity, thermal conductivity, mass diffusivity, or radiative heat loss enhancement is apparent.

Figure 3 shows smoke point volumetric fuel flow rate (non-dim. by the undiluted fuel flow rate) as a function of volumetric diluent flow rate measured in this burner with two different fuel exit velocity profiles. Data extracted from McLintock and Schug is also displayed. As observed in this figure, the effect of carbon dioxide addition on smoke point depends strongly on

whether the fuel exit velocity profile is parabolic or plug. The parabolic exit velocity measurements agree reasonably well with the measurements of McLintock and Schug. However, with a plug flow velocity profile, the effect of carbon dioxide on smoke point is markedly decreased. In contrast, the effect of helium addition on smoke point is noticeably insensitive to fuel exit velocity profile, and neither case is dramatically different from the results found by McLintock or Schug and co-workers. As seen in this figure, with a plug flow exit velocity profile, there is little difference between carbon dioxide and helium.

The volumetric fuel flow and smoke point height as a function of fuel-to-air velocity ratio is shown in Fig. 4 for undiluted ethylene. Interestingly enough, the volumetric fuel flow and smoke point height are both approximately parabolic with velocity ratio, both peaking near a velocity ratio of unity for the plug flow exit velocity profile, whereas the flow rate and flame height both decrease nearly linearly with increasing velocity ratio for the parabolic exit velocity profile.

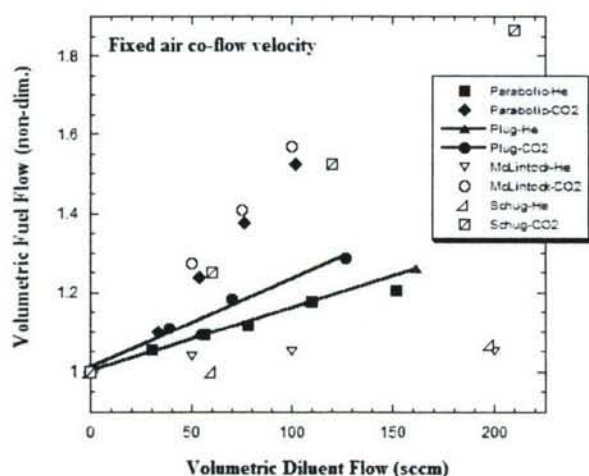


Fig. 3 Fuel flow vs diluent flow at 1 atm

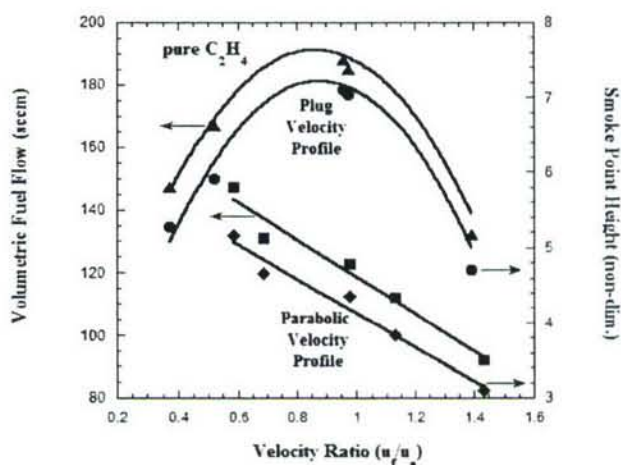


Fig. 4 Fuel flow and smoke pt vs vel. ratio

Observations:

With a parabolic fuel exit velocity profile, carbon dioxide and helium show extremely pronounced differences in their effectiveness at increasing the smoke point with dilution. Carbon dioxide is shown to be effective while helium is very ineffective. This has been demonstrated experimentally by McLintock and Schug et al. However, when a plug exit velocity profile is used, there is little difference between the two diluents. Thus, the exit velocity profile may be as important, if not more important, than the diluent itself.

References

1. S. McLintock, Combust. Flame 12 (1968) 217-225.
2. K. P. Schug, Y. Manheimer-Timnat, P. Yaccarino, I. Glassman, Combust. Sci. Tech. 22 (1980) 235-250.
3. K.-C. Lin, G. M Faeth, J. Prop. Power 12 (1) (1996) 10-17.

Advanced Controls of Diesel Engines

N. A. Henein

Wayne State University

Abstract

Major developments in diesel engine technology enabled accurate control of the combustion process, to meet the stringent emissions standards, particularly for NO_x and particulate matter (PM). This led to the development of advanced combustion regimes to decrease NO_x and PM engine-out emissions and reduce the reliance on after-treatment devices. This work examines the effects of exhaust gas recirculation (EGR), injection pressure and swirl motion on engine-out emissions in the conventional and Low Temperature Combustion Regimes (LTC). Experiments were conducted on a single cylinder, 4-valve, direct injection diesel engine equipped with a common rail injection system. The pressure and temperature in the inlet and exhaust surge tanks were adjusted to simulate turbocharged diesel engine conditions. Engine-out emission measurements included hydrocarbons, carbon monoxide, smoke and NO_x. EGR rates were varied over a wide range to cover the engine operation from the conventional to the low temperature combustion regime, up to the misfiring point. The effects of different engine control parameters on the autoignition reactions, cool flames, and premixed and mixing controlled combustion fractions are examined. The trade off between NO_x and BSU are determined in 2-D and 3-D maps that show the iso-EGR lines and surfaces. The penalty in BSU, HC, CO and indicated specific fuel consumption (ISFC) were determined over the whole EGR range. A comparison between the use of higher injection parameters and higher swirl ratios to control engine-out emissions is made.

Background

Different combustion regimes, developed to reduce engine out emissions, include the smokeless lean combustion (MK) concept [1], the low temperature smokeless rich combustion [2] and the UNIBUS system [3] and modified low LTC [4]. These regimes require the control of the injection pressure, EGR, injection timing and swirl ratio. This work examines the effect of these controls on engine-out emissions in the conventional and the low temperature lean combustion regime, LTC.

Diesel Combustion: Conventional and LTC Regimes

Figure 1 shows the effect of increasing EGR on engine-out emissions over a wide range, till the engine misfired. This figure can be divided in three parts:

(a) Conventional diesel combustion where EGR was increased from 0% to 60% causing NO_x emissions to continuously drop, while BSU and CO increased at an accelerating rate at the high EGR rates. Slight changes are observed in HC and ISFC as EGR increased to 50%, after which incomplete combustion products appeared at a higher concentration, and ISFC increased.

(b) Low Temperature Combustion (LTC) where EGR increased from 60% to 64% EGR, causing BSU to drop sharply, while the already low NO_x dropped to fairly lower values. CO increased at a high rate and HC almost remained constant. The operation of the engine in this zone was unstable and the COV was lower than that in the conventional combustion regime.

(c) Unstable Operation and Misfiring Zone:

Any increase in EGR beyond 64% resulted in unstable engine operation due to large cycle-to-cycle variations and occasional misfiring.

Effect of EGR on Engine-out Emissions in the Conventional Diesel Combustion Regime

The increase in EGR has the following effects on the combustion process and engine out emissions in the conventional combustion regime:

1. It slowed down the auto ignition reactions as indicated by a 44% increase in ID at 60% EGR.
2. Increase in EGR enhanced the production of cool flames that remained for a longer period of time at the higher EGR rates. The long cool flame periods allowed more time for the liquid fuel evaporation and mix with the fresh charge.
3. EGR reduced the rate of the oxidation reactions during the whole combustion process due to the lower concentration of oxygen and lack of proper mixing with oxygen, in addition to the drop in temperature at the higher EGR rates. The reduction in the rate of burning occurred in spite of the increase in evaporation and mixing.
4. EGR increased the CO emissions in spite of the better mixing at the higher EGR rates, is caused mainly by the drop in the oxygen content of the charge. Other factors that might have contributed to the increase in CO at higher EGR are the increase in the fuel deposited on the walls and the poor oxidation reactions. At higher EGR rates, the longer ID and cool flame periods allow more time for the light components of the fuel to evaporate leaving the heavier components on the walls. As these heavier components evaporate late in the expansion stroke, their oxidation reactions suffer because of the low oxygen contents, in addition to the lower mass average temperature of the combustion products.

Effect of EGR on Engine-out Emissions in the LTC Regime

Increasing EGR from 60% to 64% caused a drop in both NO_x and BSU. A possible explanation for the drop in smoke at the highest EGR rate is given in a recent publication by Aceves 2005 [17]. The model predicted the chemical composition and concentration of soot precursors, which were considered good indicators of soot production in the engine. Aceves concluded that reducing the temperature and increasing the rate of mixing tend to reduce the production of the soot precursors. These findings can explain some of the trends observed in this investigation where the mixing was increased during the long ignition delays and the temperatures were reduced at the very high EGR rates in the LTC regime. But the cause of the sudden change in soot emissions by an increase of one or two percent in EGR cannot be explained.

Effect of swirl ratio in the conventional diesel combustion at Zero EGR

Figure 3 shows that ISNO_x emissions increased by about 50% as the SR increased from 1.44 to 7.12. This is mainly caused by the following; (1) Better fuel evaporation and mixing with the fresh charge, due to (a) the higher relative velocity and its effect on increasing the heat and mass transfer coefficients between the liquid phase and gas phase, (b) the spread of the spray over a wider angle [5], and the increase in the lean flame region down stream the swirl motion [6] and (c) the increase in the wetted surface area of the wall after the spray impinges on the wall. All these factors contribute to the increase in the volume of the premixed charge. (2) Higher swirl ratios increase turbulence and mixing and enhance the reaction rate, as evident from a 40% increase in the rate of heat release from premixed combustion fraction. This increase occurred, in spite of the increase in the cooling losses at the higher SR. The analysis shows the increase in the swirl ratio from 1.44 to 7.12 caused a drop of 2 bar in compression pressure and about 80 °C in the compression temperature.

Effect of swirl ratio on Engine-out Emissions in the Conventional Diesel Combustion at 60%EGR

The effect of swirl at 60% EGR is significantly different than its effect at 0% EGR. The increase in SR from 1.44 to 4.94 reduced BSU sharply. This can be attributed to the better mixing. But a further increase in swirl ratio from 4.94 to 7.12 caused an increase in both the BSU and CO, which can be attributed to the drop in the charge temperature caused by the higher cooling losses, possible overlapping of the adjacent

sprays creating a rich mixture, and the change in the gas dynamics caused by the interaction between the squish and swirl components.

The penalty in fuel economy caused by the high SR increased at the 60% EGR, because of the longer period and late fuel burning.

Effect of Injection Pressure on Engine-out Emissions in the Conventional and LTC Regimes

Figure 5 shows that the increase in injection pressure is very effective in reducing BSU, at all the EGR ratios in both the conventional and LTC regimes. It is interesting to notice the drop in NO_x at the higher injection pressures in the LTC regime.

Comparison Between the Effects of Injection Pressure and Swirl Ratio on the Trade Off Between NO_x and BSU Emissions in the Conventional Diesel Combustion and LTC Regimes

Figure (6) shows a comparison between the effects of injection pressure and swirl ratios on the trade-off between NO_x and BSU in the conventional diesel and LTC regimes. Increasing the injection pressure by a factor of 2, from 600 bar to 1200 bar, reduced BSU by 80%. Meanwhile, increasing the swirl ratio from 1.44 to 2.59 reduced BSU by a factor of 66% in LTC regime. However increasing swirl by a factor of ~5 (1.44 to 7.12) reduced BSU by a factor of only 33% in the LTC regime. Increase of Injection pressure to 1200 increased fuel consumption by about 10% in both conventional and LTC combustion regimes. However these data does not reflect the additional energy required for driving the high pressure pump. Increase of swirl ratio from 1.44 to 7.12 increased fuel consumption by about 20% in both the regimes.

Conclusions

1. The major difference between the conventional and LTC regimes is in the % EGR applied to the fresh charge. Increasing EGR reduces NO_x continuously in both regimes. However, increasing EGR increases engine-out soot emissions in the conventional diesel combustion, to a point where it peaks. Any further increase in EGR brings the engine in the LTC regime where any increase in EGR reduces soot to a level still higher than that at 0% EGR. This has been observed at all the injection pressures in this investigation.
2. The LTC regime requires very accurate controls since combustion is very sensitive to small variations in EGR. The high EGR required for LTC is very close to the misfiring EGR limit.
3. Soot, at the high EGR rates in the two regimes, can be reduced by applying high injection pressures and a moderate swirl ratio. There is an optimum SR beyond which any increase results in a penalty in BSU.
4. There is a penalty in fuel economy and a fairly high increase in CO at the higher EGR rates particularly in the LTC regime.
5. The penalties reported in this investigation do not reflect the additional energy required to drive the fuel pump at the high injection pressures, the increase in the cooling losses and drop in the volumetric efficiency at the high swirl ratios.

REFERENCES

- 1- Kimura, S., Aoki, O., Ogawa, H., Muranaka, S., Enomoto, Y., "New Combustion Concept for Ultra-Clean and High-Efficiency Small DI Diesel Engines," SAE 1999-01-3681.
- 2- Akihami, K., Takatori, Y., Inagaki, K., Sasaki, S., Dean, A. M., (2001), "Mechanism of the smokeless Rich Diesel Combustion by Reducing Temperature," SAE 2001-01-0655.
- 3- Ssaki, S., Ito, T., Goto, M., Yoshizaki, K., "A Study of Low Temperature Diesel Combustion System, (2001), " Toyota Technical Review, Vol. 50 No. 2, Mar., 2001.
- 4- Aceves S M and Flowers D L, (2005), "A Detailed Chemical Kinetic Analysis of Low-Temperature, Non-Sooting Diesel Combustion", SAE2005-01-0923.
- 5- Rao, K. K., Winterbone, D. E., Clough, E., "Influence of Swirl on High Pressure Injection in Hydra Diesel Engine," SAE paper number 930978, 1993.
- 6- Henein, N. A. "Analysis of Pollutant Formation and Fuel Economy in Diesel Engines," Progress in Energy and Combustion Science., pp. 165-207, Pergamon Press, 1976.

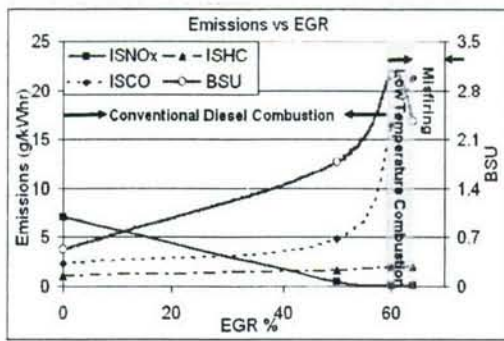


Figure 1. Effect of EGR on engine-out emissions in the conventional and LTC regimes.

[P_{inj} = 600 bar, EGR= variable, LPPC= 0.5aTDC, Swirl Ratio= 1.44 for all]

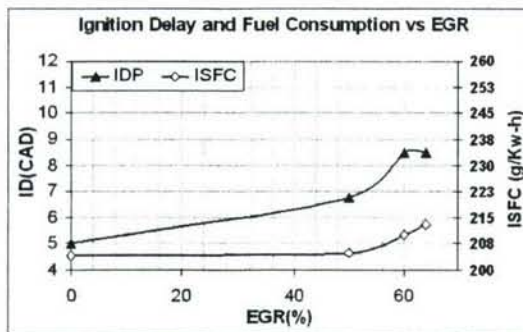


Figure 2. Effect of EGR on engine-out emissions in the conventional and LTC regimes.

[P_{inj} = 600 bar, EGR= variable, LPPC= 0.5aTDC, Swirl =1.44]

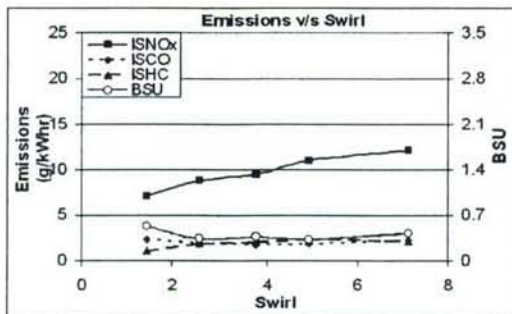


Figure3. Effect of swirl Ratio on engine-out emissions in conventional zone.

[P_{inj} = 600bar, EGR= 0%, LPPC= 0.5aTDC, Swirl Ratio = 1.44-7.12 for all]

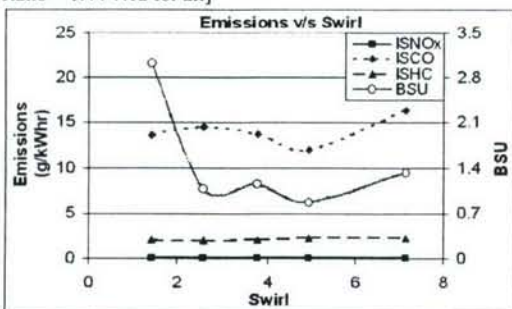


Figure 4: Emissions versus Swirl in LTC Regime.
[P_{inj} = 600bar, EGR= 0%, LPPC= 0.5aTDC, Swirl= 1.44-7.12]

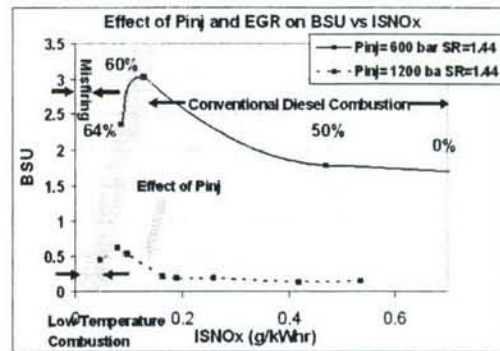


Figure 5. Trade-Off between NOx and BSU at different injection pressures in the conventional and LTC Regimes

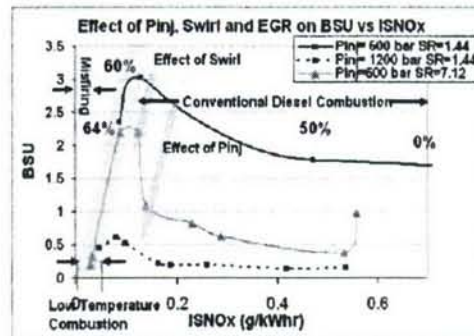


Figure 6. Trade-Off Between NOx and BSU at different injection pressures, EGR and Swirl Ratios in the conventional and LTC Regimes.

BREAKUP OF LIQUID STREAMS AT HIGH PRESSURES

49296-EG

William. A. Sirignano and Daniel D. Joseph

Department of Mechanical and Aerospace Engineering
University of California, Irvine
Irvine, CA 92697-3975

SUMMARY/OVERVIEW:

A theoretical and computational study of the break-up of injected liquid streams at high pressure by stress-induced cavitation is the research subject. The breakup criteria by stresses differs greatly from the traditional criterion in which a fluid cavitates at places and times at which the local pressure falls below the vapor pressure. Rather, cavitation occurs where the tensile stress exceeds the liquid breaking strength. The hydrodynamic stability and subsequent breakup of these liquid streams will be examined using viscous-potential-flow analysis and the direct numerical simulation of the viscous-fluid motions. The deformation of free surfaces and the fields of principal stresses are monitored to determine places and times at which the liquid is at risk to breakup.

TECHNICAL DISCUSSION:

This program just began in May, 2006. Our new approaches to the analysis of atomization are especially appropriate to systems operating at high pressures and high temperatures which cannot be explained by classical models that require low pressure; rupture can be induced at high pressure by viscous stresses. A cohesive, analytical approach is needed for the nonlinear fluid dynamics and free surface deformation, leading to the identification of critical conditions for stress-induced-cavitation, to provide engineers with a predictive capability and the understanding how liquid stream breakup is affected by various factors under the control of the designer.

Major issues which should enter into the study of breakup at high pressures are (1) determination of the regions in the round, converging orifice at risk to stress-induced cavitation; (2) hydrodynamic stability including the nonlinear dynamics for Rayleigh-Taylor (RT), Kelvin-Helmholtz (KH) and capillary instabilities; (3) viscosity and vorticity; and (4) breaking the liquid continuum. Different mechanisms which can lead to breaking and rupture of the liquid continuum are cavitation, capillary collapse, and disjoining pressures associated with molecular attractions. For the formation of sprays or droplet streams with super-micron diameters, stress-induced cavitation is the strongest candidate.

It is widely understood¹ that, for diesel injection, disintegration of the continuum begins internally in the nozzle and a continuous liquid core surrounded by fragmented fluid exits from the injector nozzle. Cavitation can play a major role in the disintegration process. The flow near the orifice walls accelerates more than the core flow resulting in lower pressure near the walls. Therefore, the region near the walls is preferred for cavitation

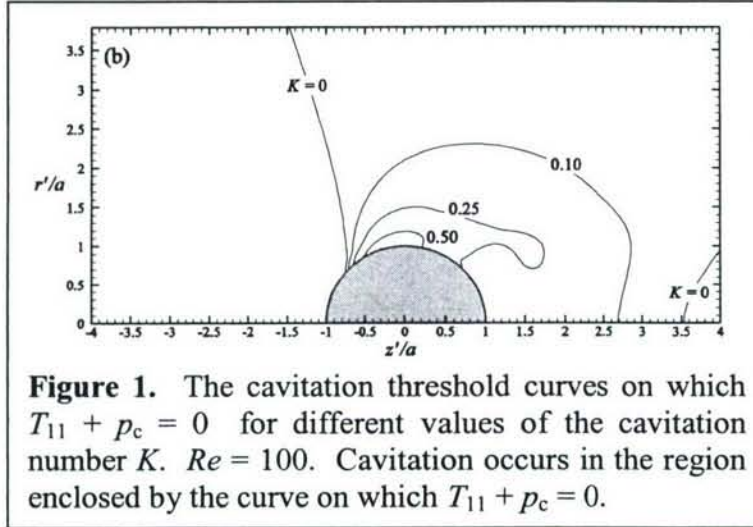
and stress-induced cavitation can occur around the liquid perimeter near the wall while the liquid still is inside the orifice. This fragments the outer shell but leaves an intact core. The bubble growth immediately following the fracture perturbs the core flow inducing Kelvin-Helmholtz (KH) capillary waves. These short, nonlinear surface waves have peaks that emerge as protrusions from the surface of the liquid core flow and might rupture, forming liquid fragments.

Experimental evidence¹ indicates that cavitation or cavitation in combination with other mechanisms is the most likely candidate for liquid-stream breakup at high flow velocities. Here an examination of the axisymmetric flow within the converging orifice is required. We will consider sub-millimeter-diameter dimensions, say $O(100\mu\text{m})$, for the orifice and velocities of $O(10\text{--}100\text{ m/s})$. For the liquids considered, this will yield Reynolds numbers in the high laminar to transitional regimes. Unsteady solutions will be allowed so as to capture flow instabilities. The cavitation number should be determined throughout the internal and near-exit flow, indicating the zones for likely cavitation. The principal viscous stresses (not merely thermodynamic pressure) should be computed. Two types of analysis can be made: numerical solutions of the Navier-Stokes equation and viscous potential flow. Analyses of stress-induced cavitation have been performed by Joseph and co-workers for flow through a planar aperture² and axisymmetric flow over a sphere.³

We expect cavitation at places where the tension exceeds the cavitation threshold p_c . The calculation would compare points of minimum pressure with points of maximum tension. Our main interest will be on axisymmetric and three-dimensional flows. In the study of Padrino et al.,³ the problem of stress-induced cavitation in the flow of a viscous fluid over a sphere is studied in the Stokes flow limit, by viscous potential flow and by direct simulation of the Navier-Stokes equation.

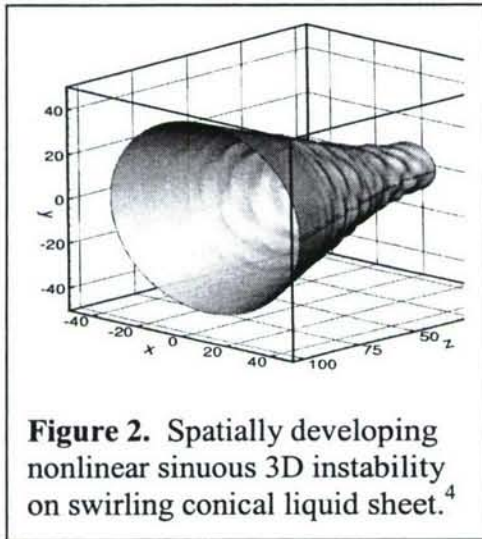
Three criteria for breakup can be applied in the theory of stress-induced cavitation. All three are framed in terms of principal stresses in the convention $T_{11} \geq T_{33} \geq T_{22}$. In the classical theory of cavitation, the viscous part of the stress tensor is not considered and the threshold pressure p_c is the vapor pressure p_v . So, $\mathbf{T} + p_c \mathbf{I} = (-p + p_v) \mathbf{I}$. The classical theory assumes that the cavitation threshold is given by the negative of the average stress, called the pressure. The fluid cannot average its stresses; it sees only principal stresses and when the actual state of stress is considered there is at least one stress which is more compressive and another which is more tensile than the average stress. The most conservative criterion is the one which requires that the most compressive stress is larger than the vapor pressure; if T_{22} is the most compressive and T_{11} is the most tensile stress, then, if $T_{22} + p_c > 0$ for cavitation, it will surely be true that $-p + p_c > 0$ and $T_{11} + p_c > 0$. We may consider the possibility that a cavity will form if all stresses are in tension; it will not form if all stress are in compression. The case in which the stresses have different signs is ambiguous; a cavity will open in tension but close in compression. This is the situation for the classical theory when the pressure is close to the vapor pressure and the motion produces viscous stresses with different signs. The maximum tension theory, which perhaps embodies the statement that liquids which are

not specially prepared will cavitate when they pass into tension, can be expressed by the condition that, if T_{11} is the maximum of the three principal stresses, then $T_{11} + p_v > 0$ where $K = \frac{p_\infty - p_c}{\frac{1}{2}\rho U^2}$ is the cavitation number. Suppose now that T_{11} is the largest of the



three principal values of stress. Then the locus of the cavitation threshold is given by $T_{11} + p_c = 0$. The threshold condition gives an isoline inside of which bubbles will nucleate. Figure 1 gives Navier-Stokes results for $Re = 100$.

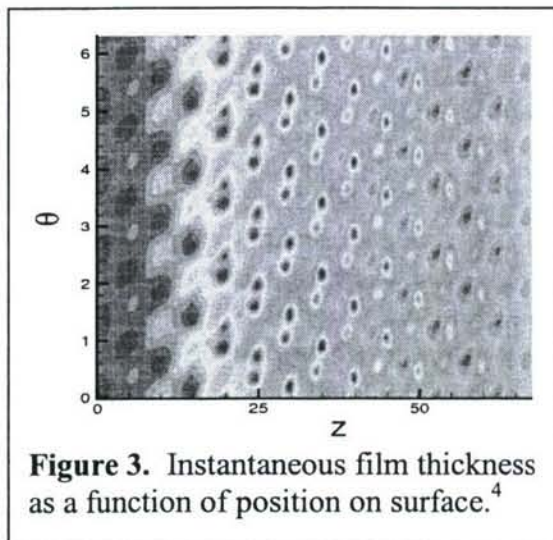
Bubbles will nucleate and coalesce in the regions inside the isolines for cavitation. This leads to bubbly flows for which interface tracking is required. We do not plan to follow the calculation into the bubbly regimes but the motion and orientation of these bubbles will be controlled by the state of stress at the interface and the bubbles will tend to elongate in the direction of maximum tension.



The existing literature on liquid-stream stability (and straining under unstable conditions) addresses collectively dilational and sinuous capillary and KH/capillary waves, temporal and spatial (and absolute and convective) instabilities, and linear and nonlinear behavior. The focus of this portion of the research will be on nonlinear behavior leading to breakup. However, linear analysis of stability is essential to establish the domain of parameters in which instability leading to collapse is expected, to identify the types of instability, to determine the wave lengths which grow most rapidly, to establish the cut-off values between stability and

instability, to determine if there are neutral curves establishing conditions under which the gas streams are always stable and to identify how all these important linear functionals of the solution depend on the control parameters of the problem. Figures 2 and 3 show the results of a calculation for a nonlinear sinuous wave on a swirling "conical" sheet that is modulated at the injection plane.⁴ Clearly, a complex pattern of "spotty" thinning can occur; this pattern would not be predicted as well by any linear theory. These regions of thinning again are the candidate locations for rupture. Large gradients occur in the neighborhoods of these locations so that, for better accuracy,

viscous effects should be included in the calculations. The results from these four figures give a conclusion that also applies for other configurations: *nonlinear and viscous effects must be considered in a theory of liquid-stream rupture.*



Emphasis in the proposed research will be on round jets operating at high pressures, high temperatures, and high flow velocities. Orifice pressure drops as high as 100 bars will be considered. Practical injectors can have larger drops but, in this first study, we plan to avoid developed turbulent flows. Decane will be used as a surrogate fuel that is representative of the relevant volatility and viscosity range. Orifice diameters will be in the sub-millimeter range of practical interest. Summary descriptions of the tasks follow. First, the internal orifice flow of viscous

fluids will be analyzed to identify zones of flow at risk to stress-induced cavitation. A variety of analytical techniques will be employed emphasizing extended analyses of the irrotational flows of viscous fluids spot checked by exact numerical simulations of flows governed by the Navier-Stokes equations. The amounts of fragmented fluid at the orifice exit and the flow in the intact core will be estimated. The exit-velocity profile for the intact core will also be determined. The hydrodynamic stability of the intact core will be studied by the imposition of modulated waves at the exit. Viscosity effects and surface tension will be included in the analysis. The cavitation number will be resolved locally at each point in the core continuously with time to identify location of rupture. Rupture of ligaments from the core surface due to both stress-induced cavitation and capillary collapse can be considered. The dynamic evolution of the core surface will be determined using numerical simulation with surface-tracking techniques. Two- and three-dimensional KH/capillary instabilities will be computed.

¹Reitz, R.D. and Bracco, F.V., "Mechanism of Atomization of a Liquid Jet," *Physics of Fluids*, Vol. 25, 1982, pp. 1730-42.

²Funada, T., Wang, J., and Joseph, D. D., "Viscous Potential Flow Analysis of Stress Induced Cavitation of Aperture Flow." *Atomization & Sprays*, Vol. 16, No. 7, 2006, in press.

³Padrino, J.C., Joseph, D. D., Funada, T., Wang, J., and Sirignano, W. A., "Stress Induced Cavitation for the Streaming Motion of a Viscous Liquid Past a Sphere," 2006. Submitted.

⁴Mehring, C. and Sirignano, W.A., "Capillary Stability of Modulated Swirling Liquid Sheets," *Atomization & Sprays* 14, 2004, pp. 397-436.

PLASMA-PROPELLANT INTERACTION STUDIES

Grant Number DAAD19-03-1-0340

Principal Investigators: Stefan T. Thynell and Thomas A. Litzinger

Department of Mechanical and Nuclear Engineering
The Pennsylvania State University
University Park, PA 16802

SUMMARY

The overall objective is to gain insights about of the various chemical and physical processes that occur during ignition of a solid propellant by a high-pressure and high-temperature plasma. The plasma is formed within a hydrocarbon capillary by an electrical discharge process. The plasma emerges into stagnant air as an underexpanded supersonic jet. Two experimental approaches are applied. A triple-quadrupole mass spectrometer is employed to examine species from the plasma and the pyrolysis products from the propellant generated by interactions with the plasma. A fast-response heat flux gauge has been designed and utilized to determine the transient variation of the radiant heat flux, with specific emphasis on the UV to near-visible components. The results show that the use of different trigger-wire and capillary materials yields significant differences in the ignition and combustion of JA2 and transparent JA2, as well as in the radiative heat flux levels.

TECHNICAL DISCUSSION

Plasma-driven Ignition and Combustion of JA2 and Transparent JA2

The focus of this part of the investigation to examine the effects of initiating-wire and capillary materials on the ignition and combustion of selected propellants. Experiments were conducted in a small chamber with a volume of 8.2cm^3 ; both JA2 and transparent JA2 (t-JA2) were studied. JA2 is a double-base propellant, containing nitrocellulose, nitroglycerine, diethyleneglycol dinitrate, akardit, and carbon black; the t-JA2 contains no carbon black. An $8\text{mm}\times 8\text{mm}$ test sample, weighing approximately 260mg, was cut from a thin (2.5mm) sheet of propellant and placed on the sample holder near the plasma exit. The distance from the exit to the sample was 3mm for all tests. The charging voltage was set at 4kV, corresponding to a peak power output about 19-20 kW. Three wire materials, aluminum (Al), copper (Cu), and nickel (Ni), were tested along with three capillary materials: polyethylene (PE), Lexan (LE) and Teflon (TE). In addition, the mass of wire was also varied. The capillary size was 4mm (i.d.) by 26mm (length) in all tests.

Figure 1 presents the traces of voltage versus time for the three different wire materials. The discharge voltage shows the transition from a trigger-wire sustained plasma to a capillary-sustained plasma, and thus it is a better parameter than the discharge current to monitor the discharge process. As shown in Fig. 1, the traces of

voltage indicate a clear sequence (in tests with both JA2 and t-JA2) in the transition with nickel being earliest followed by aluminum and then by copper. This trend was confirmed by three tests for each wire material. The difference in wire-to-capillary transition is expected to have an effect on the ignition and combustion of the propellants.

Figure 2 shows the combustion pressures for the three wires and for both JA2 and t-JA2; the measured capillary ablation mass is listed in the legend of the figure. The highest combustion pressure is obtained with the nickel wire in the case of JA2, while the aluminum wire results in the highest combustion pressure for t-JA2. Examination of the capillary ablation mass shows that combustion of these propellants is more strongly related to the ablation mass than the wire-to-capillary transition times. As seen from the figures, greater ablation mass tends to result in faster burning and higher pressure. It should be noted that the results showed variation from test to test and thus further work is needed to verify the effects demonstrated in current work. In addition, testing with the different capillary materials has begun but the test-to-test variation is not yet acceptable.

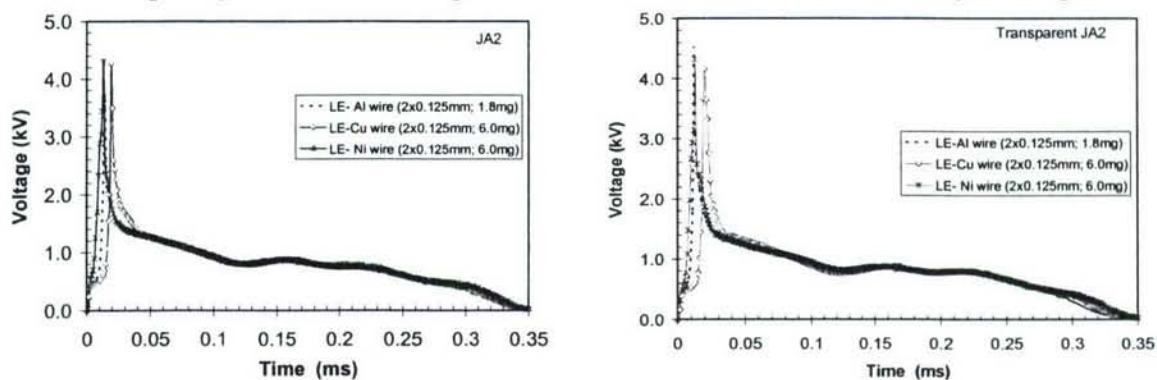


Fig. 1 Discharge voltages for different initiating wires.

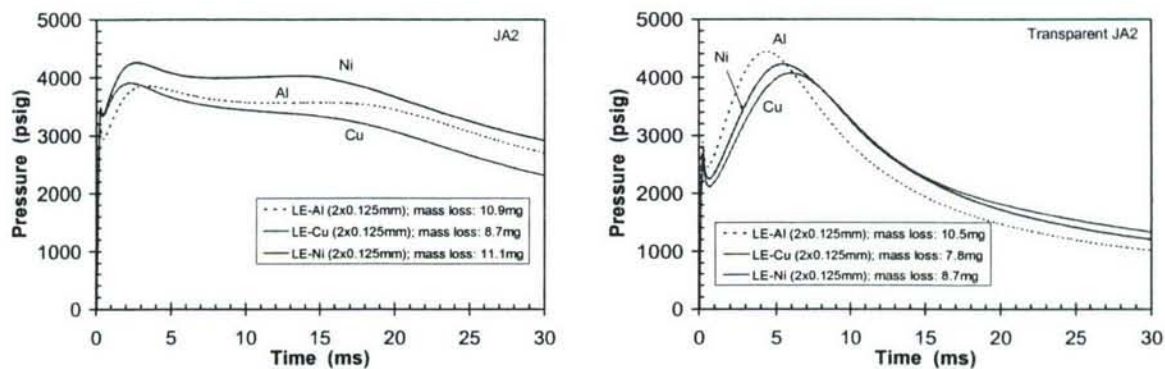


Fig. 2 Comparison of the effect of different wire materials on the combustion of JA2 and transparent JA2.

Radiant Heat Flux Measurements

Previous reports described the design and manufacturing of a thin-film Pt gage for estimating the transient radiant heat flux from ETC plasma. Initial results from the open-air experiments were also reported. These experiments were conducted with a PE capillary and Cu wire with charging voltages of 2.5 (0.60kJ) and 3.0kV (0.87kJ). The ETC plasma, generated by exploding the Cu wire and sustained by ablation of the PE

capillary, emerged from a Cu nozzle to impinge on a stagnation plate equipped with an array of heat flux gages. Gages were manufactured by sputtering 80nm Pt over 50 μ m polyimide substrate, followed by adequate heat treatment. Nozzle exit to stagnation plate distance was maintained 50 and 75mm.

Based on the initial success of the experimental procedure, a material dependence study of ETC plasma was conducted. During this investigation nine different capillary-trigger wire combinations are studied, using PE, LE and TE capillaries with Cu, Al and Ni wires. Charging voltage was maintained 2.5kV with nozzle to stagnation plate distance of 50mm. The results show that appreciable differences are present among the capillary and wire combinations, with a LE capillary and copper wire yielding the largest radiant energy deposition in the substrate. Figure 3 shows the transient temperature, radiant heat flux and stagnation pressure variation on the stagnation plate at the exit port centerline for the PE capillary with Al, and Ni trigger wires. The use of the Al wire, with its smoothly varying current, produces the largest peak radiant heat flux. The radiant heating begins around 40 μ s into the event, indicating that plasma emergence is rapid. Peak radiant heat fluxes are obtained prior to arrival of the precursor shock, and they generally coincide with the peak of the current flow. Cases with Ni wires suggest a slight change or increase (second rise) when peak stagnation pressures are achieved. It is not clear if this effect is a chemically induced effect caused by reactions between Ni and surrounding air, or differences in the radiative properties between Al, and Ni. The secondary increased radiative heat flux for Ni is not caused by the arrival of particles (from wire or nozzle), since the quartz window remains quite clear after one firing. However, inspection of atomic line data reveals that neutral and singly ionized Al has relatively few lines produced by electronic transitions covering wavelengths from 200 nm to approximately 700 nm, whereas Ni has a much larger number of lines. Any further assessment regarding spectral emission characteristics requires additional experiments. The compressible flow produces strong pressure oscillations that appear quite insensitive to the type of trigger wire material used. The large peak radiant heat flux from the case with Al wire may only partially contribute to a reduced plasma temperature and thus produces the lowest peak pressure; the reduction is much more likely due to a lower plasma density.

While the above studies clearly indicated the effectiveness of the heat flux gages, it was also observed that the gages were destroyed at higher energy levels such as, 4kV-50mm combination. An improved gage design, comprising a sapphire substrate instead of polyimide, is utilized to circumvent this issue. While a higher thermal conductivity and heat capacity of sapphire yielded in successful measurement of high heat fluxes, the same properties produce two-dimensional heat conduction effects within the substrate, which is generally neglected in a typical one-dimensional (1-D) inverse data reduction scheme. A two-dimensional (2-D) data reduction technique is, therefore, devised. Figure 4 shows the performance of 1- and 2-D data reduction schemes for 2.5kV (0.6kJ) and 7.5kV (5.4kJ) plasmas. PE capillary and Cu wire are used in both cases with a nozzle exit to stagnation plate distance of 50mm. While polyimide substrate was used for the 0.6kJ plasma, higher energy level measurements utilized a sapphire substrate. The results clearly revealed significant departure from 1-D heat conduction during higher energy level.

Based on successful redesigning of the heat flux gage as well as the data reduction scheme, a parametric study on radiative transport from ETC plasma has been

accomplished and will be reported soon. Efforts are underway to quantify the spectral variation of the radiative heat fluxes using UV-Visible spectroscopy. Further studies to identify the effects of radiant fluxes on the propellant have also been planned.

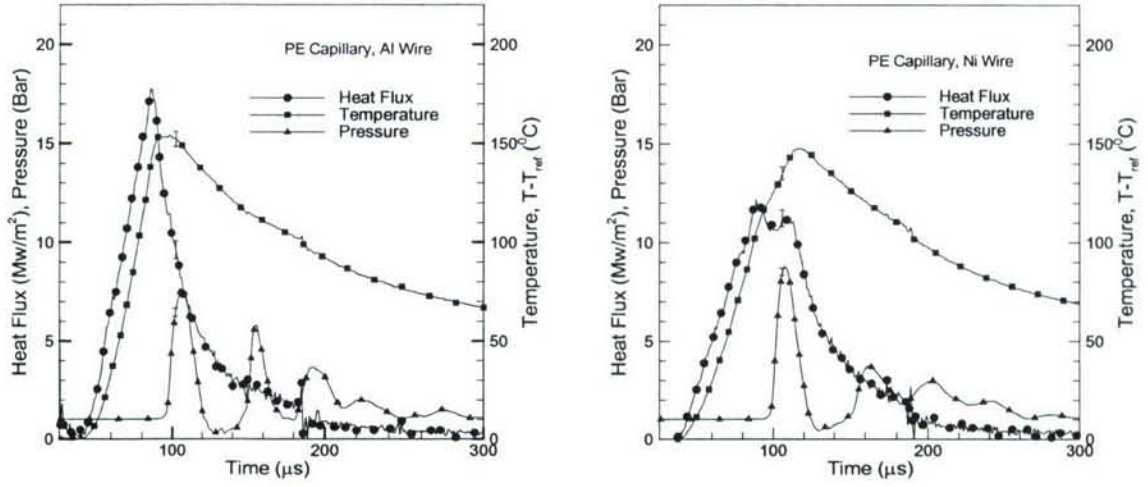


Fig. 3 Transient variation of pressure, temperature and radiant heat flux at the stagnation location for PE capillary with Cu and Ni wires for a charging voltage of 2.5 kV and a nozzle exit to stagnation plate distance of 50 mm.

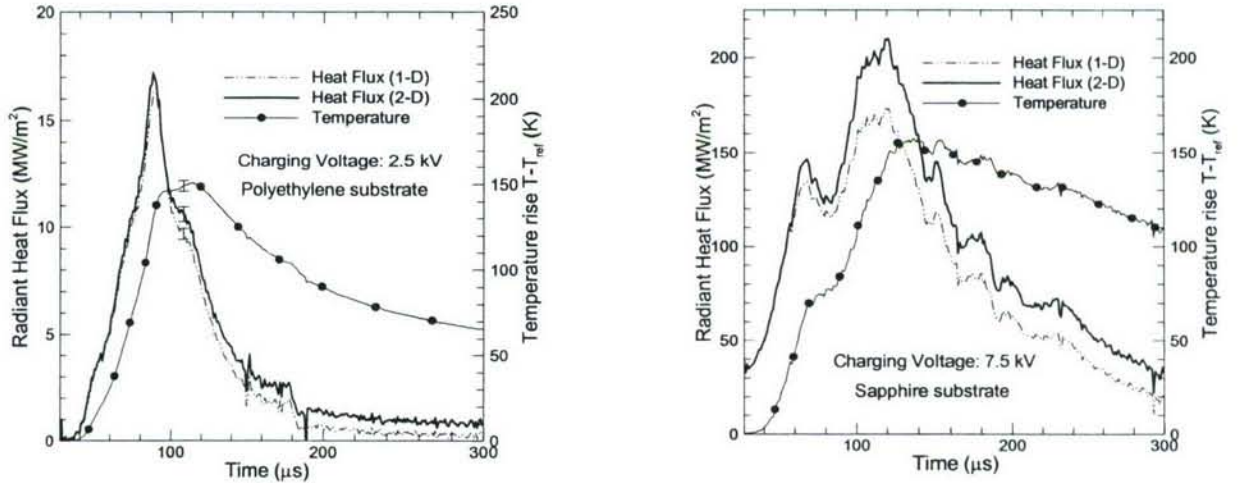


Fig. 4 Performance of 1- and 2-D data reduction approach for radiant heat fluxes using 2.5 and 7.5kV charging voltages with a nozzle exit to stagnation plate distance of 50mm.

Modeling of Plasma Induced Ignition and Combustion

Michael Keidar, Iain D. Boyd and Andy Porwitzky
University of Michigan

Abstract—Electrothermal-chemical (ETC) ignition systems have been demonstrated in gun systems to provide desirable characteristics including reproducible shorter ignition delays. We present a combined theoretical and experimental study of the capillary discharge with an aim to develop a capillary plasma source with efficient energy conversion. In addition, a detailed understanding of the dynamics of the plasma-propellant interaction is considered one of the key elements to the future success of practical ETC gun implementation. We address this issue by developing a model of the propellant ablation under plasma effect based on the kinetic theory of ablation. The major emphasis in the present capillary discharge model is the ablation phenomenon. A kinetic approach is used to determine the parameters at the interface between the kinetic Knudsen layer and the hydrodynamic layer. In parallel, a parametric experimental study of the capillary ablation process is conducted at Army Research Laboratory. Both experimental measurements and simulations indicate that the ablated mass increases with the peak discharge current and that a smaller diameter capillary yields a larger ablated mass. It is found that model predictions agree well with experimental measurements. The ablation model is coupled with a model of the plasma generation in the capillary discharge that allows calculation of the effective heat flux from the plasma. Calculations are performed for specific experimental conditions in which ablated mass of a double-base and a nitramine composite propellant are studied. One representative solution reproduces the experimentally determined ablated mass for the double-base propellant of 5.3 mg via an effective heat flux on the order of 4×10^8 J/m²s. The effective heat flux that corresponds to the experimentally measured ablated mass is determined for different propellants. Differences in the calculated effective heat flux between different propellants indicate that although heat convection from the plasma is the dominant source of energy, plasma radiation and the optical properties of the propellants themselves can not be ignored.

1. Model of a capillary sustained plasma

We present a capillary model for an ETC that includes self-consistent consideration of the ablation phenomena. In this section, the model is described for the plasma generation processes (ablation, heating, radiation, ionization etc.) and plasma acceleration along a capillary of a pulsed electrical discharge. Figure 1 shows some characteristic regions in the interface between the discharge plasma and the dielectric wall such as an electrical sheath near the dielectric, the Knudsen and hydrodynamic layers, and a quasi-neutral plasma. Different kinetic and hydrodynamic phenomena determine the main features of the plasma flow including Joule heating, radiative and convective heat transfer to the dielectric, and electrothermal acceleration of the plasma up to the sound speed at the cavity exit. The central region is the quasi-neutral plasma that occupies almost the entire capillary since typically the transition region scale length is much smaller than the capillary radius. The plasma region is separated from the dielectric surface by the vapor layers (Knudsen layer and hydrodynamic layer). Finally, the plasma-wall transition region includes the electrostatic sheath attached to the wall. The plasma is heated due to electric current flowing through the capillary. The energy transfer from the plasma column to the capillary wall consists of the heat transfer by particle fluxes and radiation heat transfer. Energy is absorbed by the capillary walls and dissipated by thermal conductivity and material evaporation.

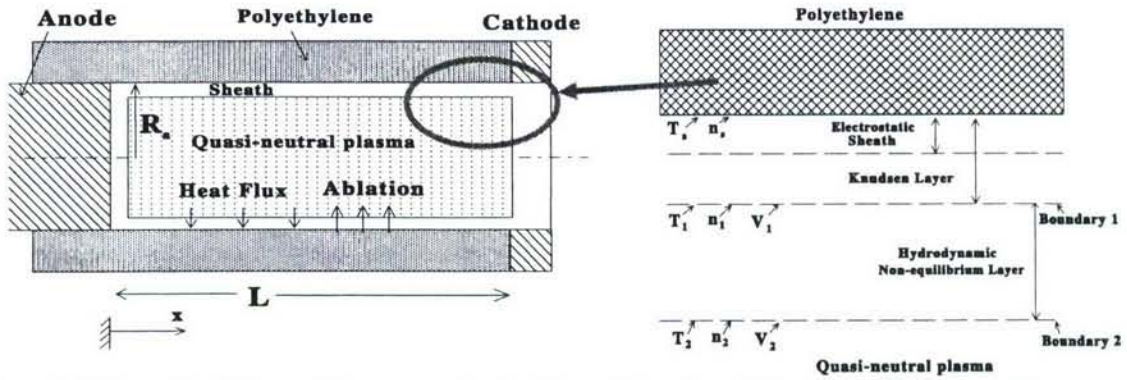


Figure 1. Schematic of the problem geometry (not to scale) and multi-layer structure near the ablated surface.

Ablated flux builds up a vapor layer in the vicinity of the wall. Under the considered conditions the mass, momentum and energy conservation equations have the following forms:

$$A \left(\frac{\partial \rho}{\partial t} + \frac{\partial \rho V}{\partial x} \right) = 2\pi R_a \Gamma(t, x) \quad (1)$$

$$\rho \left(\frac{\partial V}{\partial t} + V \frac{\partial V}{\partial x} \right) = - \frac{\partial P}{\partial x} \quad (2)$$

$$\rho \left(\frac{\partial \varepsilon}{\partial t} + V \frac{\partial \varepsilon}{\partial x} \right) = -P \frac{\partial V}{\partial x} + Q_j - Q_r - Q_F \quad (3)$$

where $\varepsilon = \frac{3}{2} \frac{T_p}{m} + \frac{V^2}{2}$. The radiation energy flux Q_r includes the radiation for a continuum

spectrum. The particle convection flux Q_F includes energy associated with electron and ion fluxes to the dielectric wall that lead to plasma cooling. More details about the capillary model can be found elsewhere [3,4]. The capillary wall ablation is modeled in the framework of the previously developed kinetic model. [5] Two different layers between the ablated surface and the plasma bulk are considered as shown in Fig. 1: (i) a kinetic non-equilibrium layer adjacent to the surface with a thickness of about one mean free path; and (ii) a collision-dominated layer with thermal and ionization non-equilibrium. The plasma-wall transition layer includes also an electrical sheath described below. Based on the developed, the model plasma parameter distribution in the capillary was calculated.

In this study we consider a specific capillary plasma source for an ETC developed at the Army Research Laboratory and described recently elsewhere [1,4]. Capillary geometry determines the ablation process in the capillary by affecting the mass and energy balance. The dependence of the ablated mass on the peak discharge current is shown in Fig. 2. The ablated mass has a linear dependence on the discharge peak current. For comparison, experimental data are also shown in Fig. 2. It can be seen that both simulations and experiment suggest that the ablated mass increases as the capillary inner diameter decreases. This effect is explained by increased current density in the capillary, which affects the ablation rate through Joule heating. Reasonable agreement is obtained although the predicted ablated mass is lower than that measured in the experiments. It should be pointed out that the above calculations were performed assuming that returned atoms and ions do not form film at the polyethylene surface. On the other hand it can be considered that only carbon atom and carbon ion deposition takes place, as the hydrogen atoms and ions will be re-evaporated [8]. The last assumption is supported by previous studies of dielectric (Teflon) ablation into C-F plasmas which indicated that a dielectric can be significantly carbonized (charred) dependent on operational conditions.[8] In this study we also investigate parametrically effects of condensation at the dielectric surface. We introduce a new parameter, v , which is the

fraction of the backflux that condenses at the surface. In the case of $v=1$, all particles returning to the surface will condense, while small parameter v means that only a fraction of the backflux forms the film. Dependence of the ablated mass on this parameter is shown in Fig.3. One can see that the best agreement with experimental data is achieved if $v=0.6-0.7$.

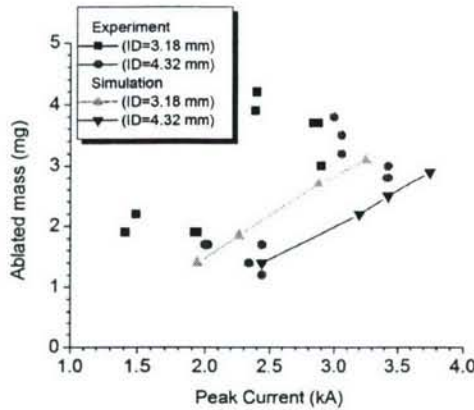


Figure 2. Dependence of the ablated mass (polyethylene) on the peak discharge current. Comparison of experiment and simulations.

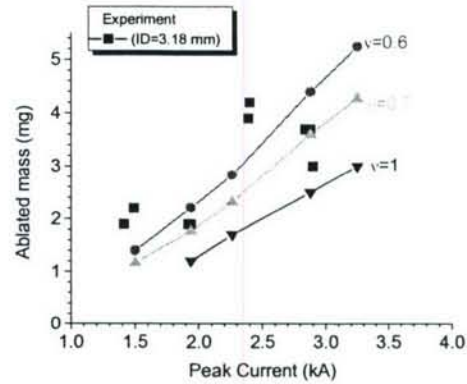


Figure 3. Dependence of the ablated mass (polyethylene) on the peak discharge current with deposition fraction as a parameter. Comparison of experiment and simulations.

2. Modeling of the plasma-propellant interactions

Plasma-propellant interactions are modeled based on the kinetic theory of ablation model which was adapted from previous work by Keidar *et al* [5]. To model the propellants, vapor pressure and enthalpies of sublimation are calculated via an averaging technique based on their percent composition of constituent compounds obtained from Miller [6], as no experimental data is available. The ablation model is coupled with a 1-D thermal model to predict the surface heat flux, q , incident on the propellant. More details can be found in Ref. 7.

The effective heat flux can be modeled as $q = q_{\text{conv}} + q_{\text{rad}}$, the sum of the convective (particle flux) and radiation heat fluxes, respectively. The radiation flux is thus the difference of q and q_{conv} . Heat flux q

and plasma density n_0 are used as parameters in the thermal model. Once the surface temperature profile during the pulse is determined it is combined with the estimate for surface temperature after the pulse and numerically integrated to yield a total ablated mass for some q , n_0 pair. It is assumed that for both propellant samples, the capillary generates a plasma with identical properties. Thus any differences in the incident heat fluxes are due to differences in the propellants themselves. The model predicts that JA2 will consistently have a higher effective heat flux than XM39 (Fig. 4), and that XM39 will have a higher surface temperature. As plasma density increases, heat flux (or surface temperature) will decrease, as evident in Fig. 4.

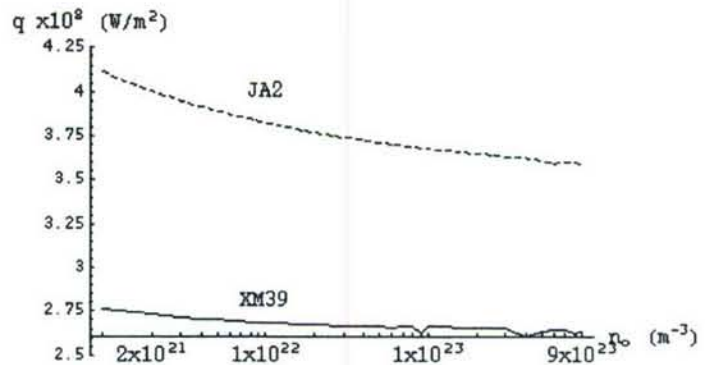


Fig. 6. Effective plasma heat flux to each propellant predicted by model, where ΔM is the experimental value.

A comparison of the optical properties of the two propellants is made. Nitramine composite propellants are opaque to most wavelengths, and studies indicate that they do not allow radiation to penetrate and effect change in-depth. It has been demonstrated that JA2 allows radiation to penetrate in-depth, with physical and chemical changes occur up to approximately 1 mm into the propellant. In addition, it has been determined in experiments that XM39's reflectivity may be as high as 50% [7]. This evidence

suggests that the difference between the heat flux to JA2 and XM39 is due to the optical properties of each propellant, specifically to penetrating radiation from the plasma. As noted earlier, the radiative heat flux for JA2 is expected to be much higher than for XM39, although XM39 should still have a small radiative flux due to surface heating. Thus the difference between the heat flux to each propellant, Δq , can be roughly interpreted as the difference in penetrating radiation flux between the propellants. It should be noted that Δq represents only a small fraction of the radiative heat available in a black body plasma at $T_e=1.5$ eV. This can be partially explained by indications that vaporized propellant can act as a plasma radiation shield, helping to block some of the radiation flux [1]. Continuing this line of reasoning, $\Delta q/q_{JA2}$ can be approximated as the percent of JA2's heat flux attributable to penetrating radiation (Fig. 5), which drops from 33% at low density to 28% at high density. This indicates that the percentage of heat flux due to radiation is responsible for between a quarter and a third of the total effective heat flux received by the propellant.

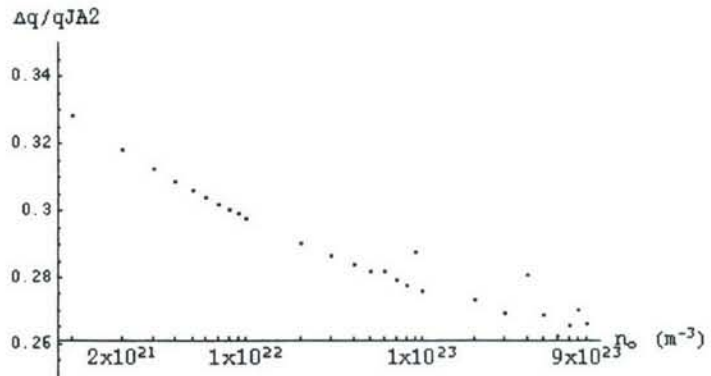


Fig. 5. $\Delta q/q_{JA2}$, the dependence of the fraction of radiation flux on the plasma density, in the vicinity of the propellant.

Acknowledgment

The authors gratefully acknowledge the financial support by the Army Research Office, Grant No. W911NF-04-1-0251 (Dr. Kevin McNesby, technical monitor). The authors also thank Dr. Dick Beyer, Dr. Michael Nusca, Dr. Anthony Williams, and Dr. Rose Pesce-Rodriguez from the Army Research Laboratory for very useful discussions and suggestions.

References

- [1] R.A. Beyer and R. A. Resce-Rodrigues, "Experiments to define plasma-propellant interactions", IEEE Trans. Magnetics, vol. 39, 2003, p. 207
- [2] J. Li, T.A. Litzinger and S.T. Thynell, "Interaction of capillary plasma with double-base and composite propellants", J. Prop. Power, vol. 20, 2004, p. 675
- [3] M. Keidar and I.D. Boyd, Ablation study in the capillary discharge of an electrothermal gun, *Journal of Applied Physics*, vol. 99, 053301, 2006.
- [4] M. Keidar, I.D. Boyd, A.W. Williams and R.A. Beyer, Ablation phenomena in a capillary sustained plasma, 13th Electromagnetic launch Symposium, Berlin, Germany, June 2006, Paper 161
- [5] M. Keidar, I. D. Boyd and I. I. Beilis, "On the model of Teflon ablation in an ablation-controlled discharge," *J. Phys. D: Appl. Phys.* vol. 34, pp. 1675-1677, 2001.
- [6] M. S. Miller, "Thermophysical Properties of Six Solid Gun Propellants," *ARL-TR-1322*.
- [7] A. J. Porwitzky, M. Keidar and I.D. Boyd, Modeling of the plasma-propellant interaction, 13th Electromagnetic launch Symposium, Berlin, Germany, June 2006, Paper 162
- [8] M. Keidar, I.D. Boyd, E. Antonsen, F. Gulchinski, G.G. Spanjers, "Propellant charring in pulsed plasma thrusters", J. Prop. Power, vol. 20, pp. 978-984, Nov. 2004.

LIQUID FUEL COMBUSTION USING POROUS INERT MEDIA

(Grant/Contract Number DAAD 190210082)

Principal Investigators: Ajay K. Agrawal¹ and Subramanayam R. Gollahalli²

¹Department of Mechanical Engineering
University of Alabama, Tuscaloosa, AL 35487

²School of Aerospace and Mechanical Engineering
University of Oklahoma, Norman, OK 73019

SUMMARY/OVERVIEW:

Combustion using porous inert media (PIM) offers benefits such as high power density, stable operation over a wider turndown ratio, homogeneous product gases, lower combustion noise and reduced emissions of NO_x, CO, particulates, etc. Much of the previous research using PIM has focused on combustion of gaseous fuels, whereby the reactants are preheated by upstream transfer of heat from the flame region. In case of the flame stabilized within the PIM, the heat transfer is dominated by radiation and conduction from the reaction zone. The focus of the present study is to achieve lean premixed combustion (LPM) of liquid fuels using PIM. In particular, we seek to recirculate energy released in the reaction zone to pre-vaporize the liquid fuel and preheat the fuel-air mixture upstream of the combustor. Further, a PIM section is used upstream of the combustor section to promote fuel-air mixing and hence, to achieve uniform combustion without the fuel-rich or fuel-lean regions that tend to increase the emissions of particulates, CO, NO_x, and UHCs. Two test facilities were developed in this project; (i) a non-reacting set up with controlled heat input to the PIM to simulate upstream heat transfer, and (ii) a combustor set up capable of providing emissions data over a range of operating conditions. The experiments are complemented with computational fluid dynamic analysis to model the fuel vaporization, fuel-air premixing and reactant preheating. Combustion experiments were conducted using a commercially available injector and a custom designed two-fluid atomizer. Results show that a finite fuel-air premixing region upstream of the PIM section is necessary for complete mixing, and hence, to achieve low-emissions with liquid fuel combustion. The length of the premixing section can be reduced significantly through injector design. The study has resulted in a combustor concept with an annular heat recirculation zone to further increase the heat recirculation by minimizing the heat loss through the combustor wall.

TECHNICAL DISCUSSION

Combustion in porous inert media is based on excess enthalpy concept in which thermal energy from the reaction zone is recirculated upstream to preheat the fresh fuel-air mixture via solid radiation and conduction¹. Much of the research on PIM combustion in the past has focused on gaseous fuels²⁻³. One of the first studies using liquid fuel (heptane) in PIM was conducted Kaplan and Hall⁴. They found that the combustion stabilized over the equivalence ratio (ϕ) range of 0.57-0.67. The burner stability was dependent upon the droplet size and the distance between the PIM and fuel injector. Emission measurements indicated complete combustion with single digit CO emissions and NO_x emissions ranging between 15-20 ppm. Jugjai et. al.⁵ showed that strong energy feed-back by radiation from the flame enabled

evaporation of kerosene. The liquid kerosene supplied at normal temperature experienced preheating when it came in contact with the high temperature porous surface of the burner at the top. The burner acted not only as a pre-heater but also as a distributor for the liquid fuel. The evaporation of kerosene occurred within the porous burner to result in lean premixed (LPM) combustion.

PIM combustor consists of a fine pore region followed by a coarse pore region, where the flame is stabilized. The fine pore region serves as the pre-heater by facilitating upstream heat transfer by conduction and it also prevent flashback into the premixing region. An important requirement to achieve low pollutant emissions in liquid fuel combustion is that the fuel is fully pre-vaporized and premixed with air, prior to reaching the reaction zone. If the injector is placed very close to the PIM, the fuel pre-vaporization and/or fuel-air premixing may be inadequate and hence, droplet combustion mode producing diffusion flames would ensue. Thus, the distance between the fuel injector and PIM (denoted as the premixing length) is an important parameter to maintain LPM combustion needed for low-emissions. From practical considerations, the premixing length must be minimized to yield a compact combustion system. The trade-off between the premixer length and completeness of fuel-air premixing depends upon the operating conditions such as the co-flow air temperature and geometric parameters including the PIM configuration affecting thermal feedback upstream of the combustion zone.

The test setup for combustion experiments shown in Fig. 1 consists of four sections, namely, the inlet plenum, the vaporization and mixing section, the PIM section, and the emissions shield. The combustion air entered through fittings mounted on the inlet plenum on the upstream end of the apparatus. The injector could be located at any axial position within the vaporization and mixing section. Two injectors were investigated in this study as shown in Fig. 2. The air-assist atomizer is commercially available product (Delavan, Type SNA) and the swirling-air atomizer

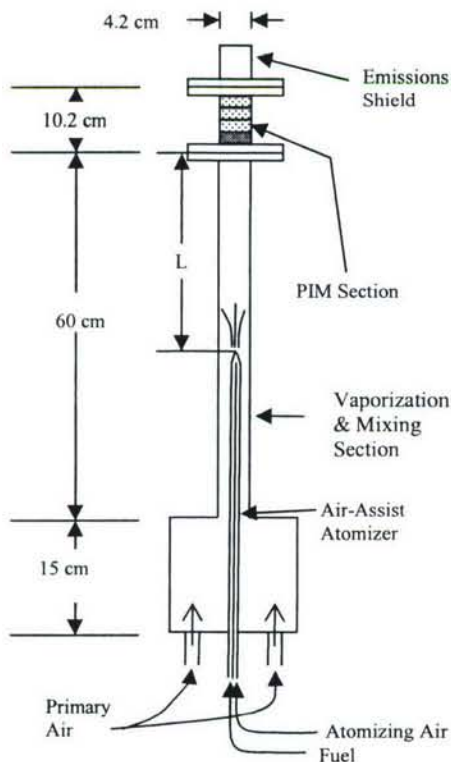


Figure 1. Schematic Diagram of the Combustor Setup

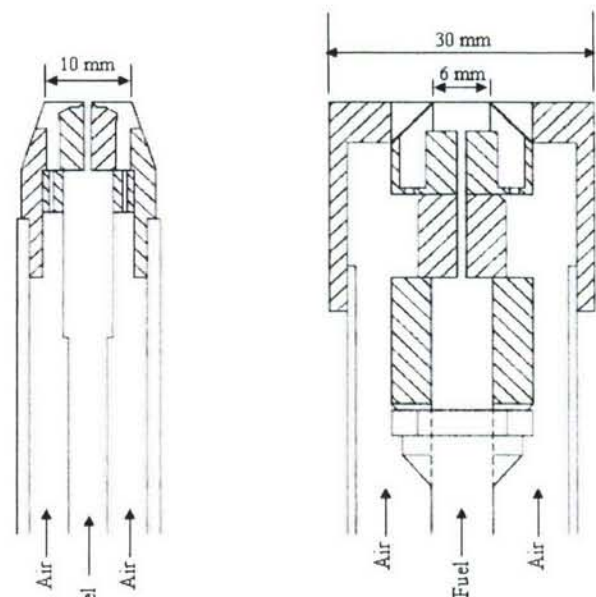


Fig. 2 (a) Air-assist atomizer (left), and (b) Swirl-air atomizer (right)

provided by Parker Hannifin.⁶ PIM is placed in the preheating section and the combustion section. The flow cross-section of both of these sections is 4.2 cm x 4.2 cm. Several PIM configurations were tested as shown in Fig. 3. In the baseline configuration C1 (or 26/4-4-4), the preheating section was a 2.5 cm thick, 26 pores per cm (ppcm) porous piece and the reaction zone consisted of three 4 ppcm porous pieces occupying the 7.5 cm length downstream of the preheating zone. Each porous piece fit tightly into the test section. Product gas was sampled by quartz probe with a tapered tip to quench the reactions. The cooled sample was passed through water traps prior to measuring the CO and NO_x emissions by electrochemical analyzers.

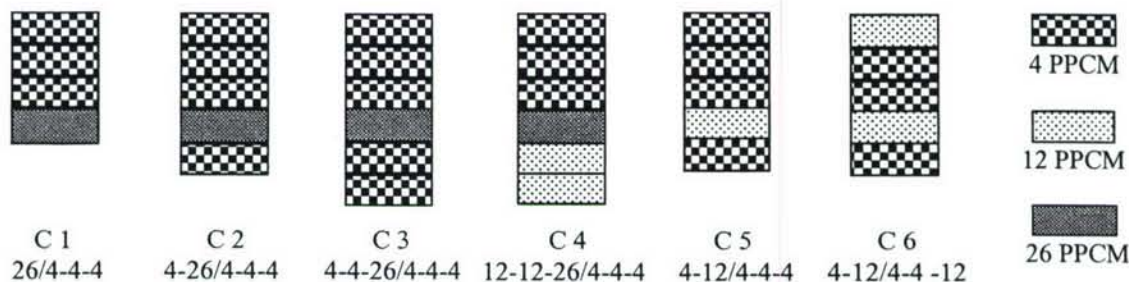


Figure 3. Porous Media Configurations

Base line conditions were established as equivalence ratio (Φ) of 0.67, primary inlet air temperature (T_{in}) of 475 K and heat release rate (Q) of 3.3 kW and air flow rate of 135 standard liters per minute (slpm). Measurements were taken at the center of the emissions shield to determine the variation in emissions in the streamwise direction. Results showed that the reactions occur mainly within the porous inert media. The effect of the injector location on CO and NO_x concentration is shown in Fig. 4 (a) and (b) for both the air-assist atomizer and the swirling-air atomizer. The CO and NO_x concentrations are nearly the same for $L = 60$ cm to about 40 cm suggesting that the fuel is fully vaporized and premixed with air. For $L = 35$ cm to about 25 cm, there is a slight increase in the CO and NO_x concentration for the air-assist atomizer. However, the CO and NO_x concentration for the swirling-air atomizer are lower indicating improved premixing of fuel and air within the injector. For $L < 17.5$ cm, soot emitting orange flamelets signifying droplet combustion in diffusion mode were visually observed.

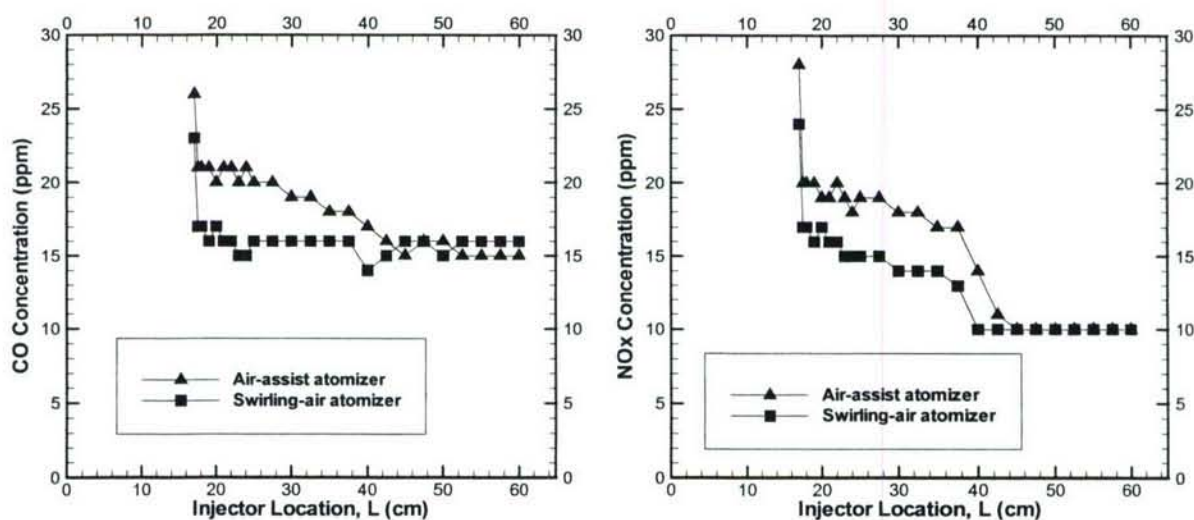


Figure 4. CO and NO_x Concentration at Centerline for Baseline Conditions

Figures 5 (a) and (b) show the CO and NO_x emissions versus injector location for the baseline configuration (C1) and modified configuration (C2). For each case, L was varied until combustion in droplet mode was visually observed. Results show that configuration C2 required a shorter premixing length ($L = 9$ cm) to avoid droplet combustion compared to configuration C1. The additional porous piece in configuration C2 increased the heat transfer from the combustion zone to the pre-vaporizing porous pieces. Results in Fig. 5 show that CO emissions decrease significantly with either one or two preheat pieces compared to the case with no preheat piece. However, the number of preheat pieces does not significantly affect the emissions.

The combustor used above is prone to significant heat loss from the walls. We have developed a combustor concept with an annulus to recover wall heat transfer to preheat the reactants. The concept shows excellent performance in both large and small scales combustion systems⁷⁻⁸. Experimental results with non-reacting set up are presented in detail in Ref. 9.

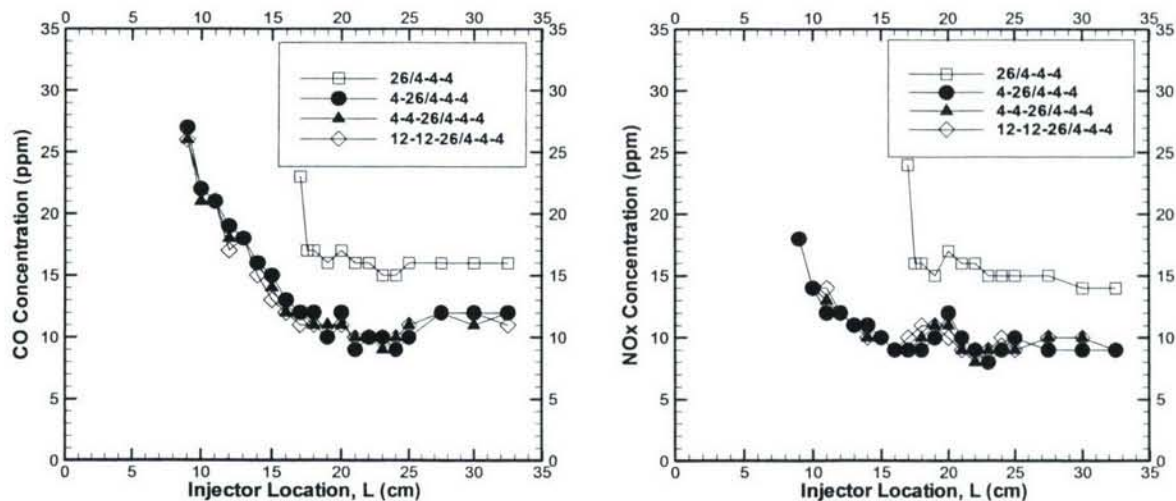


Figure 5. Effect of Preheat Section on (a) CO and (b) NO_x Concentrations

REFERENCES

- Hardesty, D. R., and Weinberg, F. J., "Burners Producing Large Excess Enthalpies," *Combustion Science & Technology*, Vol. 8, 1974, pp. 201-214.
- Smucker, M. T., and Ellzey, J. L., "Computational and Experimental Study of a Two-Section Porous Burner," *Combustion Science & Technology*, Vol. 176, 2004, pp. 1171-1189.
- Marbach, T. L., and Agrawal, A. K., "Experimental Study of Surface and Interior Combustion Using Composite Porous Inert Media," *Journal of Engineering for Gas Turbines and Power*, Vol. 127, 2005, pp. 307-313.
- Kaplan, M., and Hall, M. J., "The Combustion of Liquid Fuels Within a Porous Media Radiant Burner," *Experimental Thermal & Fluid Science*, Vol. 11, 1995, pp. 13-20.
- Jugjai S., Wongpanit N., Laoketkan T., and Nokkaew S., "The Combustion of Liquid Fuels Using a Porous Medium," *Experimental Thermal & Fluid Science*, Vol. 26, 2002, pp. 15 – 23
- Mansour, Adel, Parker Hannifin Corporation, Personnel communication, 2006.
- E.R. Newburn and A.K. Agrawal, 2006, "Liquid Fuel Combustion using Heat Recirculation through Annular Porous Media," *Journal of Engineering for Gas Turbines & Power*, in press
- Marbach, T., and Agrawal, A.K., 2006, "Heat Recirculating Combustor Using Porous Inert Media for Mesoscale Applications," *Journal of Propulsion and Power*, vol. 22, pp. 145-150.
- Periasamy, C., Sankara, Chinthamony, S.K., and Gollahalli, S.R., 2006, "An Experimental Evaluation of Evaporation Enhancement with Porous Media in Liquid Fueled Burners," *Journal of Porous Media*, in press.

TURBULENT MIXING AND COMBUSTION FOR HIGH-SPEED, AIR-BREATHING PROPULSION APPLICATIONS

AFOSR Grant FA9550-04-1-0020

Paul E. Dimotakis

Graduate Aeronautical Laboratories, California Institute of Technology, Pasadena, CA 91125

Summary/Overview

This research focuses on fundamental investigations of mixing and combustion, in turbulent, subsonic, and supersonic flows and is motivated by problems in high-speed air-breathing propulsion. The work is a closely coordinated effort between experiments and numerical simulation, and exploits recent developments in diagnostics and instrumentation.

Technical Discussion

A successful hydrocarbon-fueled scramjet engine will rely on a detailed understanding of the turbulent processes that mix fuel and air within the device, as well as the chemical kinetics and flame processes that result in conversion of the reactants to products.

Work on compressible turbulent mixing in complex geometries under this grant is focused on studying the flow control and mixing achieved in the expansion-ramp geometry (Figs. 1–2). In this geometry, a high-speed upper “air” stream is expanded over a ramp inclined at 30 degrees to the flow. A low-speed “fuel” stream is injected through perforations in the ramp and generates a mixing layer between the two streams. A key feature of this flow is the recirculation zone that transports hot products back toward the fuel injection location and provides a low-strain-rate flameholding region. In fully subsonic flow, the total amount of mixed fluid exiting the device was found to decrease with increasing top stream velocity for a velocity ratio of $U_2/U_1 = 0.1$.

Ongoing work targets flow control and mixing in the expansion-ramp geometry for supersonic top-stream flows. Figure 1 shows a composite Schlieren image from a pair of experiments with a $M_1 = 1.5$ flow with an injection resulting in $U_2 = 5$ m/s. The flow expands down the ramp, creating a corrugated mixing layer that interacts with the reflected waves off of the upper guidewall. The top-wall boundary layer separates upstream of the measurement rake.

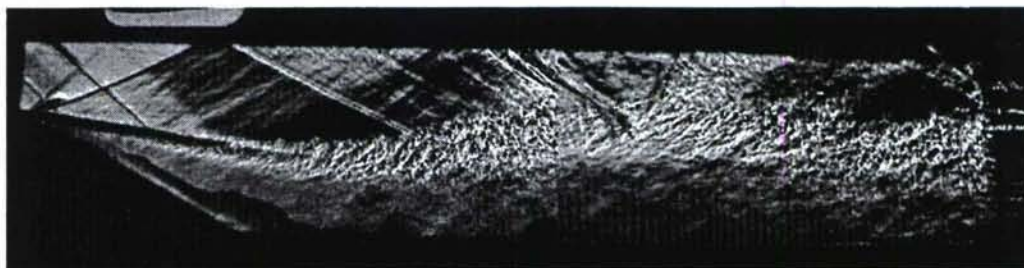


Figure 1 Composite Schlieren image of the expansion-ramp flow for $M_1=1.5$ and $U_2=5$ m/s.

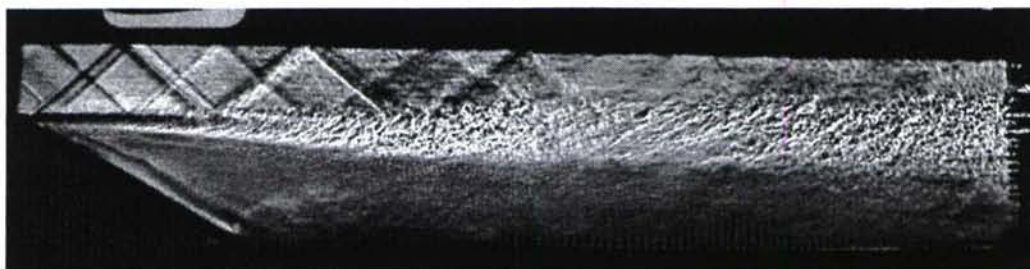


Figure 2 Composite Schlieren image of the expansion-ramp flow for $M_1 = 1.5$ and $U_2 = 45$ m/s.

As found for a subsonic upper stream, this flow can be controlled by varying the mass injected through the perforated ramp. Figure 2 is a composite Schlieren image for a lower-stream injection of $U_2 = 45$ m/s and the same top-stream conditions and illustrates the considerable control that be exercised. The shear layer is almost horizontal, the upper-stream wave system remains uniform, and no boundary-layer separation occurs. A measure of the aerodynamic performance of the device is the overall pressure coefficient, $C_p = 2(p_e - p_i)/(\rho U_1^2)$, where p_e and p_i are the exit and inlet pressures, respectively. The pressure coefficient is plotted in Fig. 3 for the $M_1 = 1.5$ experiments with variable injection and heat release. As expected, the slope of this profile has the opposite sign as for a subsonic inlet. As in the subsonic flow (Johnson 2005), mass injection exerts significant control authority. Addition of heat release allows the same pressure coefficient to be achieved with a mass injection almost a factor of four lower than the nonreacting flow. These experiments are being performed by J. Berghthorson and A. Bonanos.

An accompanying computational effort has concentrated on verification of the complex code and simulations in complicated geometries. The Compressible LES fluid dynamics solver of the Virtual Test Facility developed under the DOE-sponsored Caltech ASC program is used for the simulations. The solver has Adaptive Mesh Refinement capabilities and implemented in a fully parallel manner with dynamic data redistribution (Pantano *et al.* 2006). The solver was verified against the theoretical predictions of the Linear Stability Analysis (LSA) theory for both free and confined spatially evolving shear layers. The growth rates from two-dimensional simulations exhibit very good agreement with the LSA predictions.

Figure 3 also shows the computed instantaneous isosurfaces of the spanwise vorticity from a three-dimensional LES using the stretched-vortex subgrid-scale model (Voelkl & Pullin 2000), with no injection through the ramp. This is the first of a series of simulations that include the complex geometry of the corresponding experiments. The computed flow shows good agreement with the experimentally observed behavior. A quantitative comparison is currently underway. The numerical simulations are part of the Ph.D. research of G. Matheou.

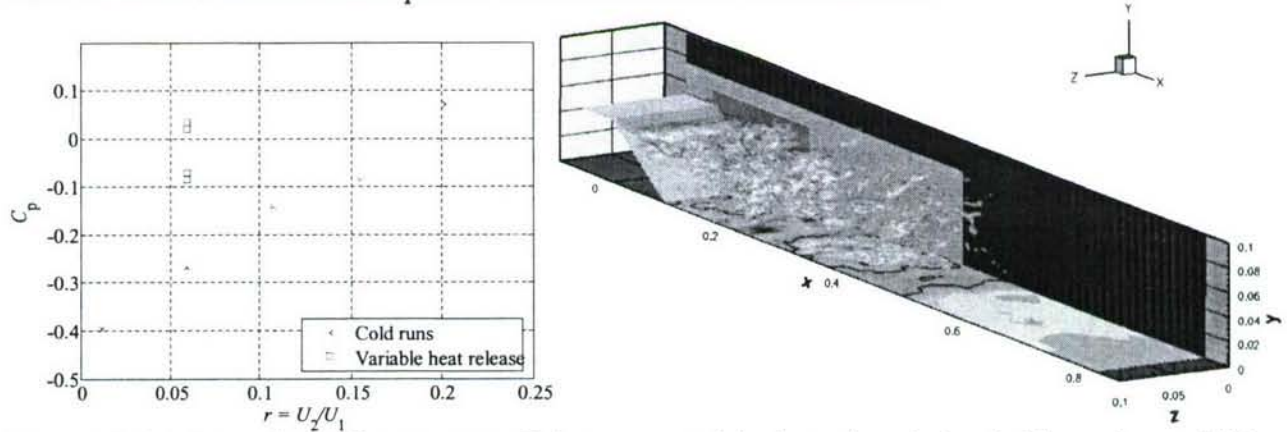


Figure 3 Left: Measured overall pressure coefficient vs. mass injection ratio and chemical heat release. Right: Computational subsonic top stream with no injection through a solid ramp (spanwise vorticity isosurfaces). Streamwise velocity contours are shown on the bottom wall and the grid density is depicted on the back wall.

A second experimental and numerical-simulation effort targets the combustion chemistry for hydrocarbon fuels of interest for scramjet propulsion applications. The dimensionality of the data sets used to validate chemical-kinetic models for hydrocarbon combustion is considerably lower than the number of constants involved leading to indeterminacies and non-uniqueness. To fully validate chemical-kinetic/thermodynamic/transport models for combustion, experimental data must be provided over a wide range of parameters. The key parameters affecting flame propagation are fuel type, mixture composition, and pressure. High accuracy measurements in methane, ethane, and diluted ethylene flames have been recorded for different compositions at

atmospheric pressure (Bergthorson and Dimotakis 2006b). The experiments provide a test-bed for systems to be integrated into variable-pressure experiments ($p \leq 12$ atm). The approach relies on simultaneous measurements of flow velocity and CH-radical profiles in strained flames in a jet-wall stagnation flow using Particle Streak Velocimetry (PSV) and Planar Laser Induced Fluorescence (PLIF), respectively. Concurrent measurements of mixture composition and stagnation-plate temperature provide accurate boundary conditions for numerical simulations using the *Cantera* software package. These simulations rely on an axisymmetric one-dimensional hydrodynamic model, a multicomponent transport formulation, and various detailed chemistry models. This part of the work is part of the PhD research of J. Bergthorson and L. Benezech.

Systematic uncertainties in particle velocimetry are accounted for by modeling particle-inertia, thermophoretic, and finite particle-track interval effects (Bergthorson and Dimotakis, 2006a). Figure 4 shows a sample comparison of modeled-PSV profiles to PSV data in a $\Phi = 1.0$ diluted C_2H_4 flame for several state-of-the-art kinetic mechanisms: GRI-Mech 3.0, Davis-Law-Wang 1999, San-Diego 200308 and San-Diego 200503. GRI-MECH and San-Diego 200308 mechanisms significantly overpredict ethylene flame speeds, whereas the DLW99 and San-Diego 200503 predictions agree with the experiment. A new Particle Tracking Velocimetry (PTV) technique is being developed that relies on a high-power, high-repetition rate Nd:YLF laser (up to 20 kHz) and a high-resolution CCD camera (11 Mpix). The new PTV technique retains the low particle loading advantages of PSV, increasing temporal and spatial resolution, and signal amplitude at higher speeds, and will greatly expand the range of flow velocities that can be measured. Investigations of pure ethylene flames, blends of C_1 - C_2 and hydrogen flames, and larger hydrocarbon fuels will be undertaken at variable pressure.

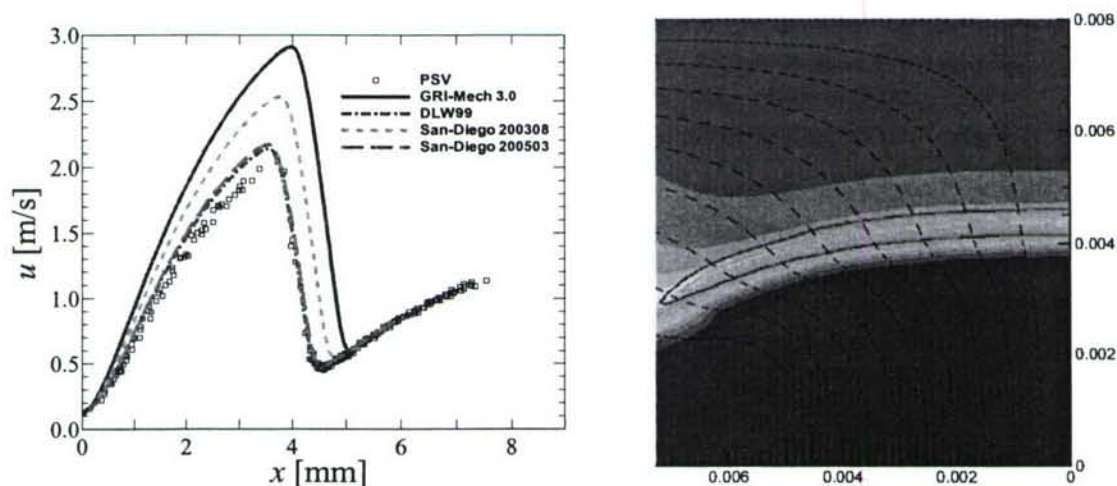


Figure 4 Left: $\Phi = 1.0$ C_2H_4 flame, 17% $O_2/(O_2+N_2)$. Right: Two-dimensional simulation of low Mach number stagnation flame. The solid background color shows temperature field, the color solid lines represent CH mass fraction contours, and the black dashed lines represent streamlines with dash length proportional to velocity.

In a parallel numerical simulation effort, a code has been developed to perform Direct Numerical Simulations (DNS) of the experimental geometry in a 2D axisymmetric domain with detailed hydrocarbon chemistry modes that resolves all relevant length scales. The code integrates the unsteady low Mach number Navier-Stokes equations. Our new formulation satisfies both the state equation and the continuity equation while successfully removing sound waves from the simulation and allows temporal integration with time steps unrestricted by acoustic waves. The code was verified by the method of manufactured solutions and exhibits spectral convergence. A snapshot from the simulation is shown in Fig. 4 (right). This work is part of the Ph.D. research of K. Sone, performed in collaboration with D. Meiron, and cofunded by Caltech's ASC Center.

Modeling CH₄ combustion in air requires more than 50 species and ~ 200 reactions, or more. A state-of-the-art approach combining sensitivity analysis of laminar flame speed to each reaction rate and reaction-pathway analysis is under development to automatically identify causes of discrepancies between the predictions of multiple mechanisms. Sensitivity analysis alone already provides answers, such as in the case of the systematic overprediction of flame speeds by all mechanisms except DLW99, in an atmospheric lean methane-air flame. Sensitivity analysis first identifies reactions that affect the solution the most. Rates for these reaction rates can then be compared between mechanisms. This work is part of the PhD research of L. Benezech.

Using high frame-rate imaging with the in-house developed KFS imaging system, the NSF-funded Teravoxel high-speed/-volume data-acquisition system, and a synchronized scanning laser beam, or sheet, three- and four-dimensional imaging of the scalar field in grid turbulence was recorded for the first time, to our knowledge. Preliminary experiments were performed in the GALCIT Free Surface Water Tunnel (FSWT) at Taylor Reynolds numbers below the mixing transition of $Re_T \sim 100$. Extensions in optics and a new flow facility presently under development will allow such measurements to be performed over a range of Reynolds numbers spanning from below to above the mixing transition. This part of the work is performed by J. Berghorson, D. Lang, B. Valiferdowski, and P. Dimotakis.

References

- BERGTHORSON, J.M. & P.E. DIMOTAKIS 2006a Particle velocimetry in high-gradient/high-curvature flows. *Experiments in Fluids* (to appear).
- BERGTHORSON, J.M. & P.E. DIMOTAKIS 2006b Premixed laminar C1-C2 stagnation flames: experiments and simulations with detailed thermochemistry models. *Proceedings of the Combustion Institute* 31 (to appear).
- JOHNSON, M.B. 2005 *Aerodynamic Control and Mixing with Ramp Injection*. Engineer's thesis, California Institute of Technology.
- PANTANO, C., R. DEITERDING, D.J. HILL, & D.I. PULLIN 2005, A low-numerical dissipation patch-based adaptive mesh refinement method for large-eddy simulation of compressible flows. *Journal of Computational Physics* (submitted).
- VOELKL, T., & D.I. PULLIN 2000 A physical-space version of the stretched-vortex subgrid-stress model for large-eddy simulations. *Physics of Fluids* 12:1810-25.

PLASMA RESEARCH FOR AEROSPACE PROPULSION

Principal Investigator: Biswa N. Ganguly

AFRL/PRPE
WPAFB OH 45433

SUMMARY/OVERVIEW:

Develop plasma devices for improved ignition, flame holding, and flow control. Also, generate microscopic non-equilibrium conditions to control macroscopic transport properties and kinetics of gas flows

TECHNICAL DISCUSSION:

We report experimental investigations of the effects of DC electric fields on pre-mixed propane/air flames. The current study complements previous work^{1,2} and extends recent results³ which showed that dramatic modifications of the reaction zone of propane/air flames could be achieved with 3-6 kV applied voltages. Potential practical applications in a wide variety of combustors include providing for controlled flame holding and enhancement of reactant mixing, the latter possibly offering reductions in emissions of unwanted combustion products such as CO and carbon clusters (soot). More specialized applications to combustion in microgravity might also be possible.

Modest applied voltages are capable of driving the flame from laminar (stable, conical flame geometry) to a wrinkled laminar geometry (cellular; multiple laminar flamelets), with some evidence of the approach to turbulence regimes. The electric field acts directly on the highly localized, chemiionization-derived H_3O^+ , HCO^+ and other positive ions in the flame reaction zone, significantly increasing their mass diffusivities and thereby modifying the Lewis numbers of the ionic species. The observed result is a diffusive-thermal instability, typical of flames with global Lewis numbers less than one; it is most likely caused by the production of H atom and OH radicals by the dissociative recombination of $\text{H}_3\text{O}^+ + e \rightarrow \text{H}_2\text{O} + \text{H}$ or $\text{H}_2 + \text{OH}$, and $\text{HCO}^+ + e \rightarrow \text{H} + \text{CO}$ near the burner head, which is the cathode surface for the polarity of the applied voltage. The increased differential diffusional velocity of the reaction zone positive ions strongly affects the bulk flame speed, and the thermo-diffusive instability results in the flame front collapsing toward the burner head and taking on a wrinkled laminar geometry. High-speed two-dimensional imaging of the flame response to a pulsed voltage showed that the characteristic time³ required to complete the field-induced flame stretch is on the order of 5 ms, somewhat more rapid than that found in previous work⁴, but still indicative of the fluid mechanical nature of the flame response to the external field. Such images also show electric-field-induced unburned pocket formation which is a characteristic of turbulent combustion.

At higher continuous bias voltages (up to 6 kV), the flames are observed to make a further transition from cellular to highly turbulent flame fronts over a wide range of flow/bias voltage conditions. In much of the previous work^{1,2,4}, the effects of DC electric fields on flames was described in terms of the body force known as the ionic wind, which has been shown to be capable of providing a maximum pressure difference across the flame^{3,5} of only 0.0004 atm. This applied voltage-current induced pressure change is very small to cause the observed change in either the flame speed or the

flame heat release rate fluctuations through direct pressure effects. The DC-field-induced transition from laminar to highly turbulent combusting flows is quantified by direct high-speed imaging of the flame heat release rate fluctuations by measuring the chemiluminescence intensity using 200 μ sec gated ICCD as well as by wide band width spectral intensity measurements of flame radical species CH^* , C_2^* and OH^* emissions. Fast Fourier Transforms (FFT) of the oscillating flame front emission signals were used to document the large differences between zero field (laminar flow) and DC-field driven turbulence conditions. Additionally, under DC applied voltage, the collapsed reaction zone is observed to undergo a transition from a low amplitude and low frequency oscillation typical of a laminar flame, to a large amplitude high frequency oscillation, similar to a thermo-acoustically perturbed flame⁶. Efforts to quantify these newly observed oscillatory modes of the flame front are presented.

The burner, used in this experiment, produces stable, laminar flow, conical reaction zones with a base diameter of 17 mm and height that varies with equivalence ratio and overall flow rate. Total flow rates varied between 12,000 – 30,000 sccm, which provides flow velocities on the axis of the burner from roughly twice propane's stoichiometric laminar flame speed (0.44 m/s) to well past the burner's blow off flow rate at zero applied voltage. Equivalence ratios used range from 0.8 to 1.4. DC fields are applied to the flames by connecting a 6 kV power supply across the grounded burner head, and positively biasing an electrode centered typically 40 mm above the grounded burner.

The magnitude of the current drawn, for a given applied voltage, with our anode configuration is nearly an order of magnitude higher than previously reported^{1, 2} measurements for electrically biased pre-mixed hydrocarbon flames. Since the current is mobility limited, the larger current drawn at lower applied voltage will result in a significant increase of the positive ion flux in our experimental conditions, as compared to the previous measurements. If the dissociative recombination driven production of limiting light reactants is the source for the lowering of the Lewis number below a critical Lewis number, this could be one of the most important reason why it was possible to us achieve the level of thermo-diffusive instability that was not possible in previous measurements.

A transition from cellular flame structure, at lower pulsed applied voltage, to a flame instability caused by the larger pulsed applied voltage is presented in Figure 1, which shows an unburned pocket formation (images were acquired with 1 ms time separation), suggesting the onset of intense turbulence conditions. Chen et. al.⁷ have published an extensive numerical study of the pocket formation, and among their findings they note that pocket formation, channel closing and pocket burnout all correspond to strongly curved flames.

The observations cited above, including the images of unburned pocket formation of Figure 1, point to the onset of significant levels of electric-field-induced turbulent combustion. Further improvements in the coupling of the electric field to the flame, and the use of a higher voltage DC power supply that permit larger electrical energy input to the flame would drive the flames toward increasingly turbulent conditions (i.e. increasingly smaller scale turbulence features) associated with the distributed reactions regime. At particular higher electric field/flow combinations (3-6 kV applied voltage), the electric pressure effect causes the flame front to undergo large amplitude, high frequency oscillations over large portions of the flame front surface. These conclusions are supported by the high speed, two-dimensional images of the flame front which includes CH^* emissions at 431 nm, OH^* emissions at 308 nm, and C_2 emissions at 516 nm, as shown in Figures 2, 3, and 4 respectively. Those images show that OH and CH radicals are redistributed by the applied electric field in essentially the same way. However, the total integrated OH and CH emission intensities are independent of the applied field. Given that the electric field depresses the flame front toward the burner head, this behavior suggests that the effect of the thermo-diffusive instability is also to increase the combustion intensity.

The final data reported here are derived from measurements of the current and flame front optical signal oscillations. Figure 5 shows a series of fast Fourier transforms (FFTs) of broadband and spectrally

filtered flame front emissions, as well as the FFT of the oscillating current drawn from the external bias supply. Again, the experimental conditions are the same as those used for the imaging data shown in Figures 2, 3, and 4 (21 slm overall flow and equivalence ratio of 1.2) except that the bias used was only 4 kV.

The top left FFT of Figure 5 shows the very low amplitude, featureless power spectrum of the flame's broadband emissions under zero bias. It indicates stable laminar flow. With a 4 kV bias the flame front is driven into a large amplitude resonate-like oscillation with a fundamental frequency near 300 Hz and harmonics ranging up to 1.8 kHz. Essentially the same responses are seen again from broadband emissions and those corresponding to chemi-excited CH, C₂ and OH. Furthermore, the current passing through the flame also exhibits a power spectrum that is essentially identical to that of the flame front emissions. This is indicative that the voltage-current behavior is also dependent on the heat release rate modulation similar to the chemiluminescence intensity.

References

1. Calcote, H.F. and Berman, C.H., in *Fossil Fuels Combustion Symposium PD-Vol. 25*, S.N. Singh, Ed., 25 (1989).
2. Bradley, D. and Nasser, S.H., *Combust. Flame* 55, 53 (1984).
3. Marcum, S.D. and Ganguly, B.N., *Combust. Flame* 143, 27 (2005).
4. Kono, M., Carleton, F.B., Jones, A.R. and Weinberg, F.J., *Combust. Flame* 78, 357 (1989).
5. Pedersen, T. and Brown, R.C., *Combust. Flame* 94, 433 (1993).
6. Nicuod, F and Poinso, T, *Combust. Flame* 142, 153 (2005).
7. Chen, J.H., Echekki, T., and Kollmann, W., *Combust. Flame* 116, 15 (1999)

Figures:

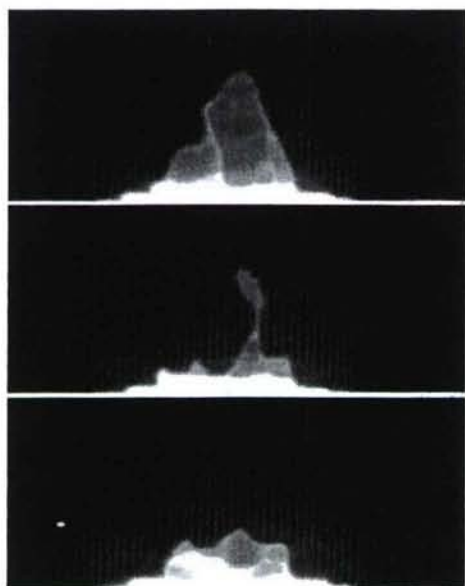


Figure 1. Images of unburned pocket formation.

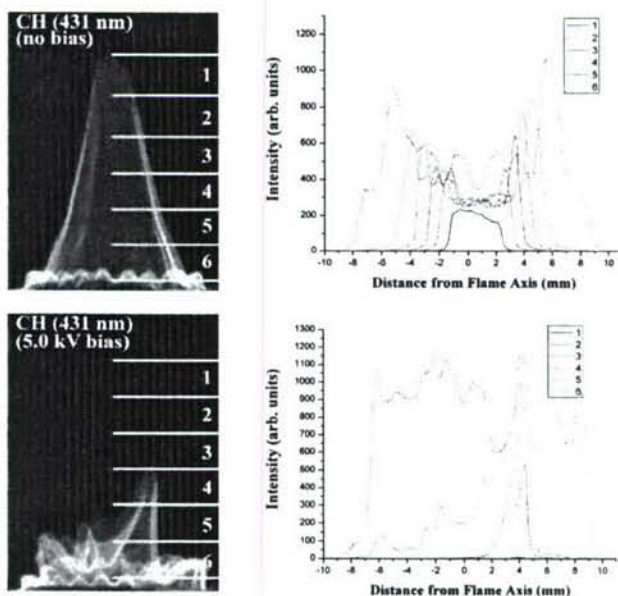


Figure 2. CH emission with and without applied voltage.

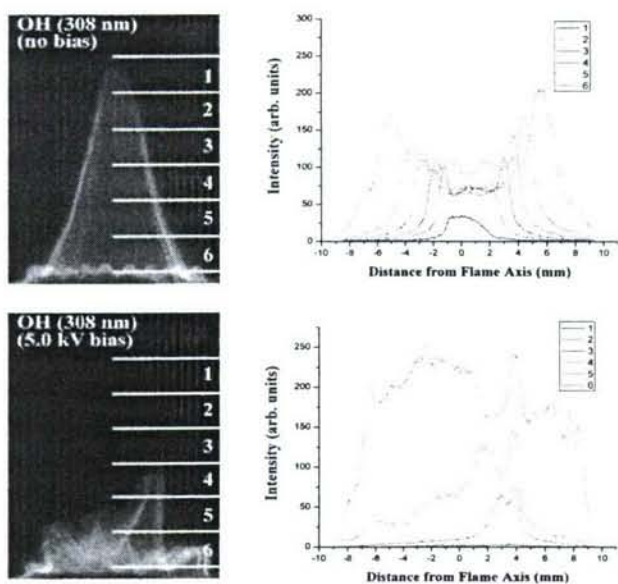


Figure 3. OH emission with and without applied voltage.

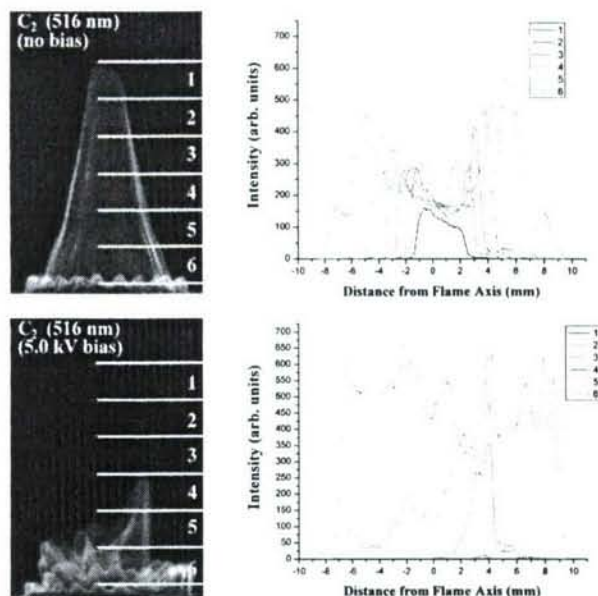


Figure 4. C_2 emission with and without applied voltage.

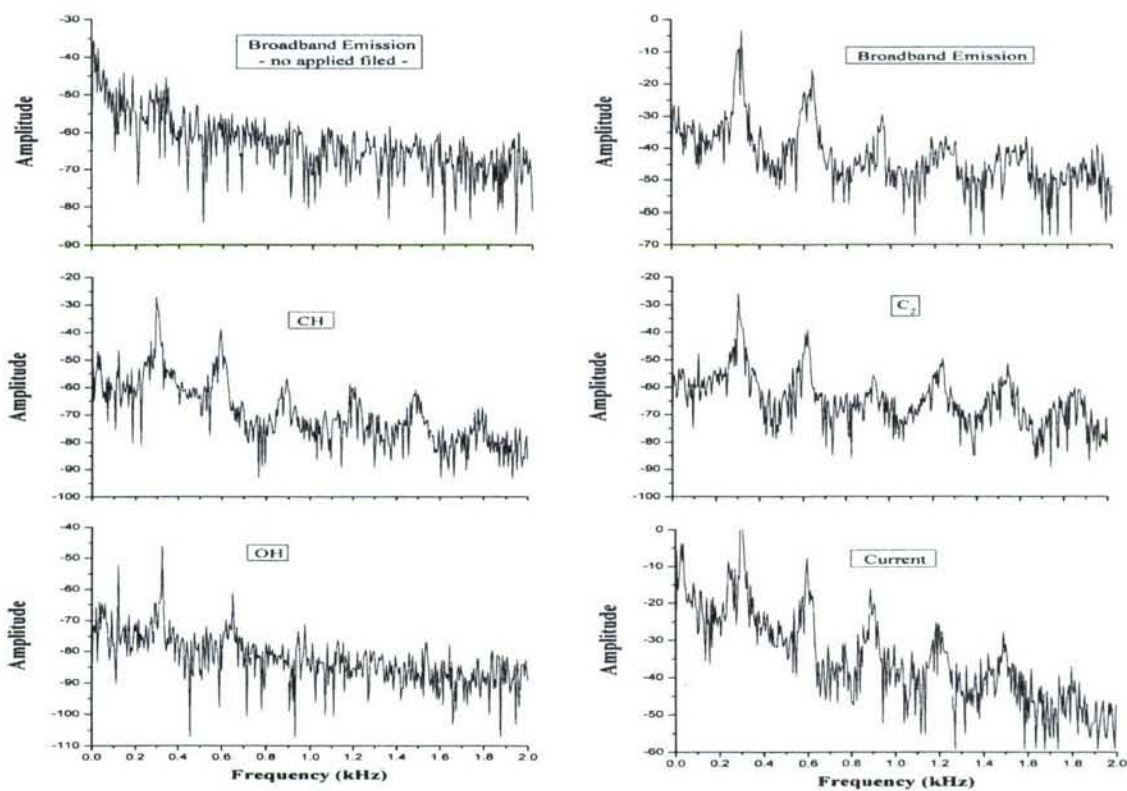


Figure 5. FFTs of broadband emission from unperturbed flame along with DC electric field induced perturbed flame and filtered CH , C_2 and OH chemiluminescence, and current fluctuations are shown.

FILTERED DENSITY FUNCTION FOR SUBGRID SCALE MODELING OF TURBULENT DIFFUSION FLAMES

Grant Number FA9550-06-1-0015

Principal Investigator(s): Peyman Givi

Department of Mechanical Engineering
University of Pittsburgh
Pittsburgh, PA 15261

SUMMARY/OVERVIEW:

Within the past year, our work was concentrated primarily on three issues: (1) further development and improvements of the joint velocity-scalar filtered mass density function (VSFMDf) as a subgrid scale (SGS) closure, (2) finalizing the implementation of the scalar filtered mass density function (SFMDf) for large eddy simulation (LES) of a turbulent bluff-body flame, and (3) improvement of the computational efficiency of our FDF codes.

TECHNICAL DISCUSSION:

This research is focused on development and implementation of the filtered density function (FDF) method for subgrid scale (SGS) closure of turbulent combustion. Within the past few years, the FDF methodology has become very popular; see Givi [1] for a recent review. In addition to our previous AFOSR-sponsored work [2–6], the methodology has experienced widespread usage by many others. Examples are contributions in its basic implementations [7, 8], fine-tuning of its sub-closures [9–11], and its validation via laboratory experiments [12–15]. The methodology is finding its way into commercial codes such as Fluent, and has been the subject of detailed discussions in several recent textbooks [16–18].

The latest development in, and up to now the most comprehensive means of, the FDF formulation is via the joint velocity-scalar filtered mass density function (VSFMDf). Within the past year, we have fine-tuned the physical modeling and the computational procedure of the VSFMDf. Simulations were conducted of a three-dimensional temporally developing, variable density mixing layer involving transport of a passive scalar. Direct numerical simulation (DNS) was conducted of this flow, and comparisons were also made with LES via the Smagorinsky model. Various effects of density variations [19] are investigated. The results of this study are discussed in detail in a recent Ph.D. dissertation [20]. Some sample results are presented here. Figure 1 shows the filtered fluid density field for several values of the free-stream density ratios of s . As shown, there are good agreements between VSFMDf and DNS. As the density ratio increases, the shear layer center is shifted further to the low-density side. As a result, the peak values of the Reynolds stresses and scalar fluxes also shift

to the low-density side. This shift is responsible for the reduction of the turbulent production terms [19], and thus the decrease of the shear layer thickness [21]. The temporal variation of the “scalar thickness” is presented in Fig. 2. The Smagorinsky model underpredicts the spread of the layer due to its dissipative nature. All VSFMDF predictions compare well with DNS data.

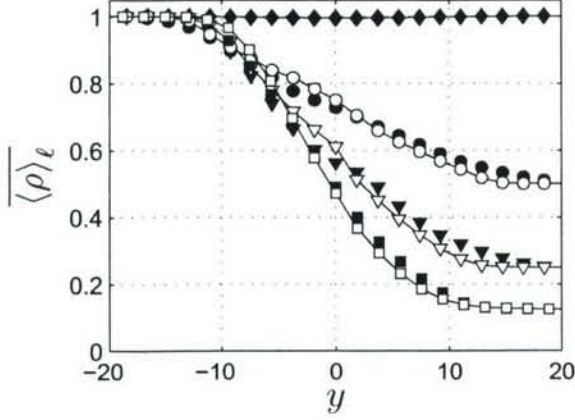


FIGURE 1: Cross-stream variation of Reynolds-averaged density in temporal mixing layer simulations. The solid lines with open symbols denote VSFMDF predictions. The filled symbols denote DNS data. The symbols denote: (diamond) $s = 1$, (circle) $s = 2$, (triangle) $s = 4$, and (square) $s = 8$.

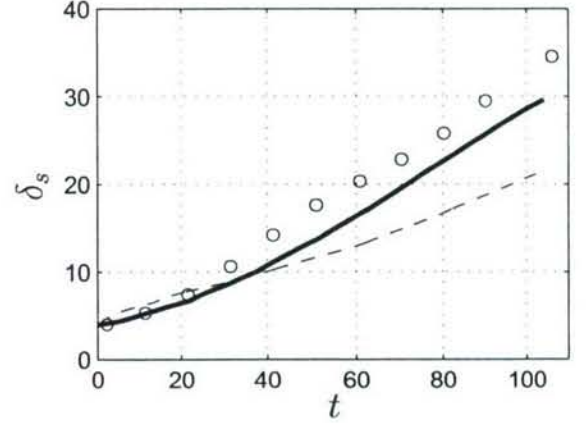
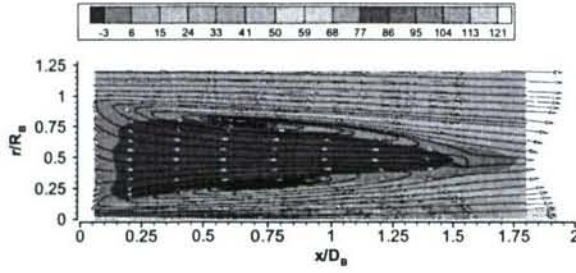


FIGURE 2: Temporal variation of scalar thickness in temporal mixing layer simulations with $s = 2$. The thick solid and thin dashed lines denote LES predictions using VSFMDF and Smagorinsky closures, respectively. The white and black circles show the filtered and unfiltered DNS data, respectively.

After our successful prediction of the piloted jet flame [2], we applied our scalar filtered mass density function (SFMDF) methodology for LES of the University of Sydney bluff-body flame [22–24]. This part of our work is described in detail in a recent Ph.D. dissertation [25]. Some sample results are shown here. The time averaged streamwise velocity contours with the streamlines and velocity vectors superimposed are shown in Fig. 3. This figure shows the recirculation region and the two characteristic counter-rotating vortices. The recirculating zones are captured well by the simulations. The comparisons also show good overall qualitative agreement with data. The quantitative agreement with data is also very good for the mean, rms values, and PDFs of various fields (see Fig. 4). Our previous work on application of the FDF to complex flames suggest that in order to apply this methodology to more realistic geometries with realistic reaction models, the hybrid finite-difference (FD)/Monte Carlo (MC) numerical solution procedure needs to be more-effectively parallelized. This allows us to take advantage of more computational power and large number of processor in FDF simulations. Therefore, within the past year, a part of our effort was devoted to improving the parallel efficiency of our FDF codes. The parallelization is implemented by dividing the computational domain into equal-sized sub-domains. Each processor performs the FD procedure separately on each of these domains. The message-passing interface (MPI) library is used to pass the variables between processors. This implementation ensures load balancing. The message-passing is implemented in a non-blocking manner,

(a) Experiment



(b) LES/FDF

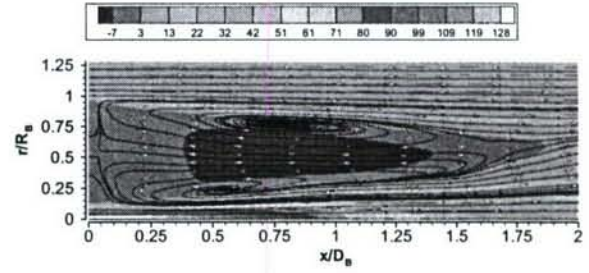
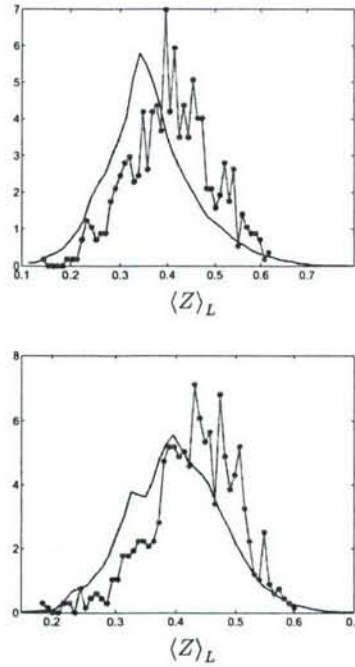


FIGURE 3: Time averaged recirculation features as predicted by FDF. The contours denote the streamwise velocity. Superimposed are the streamlines and the velocity vectors.

(a) Mixture fraction



(b) Temperature

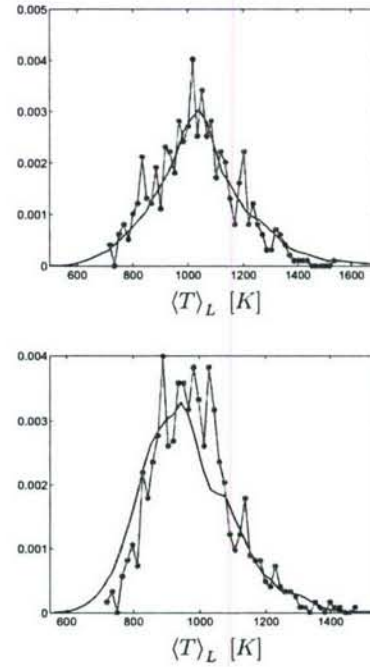


FIGURE 4: PDFs of the resolved (a) mixture fraction, and (b) temperature at the radial location $r = 5.05 \text{ mm}$ compared to the experiment. (top-to-bottom rows) $x/D_B = 0.9$, and 1.3 . — FDF, —●— Experiment.

to enable overlapping of communications with computations. This results in reduction of communication overhead. The parallelization of MC procedure is done by dividing the MC particles among the processors according to their spatial location. This way the particles have direct access to FD variable they need for their evolution. Each MC particle evolves independently, thus there is no inter-particle interactions. As the particles move, they may translate to the neighboring sub-domain. This is done by communicating the particle values between the adjacent processors. Due to random stochastic nature of particle motion, there is a substantial increase in communication overhead due to particle oscillation near the

sub-domain's boundaries. To alleviate this, a buffer zone is devised in which the particles are accumulated. With this treatment, the particle communications are not needed at each time step and the communication overhead is decreased significantly. The procedure as developed here is examined extensively on up to 64 processors. The results show good load balancing and close to linear speed-ups.

ACKNOWLEDGEMENTS:

We are indebted to Professor Stephen B. Pope for his valuable collaborations.

-
- [1] P. Givi, *AIAA J.* **44**, 16 (2006).
 - [2] M. R. H. Sheikhi, T. G. Drozda, P. Givi, F. A. Jaber, and S. B. Pope, *Proc. Combust. Inst.* **30**, 549 (2005).
 - [3] M. R. H. Sheikhi, T. G. Drozda, P. Givi, and S. B. Pope, *Phys. Fluids* **15**, 2321 (2003).
 - [4] L. Y. M. Gicquel, P. Givi, F. A. Jaber, and S. B. Pope, *Phys. Fluids* **14**, 1196 (2002).
 - [5] F. A. Jaber, P. J. Colucci, S. James, P. Givi, and S. B. Pope, *J. Fluid Mech.* **401**, 85 (1999).
 - [6] P. J. Colucci, F. A. Jaber, P. Givi, and S. B. Pope, *Phys. Fluids* **10**, 499 (1998).
 - [7] X. Y. Zhou and J. C. F. Pereira, *Flow Turbul. Combust.* **64**, 279 (2000).
 - [8] V. Raman, H. Pitsch, and R. O. Fox, *Combust. Flame* **143**, 56 (2005).
 - [9] J. Réveillon and L. Vervisch, *AIAA J.* **36**, 336 (1998).
 - [10] C. M. Cha and P. Troulet, *Phys. Fluids* **15**, 1496 (2003).
 - [11] S. Heinz, *Flow Turbul. Combust.* **70**, 153 (2003).
 - [12] C. Tong, *Phys. Fluids* **13**, 2923 (2001).
 - [13] D. Wang and C. Tong, *Phys. Fluids* **14**, 2170 (2002).
 - [14] E. van Vliet, J. J. Derksen, and H. E. A. van den Akker, *AIChE J.* **51**, 725 (2005).
 - [15] D. Wang, C. Tong, and S. B. Pope, *Phys. Fluids* **16**, 3599 (2004).
 - [16] S. B. Pope, *Turbulent Flows* (Cambridge University Press, Cambridge, UK, 2000).
 - [17] S. Heinz, *Statistical Mechanics of Turbulent Flows* (Springer-Verlag, New York, NY, 2003).
 - [18] R. O. Fox, *Computational Models for Turbulent Reacting Flows* (Cambridge University Press, Cambridge, UK, 2003).
 - [19] C. Pantano and S. Sarkar, *J. Fluid Mech.* **451**, 329 (2002).
 - [20] M. R. H. Sheikhi, Ph.D. Thesis, Department of Mechanical Engineering, University of Pittsburgh, Pittsburgh, PA (2005).
 - [21] A. W. Vreman, N. D. Sandham, and K. H. Luo, *J. Fluid Mech.* **320**, 235 (1996).
 - [22] B. B. Dally, A. R. Masri, R. S. Barlow, and G. J. Fiechtner, *Combust. Flame* **114**, 119 (1998).
 - [23] B. B. Dally, A. R. Masri, R. S. Barlow, and G. J. Fiechtner, *Combust. Flame* **132**, 272 (2003).
 - [24] Sandia National Laboratories, TNF Workshop website, <http://www.ca.sandia.gov/TNF/> (2005).
 - [25] T. G. Drozda, Ph.D. Thesis, Department of Mechanical Engineering, University of Pittsburgh, Pittsburgh, PA (2005).

TWO-POINT SCALAR TIME-SERIES MEASUREMENTS IN TURBULENT PARTIALLY PREMIXED FLAMES

AFOSR Grant Number FA9550-06-1-0064

Principal Investigators: Galen B. King, Normand M. Laurendeau and Michael W. Renfro

School of Mechanical Engineering, Purdue University, West Lafayette, IN 47907-2088
Department of Mechanical Engineering, University of Connecticut, Storrs, CT 06269-3139

SUMMARY/OVERVIEW

A two-point method has recently been demonstrated based on picosecond time-resolved laser-induced fluorescence (PITLIF). This technique is capable of simultaneously monitoring OH time series at two locations, hence allowing the characterization of spatial structures in turbulent flames in addition to their temporal behavior. Several refinements have been made to improve upon the previous one-point instrument. Using a specially designed collection-lens system, off-axis optical aberrations have been effectively minimized in the probe volume. Furthermore, additional electronics has been installed which permit absolute species concentration measurements. As a preliminary study, two-point OH time-series measurements were taken in three standard turbulent non-premixed flames (H3, DLR_A and DLR_B)¹. Two-point statistics, including space-time correlations, spatial autocorrelation functions and integral length scales were computed to help elucidate the flame structure and turbulence-chemistry interactions.

TECHNICAL DISCUSSION

Understanding complex physical and chemical processes in turbulent combustion requires temporally and spatially resolved measurement techniques. Non-premixed jet flames have been extensively studied because of their relative simplicity and well-defined flow field. Measurements of minor species concentrations in turbulent flames are important owing to their significance to chemical reactions and pollutant formation. Hydroxyl, in particular, is a good flame marker, whose fluctuations reveal important interactions between fluid mixing and chemical reactions.

Time-series measurements of important scalars, such as temperature² and concentrations of OH³ and CH⁴ have been demonstrated using high repetition-rate, laser-based techniques. These measurements provide spectral characteristics and relevant time scales for scalars; however, as pointwise measurements, they give no information on spatial structures. To circumvent this limitation, simultaneous multipoint or even 1D or 2D time-series measurements are required. Examples of this endeavor include multipoint OH chemiluminescence measurements⁵, two-point temperature measurements⁶ and high repetition-rate planar laser-

¹ TNF workshop, <http://www.ca.sandia.gov/TNF>

² R.W. Dibble, R.E. Hollenbach, Eighteenth Symposium (International) on Combustion, 1981, p. 1489.

³ M.W. Renfro, W.A. Guttenfelder, G.B. King, N.M. Laurendeau, Combust. Flame 123 (2000) 389.

⁴ M.W. Renfro, G.B. King, N.M. Laurendeau, Combust. Flame 122 (2000) 139.

⁵ J. Kojima, Y. Ikeda, T. Nakajima, Meas. Sci. Technol. 14 (2003) 1714.

⁶ G. H. Wang, N. T. Clemens, P. L. Varghese, Proc. Combust. Inst. 30 (2005) 691.

induced fluorescence (PLIF)⁷. For minor species, two-point PITLIF was previously developed, which provided quantitative concentration measurements of radical species at relevant turbulent temporal and spatial scales^{8,9}.

Modifications have been made to improve upon the earlier version of the two-point PITLIF system. Optical aberrations were found to have significant effects on our previous two-point statistics^{Error! Bookmark not defined.}. In particular, aberrations occurred when either probe volume deviated from the optical axis of the detection system. Furthermore, at large displacement distances, partial overlap arose between images of the two probe volumes. This overlap created artificial coherence between signals from the two probe volumes, which was exhibited as a secondary peak in the spatial autocorrelation function, as depicted in Fig. 1.

To address this problem, we designed a new lens system via ZEMAX software, which now produces an aberration-limited blur-spot of less than 130 μm at object positions up to 6 mm away from the optical axis. As shown in Fig. 2, the current optical system is composed of one custom-made aspherical lens (L1), a 10-cm diameter UV beamsplitter (BS) and two pairs of plano-convex and meniscus lenses (L2 and L3; L4 and L5). The new setup has a magnification ratio of 1.19 and a working $f\#$ of 2.8. Each probe volume is 485 \times 485 \times 210 μm^3 , which is determined by the diameter of the laser beam and the entrance slit width of the monochromators. PITLIF utilizes the principle of triple-bin integration¹⁰ which can correct for the effect of electronic quenching on-the-fly. The insertion of four additional multichannel scalars allows for absolute species concentration measurements at both probe volumes.

To demonstrate the effectiveness of this revised setup, two-point PITLIF data were taken at the same position (peak [OH] at $x/D=20$) within the same flame used by Zhang et al⁹. The derived spatial autocorrelation function shown in Fig.1 displays an approximately exponential decay without a secondary peak, as expected from the typical statistics of a turbulent field.

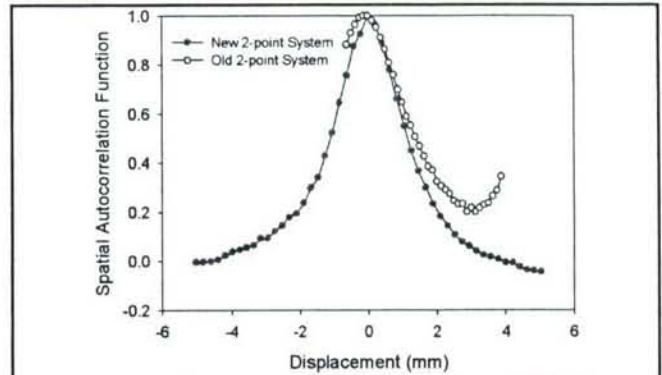


Fig. 1. Spatial autocorrelation function of H3 flame taken at the location of peak [OH] at $x/D=20$, using both the old and new two-point optical systems.

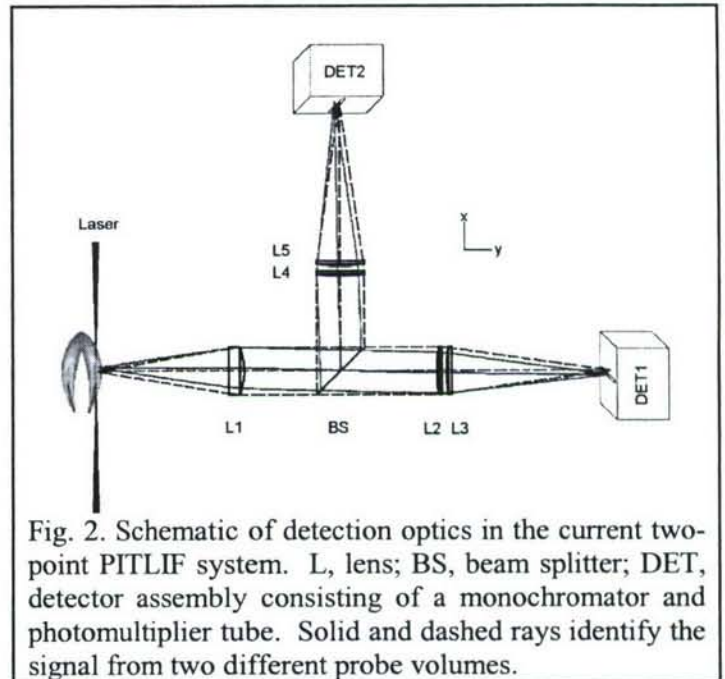


Fig. 2. Schematic of detection optics in the current two-point PITLIF system. L, lens; BS, beam splitter; DET, detector assembly consisting of a monochromator and photomultiplier tube. Solid and dashed rays identify the signal from two different probe volumes.

⁷ J. Hult, U. Meier, W. Meier, A. Harvey, C.F. Kaminski, Proc. Combust. Inst. 30 (2005) 701.

⁸ J. Zhang, K.K. Venkatesan, G.B. King, N.M. Laurendeau, M.W. Renfro, Proceedings of the 2005 Joint U.S. Sections Meeting, The Combustion Institute, Philadelphia, PA, 2005.

⁹ J. Zhang, K.K. Venkatesan, G.B. King, N.M. Laurendeau, M.W. Renfro, Opt. Lett. 30 (2005) 3144.

¹⁰ S.D. Pack, M.W. Renfro, G.B. King, N.M. Laurendeau, Opt. Lett. 23 (1998), 1215.

For this study, three non-premixed flames (H3, DLR_A and DLR_B) were investigated chosen from the TNF workshop¹. Two-point OH measurements were taken at locations corresponding to the mean peak [OH] as well as positions along the jet centerline, with x/D ranging from 10.00 to 53.25, where $x/D=35$ and $x/D=53.25$ correspond to the respective flame tips of the H3 and DLR_A flames. The mean OH concentrations were compared with the available data from the TNF database¹ (the detailed comparison can be found in Zhang et al¹¹). The measurements agree quite closely except at two locations: jet centerline at $x/D=50$ in DLR_A and peak [OH] at $x/D=20$ in DLR_B. This discrepancy is likely due to deviations in position between the two measurements and increased uncertainty at the jet centerline owing to the small signal-to-background ratio.

Given two simultaneous [OH] time series, a number of two-point statistics can be evaluated, including the space-time correlation, spatial autocorrelation function and integral length scale. The normalized space-time correlation is defined as¹²

$$f_{st}(\Delta r, \Delta t) = \frac{\langle OH'(r, t) OH'(r + \Delta r, t + \Delta t) \rangle}{\left[\langle OH'(r, t)^2 \rangle \langle OH'(r + \Delta r, t + \Delta t)^2 \rangle \right]^{1/2}},$$

where $OH'(r, t)$ is the fluctuating component of hydroxyl concentration at radial location r and time t , while Δr and Δt are the displacement between the two probe volumes and the lag time, respectively. Figure 3 displays the calculated space-time correlation at two peak [OH] locations in the H3 flame. Notice that positions near the flame tip show a broader peak along the displacement axis, indicating a larger coherence region.

The normalized spatial autocorrelation function is related to the space-time correlation by

$$f_s(\Delta r) = f_{st}(\Delta r, \Delta t = 0).$$

Figure 4 displays spatial autocorrelation functions for the DLR_A flame at peak [OH] locations. The full-width-at-half-maximum (FWHM) of the curve becomes greater farther downstream, which is a manifestation of the broadening coherence region mentioned earlier. In general, the

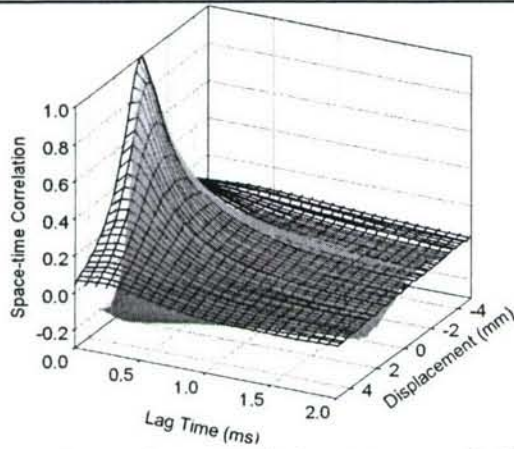


Fig. 3. Space-time correlation at two peak [OH] locations in the H3 flame: (a) $x/D=10$ (shaded surface); (b) $x/D=30$ (mesh).

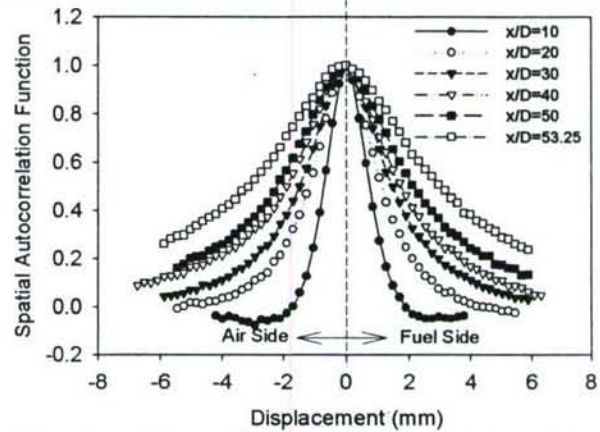


Fig. 4. Normalized spatial autocorrelation functions for the DLR_A flame: (a) at peak [OH] locations.

spatial autocorrelation function is symmetric between the air and fuel sides. Exceptions occur primarily near the nozzle ($x/D=10$). This abnormality might be explained by the evolution of

¹² M.T. Landahl, E. Mollo-Christensen, Turbulence and Random Processes in Fluid Mechanics, 2nd ed., Cambridge University Press, New York, NY, 1994.

flame structures. In turbulent jet diffusion flames, the reaction zone lower in the flame (e.g. $x/D \leq 5$ for the DLR_A flame) is composed of thin layers located outside the turbulent fuel jet^{7,13}. Because of relaminarization, the reaction zone essentially acts as a shield blocking the penetration of fuel vortices; hence, the reaction zone and air side remain laminar. Farther downstream, the flame front becomes more wrinkled as the effect of laminarization diminishes. Therefore, the asymmetry of the spatial autocorrelation function at $x/D=10$ is probably due to residual laminarization.

The OH integral length scale can be determined by integrating the spatial autocorrelation function over its displacement, Δr , so that

$$l_l = \int f_s(\Delta r) d\Delta r.$$

While the spatial autocorrelation function exhibits asymmetry near the nozzle, the calculated integral length scales are about the same on both sides (Fig. 5). The hydroxyl length scales are well resolved and increase linearly with axial distance at peak [OH] locations (Figs. 5 and 6), consistent with observations of integral length scales for mixture fraction at mean stoichiometric

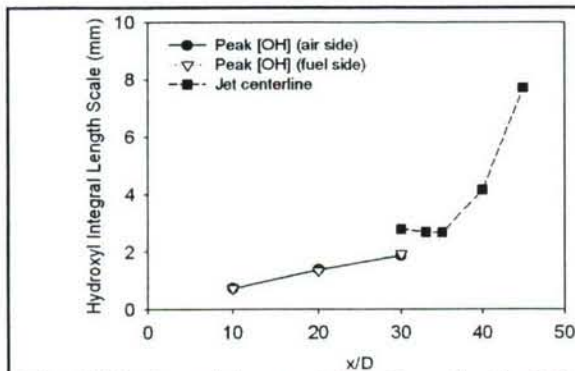


Fig. 5. Hydroxyl integral length scales for H3 flame.

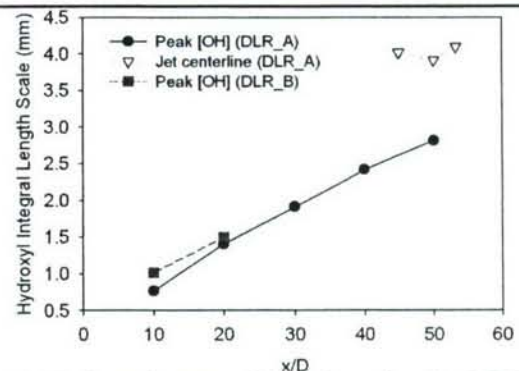


Fig. 7. Hydroxyl integral length scales for DLR_A and DLR_B flames.

radii in methane/air jet diffusion flames¹⁴. This result suggests that OH fluctuations at peak [OH] locations are essentially dominated by flame motions, a confirmation of flamelet theory. The integral length scales are basically constant along the jet centerline below the flame tip, and increase rapidly above the flame tip.

¹³ V. Bergmann, W. Meier, D. Wolff, W. Stricker, Appl. Phys. B. 66 (1998) 489.

¹⁴ R.S. Barlow, A.N. Karpetis, Flow Turb. Combust. 72 (2004) 427

PDF MODELING OF TURBULENT COMBUSTION

AFOSR Grant FA-9550-06-1-0048
Principal Investigator: Stephen B. Pope

Mechanical & Aerospace Engineering
Cornell University
Ithaca, NY 14853

SUMMARY

In both space and aircraft applications, the design of combustors in propulsion systems remains a significant technical challenge. Given the cost, difficulty and time consumed in experimental testing, it is well recognized that computer modeling is essential to exploring different design concepts, and to reducing the cost and time of the design cycle. While many phenomena may be involved – sprays, radiation, combustion dynamics, etc. – a central problem is that of modeling turbulent-chemistry interactions in turbulent combustion. The PDF approach to turbulent combustion has the advantages of fully representing the turbulent fluctuations of species and temperature, and of allowing realistic combustion chemistry to be implemented (e.g., of order 50 species). This methodology is also being applied in conjunction with large-eddy simulations, in which case it is referred to as LES/FDF. The overall objective of the proposed work is to advance and extend the PDF and LES/FDF approaches to modeling turbulent combustion in flows of relevance to aerospace propulsion systems. Currently, PDF methods are being applied to flames in vitiated co-flows, both lifted methane non-premixed flames and also attached piloted premixed flames. In future work, the LES/FDF approach will be applied to piloted jet flames and to bluff-body jet flames. This will enable a three-way comparison between experimental data, the LES/FDF calculations, and previous PDF calculations. In all of these calculations, realistic and reliable combustion chemistry is used (e.g., involving of order 20-50 species) so that turbulence-chemistry interactions such as local extinction and re-ignition can be investigated. Collaboration with the University of Pittsburgh continues and has resulted in one of the first LES/PDF calculations of a turbulent flame (Sheikhi *et al.* 2005).

PDF CALCULATIONS OF PILOTED JET FLAMES

The Barlow & Frank (1998) piloted jet flames are well recognized as providing an excellent test of turbulent combustion models, in particular of their ability to describe local extinction and re-ignition. There is a sequence of flames *A–F*, with *D*, *E*, and *F* being fully turbulent, with increasing amounts of local extinction. While there are many successful modeling studies of flame *D* – which has little local extinction – there are far fewer of the more challenging flames *E* and *F*.

PDF methods have previously been successfully applied to these flames by Xu & Pope (2000), Tang *et al.* (2000), and Lindstedt *et al.* (2000). Since the Cornell and Imperial College groups use different mixing models and different chemical mechanisms, questions arise as to the dependence and sensitivity of the calculations to these ingredients. Some progress has been made in understanding the relative behavior of the different mixing models (see, e.g., Ren &

Pope 2004). We have now concluded a series of PDF calculations addressing these issues. Cao & Pope (2005) describe joint PDF calculations of these flames using 7 different chemical mechanisms for methane, ranging from a 5-step reduced mechanism, to the 53-species GRI 3.0 mechanism. The results show that the GRI mechanisms (and the augmented reduced mechanisms based on them) are capable of accurately representing the observed local extinction and re-ignition. In contrast, C_1 skeletal mechanisms and 5-step reduced mechanisms prove to be inaccurate.

This work has been followed up by a study (Cao *et al.* 2006) of the influence of the turbulent mixing models used in the PDF model calculations. The principal finding is that (with a different value of the mixing-model constant) all three commonly used models (IEM, MC and EMST) are capable of yielding the observed level of local extinction. But only the EMST model produces, simultaneously, the observed level of mixture fraction fluctuations.

PDF CALCULATIONS OF LIFTED TURBULENT FLAMES

In laboratory experiments on turbulent flames, for obvious reasons, air at atmospheric conditions is generally used as the oxidant. In practical applications, however, the re-circulating flows used for flame stabilization generally lead to some mixing between the air stream and hot combustion products. And in thrust augmentors the oxidant stream is simply the lean combustion products from the turbine.

Motivated by these observations, a series of experiments has been performed (at Berkeley, Sandia, and Sydney) on various jet flames in vitiated co-flows. Previously we have performed two PDF studies of the lifted hydrogen flames studied experimentally by Cabra *et al.* (2002). These two studies are based on the composition PDF method incorporated in Fluent (Masri *et al.* 2004), and on the velocity-frequency-composition joint PDF method (Cao, Pope & Masri 2005). In both cases, detailed 9-species mechanisms for hydrogen are used.

We are currently investigating the lifted methane flames studied by Cabra *et al.* (2002, 2005). The calculations are based on the joint PDF method used previously, with the modified Curl mixing model and the ARM1 mechanism. Some preliminary results are given in Fig. 1. As may be seen, for the most part there is good agreement between the calculations and the measurements, but there are some discrepancies for CO and OH.

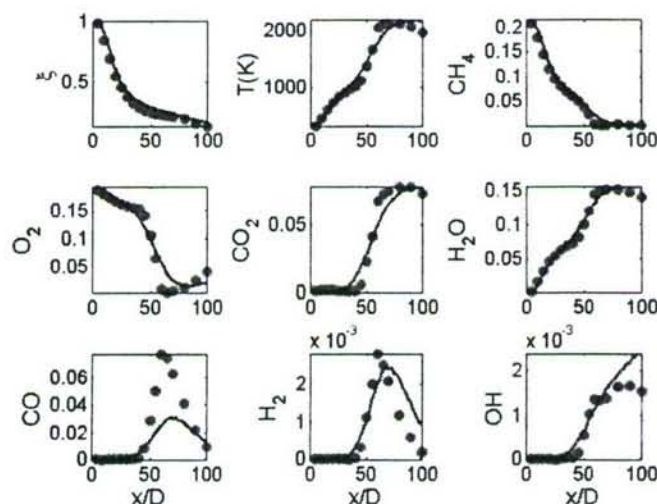


Fig. 1. Centerline profiles of mean mixture fraction, temperature and mass fractions of CH_4 , O_2 , CO_2 , H_2O , CO , H_2 and OH . Symbols: Measurement by Cabra *et al.* 2005; Lines: Joint PDF calculations.

The PDF method calculations presented above demonstrate current capabilities, e.g., using a mechanism with of order 50 species. Such calculations are possible because of the ISAT algorithm (Pope 1997) and the availability of parallel computers. As we work towards combining PDF methods with large eddy simulation (LES), larger parallel clusters are needed, and the efficient parallel implementation of ISAT becomes critical.

If there are P processors, then the load associated with solving the LES equations is well balanced if the solution domain is partitioned into P sub-domains, each containing approximately the same number of cells. Further, with such a decomposition, the computational particles used in the PDF algorithm are approximately equally distributed between the processors. Hence there is good load balancing of particle tracking and of mixing. However, the load associated with reaction (i.e., incrementing the particle compositions due to reaction over the time step) which can dominate the CPU time can be poorly balanced. For example, the particles on one processor may be inert (e.g., cold air) and hence require negligible time to evaluate their reaction; whereas the particles on another processor may be highly reactive. Even using ISAT, reactive particles take much longer to treat, especially if retrieving from a full table is not possible, and hence a direct integration of the stiff ODEs is required.

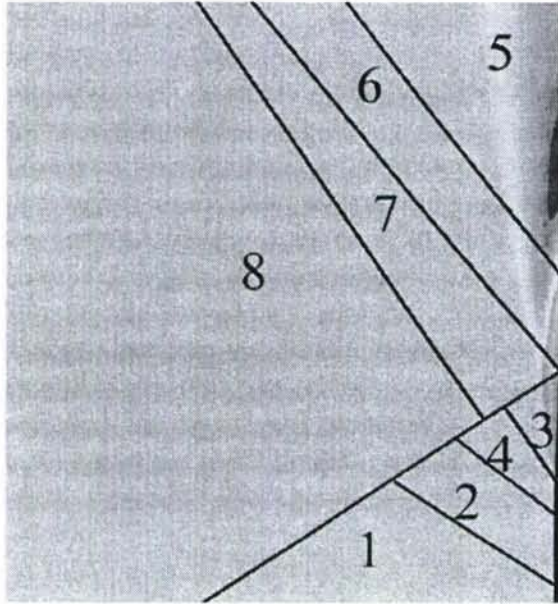


Fig. 2 Contour plot of mean temperature in PDF calculations of a lifted hydrogen jet flame, showing the sub-domains used in the Fluent parallel computation.

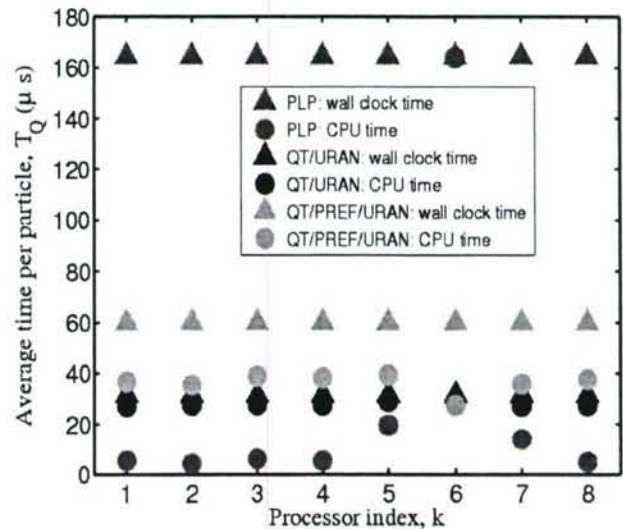


Fig. 3 Average wall clock and CPU times (per particle per reaction fractional step) for parallel Fluent computations of the lifted hydrogen flame, with different parallel ISAT strategies.

Following the preliminary work of Lu *et al.* (2005), we are continuing to develop and evaluate parallel strategies for implementing ISAT. One of the test problems considered is the composition PDF method in Fluent applied to the lifted hydrogen jet flame described above. Figure 2 shows the solution domain and its decomposition into the eight sub-domains used in the parallel computation (using 8 processors). Figure 3 shows the CPU and wall-clock times per particle step required by three different parallel strategies. The first is PLP (purely local

processing) in which no message passing is performed, but each processor invokes ISAT independently for all of the particles in its sub-domain. As may be seen from the CPU times, there is considerable load imbalance with processor 6 requiring significantly more time. Note that the corresponding sub-domain is the base of the flame, which involves the most challenging ignition chemistry. The two (non-trivial) parallel strategies lead to speed-ups (relative to PLP) of about 2.5 and 5.

PUBLICATIONS

The following papers based on AFOSR sponsored research have been published or written in 2005-2006.

- [1] R.W. Bilger, S.B. Pope, K.N.C. Bray and J.F. Driscoll (2005) "Paradigms in turbulent combustion research", Proceedings of the Combustion Institute, 30, 21-42.
- [2] R. Cao and S.B. Pope (2005) "The influence of chemical mechanisms on PDF calculations of nonpremixed piloted jet flames", 4th Joint Meeting of the U. S. Sections of the Combustion Institute, Philadelphia, PA.
- [3] R. Cao and S.B. Pope (2005) "The influence of chemical mechanisms on PDF calculations of nonpremixed piloted jet flames", Combustion and Flame, 143, 450-470.
- [4] R. Cao, S.B. Pope and A.R. Masri (2005) "Turbulent lifted flames in a vitiated coflow investigated using joint PDF calculations", Combustion and Flame, 142, 549-568.
- [5] L. Lu, Z. Ren, S.R. Lantz, V. Raman, S.B. Pope and H. Pitsch (2005) "Investigation of strategies for the parallel implementation of ISAT in LES/FDF/ISAT computations", 4th Joint Meeting of the U. S. Sections of the Combustion Institute, Philadelphia, PA.
- [6] B. Merci, D. Roekaerts, B. Naud and S.B. Pope (2006) "Comparative study of micro-mixing models in transported scalar PDF simulations of turbulent non-premixed bluff body flames", Combustion and Flame (to be published).
- [7] S.B. Pope (2005) "Computational modeling of turbulent flames", in Frontiers of Computational Fluid Dynamics 2006, World Scientific Publishing.
- [8] M.R.H. Sheikhi, T.G. Drozda, P. Givi, F.A. Jaber and S.B. Pope (2005) "Large eddy simulation of a turbulent nonpremixed piloted methane jet flame (Sandia Flame D)", Proceedings of the Combustion Institute, 30, 549-556.

OTHER REFERENCES

- [1] R.S. Barlow and J.H. Frank (1998). Proc. Combust. Inst. 27, 1087-1095.
- [2] R. Cabra, T. Myhrvold, J.Y. Chen, R.W. Dibble, A.N. Karpetis, and R.S. Barlow (2002). Proc. Combust. Inst. 29, 1881-1888.
- [3] R. Cabra, J.-Y. Chen, R.W. Dibble, A.N. Karpetis and R.S. Barlow. Combustion and Flame, (2005), 143, 491-506.
- [4] R.R. Cao, H. Wang and S.B. Pope (2005) "The effect of mixing models in PDF calculations of piloted jet flames," Proc. Combust. Inst., 31 (to be published).
- [5] R.P. Lindstedt, S.A. Louloudi, and E.M. Vaos (2000). Proc. Combust. Inst. 28, 149-156.
- [6] A.R. Masri, R. Cao, S.B. Pope and G.M. Goldin (2004) "PDF Calculations of Turbulent Lifted Flames of H₂/N₂ issuing into a vitiated co-flow," Combust. Theory Modelling, 8, 1-22.
- [7] S.B. Pope (1997). Combust. Theory Modelling 1, 41-63.
- [8] Z. Ren, and S.B. Pope (2004). Combust. Flame 136, 208-216.
- [9] J. Xu, and S.B. Pope (2000). Combust. Flame 123, 281-307.

PULSE DETONATION PHYSIOCHEMICAL AND EXHAUST RELAXATION PROCESSES

LRIR 01PR02COR

Principal Investigator: Dr. Fred Schauer (AFRL/PRTC)

AFRL/PRTC

1790 Loop Road North, Building 490
Wright-Patterson AFB OH 45433-7103

SUMMARY/OVERVIEW:

The objective of this program is to establish the scientific knowledge of detonation initiation, propagation, and blow-down needed to develop a pulse detonation engine (PDE) that will function on hydrocarbon fuels. The complex interaction of chemistry, gas dynamics, turbulent mixing, and geometry are responsible for the success or failure of the detonation phenomena required to operate a PDE. Detonation tube exhaust blow-down conditions, which are predicted to have a significant impact upon performance, will be explored in order to achieve basic understanding of the relationships between detonations, nozzles, and multiple detonation tube interactions.

TECHNICAL DISCUSSION

The technological motivation for this program is the need to develop low-cost high-performance PDE's that can operate on hydrocarbon fuels. PDE's rely upon detonation combustion to produce a pressure rise in the combustion chamber instead of the expensive rotating machinery used in gas turbine engines. Consequently, the most expensive and maintenance-intensive components of a conventional turbine engine, namely the compressor and turbine stages, will not be necessary in PDE's. PDE's operates on a near-constant-volume heat addition cycle as opposed to the constant-pressure cycle employed in nearly all conventional aero-propulsion systems. The constant volume cycle offers improvements to specific thrust, specific fuel consumption, and specific impulse at a greatly reduced cost. In theory, the PDE can efficiently operate at Mach numbers from zero to above four without using a combined cycle/rocket approach. However, there are some major technical problems that must be resolved before the full potential of PDE's can be realized.

Foremost among the hurdles for a practical PDE system are the requirements for initiation and successful propagation of a detonation with hydrocarbon fuels in air. Although this has not been achieved in 60 years of PDE research, modern computational fluid mechanics (CFD), laser diagnostics, and high-speed instrumentation have not been applied to this challenge until recently. CFD and experimental studies of deflagration-to-detonation transition (DDT) and propagation are being carried out in order to explore the parameters controlling detonation

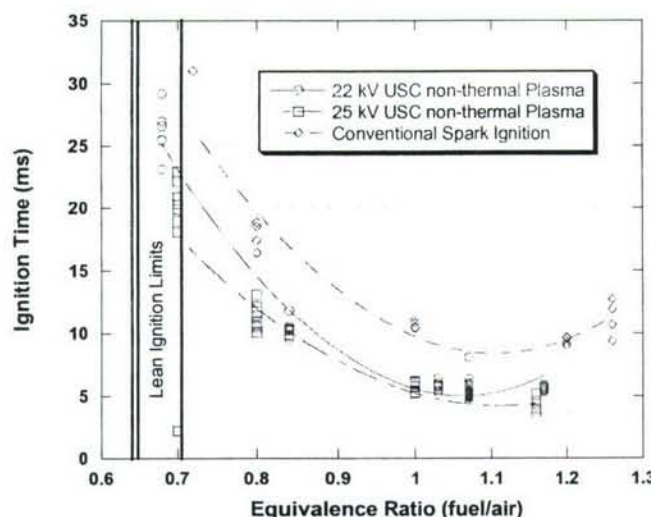


Figure 1. Non-thermal plasma ignition versus conventional spark ignition in a research PDE.

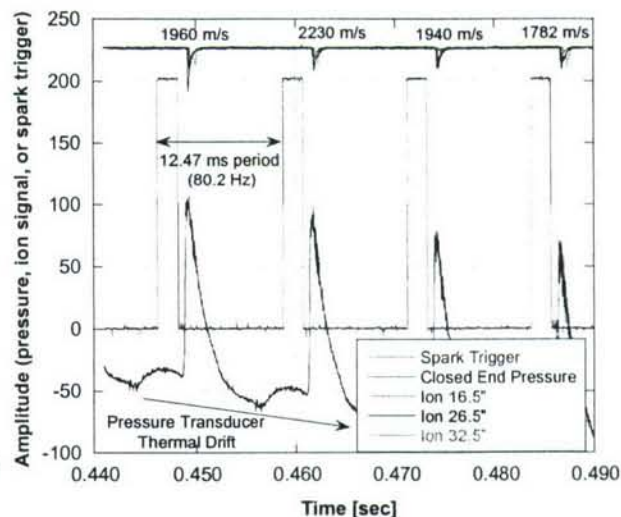


Figure 2. Hi-frequency detonation initiation in air.

initiation including: geometry effects, plasma ignition, hybrid fueled pre-detonators, and endothermic fuels.

Initiation time has previously been identified as a critical parameter for successful operation of a PDE. The majority of initiation time is chemical ignition time (from spark discharge to flame propagation). A novel method for reducing ignition time using a non-thermal plasma (or corona) ignition system has been under development. In collaboration with Prof. Martin Gunderson (USC) and Prof. John Yu (OSU), the non-thermal plasma scheme was compared to conventional spark ignition. Preliminary results, shown in Figure 1, indicate a significant reduction ignition time. However these results were not as low as those obtained at the Naval Post Graduate School in a valveless PDE. It is believed that the fill dynamics have an important role on initiation, producing turbulence and pressure gradients critical for initiation.

The fill dynamic affects become clear during high frequency operation, such as that shown in Figure 2, where prior to the detonation, high fill pressures are observed. Note the high thermal drift induced in the pressure measurements by heat flux due to the increased operating frequency. Flow dynamics from the high velocity fill process result in initial pressures well above the exit conditions. As shown here, if short initiation times can be obtained pressure losses from the expansion wave resultant from the valve closing can be avoided. However, initiation time becomes extremely critical, as the initial pressure drops well below ambient within typical hydrocarbon/air initiation times. The impact of valved versus valveless operation is a result of the complex interaction of turbulence,

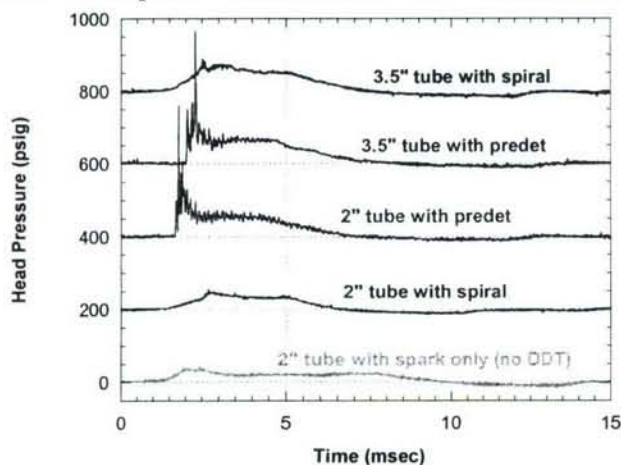


Figure 3. Head pressure versus time for various initiation methods.

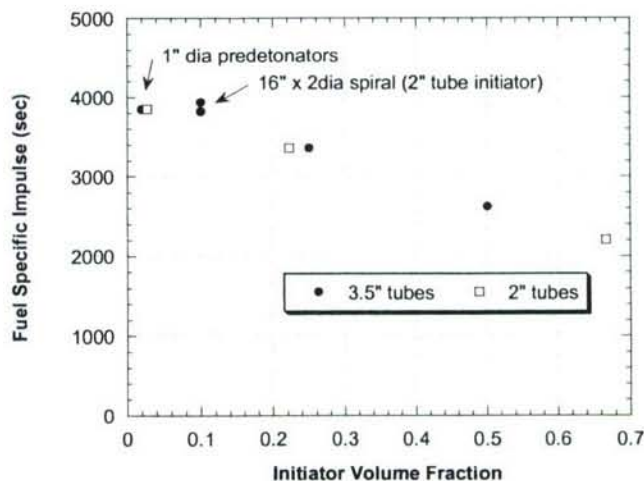


Figure 4. Specific impulse (fuel based) versus initiator volume fraction.

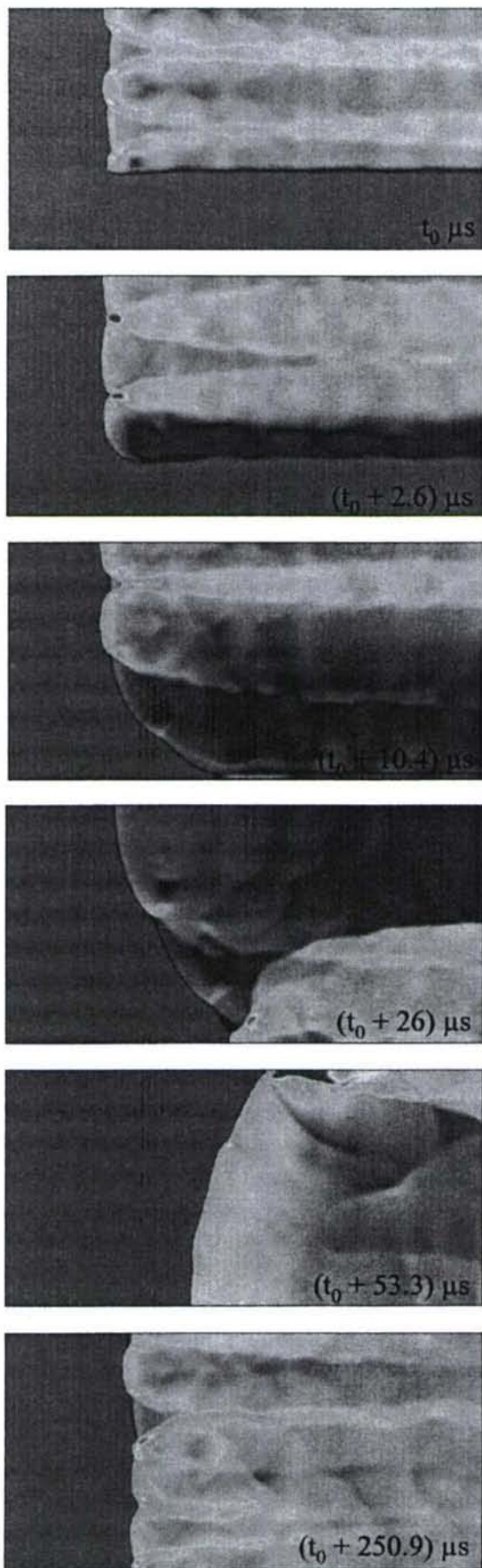


Figure 5. CFD of detonation transmission across sudden expansion.

viscosity, chemistry, wall effects and gas dynamics.

Previously, identification of loss mechanisms which arise during the DDT process were quantified. For example, spiral losses have little impact upon exhaust relaxation times but attenuate thrust by as much as 40% due to supersonic drag during DDT and blowdown. Low loss initiation methods have been successfully developed and the impact is shown in Figures 3 and 4. By minimizing the inefficient initiation process to a smaller volume, initiation times and efficiency are both improved. As shown in Fig. 4, good efficiency can be achieved with reasonable initiation volumes. The key to this performance is efficient transmission of detonation from the small initiation volume to the thrust tube. CFD (such as that shown in Figure 5) and experimental work demonstrated that detonation transmission limitations can be circumvented by taking advantage of transverse wave reflections to nearly immediately re-initiate a quenched detonation propagating across an expansion. The same physics apply to the previously demonstrated split detonation initiation technique and will be applied to propagating a detonation continuously from tube-to-tube with nearly no loss due to initiation.

Due to the difficulty associated with obtaining detonations in air, it was previously thought that any fuel/air mixture which detonated must be well mixed. However, unaccounted losses in a detonating engine eventually were revealed to be poor mixing that still resulted in DDT. A 20% reduction in thrust can be observed due to the poor coupling of heat release and shock pressure rise, resulting in the reduced P_3 or thrust pressure levels shown in Figure 2 for the inhomogeneous case.

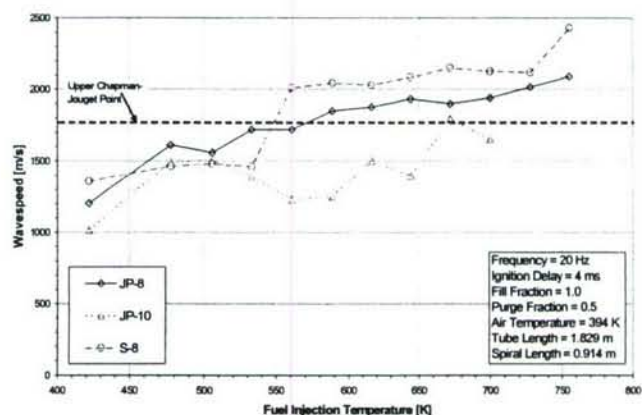


Figure 6. Detonation of standard military jet fuels compared to Fischer-Tropsch Fuel (S-8), using regenerative fuel cooled injection system.

Promising results from regenerative fuel cooling to provide supercritical fuel injection have been extended from 900F to 1100F. This system was used to take a preliminary look at the detonability of alternative military fuels, such as coal-derived Fischer-Tropsch, with results shown in Figure 6. A catalyst is being applied to the next-generation, higher temperature heat exchanger in order to promote endothermic effects which will theoretically promote DDT.

Progress in exhaust relaxation processes includes nozzle studies, back pressurization at altitude, and unsteady detonation/ejector flow dynamics. The unsteady detonation blow down process is conducive to exhaust vortex formation, which interacts with ejector inlets for dramatic performance improvements. Scaling results

Progress in exhaust relaxation processes includes nozzle studies, back pressurization at altitude, and unsteady detonation/ejector flow dynamics. The previously identified, unsteady detonation blow down process is conducive to exhaust vortex formation, which interacts with ejector inlets for dramatic performance improvements. Results were obtained for various sizes and exit conditions, such as those shown in Figures 7 and 8. In general scaling rules were found to be consistent despite the variation of parameters when scaled by vortex formation dimensions as shown in Figure 9 for a range of unsteady ejectors. These results are consistent with previous results: as the formation number goes to zero, the driver becomes steady and peak augmentation ratios become ~20%, as confirmed by conventional ejector results. The dynamic vortex formation from a pulsed detonation event can produce twice the augmentation.

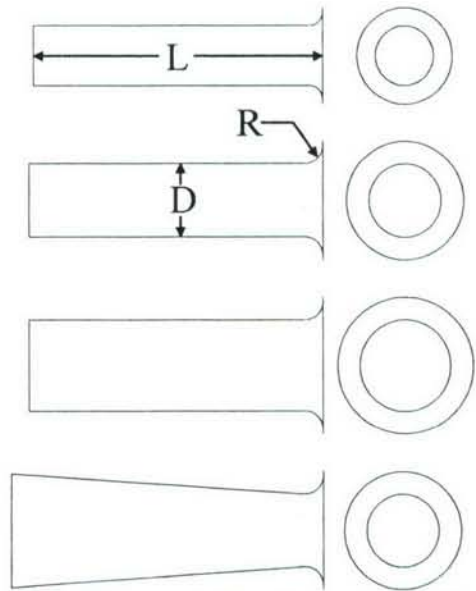


Figure 7. Representative ejector schematics and symbols for relevant dimensions for straight walled and tapered ejectors evaluated.

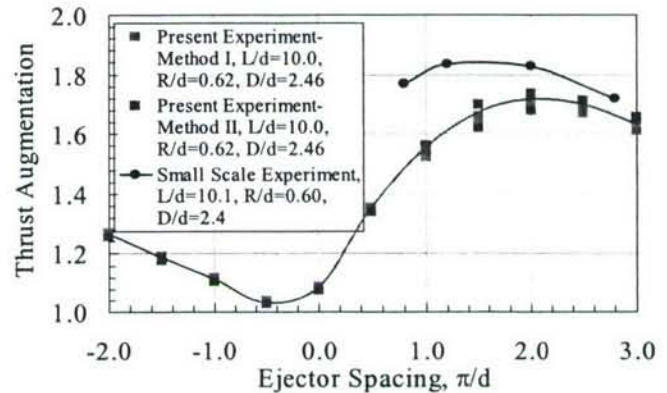


Figure 8. Thrust augmentation as a function of driver-to-ejector spacing for the $D/d=2.46$, $L/d=10.0$ ejector.

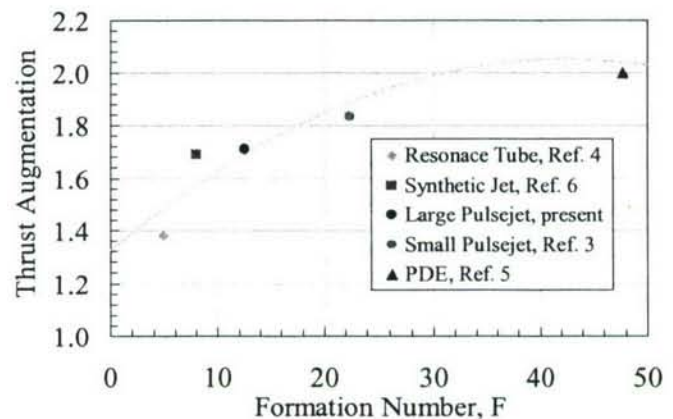


Figure 9. Peak thrust augmentation as a function of Formation Number for unsteady ejectors, see AIAA 2006-4216 for further details

TURBINE BURNERS: TURBULENT COMBUSTION OF LIQUID FUELS

FA9550-06-1-0194

William A. Sirignano, Feng Liu, and Derek Dunn-Rankin

Department of Mechanical and Aerospace Engineering
University of California, Irvine
Irvine, CA 92687-3975

SUMMARY/OVERVIEW:

The proposed theoretical/computational and experimental study addresses the vital two-way coupling between combustion processes and fluid dynamic phenomena associated with schemes for burning liquid fuels in high-speed, accelerating and turning transonic turbulent flows. A major motivation for this type of combustion configuration results from the demonstrated potential for immense improvements in the performance of gas turbine engines via combustion in the turbine passages. This program will address various fundamental issues concerning liquid-fuel combustion in an axially and centrifugally accelerating flow. The major combustion challenge involves ignition and flame-holding of the spray flame in the high-acceleration flow and associated optimization of the injection of the liquid fuel and some secondary air into a protected recirculation zone provided by a cavity.

TECHNICAL DISCUSSION:

This three-year study began on March 16, 2006. So, only limited progress can be reported. The study focuses on the upstream subsonic portion of the accelerating flow where the critical ignition and flame-holding processes occur. This research is substantially different from the studies of liquid fuel injection and burning in high-speed flows motivated by the Scramjet application because we consider injection into the low-speed portion of the flow, where the flow begins its acceleration. The combustion can extend, however, into regions of high acceleration and transonic velocity. These high accelerations in the stratified flow can have profound consequences on the mixing and flame-holding. Liquid fuel will be injected into a recirculation zone (e.g., cavity) adjacent to the accelerating flow in a curved duct. A two-phase, unsteady simulation is being developed for the reacting, multicomponent turbulent flow using Lagrangian coordinates for the droplets and Eulerian coordinates for the gas phase. In this situation, where vaporization can be a controlling process, quasi-steady vaporization models are inadequate and transient droplet behavior must be considered. Experiments will be performed with non-intrusive diagnostics for reacting and cold-flow mixing studies, both to provide inlet and boundary conditions for the computations and to verify numerical simulations.

Experimental Approach: The experimental apparatus is designed to be flexible in its ability to simulate processes that would occur with fuel addition in the curved passages of a turbine burner. Although typical nozzle guide vane geometries can be quite complex, the experiments will concentrate initially on an auxiliary combustion chamber and its interaction with the primary geometric curvature that guides the hot gases into the turbine rotor. The

experiments can also provide global evaluation of flow uniformity, flow stability, pressure losses, pollutant formation, and efficiency.

Figure 1 gives an overview of the experimental apparatus. The key feature of the experimental apparatus is to produce a combustive environment in a flow that has both centrifugal and axial accelerations by curving the duct and decreasing duct cross-sectional area with downstream distance. To simplify the grid behavior in the related numerical simulations, only one of the duct dimensions decreases. The plenum section includes a heater section and flow straightening. Both electrical preheating and a burner heater are included to provide a wide range of operating conditions. The hot-flow curved duct section is primarily ceramic coated mild steel, but it has several windows to provide optical access into reacting spray flow experiments. Liquid or gaseous fuel can be injected into the curved duct through ports upstream or downstream of the auxiliary cavity. The auxiliary segment is the heart of the experiment. It allows a variety of fuel injection locations, geometries, and orientations relative to the curved section. Windows provide full optical access to this section. The inlet channel cross-section is 100 mm x 75 mm, decreasing to 50 mm x 75 mm at the outlet, with a channel radius of curvature between 200 and 300 mm.

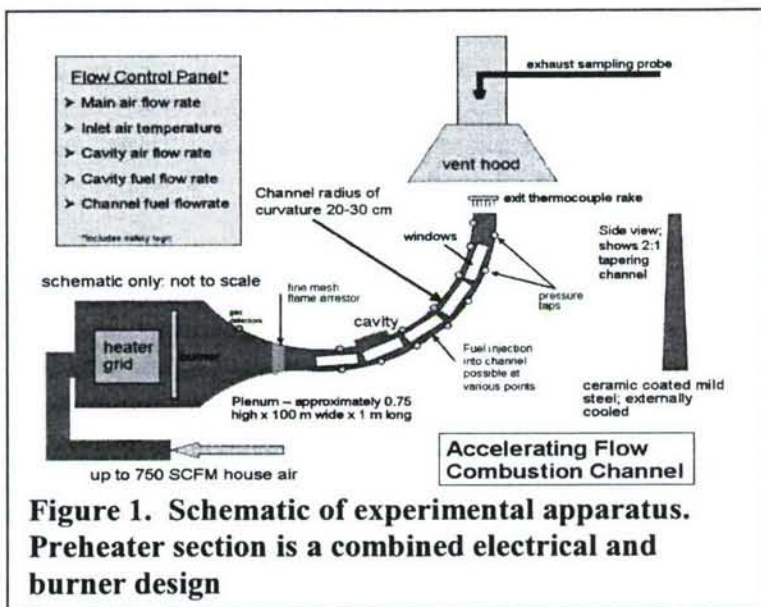


Figure 1. Schematic of experimental apparatus. Preheater section is a combined electrical and burner design

mechanism for flame-holding (i.e., a low-velocity, low-stretch-rate region where the flame can be maintained). Therefore, the turbine-burner configuration will use the small auxiliary chamber as a rearward-facing step to produce a relatively low speed vortex into which fuel can be injected. A similar approach has shown promise in some preliminary activities at the Air Force Research Laboratory.

The auxiliary chamber of the hot-flow duct houses the cavity volume and is a removable piece to allow flexibility in optical access, chamber shape, chamber size, and fuel injection location. The cold-flow experiments and the numerical simulations will have provided some guidance with regard to which configurations provide good mixing and flow field characteristics, but reaction and heat release are certain to change some of these findings. Optical access allows detailed observation of the spray and its mixing into the recirculation

zone of the chamber. The cavity will allow fuel injection in at least 6 different locations to determine the interaction between the in-chamber vortex motion and the additional momentum provided by the spray. The hot-flow experiment requires a substantial development and construction effort. We have settled on the dimensions and fabrication strategy of the plenum section and the curved duct section. Heater design, using flexible inconel heater elements, including a verification of electrical power infrastructure is completed. Detailed design of the cavity section is underway.

In cold flow conditions, we will first use acetone PLIF to assess fuel mixing from the auxiliary chamber, along with static pressure measurements along the curved duct walls and pitot pressure surveys. To these measurements we will add particle image velocimetry (PIV) of the flow in the duct under some of the key conditions. We have a PIV system, but will add seeding capability to the experiment. In the hot-flow experiments, it may be difficult to have optical access in the curved walls without leaks and without compromising the curvature. Nevertheless, we will use discrete window segments to observe particular regions of the flow. All windows in the system are flat to reduce the optical complexity of the alignment of overlapping beams. The first experiments will be chemiluminescence and schlieren visualizations of flame location.

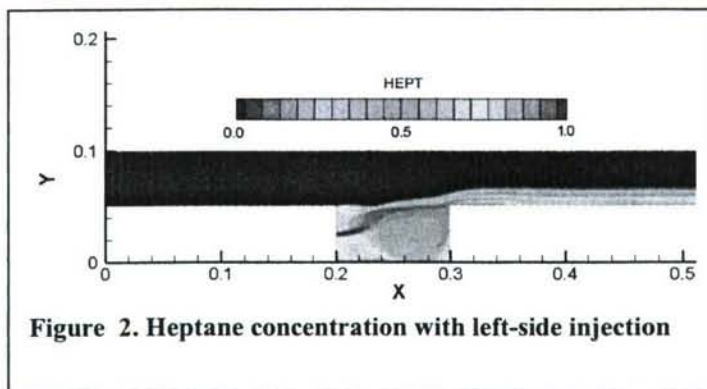
Both local and global experiments will be coordinated with the calculations to provide detailed comparison data most critical to the predictions and performance of the process. For example, PIV will give instantaneous velocity vector plots on the centerline of the duct near the auxiliary chamber to show how the flows interact. These same velocities will be predicted by the numerical code. Similarly critical particle size distribution data for injected fuel droplets will serve as inputs to the 2-phase calculations. Consultation with colleagues at the AF Research Laboratories will continue.

Computational Approach: The first approximation to the problem is a two-dimensional rectangular channel flow over a rectangular cavity, as shown in Figure 2. The numerical method used is a finite-volume, unsteady laminar code for viscous, multi-component, reacting flow, with a non-uniform Cartesian mesh. Continuity, momentum, energy, and species equations are solved simultaneously to within a 0.1% residual error. Viscosity, thermal conductivity and specific heat are modeled as functions of temperature. Density is a function of both temperature and pressure, using the assumption of a perfect gas. Binary diffusion coefficients are modeled as functions of temperature and density using kinetic theory approximations. Each species is considered to diffuse with nitrogen, the dominant species. The imposed boundary conditions for the equations are as follows: constant velocity profile at channel inlet, constant pressure at channel outlet, parabolic-velocity profile at injection points, and no-slip condition on all walls; constant inlet temperature, constant wall temperature, constant injection temperature; specified inflow species concentrations and zero normal gradient at walls for species concentration. In addition, Lagrangian derivatives of the outflow are zero.

The first calculations consider non-reacting flow at a Reynolds number of 5000. The three sides of the cavity have been considered as general injection locations for the fuel. In Figure 2, gaseous heptane is injected into the left-side of the cavity, normal to the wall.

The figure shows the concentration of the heptane as it diffuses with the air in the channel. Here, the heptane is injected at 300K at 5 m/s, and the channel inlet flow is at 1000K and 12m/s. The mass flow rate of heptane is approximately 25% of the mass flow rate of air in the channel.

The results to date have shown limited mixing of the injected fuel with the air in the cavity, with the injected fuel forming a boundary layer along the bottom wall of the channel as it exits the cavity. Several extra vortices are created inside the cavity when fuel is injected, depending on the injection location and velocity. An additional vortex also occurs downstream of the cavity on the bottom wall of the cavity for some injection conditions.



The plan is to develop the code to consider multiple points of injection of fuel or fuel with air in the cavity and at points upstream of the cavity. In an incremental way, additions/modifications to the code will allow for liquid-fuel injection and vaporizing spray analysis, oxidation reaction, three-

dimensional effects, and turbulent modeling. Choices of parameters and sub-grid models will be guided by our experimental observations and those at the Air Force Labs, plus our previous and concurrent experience with computations of a reacting mixing layer in an accelerating and turning channel flow.

Previous calculations for reacting gaseous mixing layers indicate that the flow in the channel is transitional rather than fully turbulent. Density variations in the channel lead to interesting effects whereby not only a shear-layer (Kelvin-Helmholtz) instability occurs but the turning can result in Rayleigh-Taylor and centrifugal fluid instabilities. We will look for signs of these effects in the two-phase flow with a cavity. An open question that remains is whether it is superior to model the flow in the interesting Reynolds number range as an unsteady, three-dimensional flow with some sub-grid turbulence modelling or to use some Favre-averaged equations.

Communications with Dr. Joseph Zelina of the Air Force Labs have been helpful. Inputs from several UCI graduate students, Felix Cheng, Ben Colcord, and Nicola Amade Sarzi are acknowledged.

INVESTIGATION OF SCALAR FILTERED DENSITY FUNCTION IN TURBULENT PARTIALLY PREMIXED FLAMES

(AFOSR Grant F-49620-02-1-0130)

Principal Investigator: Chenning Tong

Department of Mechanical Engineering
Clemson University
Clemson, SC 29634-0921

SUMMARY

The filtered mass density function (FMDF) of mixture fraction and other filtered variables used in large-eddy simulation of turbulent combustion are studied using measurement data obtained in turbulent partially premixed methane/air (Sandia) flames. For SGS scalar variance small compared to its mean, the FMDF is not far from Gaussian and the SGS scalar is well mixed. For large SGS variance, however, the FMDF becomes bimodal and the conditionally filtered scalar dissipation is bell-shaped, indicating the existence of a diffusion (dissipation) layer structure, which is similar to the mixture fraction profile in the counter-flow model for laminar flamelets. The conditionally filtered temperature near the stoichiometric mixture fraction decreases progressively with increasing SGS scalar variance. Furthermore, local extinction events appear to occur mostly when the SGS scalar variance is large, suggesting the possibility of flamelet extinction. The results suggest that the mixing regimes and the associated mixture fraction structure could potentially have strong influences on the combustion regime and extinction/reignition in turbulent nonpremixed flames.

TECHNICAL DISCUSSION

LES has been recognized as a very promising approach to modeling turbulent combustion. In LES the subgrid-scale (SGS) scalar mixing and the resulting instantaneous distribution of scalar values in each grid volume (i.e., the filtered density function) must be faithfully represented in order to accurately predict the chemical reaction rate. The present study investigates issues in using this approach, including SGS mixing and turbulence-chemistry interaction, which play crucial roles in LES of nonpremixed combustion.

Our previous studies of the SGS mixing of a conserved scalar in nonreacting jets (Tong 2001, Rajagopalan and Tong (2003), Wang and Tong (2002, 2004), Wang et al. 2004) have shown that the SGS scalar at a fixed location has qualitatively different FDF shapes and structures depending on the *instantaneous* SGS scalar variance. When the SGS variance is small compared to its mean value, the SGS scalar has close to Gaussian distributions, indicating well mixed SGS scalar fields. The SGS turbulence is in quasi-equilibrium, i.e., the production of the SGS variance is equal to or smaller than the SGS dissipation rate. When the SGS variance is large compared to its mean value, the conditional SGS structure on average resembles that of a counter-flow diffusion flame, which is a model for laminar flamelets. The SGS scalar has bimodal distributions, indicating highly nonpremixed SGS scalar fields. In a nonpremixed flame this would indicate that the fuel lean and rich regions of the SGS fields are highly segregated. There is a sharp interface separating the two regions, across which there is a large scalar value jump (can be as large as the integral-scale fluctuations). In addition the SGS scalar is in nonequilibrium.

The well-mixed SGS mixture fraction fields with close-to-Gaussian distributions and the highly nonpremixed SGS fields with bimodal distributions can potentially have strong influences on the flame structure. In this study we investigate the SGS mixing of the mixture

fraction in turbulent partially premixed flames and examine the effects of the different SGS mixture distributions and structures on the flame structure. We investigate the characteristics of the filtered mass density function (FMDF) of the mixture fraction

$$F_{\xi L}(\hat{\xi}; \mathbf{x}, t) = \langle \rho(\mathbf{x}, t) \delta(\xi - \hat{\xi}; \mathbf{x}, t) \rangle_{\ell} = \int \rho(\mathbf{x}', t) \delta(\xi - \hat{\xi}; \mathbf{x}', t) G(\mathbf{x} - \mathbf{x}') d\mathbf{x}', \quad (1)$$

and the mixing term in its transport equation, the conditionally filtered scalar dissipation rate,

$$\langle \chi | \xi \rangle_{\ell} = \langle D \frac{\partial \xi}{\partial x_j} \frac{\partial \xi}{\partial x_j} | \xi \rangle_{\ell}, \quad (2)$$

where ξ , ρ , and D are the mixture fraction, the fluid density and the diffusivity for the mixture fraction, respectively. The subscripts ℓ and L denote conventional and Favre filtered variables respectively. The dependences of $F_{\xi L}$ and $\langle \chi | \xi \rangle_{\ell}$ on the different mixing process will be studied. We also analyze the conditionally filtered temperature $\langle T | \xi \rangle_{\ell}$ and examine conditional SGS temperature samples to study the effects of SGS mixing on flames structure.

Experimental data and processing procedures

We use experimental data obtained in piloted turbulent partially premixed methane with a 1:3 ratio of CH_4 to air by volume (Sandia flame D and E, (Karpetis and Barlow (2004, 2004)). Their measurements employed combined line-imaging of Raman scattering, Rayleigh scattering, and laser-induced CO fluorescence. Simultaneous measurements of major species (CO_2 , O_2 , CO , N_2 , CH_4 , H_2O , and H_2), mixture fraction (obtained from all major species), temperature, and the radial component of scalar dissipation rate were made. The mixture fraction is calculated using a variation of Bilger's definition, which has been modified by excluding the oxygen terms. The length of the imaging line is 6.0 mm with a resolution of 0.2 mm.

Measurements of the filtered density functions require spatial filtering of scalar fields. In this research, both one-dimensional filtering will be employed. The filter sizes Δ employed in this work are 3.0 and 6.0 mm.

Results

The FMDF and other SGS variables are analyzed using their conditional averages. We use the Favre filtered mixture fraction,

$$\langle \xi \rangle_L = \langle \rho \xi \rangle_{\ell} / \langle \rho \rangle_{\ell}, \quad (3)$$

and the Favre SGS scalar variance,

$$\langle \xi''^2 \rangle_L \equiv \frac{1}{\langle \rho \rangle_{\ell}} \int F_{\xi L}(\hat{\xi}; \mathbf{x}, t) (\xi - \langle \xi \rangle_L)^2 d\xi = \langle \rho \xi^2 \rangle_{\ell} / \langle \rho \rangle_{\ell} - \langle \xi \rangle_L^2, \quad (4)$$

as conditioning variables. The SGS variance value normalized by its ensemble mean is denoted by $\langle \xi''^2 \rangle_L^*$.

The conditional mixture fraction FMDF for flame D for several SGS variance values is shown in Fig. 1. The results for flame E (not shown) are similar. The Favre filtered mixture fraction is set to the stoichiometric mixture fraction, $\xi_s = 0.35$, to maximize the probability of the SGS field containing reaction zones. For $\langle \xi''^2 \rangle_L^* \ll 1$ the conditional FMDF, $\langle F_{\xi L} | \langle \xi \rangle_L, \langle \xi''^2 \rangle_L^* \rangle$, is generally unimodal and probably not very far from Gaussian. This suggests that the SGS scalar is likely to follow the Kolmogorov's cascade picture. Therefore, when the filter scale decreases the SGS fluctuations become smaller, suggesting that the burden on the SGS mixing models is reduced.

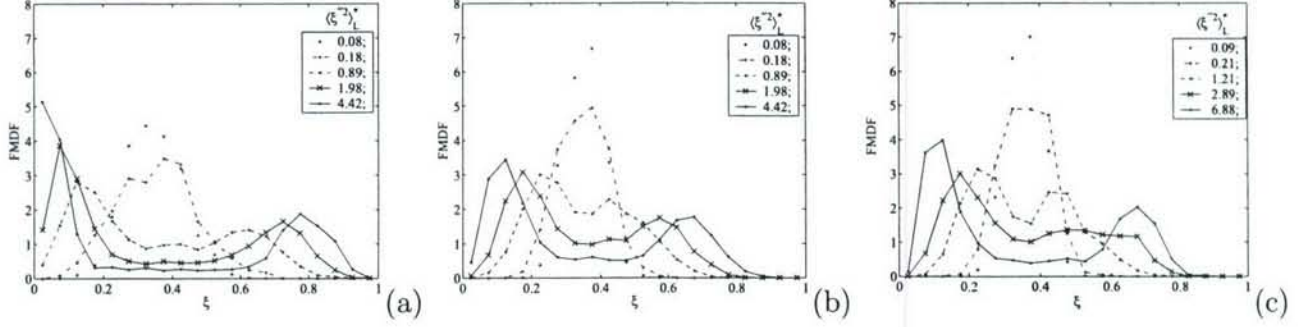


Figure 1: The mean conditional scalar FMDF for Sandia flame D for $\langle \xi \rangle_L = \xi_s$ and several $\langle \xi''^2 \rangle_L^*$ values (specified value $\times [0.67, 1.49]$). (a) $x/D=15$, $\Delta = 6.0\text{mm}$; (b) $x/D=15$, $\Delta = 3.0\text{mm}$; (c) $x/D=30$, $\Delta = 6.0\text{mm}$

For $\langle \xi''^2 \rangle_L^*$ close to or larger than one, the FMDF becomes bimodal and the bimodality is stronger for larger SGS variance. This indicates that the SGS mixture fraction is highly nonpremixed. Therefore, the rich and lean mixtures in a grid cell are essentially segregated. The bimodal FMDF is also similar to the scalar FDF for large SGS variance observed in nonreacting flows. The SGS scalar is not well described by Kolmogorov's turbulence cascade picture.

In contrast to the unimodal FMDF, the dependence of the bimodal FMDF on the filter scale is much weaker. The FMDF at $x/D = 15$ for a filter size of 3.0 mm shown in Fig. 1(b) has the same characteristics as that for a 6.0 mm filter. Therefore, large scalar value jumps exist in the SGS scalar regardless of the filter scale as long as the filter scale is larger than the scalar dissipation length scale, which is generally the case in LES. This suggests that when the SGS variance is large, the burden on the mixing model to correctly model the SGS mixing is not reduced when the filter size is decreased.

The results show that the statistical structure of the SGS mixture fraction is different for small and large SGS variance values. The difference of the ξ values between the two FMDF peaks is often larger than the equilibrium reaction zone width in the ξ space for the methane flames studied in this work ($\Delta\xi_R \approx 0.23$ (Frank et al. 2002)). Therefore, such a mixture fraction structure is likely to support laminar flamelets. This is in contrast with the well-mixed SGS mixture fraction for small SGS variance where the turbulence cascade is likely to dominate and the dissipation-scale scalar fluctuations are predicted by the Kolmogorov-Obukhov-Corrsin theory. Therefore, such a SGS mixture fraction is likely to result in distributed reaction zones.

The conditionally filtered scalar dissipation $\langle \chi | \xi \rangle_\ell$ (not shown) also has qualitatively different dependences on the mixture fraction for small and large SGS variance. For small $\langle \xi''^2 \rangle_L^*$ it depends relatively weakly on ξ , except near $\xi = 0$ and 1. This is consistent with the FMDF being unimodal and not far from Gaussian. For large $\langle \xi''^2 \rangle_L^*$, $\langle \chi | \xi \rangle_\ell$ becomes bell-shaped, with the maximum at the ξ value where the bimodal FMDF has a dip, indicating that there is an interface between the highly segregated SGS mixture fraction regions and that the interface is sharp and is essentially a diffusion layer. The FMDF and the conditionally filtered dissipation results suggest that the SGS mixture fraction structure is similar to that in the counter-flow model for laminar flamelets.

The conditionally filtered temperature $\langle \langle T | \xi \rangle_\ell | \langle \xi \rangle_L, \langle \xi''^2 \rangle_L^* \rangle$ for the Sandia flame D at $x/D = 7.5$ and 15 are shown in Fig. 2. For small SGS variance the conditionally filtered temperature is close to the equilibrium values. As the SGS variance increases, the temperature begins to decrease, especially near the stoichiometric mixture fraction. The magnitude

of the temperature reduction is considerably smaller for $x/D = 7.5$ than for $x/D = 15$ and $x/D = 30$ (not shown). Because the jump in mixture fraction is large for large SGS variance, the decreases in temperature under such conditional are likely caused by straining or extinction of laminar flamelets.

It is important to note that although the conditionally filtered temperature in Fig. 3 is somewhat similar to the conditional mean temperature obtained by using χ_s as the conditioning variables[?], conditioning on the SGS variance provides additional information than conditioning on the dissipation rate alone. This is because the SGS variance enables conditional sampling of the structure of the SGS mixture fraction, thereby allowing the effects of the mixture fraction structure on the flame structure to be studied.

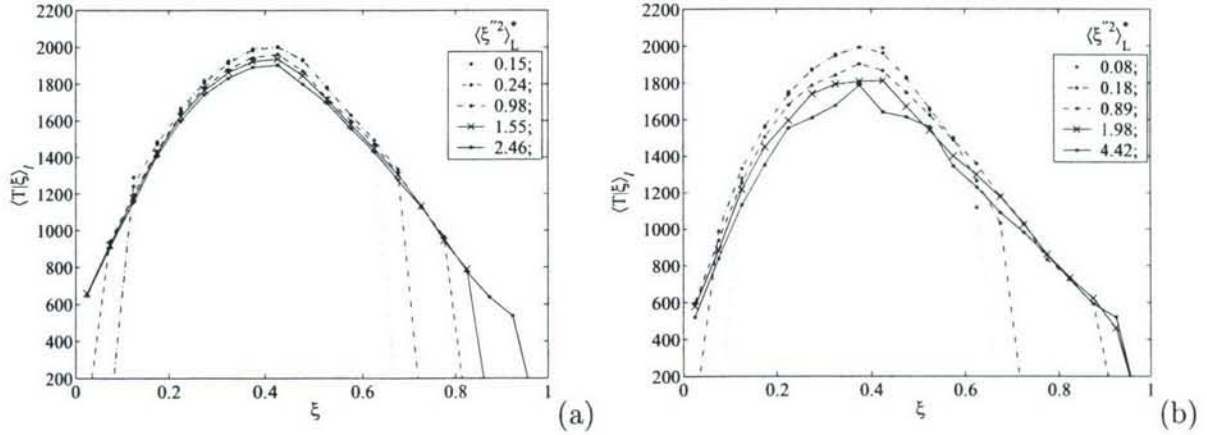


Figure 2: The mean conditionally filtered temperature for flame D for $\langle \xi \rangle_L = \xi_s$ and several $\langle \xi'^2 \rangle_L^*$ values. (a) $x/D=7.5$, $\Delta = 3.0\text{mm}$; (b) $x/D=15$, $\Delta = 6.0\text{mm}$.

REFERENCES

- Frank, J. H., Kaiser, S. A., and Long, M. B. (2002) Reaction rate, mixture fraction, and temperature imaging in turbulent methane/air jet flames, *Proc. Combust. Inst.* **29**, 2687 .
- Karpetis, A. N. and Barlow, R. S. (2002) Measurements of scalar dissipation in turbulent piloted methane/air jet flames, *Proc. Combust. Inst.* **29**, 1929.
- Karpetis, A. N. and Barlow, R. S. (2004) Measurements of flame orientation and scalar dissipation in turbulent partially premixed methane flames, *Proc. Combust. Inst.* **30**, 665.
- Rajagopalan, A.G. and Tong, C. (2003) Experimental investigation of scalar-scalar-dissipation filtered joint density function and its transport equation. *Phys. Fluids*, **15**, 227–244.
- Tong, C. (2001) Measurements of conserved scalar filtered density function in a turbulent jet. *Phys. Fluids* **13**, 2923–2937.
- Wang, D. and Tong, C. (2002) Conditionally filtered scalar dissipation, scalar diffusion, and velocity in a turbulent jet. *Phys. Fluids* **14**, 2170–2185.
- Wang, D and Tong, C. (2004) Experimental investigation of velocity-scalar filtered density function for LES of turbulent combustion. *Proc. Combust. Inst.* In press.
- Wang, D., Tong, C., and Pope, S.B. (2004) Experimental investigation of velocity filtered density function for large eddy simulation. *Physics of Fluids* **16**, 3599–3613.

CONCURRENT RESEARCH ON HIGH GRAVITY (g) COMBUSTION WITH ENABLING MATERIALS

(LRIR: 99PR12COR)

Principal Investigator: Dr. Joseph Zelina

Air Force Research Laboratory
AFRL/PRTC
WPAFB, OH 45433

SUMMARY/OVERVIEW

A gas turbine combustor concept that uses high g-loading in the circumferential cavity is being tested at AFRL to provide the foundation for development of a low-emissions, ultra-compact, high performance combustion system for future military and commercial aircraft. This work comprises experimental testing and modeling and simulation of different high g-loaded combustion cavities. Initial tests indicate that, by using highly swirling flows, the combustor performance can be enhanced in the form of improved combustor efficiencies at reduced combustor length. Understanding the impact of high g-loading on the pollutant emissions, operability limits, and combustor durability are three major areas where the AFOSR program will progress the scientific understanding of the physical processes involved in this novel combustion system.

TECHNICAL DISCUSSION

This AFOSR-sponsored work addresses fundamental combustion issues that will lead to the development of a revolutionary propulsion system that operates on a highly efficient, near constant temperature (NCT) cycle instead of the constant pressure cycle of today's engines. Such a propulsion system could provide increased power extraction, thrust augmentation, and specific thrust (ST) enhancements. A key technology essential for the development of a propulsion system that operates on a NCT cycle is an ultra-compact combustion (UCC) system that will efficiently add heat between the turbine stages and is constructed of advanced, light-weight ceramic-matrix composites (CMC) materials. This combustor has been referred to in the literature as an inter-turbine burner (ITB).

The AFRL team has been working on the premise that high g loading can provide benefits compared to conventional gas turbine combustion systems. A concept design for a high-g combustion system that can serve as a main combustor or as an ITB has been completed however, understanding of the combustion process at high g-loading conditions is necessary. The AFRL team is focused on what we believe are the key combustion issues. (1) What are the fundamental processes that control combustion in a highly accelerated (high-g) flows? (2) How does swirling flow from the main air supply impact the cavity combustion process? and (3) Can we integrate CMC vanes into flow path while turning the flow? (4) How does vitiated flow impact the high g combustion process? In this abstract, we will focus on experimental results related to vitiated flow.

Approach

Vitiated Flow Experiments: The vitiator used for these experiments was originally designed to be used in fundamental augmentor combustion research activities to simulate the core flow of an augmented

turbofan engine burning JP8 fuel. The vitiator operates at pressures of 50 psig to facilitate efficient combustion. The major components of the vitiator are shown in Fig. 1, where the vitiator is installed in front of the ITB test rig. Air is supplied to the front end of the vitiator plenum section that houses the single fuel injector/swirler module. The module employs a “cyclone” type swirler. The fuel injector is a hollow cone peanut type pressure atomizer that has an air cooled jacket surrounding the fuel feed tube to reduce potential for coking. The air delivered to the vitiator is heated via electric heaters to temperatures near 600°F with typical pressure drops across the swirler of 6-8%. The dome plate holding the swirl cup is effusion-cooled with a thermal barrier coating (TBC) on the dome surface. The combustor liner is an uncooled pipe section that is over-designed to handle the pressure-temperature combination. The vitiator combustor is ignited by a propane/air torch that incorporates a conventional automotive spark igniter to initiate the ignition of the fuel-air mixture in the torch.

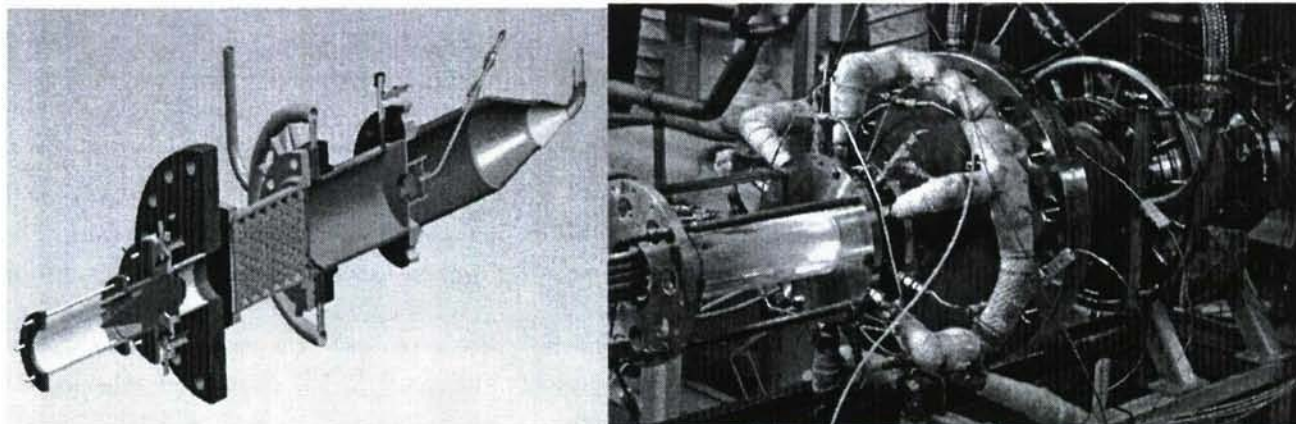


Figure 1: High g Combustor with Vitiator.

Combustion Stability Results: Combustor lean blowout (LBO) was investigated for the different configurations. The OFAR at LBO was plotted against the cavity g-loading and cavity loading parameter (LP). To determine cavity g-loading, estimates of the tangential velocity (V_{tan}) were estimated from the expression;

$$g = \frac{V_{tan}^2}{g_c r_{cav}} \quad \text{Eq. (1)}$$

is used to calculate the g-loading. These tests were run at atmospheric pressure and 500 °F inlet air temperature.

Recent work¹ with the UCC/ITB suggests a dependent behavior on reaction temperature and/or liquid fuel atomization, in addition to g-loading effects. As Yonezawa et. al² suggested by continuing Lewis³ work through introducing the observations for flame propagation by Chomiak⁴ for turbulence enhancement through the generation and movement of non-premixed buoyant “bubbles”, or eddies, of non-premixed and partially-premixed reactants, and burned reactants, such that the burning velocity (S_b),

¹ Zelina, J., Sturgess, G. J., Mansour, A., and Hancock, R. D., “Fuel Injection Design for Ultra-Compact Combustor,” ISABE 2003-1089.

² Yonezawa, Y., Toh, H., Goto, S and Obata, M., “Development of the Jet-Swirl High Loading Combustor,” Paper No. AIAA-90-2451, 26th. AIAA/SAE/ASME/ASEE Joint Propulsion Conference, Orlando, Florida, 1990.

³ Lewis, G.D., “Centrifugal-Force Effects on Combustion,” proc. 14th. Symposium (International) on Combustion, The Combustion Institute, 1973, pp. 413-419.

⁴ Chomiak, J., “Dissipation Fluctuations and the Structure and Propagation of Turbulent Flames in Premixed Gases at High Reynolds Numbers,” Sixteenth Symposium (International) on Combustion, The Combustion Institute, 1977, pp. 1665-1673.

$$S_b = \frac{\rho_u}{\rho_b} \sqrt{Rg} \quad \text{Eq. (2)}$$

where the density gradient is worked on by the centrifugal force generated through the swirl. So, at fixed radius (R) and operating pressure, and neglecting differences in gas constants,

$$S_b \propto \frac{T_b}{T_u} \sqrt{g} \quad \text{Eq. (3)}$$

T_u is taken as the air inlet temperature and T_b ideally should be a measured gas temperature at the cavity exit, but here is taken as the adiabatic flame temperature calculated for JP-8/air from an equilibrium chemistry code. When found in these ways the ratio T_b/T_u represents a maximum value. Therefore, if combustion efficiency is assumed to be proportional to S_b , and when data is plotted in terms of $(T_b/T_u)(g)^{1/2}$ as the abscissa, the systematic variation in the conditions for the maximum combustion efficiency should be eliminated, and improved correlation of combustion efficiency data would be expected, for cavity-only burning and if there are no physical effects controlling the combustion process. This correlation $((T_b/T_u)(g)^{1/2})$ will be referred to as the Swirl Parameter (SP). In these experiments, very small flow number (FN) fuel injectors were used, indicating that the atomization level was very good (~20-40 micron drops), removing this physical effect from the data.

In Fig. 2, ϕ_{cav} at blowout is plotted as a function of SP. Configuration 1 and Configuration 2 (variation in injector airflow) are shown, where the vitiation level in the main flow stream varies

from zero to $\phi_{vit} = 0.33$. It is clear from the data that Configuration 2 (reduced injector airflow) blowout level is superior to the Configuration 1 design. It is also observed that the vitiation level has very little impact on the lean blowout value. This is somewhat expected, since the circumferential cavity is fed with fresh air for all of the data plotted in the figure, and blowout occurs from the cavity. Conditions in the circumferential cavity control the flame stabilization. Notice in Fig. 14 that for both configurations that ϕ_{cav} at blowout is very close to or below flame extinction limits for premixed flames. Incorporated in the design is a geometric feature that was found to provide excellent stability characteristics. Local fuel-rich pockets exist in the circumferential cavity to stabilize the flame.

Combustion Efficiency: Combustion efficiency, determined by gas analysis, is plotted as a function of ϕ_{cav} for different levels of ϕ_{vit} and is shown in Fig. 3. Measurements were collected with a five-element probe that spanned the entire exit plane of the combustor. The probe was located at the trailing edge of the centerbody, about 12 inches downstream from the circumferential cavity. At very lean values of ϕ_{cav} , and low values of ϕ_{vit} , the combustion efficiency is 84-95%. For both configurations, the efficiency increases with increased ϕ_{cav} and approaches 99.9% efficiency near $\phi_{cav} \sim 1.0$. It is also observed that combustion efficiency increased as ϕ_{vit} increased. In fact, for Configuration 1 at $\phi_{cav} \sim 0.6$, the effect of increasing $\phi_{vit} = 0.247$ to $\phi_{vit} = 0.327$ resulted in a combustion efficiency increase from 85% to 99.5%. Since oxygen concentrations are less for the higher vitiated case, the increase in combustion efficiency is

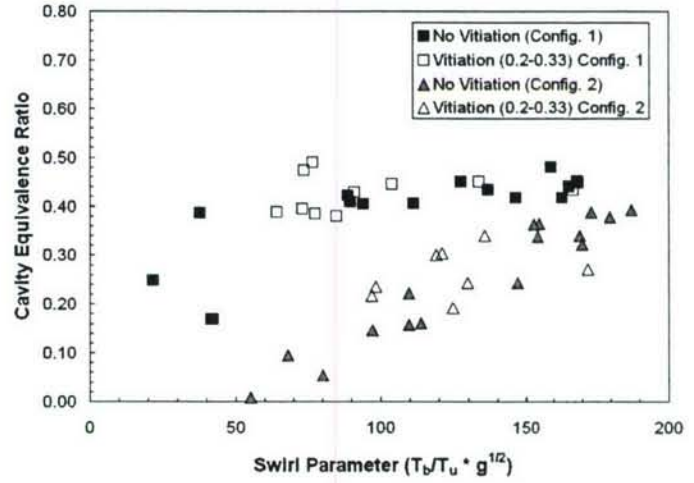


Figure 2: Cavity equivalence ratio at blowout as a function of the Swirl Parameter (SP) for two designs and vitiation level.

largely due to the increase in main stream temperature (+400°F), whereby quenching of CO and UHC is minimized.

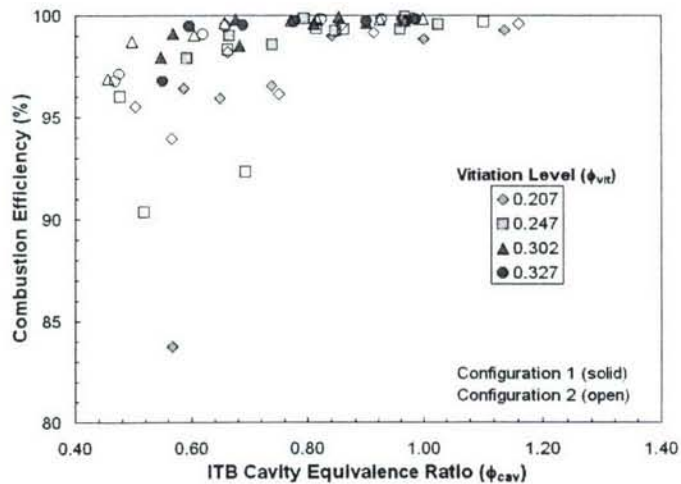


Figure 3: Combustion efficiency as a function of ITB cavity equivalence ratio and vitiation level for the two configurations.

windows located along the circumferential cavity to study the high g combustion and flame stability mechanisms in the cavity.

The modular configuration that will be used for these tests is shown in Fig. 4. The transparent area is the current circumferential cavity where air and fuel are injected. The yellow vanes represent realistic vane designs and the radial cavities will be studied to determine their effectiveness on transporting the circumferential cavity mixture to the main flow.

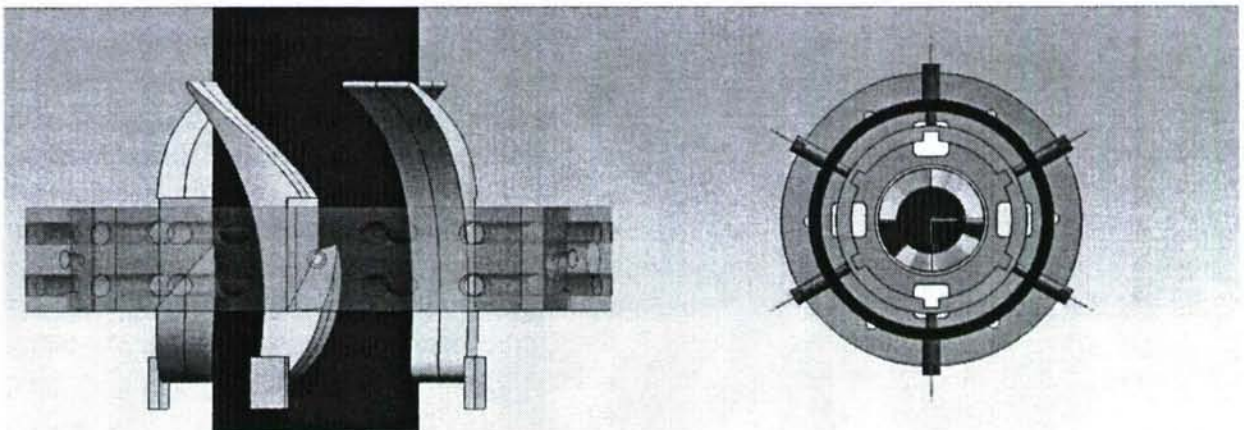


Figure 4: Modular combustor design to investigate cavity geometry, atomization effects, and impact of main swirl on cavity combustion.

External Collaboration: AFRL continues to collaborate with Air Force Institute of Technology on specific high g combustor problems. AFRL is actively involved with industry to transition compact, high g combustor concepts to industry. Currently, AFRL is working directly with three major engine companies, along with smaller businesses to incorporate design concepts. We continue to look for opportunities to start 6.2 programs utilizing our 6.1 results to demonstrate an UCC/ITB. This collaborative approach provides a clear transition path for the 6.1 research and would provide additional funds needed to demonstrate a turbine burner concept.

List of Invitees

Waldo Acosta
Army Research Laboratory
Vehicle Technology Directorate
NASA Glenn Research Center
21000 Brookpark Road
Cleveland, OH 44135-3191
Phone: (216) 433-3393
Email: waldo.acosta@us.army.mil

Ajay Agrawal
University of Oklahoma
Department of Aerospace
and Mechanical Engineering
865 Asp Avenue, Room 212
Norman, OK 73019
Phone: (405) 325-1754
Fax: (405) 325-1088
Email: aagrawal@ou.edu

M. S. Anand
Rolls-Royce Corporation
P.O. Box 420
Speed Code T14
Indianapolis, IN 46206-0420
Phone: (317) 230-2828
Fax: (317) 230-3691
Email: m.s.anand@rolls-royce.com

William Anderson
U.S. Army Research Laboratory
AMSRL-WT-PC
Aberdeen Proving Ground, MD 21005-5066
Phone: (410) 306-0731
DSN 298-9992
Fax: (410) 306-1909
Email: willie@arl.army.mil

Ralph Anthenien
AFIT/ENY
Department of Aeronautics and Astronautics
2950 Hobson Way
Wright-Patterson AFB, OH 45433-7765
Phone: (937) 255-3636
DSN 785-3636
Fax: (937) 656-4032
Email: Ralph.anthenien@afit.edu

Chris Atkinson
West Virginia University
Department of Mechanical
and Aerospace Engineering
P.O. Box 6106
Morgantown, WV 26506-6106
Phone: (304) 293-4111
Fax: (304) 293-2582

Steve Beckel
Pratt and Whitney
MS 715-83
P.O. Box 109600
West Palm Beach, FL 33410-9600

Josette Bellan
Jet Propulsion Laboratory
MS 125-109
4800 Oak Grove Drive
Pasadena, CA 91109
Phone: (818) 354-6959
Fax: (818) 393-5011
Email: josette.bellan@jpl.nasa.gov

William Berry
Director for Research
Defense Research and Engineering
3040 Defense Pentagon
Washington, DC 20301-3040

Robert Bill
Army Research Laboratory
Vehicle Technology Directorate
NASA Glenn Research Center, MS 77-12
21000 Brookpark Road
Cleveland, OH 44135-3191
Phone: (216) 433-3703
Fax: (216) 433-3000
Email: bob.bill@us.army.mil

Mitat Birkan
Air Force Office of Scientific Research
875 North Randolph Street
Suite 325, Room 3112
Arlington, VA 22203-1768
Phone: (703) 696-7234
DSN 426-7234
Fax: (703) 696-8451
Email: mitat.birkan@afosr.af.mil

Linda Blevins
National Science Foundation
Chemical and Plasma Systems
4201 Wilson Boulevard
Arlington, VA 22230
Phone: (703) 292-8371
Fax: (703) 292-9054
Email: lblevins@nsf.gov

Andreja Brankovic
Flow Parametrics, LLC
15 Debra Drive
Bear, DE 19701
Phone: (302) 838-7368
Fax: (302) 838-7369
Email: brankov@flowparametrics.com

R.C. Brown
Aerodyne Research, Inc.
45 Manning Road
Manning Park Research Center
Billerica, MA 01821-3976
Phone: (978) 663-9500
Fax: (978) 663-4918

Thomas Bruno
National Institute of Standards and Technology
Physical and Chemical Properties Division
Boulder, CO 80305-3328
Phone: (303) 497-5158
Fax: (303) 497-5224
Email: bruno@boulder.nist.gov

Walter Bryzik
USA Tank-Automotive Command
Propulsion Systems Division
Warren, MI 48397-5000
Phone: (810) 574-6461
Fax: (810) 574-5054
Email: bryzik@cc.tacom.army.mil

George Caledonia
Physical Sciences, Inc.
20 New England Business Center
Andover, MA 01810
Phone: (508) 689-0003
Fax: (508) 689-3232

Herb Carlson
Air Force Office of Scientific Research
875 North Randolph Street
Suite 325, Room 3112
Arlington, VA 22203-1768
Phone: (703) 696-7550
DSN 426-7550
Fax: (703) 696-9556
Email: herb.carlson@afosr.af.mil

Campbell Carter
Air Force Research Laboratory/PRA
1950 Fifth Street
Building 18, Room D224
Wright-Patterson AFB, OH 45433-7251
Phone: (937) 255-7203
DSN 785-7203
Email: Campbell.Carter@wpafb.af.mil

Len Caveny
13715 Piscataway Drive
Ft. Washington, MD 20744
Phone: (301) 292-5319
Fax: (301) 292-3724
Email: lhcaveny@cs.com

Chine I. Chang
Director
U.S. Army Research Office
P.O. Box 12211
Research Triangle Park, NC 27709-2211
Phone: (919) 549-4203
DSN 832-4203
Fax: (919) 549-4348
Email: jchang@aro-emhl.army.mil

Harsha Chelliah
University of Virginia
Department of Mechanical, Aerospace
and Nuclear Engineering
Charlottesville, VA 22903-2442
Phone: (804) 924-6037
Fax: (804) 982-2037
Email: harsha@virginia.edu

Jacqueline Chen
Sandia National Laboratories
MS 9051
P.O. Box 969
Livermore, CA 94551-0969
Phone: (510) 294-2586
Fax: (510) 294-1012
Email: jhchen@sandia.gov

S.Y. Cho
Princeton University
Department of Mechanical
and Aerospace Engineering
Princeton, NJ 08544-5263

S.M. Correa
GE Corporation Research and Development
P.O. Box 8, K1ES112
Schenectady, NY 12301
Phone: (518) 387-5853
Fax: (518) 387-7258
Email: correa@crd.ge.com

Werner Dahm
University of Michigan
Department of Aerospace Engineering
3056 FXB 2140
Ann Arbor, MI 48109-2140
Phone: (734) 764-4318
(734) 761-2026
Fax: (734) 763-0578
Email: wdahm@umich.edu

Eugene Danielson
US Army Tank-Automotive
and Armaments Command
Warren, MI 48397-5000

Ron Davis
National Institute of Standards and Technology
Chemical Science and Technology Lab
Building 221, Room B312
Gaithersburg, MD 20899

John DeLaat
Active Combustion Control Technology
Controls and Dynamics Branch
NASA Glenn Research Center
21000 Brookpark Road
Cleveland, OH 44135
Phone: (216) 433-3744
Email: jdelaat@nasa.gov

Paul Dimotakis
California Institute of Technology
1201 East California Boulevard
MC 301-46
Pasadena, CA 91125
Phone: (626) 395-4456
(626) 794-2594
Fax: (626) 395-4447
Email: dimotakis@caltech.edu

Gregory Dobbs
United Technologies Research Center
Silver Lane, MS 90
East Hartford, CT 06108
Phone: (860) 610-7145

James F. Driscoll
University of Michigan
Department of Aerospace Engineering
3004 FXB Building
Ann Arbor, MI 49109-2118
Phone: (734) 936-0101
Fax: (734) 763-0578
Email: jamesfd@umich.edu

C. Dutton
University of Illinois
Department of Mechanical
and Industrial Engineering
Urbana, IL 61801

Wayne Eckerle
Cummins Engine Company
P.O. Box 3005
Columbus, IN 47202-3005
Email: wayne.a.eckerle@cummins.com

Tarek Echehki
North Carolina State University
Department of Mechanical and
Aerospace Engineering
2601 Stinson Drive - Campus Box 7910
Raleigh, NC 27695-7910
Phone: (919) 515-5238
Fax: (919) 515-7968
Email: techekk@eos.ncsu.edu

J.T. Edwards
Air Force Research Laboratory/PRTG
Building 490, Room 111
1790 Loop Road North
Wright-Patterson AFB, OH 45433-7251
Phone: (937) 255-3524
DSN 785-3524
Fax: (937) 255-1125
Email: james.edwards@wpafb.af.mil

Parviz Famouri
West Virginia University
Department of Computer Science
and Electrical Engineering
P.O. Box 6109
Morgantown, WV 26506
Phone: (304) 293-0405 x 2530
Email: pfamouri@wvu.edu

Gregory W Faris
SRI International
Molecular Physics Laboratory
333 Ravenswood Avenue
Menlo Park, CA 94025-3493
Phone: (650) 859-4131
Fax: (650) 859-6196
Email: gregory.faris@sri.com

Partick Farrell
University of Wisconsin
Engine Research Center
1500 Engineering Drive
Madison, WI 53706
Phone: (608) 263-1686
Email: farrell@engr.wisc.edu

David E. Foster
University of Wisconsin
Engine Research Center
1500 Engineering Drive
Madison, WI 53706
Phone: (608) 263-1617
Email: foster@engr.wisc.edu

Bish Ganguly
Air Force Research Laboratory/PRPE
2645 Fifth Street, Suite 13
Wright-Patterson AFB, OH 45433-7919
Phone: (937) 255-2923
DSN 785-2923
Fax: (937) 656-4095
Email: biswa.ganguly@pr.wpafb.af.mil

Richard G. Gann
National Institute of Standards and Technology
Building and Fire Research Laboratory
100 Bureau Drive, Stop 8650
Gaithersburg, MD 20899-8650
Phone: (301) 975-6866
Fax: (301) 975-4052
Email: rggann@nist.gov

Alan Garscadden
Air Force Research Laboratory/PR
1950 Fifth Street, Building 18A
Wright-Patterson AFB, OH 45433-7251
Phone: (937) 255-2246
DSN 785-2246
Fax: (937) 986-4657
Email: alan.garscadden@pr.wpafb.af.mil

Kresimir Gebert
BKM, Inc.
5141 Santa Fe Street
San Diego, CA 92109
Phone: (858) 270-6760
Email: bkm-inc@worldnet.att.net

Sharath Girimaji
Texas A&M University
Department of Aerospace Engineering
College Station, TX 77843-3141
Phone: (979) 845-1674
Fax: (979) 845-6051
Email: girimaji@aero.tamu.edu

Peyman Givi
University of Pittsburgh
Department of Mechanical Engineering
644 Benedum Hall
Pittsburgh, PA 15261
Phone: (412) 624-9605
Fax: (412) 624-4846
Email: givi@engr.pitt.edu

Irvin Glassman
Princeton University
Department of Aerospace Engineering
Princeton, NJ 08544-5263
Phone: (609) 258-5199
(813) 442-1118
Fax: (609) 258-5963
Email: glassman@princeton.edu

Brendan Godfrey
Air Force Office of Scientific Research
875 North Randolph Street
Suite 325, Room 3112
Arlington, VA 22203-1768
Phone: (703) 696-7553
DSN 426-7553
Fax: (703) 696-9556
Email: brendan.godfrey@afosr.af.mil

Judah Goldwasser
Office of Naval Research
Mechanics Division, Code 333
800 North Quincy Street
Arlington, VA 22217-5660
Phone: (703) 696-2164
DSN 426-2164
Fax: (703) 696-2558
Email: goldwaj@onr.navy.mil

James Gord
Air Force Research Laboratory/PRTS
Building 5, Room 5P23
1790 Loop Road North
Wright-Patterson AFB, OH 45433-7251
Phone: (937) 255-7431
DSN 785-7431
Fax: (937) 656-4570
Email: james.gord@pr.wpafb.af.mil

Jay P. Gore
Purdue University
School of Mechanical Engineering
1003 Chaffee Hall
West Lafayette, IN 47907-1003
Phone: (317) 494-1500
Fax: (317) 494-0530

Larry Goss
Systems Research Labs, Inc.
Research Applications Division
2800 Indian Ripple Road
Dayton, OH 45440-3696
Phone: (513) 252-2706

Frederick Gouldin
Cornell University
Department of Mechanical
and Aerospace Engineering
Ithaca, NY 14853-5692
Phone: (607) 255-5280
Email: fcg2@cornell.edu

Mark Gruber
Air Force Research Laboratory/PRA
1790 Loop Road North
Wright-Patterson AFB, OH 45433-7251
Phone: (937) 255-2175
DSN 785-2175
Fax: (937) 656-4659
Email: Mark.Gruber@afrl.af.mil

Brian K. Gullett
U.S. Environmental Protection Agency
National Risk Management Research Laboratory
Air Pollution Technology Branch (MD-65)
Research Triangle Park, NC 27711
Phone: (919) 541-1534
Fax: (919) 541-0290
Email: gullett.brian@epa.gov

Rajendra Gupta
University of Arkansas
Department of Physics
226 Physics Building
Fayetteville, AK 72701
Phone: (501) 575-5933
Email: rgupta@comp.uark.edu

Nabil S. Hakim
Director, Advanced Engineering
Detroit Diesel Corporation
13400 West Outer Drive, R03-B
Detroit, MI 48239-4001
Phone: (313) 592-7455
Fax: (313) 592-5906

Robert D. Hancock
Air Force Research Laboratory/PRTS
Building 490
1790 Loop Road North
Wright-Patterson AFB, OH 45433-7103
Phone: (937) 255-6814
DSN 785-6814
Fax: (937) 255-1125
Email: hancockr@ward.appl.wpafb.af.mil

Ronald Hanson
Stanford University
Department of Mechanical Engineering
Building 530, Room 112
Stanford, CA 94305-3030
Phone: (650) 723-6850
Fax: (650) 725-4862
Email: hanson@me.stanford.edu

Naeim Henein
Wayne State University
Department of Mechanical Engineering
2121 Engineering Building
Detroit, MI 48201
Phone: (313) 577-3887
Fax: (313) 577-8789
Email: henein@me1.eng.wayne.edu

Robert Holland
United Technologies
Chemical Systems Division
P.O. Box 49028
San Jose, CA 95161-9028
Phone: (408) 224-7656

Tian-Sen Huang
Prairie View A&M University
P.O. Box 307
Prairie View, TX 77446-0307
Phone: (936) 857-2859
Fax: (936) 857-2850
Email: ts_huang@pvamu.edu

Lawrence Hunter
Johns Hopkins University
Applied Physics Laboratory
Johns Hopkins Road
Laurel, MD 20707-6099
Phone: (301) 953-5000 x7406

Frank Hurley
U.S. Army Research Office
P.O. Box 12211
Research Triangle Park, NC 27709-2211
Phone: (919) 549-4432
DSN 832-4432
Fax: (919) 549-4310
Email: hurley@aro-emh1.army.mil

Thomas Jackson
Air Force Research Laboratory/PRSC
Building 18
1950 Fifth Street
Wright-Patterson AFB, OH 45433-7251
Phone: (937) 255-2175
DSN 785-2175
Fax: (937) 656-4659
Email: thomas.jackson@afri.af.mil

Jeff Jagoda
Georgia Institute of Technology
School of Aerospace Engineering
Atlanta, GA 30332-0150
Phone: (404) 894-3060
Email: jeff.jagoda@aerospace.gatech.edu

Jay Jeffries
Stanford University
Department of Mechanical Engineering
Thermophysics Division, Building 520
Stanford, CA 94305-3032
Phone: (650) 736-0007
Fax: (650) 723-1748
Email: Jeffries@Navier.Stanford.edu

Gordon Jensen
United Technologies Chemical
Systems Division
P.O. Box 49028
San Jose, CA 95161-9028
Phone: (408) 365-5552

Craig Johnston
Lockheed Advanced Development Company
Lockheed-Martin Corporation
1011 Lockheed Way
Palmdale, CA 93599-7212

John Kelly
Altex Technologies Corporation
650 Nuttman Road, Suite 114
Santa Clara, CA 95054
Phone: (408) 980-8610

Barry Kiel
Air Force Research Laboratory/PRTC
Building 490, Room 109
1950 Fifth Street
Wright-Patterson AFB, OH 45433-7251
Phone: (937) 255-7272
DSN 785-7272
Email: Barry.Kiel@wpafb.af.mil

G.B. King
Purdue University
Department of Mechanical Engineering
West Lafayette, IN 47907-1288
Phone: (765) 494-6518
Email: kinggb@ecn.purdue.edu

David E. Klett
North Carolina Agricultural
and Technical State University
Department of Mechanical Engineering
Greensboro, NC 27401-3209

Charles Kolb
Aerodyne Research, Inc.
45 Manning Road
Manning Park Research Center
Billerica, MA 01821-3976
Phone: (978) 663-9500
Fax: (978) 663-4918

John Koshoffer
General Electric Aircraft Engines
1 Neuman Way
M.D. G52
Cincinnati, OH 45215
Phone: (513) 243-2995
Fax: (513) 243-1022
Email: john.koshoffer@ae.ge.com

Kenneth Kuo
Pennsylvania State University
Department of Mechanical Engineering
University Park, PA 16802
Phone: (814) 865-6741
Fax: (814) 863-3203

John Larue
University of California, Irvine
Department of Mechanical Engineering
Irvine, CA 92717

Allan Laufer
Office of Energy Research
U.S. Department of Energy
19901 Germantown Road
Germantown, MD 20874
Phone: (202) 903-5820
Email: Allan.Laufer@oer.doe.gov

Normand Laurendeau
Purdue University
School of Mechanical Engineering
West Lafayette, IN 47907-1288
Phone: (765) 494-2713
Fax: (765) 494-0539
Email: Laurende@ecn.purdue.edu

C.K. Law
Princeton University
Department of Mechanical
and Aerospace Engineering
Princeton, NJ 08544-5263
Phone: (609) 258-5271
Fax: (609) 258-6233
Email: cklaw@princeton.edu

C.C. Lee
Environmental Protection Agency
Cincinnati, OH 45268
Phone: (513) 569-7520

Anthony Leonard
California Institute of Technology
Graduate Aeronautical Labs
Pasadena, CA 91125
Phone: (626) 395-4465

Arthur Lewis
University of Dayton Research Institute
Aerospace Mechanics Division
300 College Park
Dayton, OH 45469-0110
Phone: (937) 229-4235
Fax: (937) 229-4251

Mark Lewis
AF/ST
1075 Air Force Pentagon
Washington, DC 20330-1075
Phone: (703) 697-7842
DSN 227-7842
Fax: (703) 697-5154
Email: mark.lewis@pentagon.af.mil

Goang Liaw
Alabama A&M University
Department of Civil Engineering
P.O. Box 367
Normal, AL 35762
Phone: (205) 851-5565

Timothy Lieuwen
Georgia Institute of Technology
School of Aerospace Engineering
Atlanta, GA 30332-0150
Phone: (404) 894-3041
Fax: (404) 894-2760
Email: tim.lieuwen@aerospace.gatech.edu

Peter Lindstedt
Imperial College, London
Department of Mechanical Engineering
Exhibition Road
London SW7 2 BX England, UK
Email: p.lindstedt@imperial.ac.uk

Mark A. Linne
Lund Institute of Technology
Department of Combustion Physics
P.O. Box 118
S-221 00 Lund, Sweden,
Phone: +46 (0) 46-2224756
Email: mark.linne@forbrf.lth.se

Thomas A. Litzinger
Pennsylvania State University
Department of Mechanical Engineering
0201 Hammond Building
University Park, PA 16802
Phone: (814) 865-4015
Email: tal2@psu.edu

Lyle N. Long
Pennsylvania State University
Department of Aerospace Engineering
233 Hammond Building
University Park, PA 16802
Phone: (814) 865-1172
Fax: (814) 865-7092
Email: ln1@psu.edu

Jeffery Lovett
Pratt and Whitney
400 Main Street
MS 163-03
East Hartford, CT 6108
Phone: (860) 557-0559
Email: jeffery.lovett@pw.utc.com

Kevin Lyons
North Carolina State University
Department of Mechanical
and Aerospace Engineering
P.O. Box 7910
Raleigh, NC 27695
Phone: (919) 515-5293
Fax: (919) 515-7968
Email: lyons@eos.ncsu.edu

Nick Makris
SA-ALC/SFT
Kelly AFB, TX 78241-5000
Phone: AV945-8212
Fax: AV945-9964

David Mann
U.S. Army Research Office
P.O. Box 12211
4300 South Miami Boulevard
Research Triangle Pk, NC 27709-2211
Phone: (919) 549-4249
DSN 832-4249
Fax: (919) 549-4310
Email: david.mann1@us.army.mil

Nagi Mansour
NASA Ames Research Center Computational
Fluid Mechanics Branch, RFT 202A-1
Moffett Field, CA 94035
Phone: (415) 604-6420

John Marek
NASA Glenn Research Center
MS 5-11
21000 Brookpark Road
Cleveland, OH 44135-3127
Phone: (216) 433-3584
Fax: (216) 433-3000
Email: cecil.j.marek@lerc.nasa.gov

Jay Martin
University of Wisconsin, Madison
Engine Research Center
1500 Engineering Drive
Madison, WI 53706
Phone: (608) 263-9460
Fax: (608) 262-6707
Email: martin@engr.wisc.edu

James McDonald
Naval Research Laboratory
Chemistry Division
Code 6110
Washington, DC 20375-5342
Phone: (202) 767-3340

Kevin McNesby
Army Research Laboratory
Army Research Office
P.O. Box 12211
Research Triangle Park, NC 27709-2211
Phone: (410) 306-0715
Email: mcnesby@arl.army.mil

A.M. Mellor
Vanderbilt University
Department of Mechanical
and Materials Engineering
512 Kirkland Hall
Nashville, TN 37240
Phone: (615) 343-6214
Fax: (615) 343-6687

Suresh Menon
Georgia Institute of Technology
School of Aerospace Engineering
270 Ferst Drive
Atlanta, GA 30332-0150
Phone: (404) 894-9126
Fax: (404) 894-2760
Email: suresh.menon@aerospace.gatech.edu

Hameed Metghalchi
Northeastern University
Department of Mechanical
and Industrial Engineering
360 Huntington Avenue
Boston, MA 2115
Phone: (617) 373-2973
Fax: (617) 373-2921
Email: metghal@coe.neu.edu

Michael M. Micci
Pennsylvania State University
Department of Aerospace Engineering
233 Hammond Building
University Park, PA 16802
Phone: (814) 863-0043
(814) 692-8751
Fax: (814) 865-7092
Email: micci@henry2.aero.psu.edu

Andrzej Miziolek
Army Research Laboratory
AMSRL-WT-PC
Aberdeen Proving Gnd, MD 21005-5066
Phone: (410) 278-6157
Fax: (410) 278-6094
Email: miziolek@arl.army.mil

Arje Nachman
Air Force Office of Scientific Research
875 North Randolph Street
Suite 325, Room 3112
Arlington, VA 22203-1768
Phone: (703) 696-8427
DSN 426-8427
Fax: (703) 696-8450
Email: arje.nachman@afosr.af.mil

Herbert Nelson
Naval Research Laboratory
Code 6110, Chemistry Division
4555 Overlook Avenue, S.W.
Washington, DC 20375-5342
Phone: (202) 767-3686

Ozden Ochoa
Air Force Office of Scientific Research
875 North Randolph Street
Suite 325, Room 3112
Arlington, VA 22203-1768
Phone: (703) 696-8457
DSN 426-8457
Fax: (703) 696-8451
Email: ozden.ochoa@afosr.af.mil

Elaine Oran
U.S. Naval Research Laboratory
LCP&FD, Code 6404
4555 Overlook Avenue, S.W.
Washington, DC 20375-5344
Phone: (202) 767-2960
Fax: (202) 767-4798
Email: ORAN@lcp.nrl.navy.mil

T.E. Parker
Colorado School of Mines
Engineering Division
Golden, CO 80401-1887
Phone: (303) 273-3657
Fax: (303) 273-3602
Email: tparker@mines.colorado.edu

Phillip H. Paul
Sandia National Laboratories
MS 9051
P.O. Box 969
Livermore, CA 94551-9051
Phone: (510) 294-1465
Fax: (510) 294-1012
Email: phpaul@sandia.gov

Lisa Pfefferle
Yale University
Department of Chemical Engineering
New Haven, CT 06520-8286
Phone: (203) 432-2222
Fax: (203) 432-7232
Email: pfefferle@htcre.eng.yale.edu

Emil Pfender
The University of Minnesota
Department of Mechanical Engineering
125 Mechanical Engineering
Minneapolis, MN 55455

Robert Pitz
Vanderbilt University
Department of Mechanical and Materials Engineering
Nashville, TN 37235
Phone: (615) 322-0209
Fax: (615) 343-8730
Email: pitzrw@ctrvan.vanderbilt.edu

S.B. Pope
Cornell University
Department of Mechanical
and Aerospace Engineering
Ithaca, NY 14853-7501
Phone: (607) 255-4314
Fax: (607) 255-1222
Email: pope@mae.cornell.edu

David Pratt
Air Force Research Laboratory/VAS
Building 45 Annex
2130 Eighth Street, Suite 1
Wright-Patterson AFB, OH 45433-7542
Phone: (937) 255-5042
DSN 785-5042
Fax: (937) 656-7915
Email: David.Pratt@va.af.mil

Ala Qubbaj
University of Texas-Pan American
Department of Mechanical Engineering, ENB 3230
1201 West University Drive
Edinburg, TX 78539-2999
Phone: (956) 318-5220
Email: qubbaj@panam.edu

Mohan K. Razdan
Rolls-Royce Company
P.O. Box 420
Speed Code T10B
Indianapolis, IN 46206-0420
Phone: (317) 230-6404
Fax: (317) 230-3691
Email: mohan.razdan@rolls-royce.com

Robert Reed
Sverdrup Technology, Inc.
AEDC
1099 Avenue C
Arnold AFB, TN 37389-9013
Phone: (615) 454-4648
DSN 340-4648
Fax: (615) 454-6317

Rolf D. Reitz
University of Wisconsin
Department of Mechanical Engineering
1500 Johnson Drive
Madison, WI 53706
Phone: (608) 262-0145
Fax: (608) 262-6717

Kyung T. Rhee
Rutgers, The State University of New Jersey
Department of Mechanical
and Aerospace Engineering
Piscataway, NJ 08854-0909
Phone: (732) 445-3651
Email: KTRhee@jove.rutgers.edu

William Roberts
North Carolina State University
Department of Mechanical and
Aerospace Engineering
Box 7910
Raleigh, NC 27695-7910
Phone: (919) 515-5294
Fax: (919) 515-7968
Email: wlrobert@eos.ncsu.edu

Gerald A. Roffe
GASL
77 Raynor Avenue
Ronkonkoma, NY 11779

W.M. Roquemore
Air Force Research Laboratory/PRTS
Building 5
Wright-Patterson AFB, OH 45433-7251
Phone: (937) 255-6813
DSN 785-6813
Fax: (937) 656-4570
Email: melvyn.roquemore@wpafb.af.mil

Daniel Rosner
Yale University
Department of Chemical Engineering
New Haven, CT 06520-8286
Phone: (203) 432-4391
Fax: (203) 432-7232
Email: daniel.rosner@yale.edu

Gabriel Roy
Office of Naval Research
Mechanics Division, Code 1132
800 North Quincy Street
Arlington, VA 22217-5660
Phone: (703) 696-4406
Fax: (703) 696-0934
Email: roy@ocnr-hq.navy.mil

Robert C. Ryder
Flow Parametrics, LLC
15 Debra Drive
Bear, DE 19701
Phone: (302) 838-7368
Fax: (303) 838-7369
Email: rryder@flowparametrics.com

Kurt Sacksteder
NASA Glenn Research Center
MS 500-217
21000 Brookpark Road
Cleveland, OH 44135
Phone: (216) 433-2857

Mohammad Samimy
Ohio State University
Department of Mechanical Engineering
206 West 18th Street
Columbus, OH 43210-1107
Phone: (614) 422-6988
(614) 848-9439
Fax: (614) 292-3163
Email: msamimy@magnus.acs.ohio-state.edu

Lakshmi Sankar
Georgia Institute of Technology
School of Aerospace Engineering
Atlanta, GA 30332
Phone: (404) 894-3014

Domenic Santavicca
Pennsylvania State University
Propulsion Engineering Research Center
106 Research Building East - Bigler Road
University Park, PA 16802-2320
Phone: (814) 863-1863

R.J. Santoro
Pennsylvania State University
Department of Mechanical Engineering
University Park, PA 16802-2320
Phone: (814) 863-1285
Fax: (814) 865-3389
Email: rjs2@email.psu.edu

Sutanu Sarkar
University of California
Department of Applied Mechanics
and Engineering Science, MC 0411
La Jolla, CA 92093-0411
Phone: (858) 534-8243
Fax: (858) 534-7599
Email: ssarkar@ucsd.edu

Frederick Schauer
Air Force Research Laboratory/PRTS
Building 490, Room 112
1790 Loop Road North
Wright-Patterson AFB, OH 45433-7251
Phone: (937) 255-6462
DSN 785-6462
Fax: (937) 255-1125
Email: frederick.schauer@wpafb.af.mil

Peter Schihl
USA Tank Automotive Command
Propulsion Systems Division
Warren, MI 48397-5000
Email: schihlp@tacom.army.mil

John Schmisser
Air Force Office of Scientific Research
875 North Randolph Street
Suite 325, Room 3112
Arlington, VA 22203-1768
Phone: (703) 696-6962
DSN 426-6962
Fax: (703) 696-8451
Email: john.schmisser@afosr.af.mil

Ernest Schwarz
USA Tank-Automotive Command
Propulsion Systems Division
Warren, MI 48397-5000
Phone: (810) 574-5656
Fax: (810) 574-5054
Email: schwarze@cc.tacom.army.mil

Jerry Seitzman
Georgia Institute of Technology
School of Aerospace Engineering
Atlanta, GA 30332-0150
Phone: (404) 894-0013
Fax: (404) 894-2760
Email: jerry.seitzman@ae.gatech.edu

Kalyanasundaram Seshadri
University of California
Center for Energy and Combustion Research, 0407
La Jolla, CA 92093-0407
Phone: (619) 534-4876
Email: seshadri@ames.ucsd.edu

Robert Shaw
U.S. Army Research Office
Division of Chemical and Biological Sciences
Research Triangle Park, NC 27709-2211
Phone: (919) 549-0641

Adam Siebenhaar
Aerojet Propulsion Division
P.O. Box 13222
Sacramento, CA 95813-6000

William Sirignano
University of California, Irvine
Department of Mechanical
and Aerospace Engineering
Irvine, CA 92697-3975
Phone: (949) 824-3700
Fax: (949) 824-3773
Email: sirignan@uci.edu

Davey Smith
Northrop Grumman Corporation
B-2 Division Dayton Office
2850 Presidential Drive, Suite 100
Fairborn, OH 45324

Gregory Smith
SRI International
Department of Chemical Kinetics
333 Ravenswood Avenue
Menlo Park, CA 94025-3493
Phone: (415) 859-3496

Kenneth A. Smith
Massachusetts Institute of Technology
Department of Chemical Engineering
Room 66-540
Cambridge, MA 02139
Phone: (617) 253-1973
Fax: (617) 253-2701
Email: kas@mit.edu

Mitchell Smooke
Yale University
Department of Mechanical Engineering
205 Becton Center
15 Prospect Street
New Haven, CT 06520
Phone: (203) 432-4344
Fax: (203) 432-6775
Email: mitchell.smooke@yale.edu

Judi Steciak
University of Idaho, Boise
800 Park Boulevard
Boise, ID 83712-7742
Phone: (208) 364-4080
Fax: (208) 387-1246
Email: jsteciak@uidaho.edu

David Stewart
University of Illinois
Department of Theoretical and Applied Mechanics
Urbana, IL 61801

Geoffrey J. Sturgess
Email: gsturgess@aol.com

G Sullins
Johns Hopkins University
Applied Physics Laboratory
Johns Hopkins Road
Laurel, MD 20707-6099
Phone: (301) 953-5000

Rodney Tabaczynski
Director, Power Train Research Laboratory
Ford Motor Research Laboratory
3623 Scientific Research Lab
P.O. Box 2053
Dearborn, MI 48121-2053
Phone: (313) 322-8930

Douglas Talley
Air Force Research Laboratory/PRSA
10 East Saturn Boulevard
Edwards AFB, CA 93524-7660
Phone: (661) 275-6174
DSN 525-6174
Fax: (661) 275-6245
Email: Douglas.Talley@ple.af.mil

Jefferson W. Tester
Massachusetts Institute of Technology
Energy Laboratory
Room E40-455
Cambridge, MA 02139
Phone: (617) 253-3401
Fax: (617) 253-8013
Email: testerel@mit.edu

Julian Tishkoff
Air Force Office of Scientific Research
875 North Randolph Street
Suite 325, Room 3112
Arlington, VA 22203-1768
Phone: (703) 696-8478
DSN 426-8478
Fax: (703) 696-8451
Email: julian.tishkoff@afosr.af.mil

Chenning Tong
Clemson University
Department of Mechanical Engineering
248 Fluor Daniel EIB
Clemson, SC 29634-0921
Phone: (864) 656-7225
Fax: (864) 656-4435
Email: ctong@ces.clemson.edu

Michael Trenary
The University of Illinois
Department of Chemistry
Chicago, IL 60680

James Trolinger
MetroLaser
2572 White Road
Irvine, CA 92614
Phone: (949) 553-0688
Fax: (949) 553-0495
Email: jtrolinger@vmsa.oac.uci.edu

Gretar Tryggvason
The University of Michigan
Department of Mechanical Engineering
and Applied Mechanics
2350 Hayward, Room 2250
Ann Arbor, MI 48109-2125
Phone: (734) 763-1049
Fax: (734) 764-4256
Email: gretar@umich.edu

Wing Tsang
National Institute of Standards and Technology
Physical and Chemical Properties Division
Route 270 and Quince Orchard Road
Gaithersburg, MD 20899
Phone: (301) 975-2507
Email: wing.tsang@nist.gov

Frank Tully
U.S. Department of Energy
SC-141
19901 Germantown Road
Germantown, MD 20874
Phone: (301) 903-5998
Email: Frank.Tully@science.doe.gov

Jeffrey Turcotte
Air Force Office of Scientific Research
875 North Randolph Street
Suite 325, Room 3112
Arlington, VA 22203-1768
Phone: (703) 696-7555
DSN 426-7555
Fax: (703) 696-9556
Email: jeffrey.turcotte@afosr.af.mil

Mark Valco
Army Research Laboratory
Propulsion Directorate, MS 49-1
NASA Glenn Research Center
Cleveland, OH 44135-3127
Phone: (216) 433-3717
Fax: (216) 433-2182
Email: aamark@lims01.lerc.nasa.gov

David Van Wie
The Johns Hopkins University
Applied Physics Laboratory
11100 Johns Hopkins Road
Laurel, MD 20723-6099
Phone: (240) 228-5194
Fax: (240) 228-5850
Email: David.VanWie@jhuapl.edu

Angela Violi
University of Michigan
Department of Mechanical Engineering
2150 GG Brown
Ann Arbor, MI 48109-2125
Phone: (734) 615-6448
Fax: (734) 647-3170
Email: avioli@umich.edu

Ian Waitz
Massachusetts Institute of Technology
Department of Aeronautics and Astronautics
Building 33-207
77 Massachusetts Avenue
Cambridge, MA 02139-4307
Phone: (617) 253-0218
Fax: (617) 258-7566
Email: iaw@mit.edu

Hai Wang
University of Southern California
Department of Mechanical
and Aerospace Engineering
OHE 400, Mail Code 1453
Los Angeles, CA 90089
Phone: (213) 740-0499
Email: haiw@usc.edu

Zhicheng Wang
Clark Atlanta University
223 James P. Brawley Drive, S.W.
Atlanta, GA 30314
Phone: (404) 880-6125
Fax: (404) 880-6615
Email: zhicheng_wang@hotmail.com

Charles Westbrook
Lawrence Livermore National Laboratories
P.O. Box 808
Livermore, CA 94551
Phone: (925) 422-4108
Fax: (925) 422-2644
Email: westbrook1@llnl.gov

Phillip R. Westmoreland
University of Massachusetts
Department of Chemical Engineering
Amherst, MA 01003
Phone: (413) 545-1750
(413) 545-2507
Fax: (413) 545-1647
Email: westm@ecs.umass.edu

Skip Williams
Air force Research Laboratory/PRAS
1950 Fifth Street
Building 18D, Room D234
Wright-Patterson AFB, OH 45433-7251
Phone: (937) 255-7292
DSN 785-7292
Email: skip.williams@wpafb.af.mil

Bernard T. Wolfson
Wolfson Associates International
4797 Lake Valencia Blvd West
Palm Harbor, FL 33563
Phone: (813) 786-3007

Mary J. Wornat
Louisiana State University
Department of Chemical Engineering
South Stadium Drive
Baton Rouge, LA 70803
Phone: (225) 578-7509
Fax: (225) 578-1476
Email: mjwornat@lsu.edu

J.M. Wu
University of Tennessee
Space Institute
Tullahoma, TN 37388

Richard Yetter
Pennsylvania State University
Department of Mechanical and
Nuclear Engineering
State College, PA 16802
Phone: (814) 863-6375
Email: rayetter@psu.edu

Joseph Zelina
Air Force Research Laboratory/PRTC
Building 490, Room 109
1790 Loop Road, North
Wright-Patterson AFB, OH 45433-7251
Phone: (937) 255-7487
DSN 785-7487
Email: joseph.zelina@wpafb.af.mil

Ben Zinn
Georgia Institute of Technology
School of Aerospace Engineering
Atlanta, GA 30332-0150
Phone: (404) 894-3033
Fax: (404) 894-2760
Email: ben.zinn@aerospace.gatech.edu